TECHNISCHE
UNIVERSITÄT
WIEN

VIENNA
UNIVERSITY OF
TECHNOLOGY

**Dissertation**

# Design, Construction and Commissioning of the CMS Tracker at CERN and Proposed Improvements for Detectors at the Future International Linear Collider

ausgeführt zum Zwecke der Erlangung des akademischen Grades eines Doktors der technischen Wissenschaften unter der Leitung von

Univ.Doz. Dipl.-Ing. Dr. techn. Manfred KRAMMER

Institut für Hochenergiephysik
der Österreichischen Akademie der Wissenschaften
und
Atominstitut der Österreichischen Universitäten

eingereicht an der Technischen Universität Wien
Fakultät für Physik

von

## Dipl.-Ing. Thomas Bergauer

Matrikelnummer: 9525273
Schumanngasse 67/3/2
1170 Wien

Wien, am 17. März 2008

# Kurzfassung

Der CMS (*Compact Muon Solenoid*)-Detektor ist ein Experiment der Teilchenphysik von gewaltigem Ausmaß und befindet sich an einem der vier Proton-Proton-Kollisionspunkte des *Large Hadron Collider* (LHC) am CERN, der Europäischen Organisation für Kernforschung in Genf (Schweiz). Der LHC selbst ist mit seinen 27 km Umfang nicht nur der größte Teilchenbeschleuniger der Welt, er setzt auch neue Maßstäbe, was seine Schwerpunktsenergie von $2 \times 7$ TeV betrifft.

Der CMS Detektor selbst ist aus mehreren Teilen aufgebaut. Der in dieser Arbeit hauptsächlich besprochene Teil ist die innere Spurkammer, genannt *Tracker*. Er hat einen Durchmesser von 2,4 m und eine Länge von 5,4 m. Die in ihm verbauten 15 000 Detektormodule, welche aus mehr als 24 000 Siliziumsensoren bestehen, ergeben eine Siliziumfläche von 206 m², um geladene Teilchen zu detektieren, die bei Proton-Proton-Kollisionen entstehen. Der Tracker ist starker Strahlenbelastung ausgesetzt und arbeitet in einem 3.8 Tesla starken solenoiden Magnetfeld bei $-10°$C.

Diese Dissertation wurde am Institut für Hochenergiephysik der österreichischen Akademie der Wissenschaften (abgekürzt *HEPHY*) geschrieben, welches seit mehr als zehn Jahren an der Entwicklung und Konstruktion des CMS Trackers beteiligt ist. Sie behandelt die Qualitätsprüfung der Siliziumsensoren und beschreibt die am Institut durchgeführten Messungen an diesen, welche maßgeblich von mir entwickelt und überwacht wurden. Weiters wird die Datenbank beschrieben, in der diese Messergebnisse gespeichert wurden und die zur Inventarisierung und Logistik der mehr als 200 000 Komponenten des CMS Trackers dient. Ich war nicht nur an ihrem Design beteiligt, sondern habe auch Werkzeuge zur Datenabfrage programmiert. In einem weiteren Kapitel werden die Module für die Endkappen des Trackers (TEC) vorgestellt und Probleme während der Konstruktionsphase diskutiert. Die von mir entwickelten Hilfsmittel zur Überwachung und Steuerung der Modulproduktion werden ebenfalls präsentiert. Nach einem kurzen Überblick über die größeren TEC-Substrukturen (genannt *petals*), werden letztendlich die durchgeführten Tests an einem Teil des gesamten Trackers ("*slice test*") dargestellt, an denen ich beteiligt war.

Der Bau des CMS Trackers war an strenge Auflagen gebunden, was Qualität und Ausführung betrifft. Das lösungsorientierte Arbeiten bei auftretenden Problemen führte dazu, daß schlußendlich viele Erfahrungen gesammelt werden konnten. Um dieses Wissen für mögliche neue Experimente am geplanten *International Linear Collider* (ILC) zu sichern, wird abschließend auf Probleme des vorliegenden Designs eingegangen sowie potentielle Optimierungen diskutiert.

# Abstract

The CMS (*Compact Muon Solenoid*) detector is a huge particle physics experiment located at one of the four proton-proton interaction points of the *Large Hadron Collider* (LHC) at CERN, the European Organization for Nuclear Research (Geneva, Switzerland). With 27 km circumference it is the not only the largest particle accelerator in size, but with a *center of mass energy* of $2 \times 7$ TeV it will also set the world record in terms of energy.

The inner tracking system of the CMS experiment has a diameter of 2.4 m and a length of 5.4 m and is representing the largest silicon tracker ever built. About 15,000 detector modules consisting of more than 24,000 silicon sensors create a silicon area of 206 m$^2$ to detect charged particles from proton collisions. They are placed on a rigid carbon fibre structure in the center of the experiment, and have to operate reliably within a harsh radiation environment and the working conditions of a 3.8 Tesla solenoid magnetic field at $-10°$C temperature.

This thesis was conducted at the Institute of High Energy Physics of the Austrian Academy of Sciences (HEPHY), which has been involved in the design and construction of the CMS Tracker for more than 10 years. It reviews the quality assurance scheme established for testing the silicon sensors and describes the measurements done within this framework, which were developed and supervised mostly by myself. Furthermore, the *Tracker Construction Database* is presented, which was used to store not only these measurement results, but also helped with the logistics of the approximately 200 000 components of the CMS Tracker. I was involved in its design and developed tools for data retrieval. In the next chapter, the modules for the Tracker End Caps (TEC) are presented and problems during their construction are discussed. The tools which I developed for supervision and production steering are presented. After a short overview about larger TEC substructures called *petals*, the tests of a fraction of the whole tracker (called *slice test*) at CERN – to which I also contributed – are reviewed.
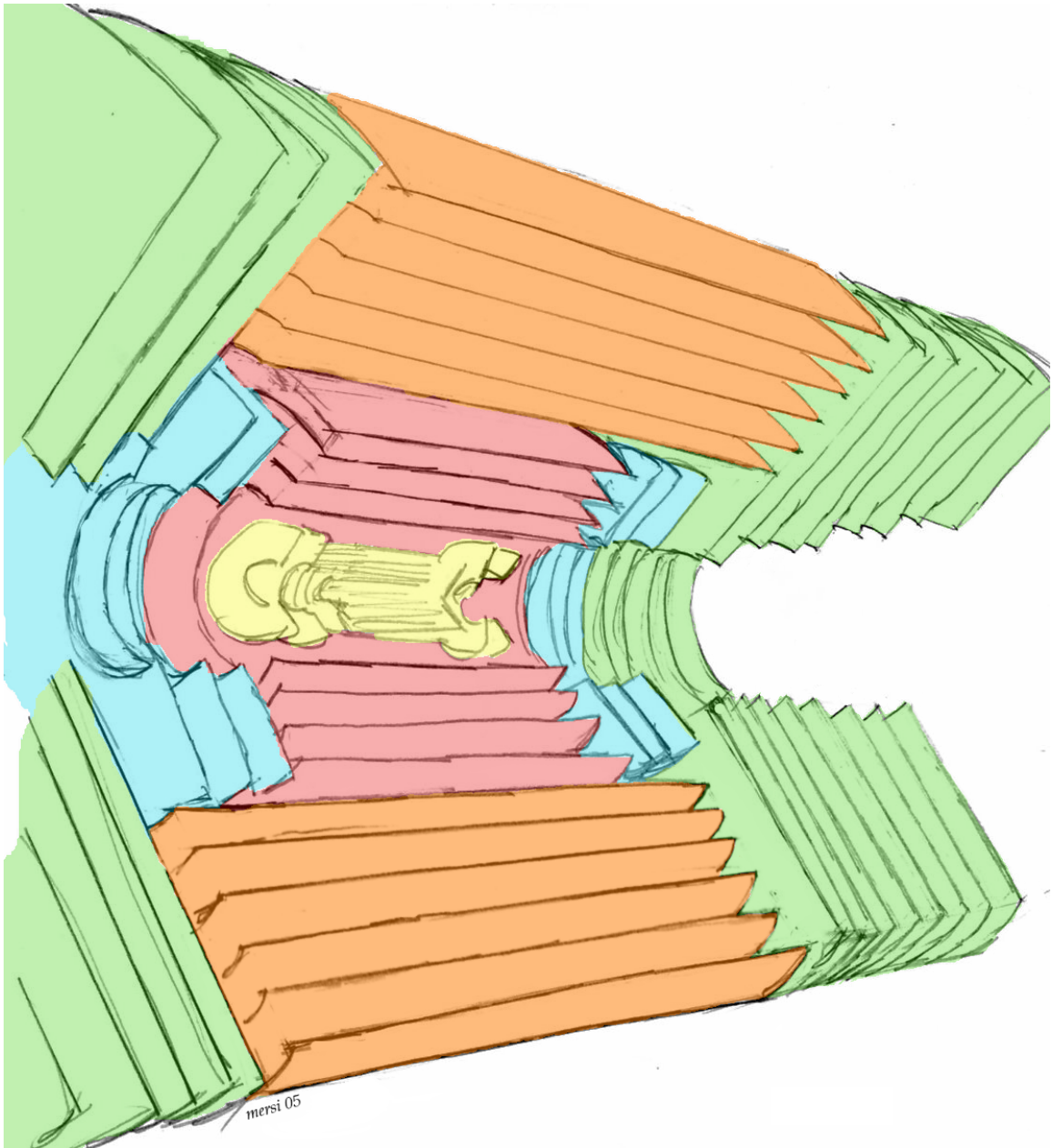
The stringent requirements imposed on the quality and performance of the CMS Tracker required the solution of various problems and led to rich experience in semiconductor detectors for high energy physics experiments and its related large-scale quality assurance. To preserve this knowledge for new future detectors at the proposed *International Linear Collider* (ILC), this thesis concludes with a discussion about conceptual problems in the current design and proposes potential improvements.

# Contents

# The (long) story about the largest

# Silicon Strip Tracker in the World

# 1 Introduction

> My goal is simple. It is complete
> understanding of the universe,
> why it is as it is and why it exists
> at all.
>
> *(Stephen Hawking)*

The Standard Model of Particle Physics [1] has proven to be a successful theory to describe nature. However, there are still some open questions. One of the most important problems is the question for the origin of mass. The Standard Model does not predict a mass for fermions and the exchange particles of the weak interaction, the *W* and *Z*-bosons. However, it was shown from measurements at former particle accelerators, that these bosons are some of the heaviest known particles [2, 3]. Thus, the so-called Higgs mechanism was postulated to solve this problem by explaining the masses of the particles by its coupling to an additional scalar field, the Higgs field [4]. As a consequence, an additional particle, called the Higgs boson *H*, must exist. Its mass $m_H$, however, is not predicted by this theory.

Previous particle physics experiments like the *Large Electron Positron Collider* (LEP) were not able to detect the Higgs boson directly, but defined a lower limit of $114.4\,\mathrm{GeV}/\mathrm{c}^2$ for the Higgs mass by direct exclusion [5]. Theoretical considerations combined with other constraints define an upper limit of approximately $1\,\mathrm{TeV}/\mathrm{c}^2$.

## 1.1 The Large Hadron Collider

The direct search for the Higgs boson and the determination of its mass is one of the main objectives of the new *Large Hadron Collider* (LHC), currently being commissioned at CERN[1]. Its center-of-mass energy has been increased by a factor of 70 compared to its predecessor LEP. At the LHC, particles with masses within the predicted range of the Higgs particle and even beyond will be artificially produced for the first time.

Beside this most prominent objective, there is a wide variety of other possible discoveries in this energy range, which would then require an extension of the Standard Model. One candidate is the Supersymmetry (SUSY) theory, which postulates a supersymmetric bosonic partner to each fermion and vice versa. If it exists, a broken symmetry must allow the supersymmetric *sparticles* to be so heavy. It would solve to the so-called hierarchy problem, where huge correlations of the particles'

---

1. *CERN*, (literally for *Conseil Européen pour la Recherche Nucléaire*) is the European Organization for Nuclear Research, located near Geneva (Switzerland). http://www.cern.ch/

masses are expected and help to understand the unification of the weak interaction, the strong interaction and electromagnetism on the *Grand Unification Theory* (GUT) scale of $10^{16}$ eV. The LHC will also lead to a deeper understanding of the *Charge-Parity* (CP) violation and the quark-gluon plasma as described within quantum chromodynamics (QCD).

The LHC will be the first particle accelerator to reach energies in the Terascale with a center-of-mass energy of $2 \times 7$ TeV at a design luminosity of $10^{34}$ cm$^{-2}$ s$^{-1}$. If there is a Higgs boson, it is almost certain that it will be discovered there, together with potential other phenomena, like the evidence of extra dimensions or Supersymmetry. However, it will be difficult for the LHC to measure the spin and parity of the Higgs particle precisely. Because of its nature as a proton-proton collider and because of the quark-gluon-structure of protons, the collision energy is not well defined. A new experimental problem will be the high multiplicity in each event. Already at the luminosity for the LHC startup phase of $2 \cdot 10^{33}$ cm$^{-2}$ s$^{-1}$ seven $pp$ interactions per bunch collision will take place on average. This number will increase to 35 at high luminosities, creating thousands of particles per event. All these interactions must be, at least on a statistical basis, separated.

## 1.2 The International Linear Collider

Physics life is much easier in an $e^+ e^-$ collider, as it was for the decommissioned Large Electron Positron Collider. Because of the point-like nature of the lepton, the center-of-mass energy of such collisions is well defined and there are only a few collision products which need to be recorded and analyzed. However, there is one drawback: Electrons lose a large amount of their energy by synchrotron radiation in a circular collider. This issue can only be avoided by a linear accelerator.

The proposed *International Linear Collider* (ILC) will take advantage of both, a center-of-mass energy in the Terascale range without any limitation caused by synchrotron radiation and the 'clean' environment of lepton collisions. It will allow measurements of the spin and parity of the Higgs particle more accurately than at the LHC. If there is more than one decay channel of the Higgs, the LHC experiments will determine the branching ratios, but the ILC will measure these couplings to quarks and vector bosons at the few percent level, much more precise than the LHC can do.

The precision measurements imply new requirements on both theoretical and experimental accuracies. While the first needs more precise theoretical calculations for standard, Higgs and SUSY processes, a similar effort needs to eliminate all known instrumental limitations which could compromise the precision of the measurements, like momentum resolution and reconstruction of short-lived particles. Thus, the detectors at the ILC need to have tremendous accuracy and thus need new techniques to achieve this ambitious goal.

# 2  The CMS Experiment at the LHC

Without suitable detectors, a
particle accelerator is about as
useful as a microscope without an
eyepiece.

## 2.1  The Large Hadron Collider

The Large Hadron Collider (LHC) is a ringlike particle accelerator with a circumference of 26.7
km (see figure 2.1).  It is located around 100 meters below the Earth's surface in the tunnel of
the former LEP accelerator at CERN. It is designed to gear up two beams of protons in opposite
directions up to a kinetic energy of 7 TeV per beam, resulting in a center-of-mass energy of 14 TeV
during their collision.  This is the highest energy ever reached in man-made machines.  More than
1200 thirty-meter long superconducting dipole magnets with a magnetic field of 8.33 Tesla are
necessary to keep the protons on their orbit, each cooled by liquid Helium to a temperature below
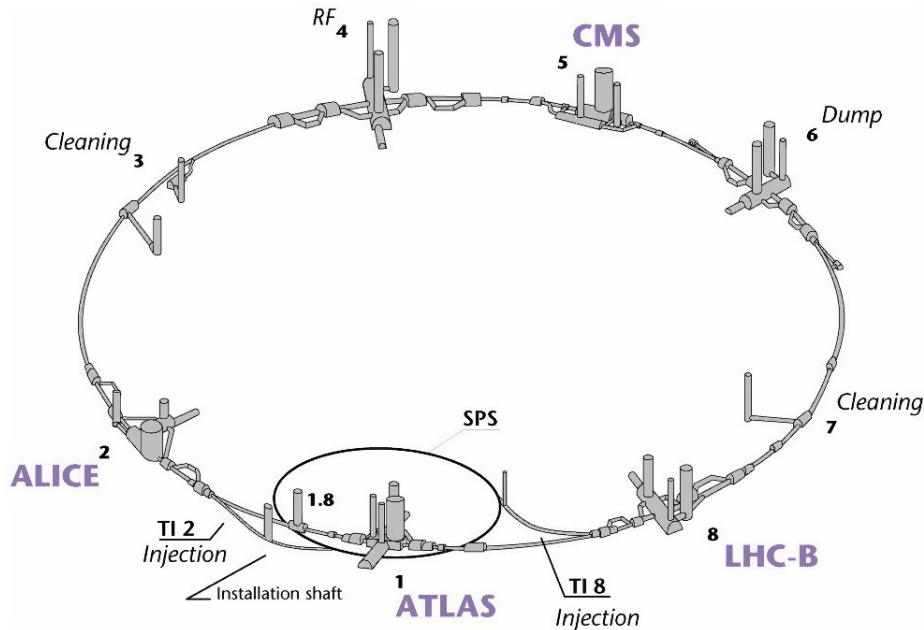2 K.



**Figure 2.1:** The LHC accelerator with its largest pre-accelerator, the SPS, and its four experiments:  ATLAS (access
point 1), ALICE (point 2), CMS (point 5) and LHC-B (point 8).

Several pre-accelerators like the *Linear Accelerator 2* (Linac2), the *Proton Synchrotron Booster* (PSB), the *Proton Synchrotron* (PS) and the *Super Proton Synchrotron* (SPS) are necessary to accelerate protons up to an energy of 450 GeV. At this energy, they are filled into the LHC in up to 2808 bunches, each consisting of up to $1.15 \cdot 10^{11}$ protons. The particles are then brought to their nominal energy during an approximately 20 minutes long phase of acceleration, which is continued by several hours, when the machine operates as a storage ring. During this time the protons are focussed to intersect and collide every 25 ns in four distinct locations, the interaction points (IPs). Around them, four large detector systems have been built to measure the particles produced by the collisions.

Since the LHC ring is located below the Earth's surface, access to the tunnel and the detector systems is limited to shafts and elevators. Eight access points called P1 to P8 are located along the ring, four of which contain the experiments. Two of them are dedicated to a special field of physics. The ALICE[1] detector was built to investigate the collisions of heavy ions to search for quark-gluon-plasma. This is a very special state of matter that only exists at very high densities of strongly interacting particles. Heavy ion collisions require a special operation mode of the LHC, which is foreseen for approximately one or two months per year, where heavy ions – mostly lead nuclei – are accelerated. The LHCb[2] detector is designed for precision measurements of CP violation and rare decays in events including *b*-quarks.

The two other experiments, ATLAS[3] and CMS[4], are so called general-purpose detectors, built for the investigation of a wide field of physics, such as the search for the Higgs particle or Supersymmetry. Although their objectives are identical, both detectors are different in many details, thus avoiding systematic errors if only one single technique was used for both. While ATLAS is located just opposite the CERN main site at the LHC access point 1 (P1), CMS is based near the village of Cessy (France) at point 5 (P5).

The collision rate $R$ in the LHC is proportional to the interaction cross-section $\sigma_{\text{int}}$,

$$R = \mathcal{L}\,\sigma_{\text{int}} \quad , \tag{2.1}$$

with the factor $\mathcal{L}$ called luminosity [1]. When two bunches, each containing $n$ particles, collide with the frequency $f$, the luminosity is given by

$$\mathcal{L} = f \frac{n^2}{4\pi\sigma_x\sigma_y} \tag{2.2}$$

where $\sigma_x$ and $\sigma_y$ characterize the beam spreads in horizontal and vertical directions. The LHC is designed for a nominal luminosity of $10^{34}\,\text{cm}^{-2}\,\text{s}^{-1}$, with a reduced luminosity of $10^{32}\,\text{cm}^{-2}\,\text{s}^{-1}$ in the startup-phase.

---

1. ALICE: A Large Ion Collider Experiment
2. LHCb: LHC-beauty experiment
3. ATLAS: A Toroidal LHC Apparatus
4. CMS: Compact Muon Solenoid

## 2.2 The Compact Muon Solenoid

Even though the mass of the Higgs boson is still unknown, its decay channels are predictable. Among a great variety of possible final states only those with unique signatures with respect to the high background interactions that occur in proton-proton collisions are of interest for a discovery of the Higgs boson. Different decay channels with clear signatures are used for Higgs searches in different mass regions. In the mass range below $140\,\mathrm{GeV/c^2}$ the decay $H \to \gamma\gamma$ or at higher masses the channel $H \to 4$ leptons have such clear signatures. The different decay channels for Higgs masses up to 1 TeV are given in table 2.1.

| Energy range | typical decay channels |
|---|---|
| $80\,\mathrm{GeV} < m_H < 140\,\mathrm{GeV}$ | $H \to \gamma\gamma,\ H \to b\bar{b}$ |
| $130\,\mathrm{GeV} < m_H < 700\,\mathrm{GeV}$ | $H \to ZZ^* \to 4\ \mathrm{leptons}(l)$ |
| $500\,\mathrm{GeV} < m_H < 1000\,\mathrm{GeV}$ | $H \to ZZ \to 2l + 2\ \mathrm{jets}$ |
| $500\,\mathrm{GeV} < m_H < 1000\,\mathrm{GeV}$ | $H \to ZZ \to 2l + 2\nu$ |
| $800\,\mathrm{GeV} < m_H < 1000\,\mathrm{GeV}$ | $H \to WW \to l + \nu + \mathrm{jets}$ |
| $800\,\mathrm{GeV} < m_H < 1000\,\mathrm{GeV}$ | $H \to ZZ \to 2l + 2\ \mathrm{jets}$ |

**Table 2.1:** Decay channels of the Higgs boson with clear signatures for different energy ranges.

A detector experiment must be designed for sensitivity to all different decay signatures. The CMS experiment has chosen the following configuration for this challenge (see figure 2.2): The innermost part located directly around the interaction point is covered by a vertex detector comprising silicon pixel detectors, surrounded by a huge tracking detector made of silicon strip sensors. For the energy measurement, electromagnetic and hadronic calorimeters are foreseen. These parts are placed inside the coil of a superconducting magnet with a field strength of 3.8 Tesla. On its outside, an iron return yoke, equipped with muon detectors is located. In the very forward region, a Hadron Forward (HF) calorimeter is placed outside the yoke. Purpose and key elements of each sub-detector will be briefly introduced below, but omitting silicon strip and pixel detectors, which are described in more detail later.

The whole CMS experiment has a length of 22 m and a diameter of 14.6 m. With its total mass of about 12,500 tons it is heavier than the Eiffel Tower in Paris.

### 2.2.1 Electromagnetic Calorimeter

The Electromagnetic Calorimeter (ECAL) is placed around the vertex detector and the Silicon Strip Tracker (described in the next section). Its aim is to measure the energy of electromagnetically interacting particles like electrons and photons by stopping them in an absorber of dense matter. The emerging electromagnetic shower creates photons which are amplified and detected by silicon Avalanche Photo Diodes (APDs) and Vacuum Phototriodes (VPTs). Lead tungstate ($PbWO_4$) has been chosen as dense absorbing and scintillating material [6]. It is arranged in brick-shaped crystals with a size of $23 \times 2.2 \times 2.2\,\mathrm{cm^3}$. Beside of its excellent properties for calorimeters like a short radiation length of 0.89 cm and a small Moliere radius of 2.2 cm, it is also radiation hard beyond the levels expected within 10 years of full LHC collision rate.
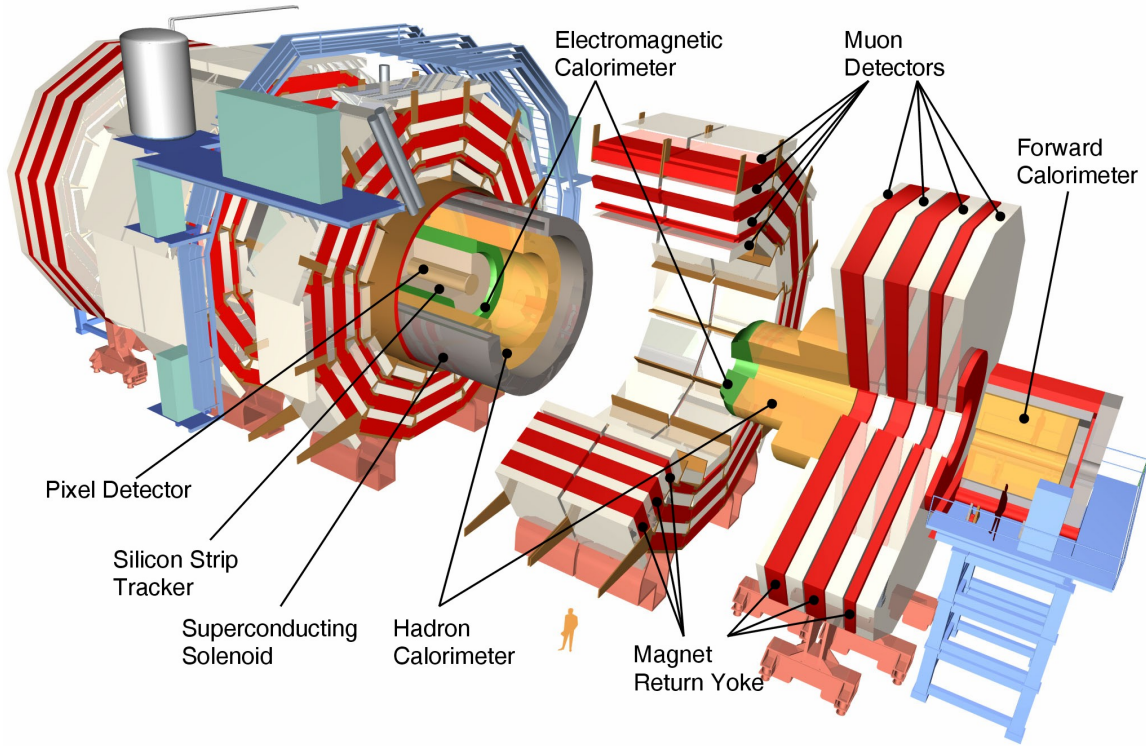
**Figure 2.2:** The Compact Muon Solenoid (CMS) Experiment with its subsystems. For comparison, the size of a person is shown in front.

The electromagnetic calorimeter plays an important role for the Higgs decay mode $H \to \gamma\gamma$ by detecting two photons. It is also essential for the measurement of electrons with large transverse momenta, since these particles are clear signatures for many interesting decays.

## 2.2.2 Hadronic Calorimeter

The Hadronic Calorimeter (HCAL) surrounds the ECAL. It consists of an inner barrel region, located inside the superconducting solenoid, an outer barrel part inside the iron return yoke of the magnet, two end caps and two very forward calorimeters. The latter ones are called *Hadron Forward* (HF) calorimeters and are placed outside the magnet return yoke in about 12 m distance from the intersection point.

In contrast to the homogeneous ECAL, the HCAL is of sampling type comprising copper as absorber material and mostly plastic scintillators in between as light emitting active material. Wavelength-shifters are used to guide the signals from the scintillators to the endcap region, where APDs and Proximity Focused Hybrid Photo Diodes (PFHPD) are converting and amplifying them to electrical signals. In the HF, quartz fibers embedded into copper absorbers are used as scintillators [7].

Hadrons strongly interact with nuclei in the copper absorbers creating hadronic jets. The energy of these jets is determined, as well as missing transverse energy. This is possible because of the hermetic design of the HCAL.

### 2.2.3 Superconducting Solenoid

The superconducting magnet surrounds the tracking detectors, the ECAL and most parts of the HCAL. It plays an essential role for the momentum measurement of charged particles by bending their track while they are escaping from the interaction point. Also most parts of the calorimeters are placed inside the solenoid to reduce the absorbing material in front of them, which increases their energy resolution. The magnet coil has a length of about 12.5 m, a diameter of about 6 m and is made of superconducting Niobium Titanium (*NiTi*) wires, which are powered by an electrical current of 20,000 Ampers to reach the nominal magnetic field of 4 Tesla. The solenoidal shape of the field lines are closed by an iron return yoke surrounding the coil, in which the muon detectors are installed.

### 2.2.4 Muon System

The outermost detectors are embedded into the iron return yoke of the superconducting magnet. Three different gaseous detector systems are used there for the detection of muons: The barrel region is based on Drift Tubes (DT), while strong magnetic field variations in the end cap regions require the use of cathode strip chambers (CSC). In both parts, Resistive Plate Chambers (RPCs) are used in addition for fast signals needed for the trigger (see below).

Muons are the only particles (except the almost non-interacting neutrinos) which are not absorbed by the calorimeters in the inner detector region. Since they are decay products of many interesting physics processes like the Higgs decay cascade to two Z-bosons (see table 2.1), their detection is a clear signature that something interesting happened. Thus, signals from the RPCs are taken into account for building the first-level global trigger decision for the experiment.

### 2.2.5 Trigger and Data Acquisition System

With the LHC bunch crossing rate of 25 ns, there will be 40 Million bunch collisions every second. During the high luminosity phase, each bunch collision will contain approximately 20 head-on proton-proton collisions, producing about 1000 tracks of charged particles. All recorded data of one bunch collision is called *event*. A typical event size will be approximately 1.5 Megabyte. Even with the fastest computers and networks, it is impossible to store all events on disk or tape. Thus, a data selection algorithm needs to select (i.e. trigger on) interesting events, like a signature of 4 muons from the Higgs decay. To cope with the high data rate, CMS has chosen two trigger levels, the Level-1 (L1) and the *High Level Trigger* (HLT).

The Level-1 Trigger operates at the LHC beam crossing rate using information from the calorimeters and RPCs and is implemented in dedicated custom ASICs[5]. It will reduce the event rate to 100 kHz. During the Level-1 Trigger latency of $\approx 3\,\mu s$, the data from all detector channels are stored in buffers. For the events accepted by the Level-1 Trigger (L1 accept; L1A), all data are read out in parallel into the Front-End Drivers (FEDs; see below).

The High Level Trigger (HLT) is implemented by analysis software running on a commercial computer farm and reduces the L1 output rate further down to a rate of 100 Hz. For HLT trigger calculations, the L1 decisions are refined and the full detector information, especially from the Tracker, is taken into account. Its data – hit information from the pixel and strip layers – is used for vertex reconstruction and track finding and allows very sophisticated trigger decisions. All events passing both the L1 and HLT trigger are then stored on hard disks or tapes.
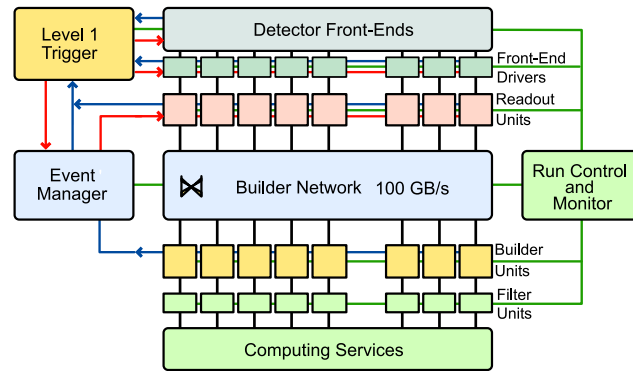


**Figure 2.3:** CMS Event builder network.

The CMS *Data Acquisition System* (DAQ) must take these considerations into account. Shown schematically in Fig. 2.3, it is composed of the detector front ends (FE), which store the event data in analog pipeline cells located in readout chips. L1A signals initiate the data transfer to the FEDs. A fast switching network is responsible for event building, in which all the data corresponding to a single event are collected from the FEDs to Builder Units. The events are then processed by the Filter Units of the HLT, and accepted events are finally selected and forwarded to the computing services for storage or for further analysis, like calibration or data quality monitoring. Data stored on disk or tape is then available for offline physics analysis.

## 2.3  The CMS Tracker

The trajectory of a particle with an electrical charge $e = \pm 1$ moving in a magnetic field $B$ is bent because of the Lorentz force. The particle moves on a path described by a helix with curvature and

---

5. *Application Specific Integrated Circuits* (ASICs) are integrated circuits customized for a particular use, rather than intended for general-purpose use. The APV25 readout chip of the CMS Tracker belongs also to this type of integrated circuits. *Field-programmable gate arrays* (FPGAs) containing programmable logic components and programmable interconnects are often used for this purpose for digital circuits.

track length $L$. Its transverse momentum $p_T$ with respect to the magnetic field can be determined (non-relativistic) by:

$$p_T = e \int B dL \approx e B R \qquad (2.3)$$

with $R$ being the radius of the curved track. Thus, the CMS Tracker utilizes position-sensitive devices like pixel (two-dimensional) and strip (one-dimensional) detectors in several layers around the interaction point, to reconstruct tracks of charged particles through the tracker volume. These data can then be used to calculate the transverse momentum $p_T$. Moreover, the charge polarity can be obtained by the bend orientation. The angular resolution can be approximated using

$$\frac{\Delta p}{p} = 26.4 \frac{p}{L^2 B} \frac{\sigma_x}{\sqrt{n}} \qquad (2.4)$$

where $\sigma_x$ is the single point variation of the hit measurement (in meters) and $n$ the number of hit measurements (e.g. layers of the Tracker). For the momentum $p$ the unit $\left[\frac{\text{GeV}}{\text{c}}\right]$ has to be used [8]. For the CMS Tracker, a momentum resolution of below $1\,\%$ can be achieved for particles with $p_T < 100\,\text{GeV}/c$ in the barrel region, while for higher energies the resolution decreases because of (almost) straight tracks (see fig 2.4).
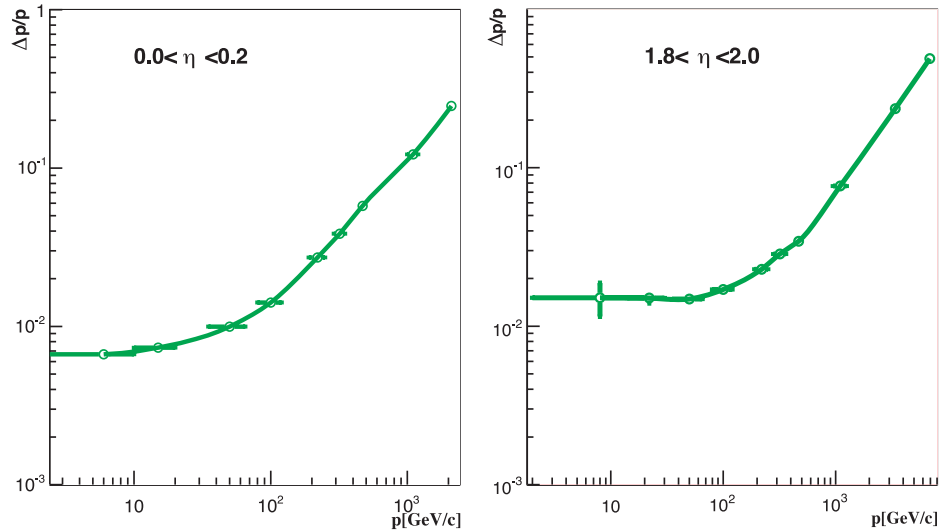


**Figure 2.4:** Transverse momentum resolution $\Delta p/p$ as a function of particle momentum $p$ for the barrel (left) and the endcap region (right) [9]. The parameter $\eta$, is explained later in equation 8.2.

The Tracker consists of two main parts, the vertex or pixel detector, and the Silicon Strip Tracker (SST), which have various different single point resolutions $\sigma_x$ depending on the pixel size and the strip pitch of the sensors.

## 2.3.1 Vertex Detector

The innermost CMS detector sub-system is located close to the interaction point and is made of three barrel layers and two end caps on each side (see figure 2.5). It consists of $250\,\mu\text{m}$ thin silicon pixel

detectors with a pixel size of $100 \times 150 \, \mu m$. The devices are made of $n^+$ pixels on $n$ type oxygenated silicon substrate with a resistivity of approximately $2 \, k\Omega \, cm$. As shown in figure 2.6, the sensors are bump-bonded to custom-made ASICs manufactured utilizing the radiation-hard 250 nm IBM CMOS process [10].



**Figure 2.5:** Layout of the pixel detector showing three barrel and two endcap layers.



**Figure 2.6:** Schematic view of the pixel sensor and the bump-bonded readout chip

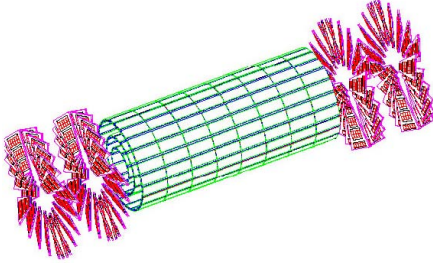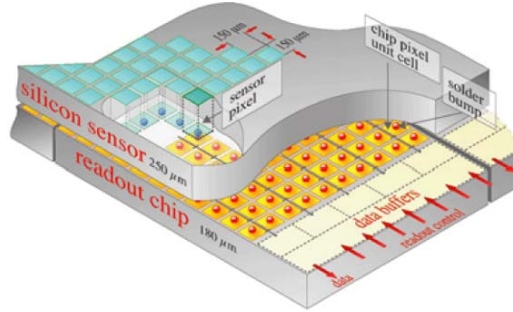Due to analog readout, a hit resolution of $10 \, \mu m$ can be achieved which is necessary for precise particle track reconstruction, but also for determination of primary and secondary vertices needed for the tagging of short-lived particles like $b$- or $c$-quarks or $\tau$-leptons. Particles escaping from the interaction point with very short lifetimes decay after very short flight distances in the beampipe before reaching any tracking detectors. Identification (tagging) of such particles is possible via secondary vertices only and requires high granularity of the detectors near the interaction point to distinguish neighboring vertices. In particular, $b$-tagging plays an important role for Higgs and SUSY search.

### 2.3.2 Silicon Strip Tracker

The basic building blocks of the CMS Silicon Strip Tracker (SST) are silicon modules. Each module is equipped with one or two silicon sensors and a so-called Front End (FE) hybrid, containing readout electronics. The modules are arranged in layers and disks around the vertex detector, as shown in figure 2.7. The SST is composed of ten layers of silicon modules in the barrel region, separated in an inner (*Tracker Inner Barrel*; TIB) and outer (*Tracker Outer Barrel*; TOB) part. Several modules within one layer are grouped together. These assemblies or sub-structures are called *strings* (TIB) or *rods* (TOB). The forward region consists of three *Tracker Inner Disks* (TID) on each side and is completed by the *Tracker End Caps* (TEC), comprising nine disks on each side. The TEC sub-structures housing the silicon modules are called *petals*. To build one disk, 16 petals are needed.

The entire SST will be kept at a nominal temperature of $-10 \, °C$, in order to minimize the degradation of the sensor performance due to irradiation effects. This keeps the sensor dark currents on a low level and minimizes reverse annealing effects. As a consequence, the full depletion voltages of the sensors will remain below 450 V, even after ten years of operation at nominal LHC luminosity [11].
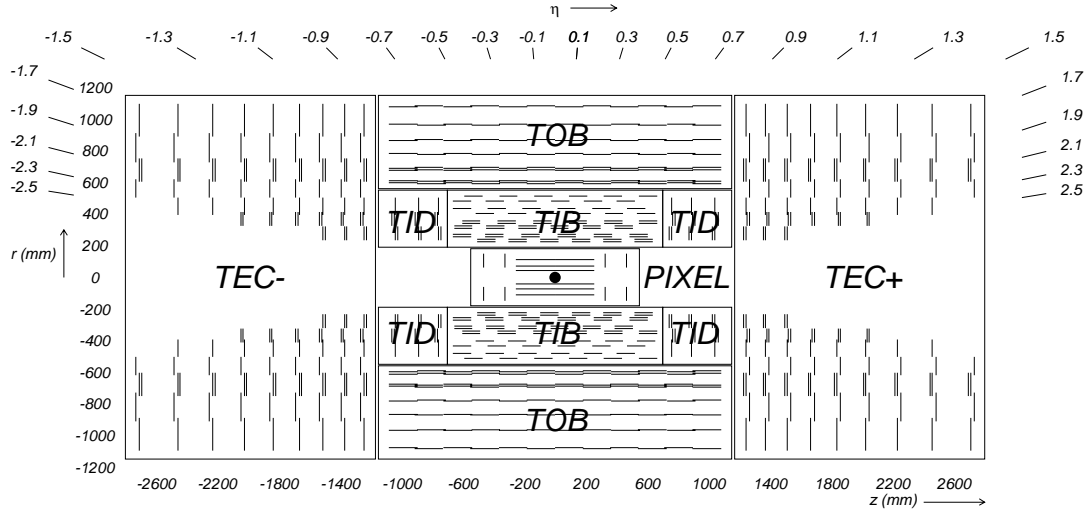
**Figure 2.7:** Layout of the CMS Tracker with its subsystems. Each short line represents a silicon module. The parameter $\eta$ is called pseudorapidity and is explained later in equation 8.2.

In total, the SST contains 15,148 silicon modules made of 24,244 silicon sensors. All sensors cover an active area of 206 m$^2$ and represent the largest silicon detector ever built. Both the silicon sensors and the modules will be discussed in more detail in the following chapters with particular emphasis on the TEC design.

### 2.3.3 Control and Readout System

The large number of silicon modules require a fast and effective way of communication between the FE electronics located in the tracker volume and the off-detector electronics located in electronics racks several tens of meters away from the detector in the service cavern. On one side, clock and trigger signals as well as configuration data must be sent to the FE, while the data containing the hit information must be transferred out of the detector after a first-level trigger (L1A) signal was received.

For this purpose, the SST utilizes optical connections for both the control and the data path (see figure 2.8). The control path consists of custom-made 9U VME electronics boards called *Front End Controller* (FEC) [12], which communicate with the *Communication and Control Units* (CCU's) located on the sub-detector assemblies, e.g. on each petal (TEC), rod (TOB), string (TIB) and disc (TID). Optical-to-electrical signal conversion is done using a dedicated PCB called *Digital Opto-Hybrid* (DOH) [13]. On the other side, the electrical charge recorded in groups of 128 silicon strips is converted to voltages and serialized by the APV25 readout chip. The data of two APV25 chips are combined and transformed to light pulses by the *Analog Opto-Hybrid* (AOH) [14]. The *Front End Driver* (FED) boards [15], which are also based on 9U VME boards, convert the analog light pulses fist to analog electrical and later to digital electrical signals. FPGAs are used for further

processing of this data (e.g. zero suppression and cluster finding). The resulting information is then sent to the upstream CMS event builder via the switching network.
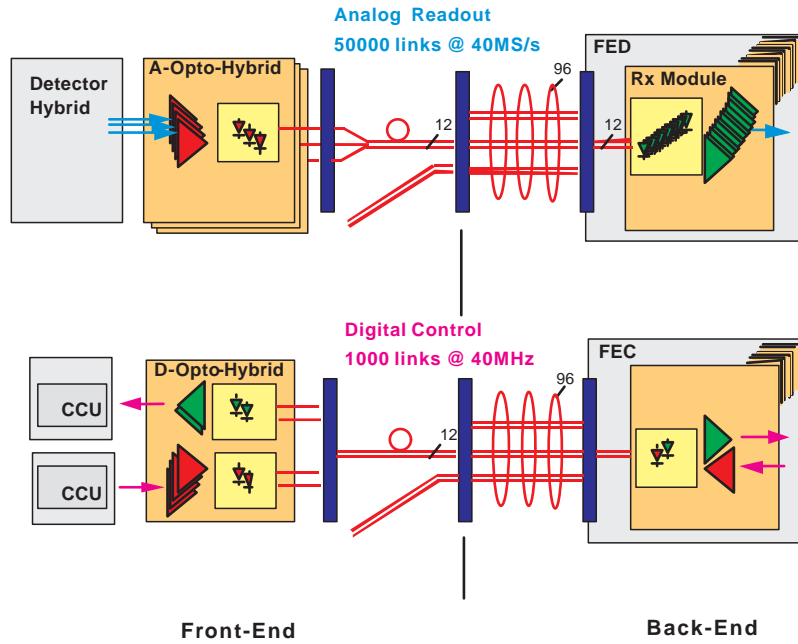


**Figure 2.8:** Control (bottom) and readout system (top) of the SST utilizing optical links (shown in red).

## 2.3.4 Power Systems

The silicon modules of the SST are divided into 1944 so-called power groups which share power, control, and cooling services. Each power group is connected to the power supply system by up to 80 m long Multi Service Cable (MSC) inside the Tracker and Low Impedance Cables (LIC), located outside of the Tracker. The high voltages used for biasing the silicon sensors (0-600 V) and the low voltages (1.25 V and 2.5 V) required by the FE electronics are provided by a modular system of *Power Supply Units* (PSUs). The voltage drop along the up to 50 m long cables is compensated using the sense wire technique. In total, the power supply system has a design power of 64 kW (131 kW peak). After subtracting the power loss in the cables of 31 kW, the total power consumption of the FE electronics is 33 kW.

The PSU modules are boards located in special crates[6]. They receive their power by a 48 V line from AC/DC power converters. Each PSU communicates with the system controller (supervisor) via intermediate *Array Controllers* using the *Controller Area Network* (CAN) bus system (see figure 2.9). The supervisor itself communicates with the *Detector Control System* (DCS) via Ethernet connection. In parallel, the *Detector Safety System* (DSS) can issue interlocks to initiate shutdown in case of emergency.

---

6. The crates of the power supply system belong to the *Easy 4000 System*, which is a commercial product by CAEN Nuclear. http://www.caen.it/
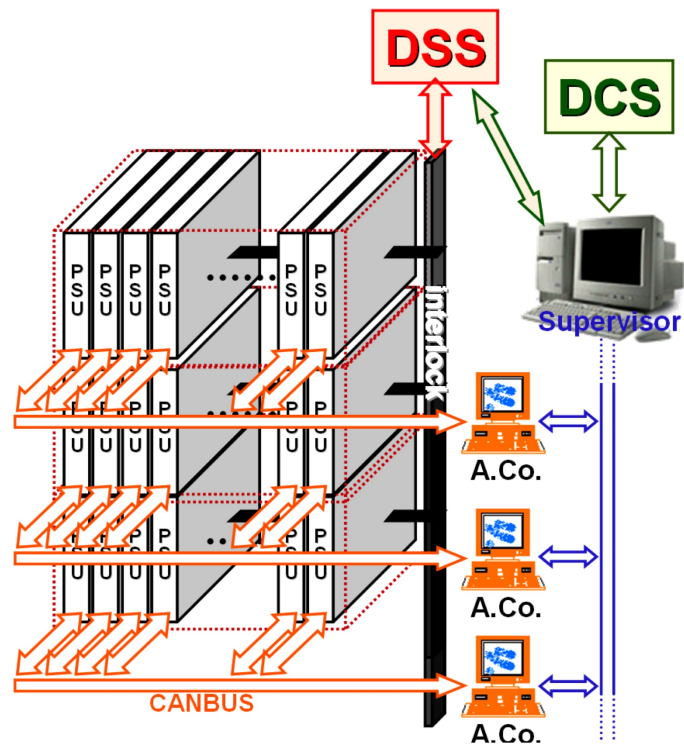
**Figure 2.9:** Power distribution system of the SST.

# 3 Silicon Detector Theory

> The universe is simple; it is the
> explanation that is complex.
>
> *(Unknown Source)*

Silicon (symbol *Si*) is the eighth most common chemical element in the universe and the second most common element after oxygen in the Earth's crust. Its position in the periodic table of the elements is in the fourth main group with atomic number 14. Silicon occasionally occurs as pure free element in nature, but is more widely distributed as various forms of silicon dioxide $SiO_2$ or silicate[1].

## 3.1 Properties of Pure Silicon

Pure silicon has four covalent-bonded electrons and forms a diamond cubic crystal structure, which can be seen in figure 3.1. Electrons of the lattice atoms form energy bands, which are shown
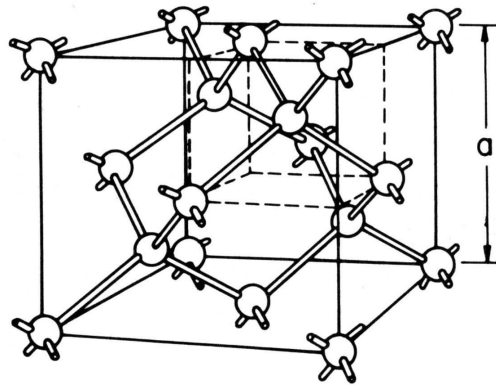


**Figure 3.1:** Diamond cubic crystal structure of silicon with four valence electrons. The distance *a* is called *lattice parameter* and its size is $a = 5.431$ Å [16].

in figure 3.2. Their shape and levels depend on the lattice spacing parameter *a*. The uppermost occupied band is called *valence band* with its upper energy border $E_V$. The lowermost unoccupied band is called *conduction band* because only when electrons are excited to the conduction band, electric currents can flow and the material becomes conductive. In this state, electrons can be

---

1. Silicates are compounds consisting of one or more central silicon atoms surrounded by other, mostly oxygen atoms. Thus, silicates are often of the form $Si_xO_y$.

treated like free particles, but with an effective mass $m_n$ different from elementary electrons[2]. The lower energy edge of the conduction band ist called $E_C$. For metals, the valence and conduction
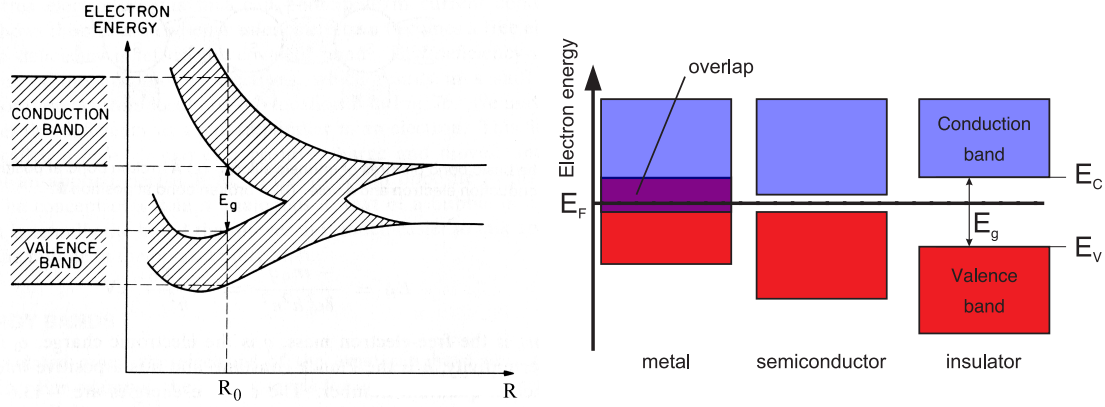


**Figure 3.2: Left:** Energy bands in silicon lattice [17]. The size of the energy bands is defined by the separation distance $R$. The equilibrium separation distance $R_0$ is the silicon lattice parameter $a$.
**Right:** The difference between metals, semiconductor and insulators is only given by the size of the band gap energy $E_g = E_C - E_V$

band are overlapping. Therefore the excitation of electrons to higher energy levels requires only very small energies. For semiconductors or insulators, there is a clear gap between the two energy bands and the size of the band gap energy $E_g$ is defined by the difference between conduction and valence band edges:

$$E_g = E_C - E_V \quad . \tag{3.1}$$

The distinction between semiconductor and insulator is defined by the size of the band gap. For Silicon, $E_g$ is 1.12 eV and therefore it is called a semiconductor. Materials with band gaps larger than approximately 5 eV are usually considered as an insulator. The properties of pure, intrinsic silicon are listed in Table 3.1.

At finite temperatures the covalent-bonded electrons can flip from the valence band to the conduction band due to excitation by phonons, which are quasi-particles describing lattice vibrations. The occupation probability for an electronic state is given by the Fermi-Dirac function:

$$F(E) = \frac{1}{1 + \exp\left(\frac{E - E_F}{k_B T}\right)} \tag{3.2}$$

with the Fermi energy level $E_F$ at which the occupation probability is exactly one half, the Boltzmann constant $k_B$ and the temperature $T$. For $|E - E_F| > 3k_B T$ the Fermi-Dirac-statistics for electrons $F_e$ and holes $F_h$ can be approximated by

$$F_e(E) \approx \exp\left(-\frac{E - E_F}{k_B T}\right), \qquad F_h(E) \approx \exp\left(-\frac{E_F - E}{k_B T}\right) \tag{3.3}$$

with $F_e + F_h = 1$. The state density for electrons at the bottom of the conduction band is

$$N(E) = \frac{(2m_n)^{3/2}}{2\pi^2 \hbar^3 \sqrt{E - E_C}} \tag{3.4}$$

---

2. Similarly, the same is true for holes in the valence band.

| Property | Value |
|---|---|
| Atomic number | 14 |
| Atomic weight [u] | 28.09 |
| Density [g/cm$^3$] | 2.329 |
| Atomic concentration [atoms/cm$^3$] | $5 \times 10^{22}$ |
| Relative permittivity $\varepsilon_r$ | 11.9 |
| Crystal structure | Diamond |
| Lattice parameter a [Å] | 5.431 |
| Band gap energy $E_g$ [eV] | 1.12 |
| Intrinsic charge carrier concentration $n_i$ (300K) [cm$^{-3}$] | $1.45 \times 10^{10}$ |
| Energy for creation of e-h pair [eV] | 3.63 |
| Electron mobility $\mu_e$ [cm$^2$/Vs] | 1450 |
| Hole mobility $\mu_p$ [cm$^2$/Vs] | 450 |
| Intrinsic resistivity [kΩ cm] | 235 |
| Radiation length [cm] | 9.36 |

**Table 3.1:** Physical properties of pure (intrinsic) silicon [16].

with $m_n = 0.32 m_e$ as the effective electron mass, which depends on the orientation of the silicon lattice [18]. The free electron density $n$ is a convolution of the state density $N(E)$ and the occupation probability $F_e(N)$:

$$n = \int_{E_C}^{+\infty} N(E) \cdot F(E)\, dE \tag{3.5}$$

$$= 2 \left( \frac{2\pi m_n k_B T)}{\hbar^2} \right)^{3/2} \exp\left( -\frac{E_C - E_F}{k_B T} \right) \tag{3.6}$$

$$= n_0 \exp\left( -\frac{E_C - E_F}{k_B T} \right) \tag{3.7}$$

Similarly, for holes the density is given by

$$p = p_0 \exp\left( -\frac{E_F - E_V}{k_B T} \right) \quad . \tag{3.8}$$

In an intrinsic semiconductor under thermal equilibrium, the concentration of electrons and holes is equivalent:

$$n_i = n = p \tag{3.9}$$

and $n_i$ becomes

$$n_i = \sqrt{n \cdot p} = \sqrt{n_0\, p_0} \exp\left( -\frac{E_g}{2 k_B T} \right) \tag{3.10}$$

resulting in $n_i \approx 1.45 \times 10^{10}/\text{cm}^3$ at $T = 300$K. The Fermi energy level of intrinsic silicon is

$$E_{F,i} = \frac{E_C + E_V}{2} + \frac{3}{4} k_B T \ln\left( \frac{m_p}{m_n} \right) \tag{3.11}$$

which is located approximately in the middle between valence and conduction band, with the variation in the second term coming from the different effective masses of electrons and holes.

## 3.2 Doping of Silicon

The concentration of dopants introduced to an intrinsic semiconductor affects many of its electrical properties. Depending on the doping material and its position in the periodic table of the elements these properties differ.

Donors are elements with five valence electrons and thus silicon doped with these materials is called *n-type* (see left side of fig 3.3). A donor atom that is incorporated into the crystal lattice provides weakly-bound valence electrons to the material, creating excessive negative charge carriers. The donor atoms introduce some states below, but very close to the conduction band edge. Typical chemical elements used for this purpose are phosphorus (P) and arsenic (As), while antimony (Sb) and bismuth (Bi) have the same effect but are not commonly used.

Acceptors are used to form *p-type* regions in silicon by using elements from the third main group of the periodic table as dopant. Once incorporated into the lattice, the missing negative electron acts like a positive charge, thus called *hole* (see right side of figure 3.3). It introduces energy states closely above the valence band. Typical materials used for this purpose are boron (B) or aluminum (Al)[3]. For boron doping of silicon bulk, the energy gap between the introduced energy states and the conduction band edge is only 0.045 eV.
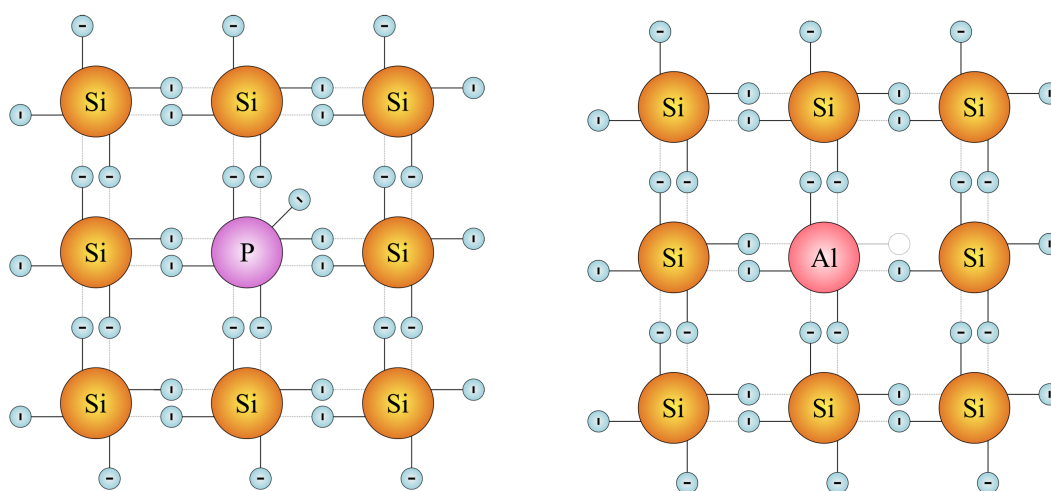


**Figure 3.3:** Silicon lattice doped with phosphorus forming n-type material (left) and aluminum forming p-type silicon material (right).

In general, doping a semiconductor crystal introduces allowed energy states within the band gap but very close to the energy band that corresponds with the dopant type and the Fermi energy $E_F$ is shifted towards these states. This is shown in figure 3.4. Since the Fermi level must remain constant in a system in thermodynamic equilibrium, stacking layers of materials with different properties leads to many useful electrical properties. For example, the p-n junction's properties are due to the energy band bending that happens as a result of lining up the Fermi levels in contacting regions

---

3. Since the solubility of aluminum in silicon is poor, it is not commonly used.
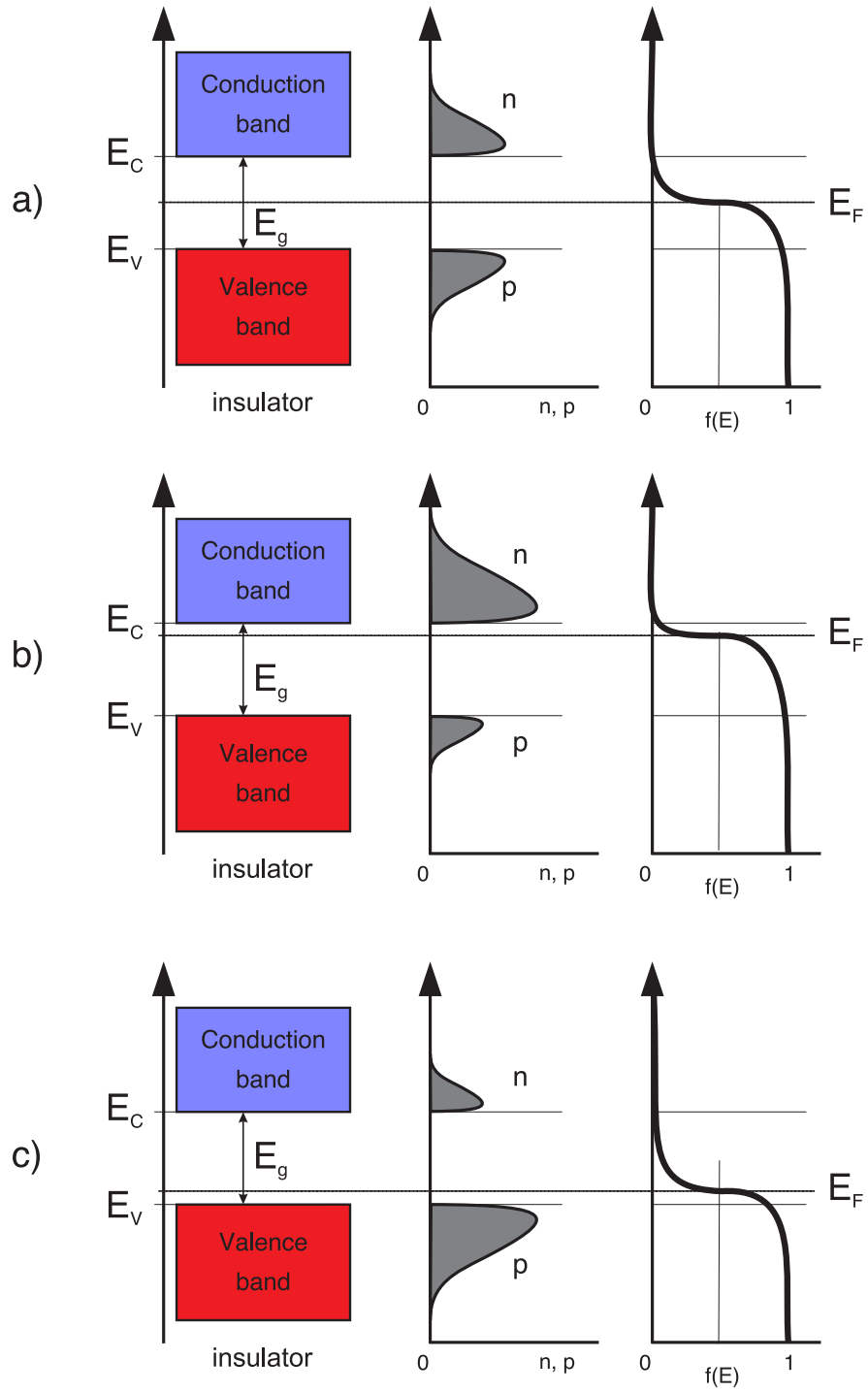
**Figure 3.4:** Charge carrier distribution and Fermi levels for intrinsic (a), *n*-doped (b) and *p*-doped (c) semiconductor materials (after [19]). The three diagrams on the left show the position of the valence and the conduction bands, the center plots illustrate the *n*- and *p*-type charge carrier densities, and the right diagrams show the Fermi distribution for the different doping scenarios.

of p-type and n-type material. This can be seen in figure 3.5 and is described in more detail in section 3.4.
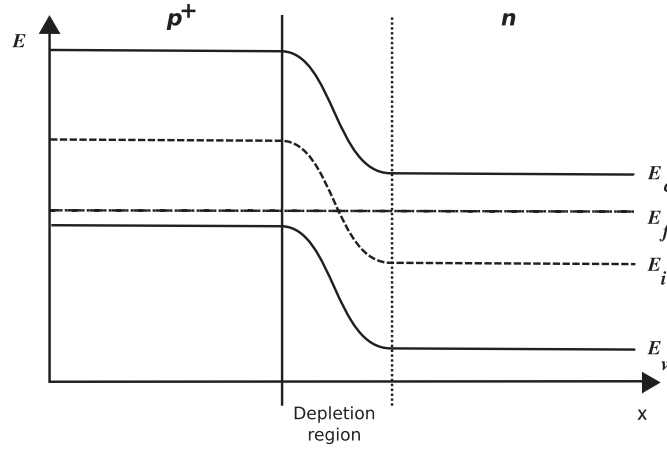


**Figure 3.5:** Bandmodel for a *pn*-junction.

An increase in doping concentration also results in better electrical conductivity due to higher concentration of carriers available for conduction. Very highly doped semiconductors have conductivity levels comparable to metals and are often used as its replacement. Usually, superscript plus- and minus-symbols are used to denote relative doping concentration in semiconductors. For example, $n^{++}$ denotes an n-type semiconductor with very high doping concentration, possibly acting as an ohmic contact. The electrical resistivity $\rho$ is given by

$$\rho = \frac{1}{q_e(n \cdot \mu_e + p \cdot \mu_p)} \quad , \tag{3.12}$$

where $\mu_e$ and $\mu_p$ are the electron or hole mobilities, respectively, and $q_e$ is the electron charge. For intrinsic silicon at room temperature, the resistivity is about 235 k$\Omega$ cm. The resistivity of doped materials is lower because of a higher charge carrier concentration. In *n*-type silicon, where donor atoms are dominant, the resistivity can be simplified to

$$\rho \approx \frac{1}{q_e \, \mu_e \, N_d} \tag{3.13}$$

and accordingly for *p*-type silicon.

## 3.3 Generation and Recombination of Charge Carriers

Silicon is often referred to as having an *indirect band gap*, in which the minimum energy in the conduction band is shifted by a *k*-vector relative to the valence band in momentum space (see figure 3.6) [18]. The *k*-vector represents a difference in momentum. In a direct bandgap semiconductor like Germanium or Gallium-Arsenide, electrons at the conduction band minimum can

combine directly with holes at the valence band edge, while conserving momentum. This process is called spontaneous emission, since the energy from the recombination will be emitted as light.
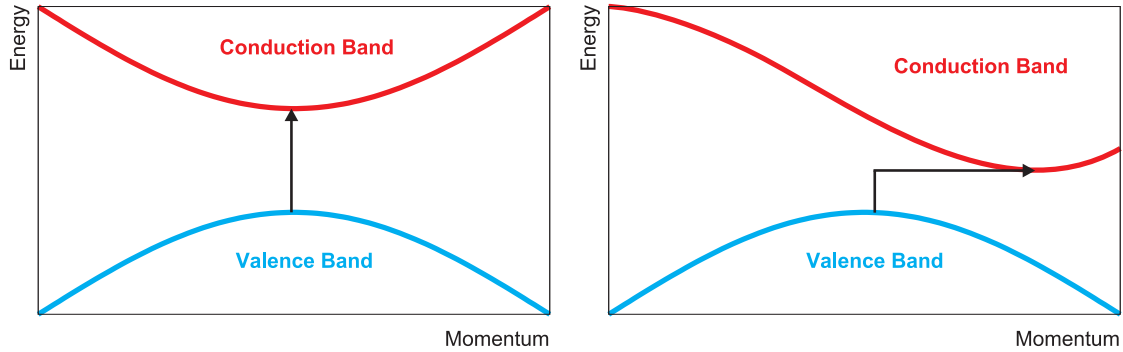


**Figure 3.6:** Direct (left) and indirect (right) semiconductor. The indirect semiconductor requires a momentum transfer (horizontal arrow) for a state transition.

Semiconductors like silicon, which has an indirect band gap, are inefficient for emitting light. This is because any electrons present in the conduction band need some source of momentum allowing them to fall into the valence band.

Up to now only perfect silicon crystals have been considered. In reality, the silicon lattice has imperfections and comprises foreign atoms as well. Both effects introduce many energy levels in the band gap region which act as momentum source. Thus, they increase the generation and recombination probability of electrons and holes significantly, especially when energy is deposited in the semiconductor.

### 3.3.1 Thermal Generation

Electron-hole pairs are constantly generated from thermal energy in the absence of any external energy source.[4]. For direct semiconductors (e.g. Ge) there is a rather high probability that electrons are getting excited directly from the valence to the conduction band because of its very low band gap. Therefore these detectors must be operated at low temperature. In other materials such as Si, the direct excitation happens rarely and occurs in two steps through intermediate local states inside the band gap. These intermediate states are caused by impurities and crystal imperfections.

---

4. This effect is discussed in section 3.4.3 for depleted *pn*-junctions in detail (see equation 3.34).

### 3.3.2 Generation by Photons

Photons can interact with electrons in the silicon lattice and excite them to higher energy states. In silicon, an energy of 3.6 eV is necessary to lift an electron from the valence to the conduction band. Because of the indirect band gap, some of the energy of the incident photon is needed to supply momentrum transfer for the electron. A direct transition without change of momentum would require a higher energy. An absorption of a photon below the mentioned energy is only possible if there are intermediate states in the band gap, e.g. caused by imperfections of the crystal.

### 3.3.3 Generation by Electrons

High-energy electrons traversing matter lose energy by bremsstrahlung, while photons cause $e^+e^-$ pair production. The mean distance over which a high-energy electron loses all but $1/e$ of its energy by bremsstrahlung is called *radiation length* $X_0$. It is commonly used as scale length for describing high-energy electromagnetic cascades in calorimeters. $X_0$ can be approximated using [20]:

$$X_0 = \frac{716 \cdot A}{Z(Z+1) \ln \frac{287}{\sqrt{Z}}} \quad \mathrm{g\,cm^{-2}} \tag{3.14}$$

for materials with atomic number $Z > 4$ and mass number $A$.

At low energies, electrons and positrons primarily lose energy by ionization, although other processes like Møller scattering, Bhabha scattering and $e^+$ annihilation contribute (see figure 3.7). Ionization loss caused by leptons differs from loss by heavy particles because of the kinematics, spin, and the identity of the incident electron with the electrons which it ionizes.

For the energy loss by photons at low energies the photoelectric effect dominates, but Compton scattering, Rayleigh scattering, and photonuclear absorption contribute as well. The photoelectric cross section is characterized by discontinuities (absorption edges) as thresholds for photo-ionization of various atomic levels are reached. For higher energies pair production becomes the dominant effect.

### 3.3.4 Generation by Heavy Charged Particles

Charged particles traversing silicon interact with the Coulomb field of the lattice atoms and electrons. The energy loss of moderately relativistic charged particles (except electrons) in matter was first described by H.A. Bethe and F. Bloch using equation 3.15 [20].

$$-\frac{dE}{dx} = C_0 z^2 \frac{Z}{A} \frac{1}{\beta^2} \left[ \frac{1}{2} \ln \left( \frac{2m_e c^2 \beta^2 \gamma^2 T_{\max}}{I^2} \right) - \beta^2 - \frac{\delta(\gamma)}{2} - \frac{C}{Z} \right] \tag{3.15}$$
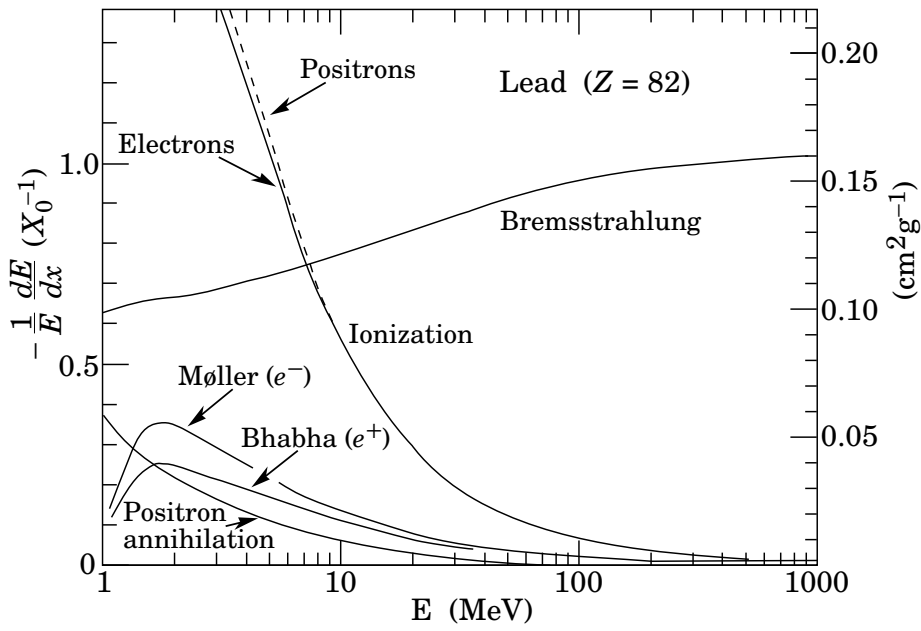
**Figure 3.7:** Fractional energy loss per radiation length in lead as a function of electron or positron energy up to 1 GeV [20].

It represents the differential energy loss per unit length in terms of $[\text{MeV cm}^{-1}]$. The symbols denote

$C_0$ $=$ $4\pi\rho N_A r_e^2 m_e c^2$

$ze$ ... charge of the incident particle

$N_A$ ... Avogadro's number

$Z$ ... atomic number

$A$ ... atomic mass

$m_e$ ... electron mass

$r_e$ $=$ $\frac{e^2}{4\pi\varepsilon_0 m_e c^2}$ (classical electron radius)

$T_{\max}$ ... maximum kinetic energy which can be imparted to a free electron in a single collision

$I$ ... mean excitation energy

$\delta(\gamma)$ ... density effect correction

$C$ ... shell correction term

$\beta$ $=$ $v/c$

$\gamma$ $=$ $(1-\beta^2)^{-1/2}$

Figure 3.8 shows the energy loss of particles versus its momenta in various materials according to Equation 3.15. Particles with energies in the range of the curves' minima are called *minimum ionizing particles* (MIPs). Since to the number of electron-hole pairs created in the solid state body is directly proportional to the energy deposition of traversing particles, the working principle of semiconductor detectors is based on the detection of the signals created by the electron-hole pairs. They are called the "signal" and this number is used to calculate signal-to-noise ratios (SNR), which always refer to MIPs, as those represent the smallest possible (measured) signals. Since the energy
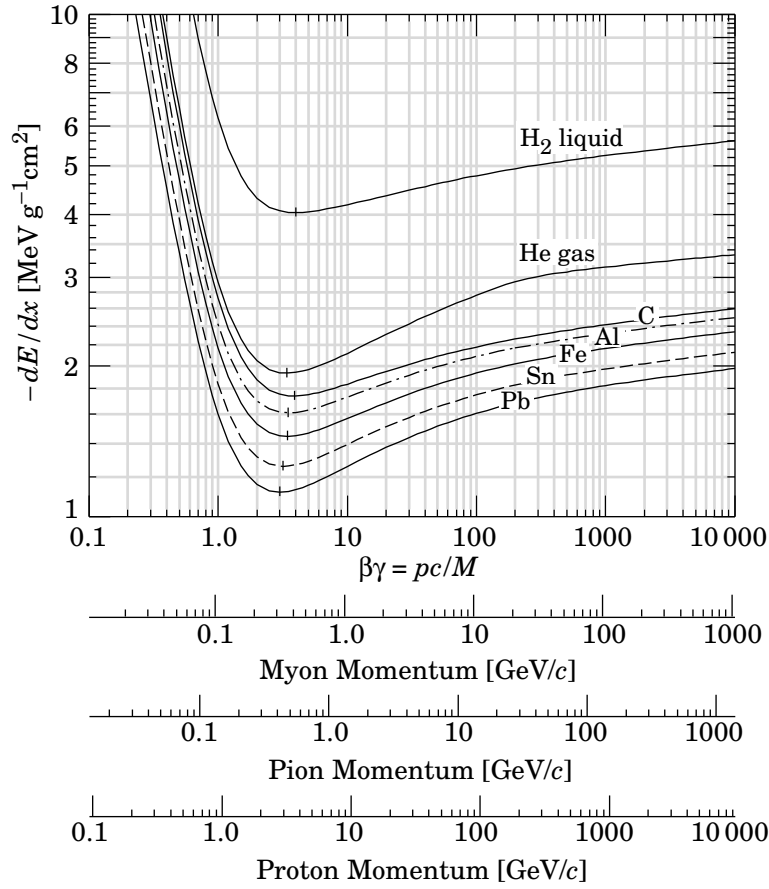
**Figure 3.8:** Energy loss for various particles and materials [20].

where the energy loss is minimal depends on the type of particles, table 3.2 shows the typical MIP energies for muons, pions and protons.

|         | approx. energy |
|---------|:--------------:|
| Particle | [MeV]         |
| muon    | 350            |
| pion    | 471            |
| proton  | 3200           |

**Table 3.2:** Typical MIP energies for heavy charged particles in thick layers, like it is used for calorimeters.

In thin solid state body layers like semiconductor detectors (typical thickness of 300-500 µm) the deposited energy is less than expected because a fraction of the energy is carried off by highly energetic $\delta$ electrons. These considerations lead to the restricted energy loss, which is expressed by an additional term in the Bethe-Bloch equation [20], which then denotes to:

$$-\frac{dE}{dx} = C_0 z^2 \frac{Z}{A} \frac{1}{\beta^2} \left[ \frac{1}{2} \ln \left( \frac{2 m_e c^2 \beta^2 \gamma^2 T_{\text{upper}}}{I^2} \right) - \beta^2 \left( 1 + \frac{T_{\text{upper}}}{T_{\text{max}}} \right) - \frac{\delta(\gamma)}{2} - \frac{C}{Z} \right] \qquad (3.16)$$

where

$$T_{\text{upper}} = \min(T_{\text{cut}}, T_{\text{max}}) \tag{3.17}$$

with $T_{\text{cut}}$ depending on the material and the incident particle momentum. Figure 3.9 shows a comparison of the standard Bethe-Bloch equation to the restricted form for a pion traversing 300 $\mu$m of silicon. The MIP energy for pions in the restricted model is 763 GeV. No difference in $dE/dx$ can be

**Energy deposition of pions in silicon**
Standard and restricted Bethe-Bloch
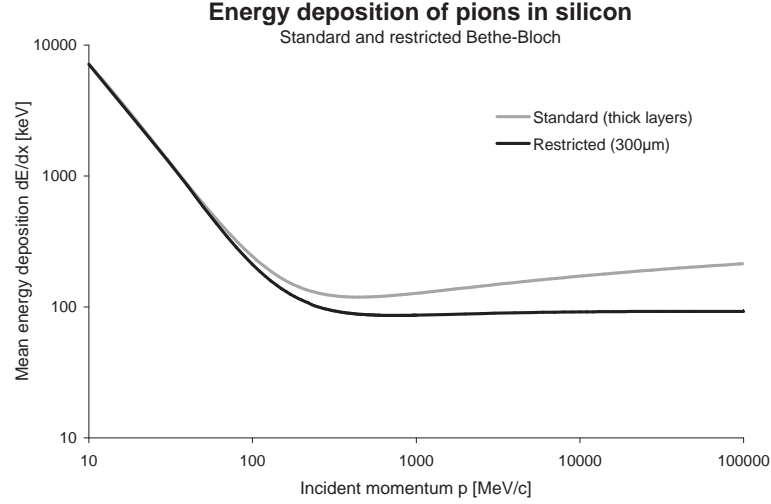


**Figure 3.9:** Comparison of the standard Bethe Bloch equation to the restricted form for a pion traversing 300 μm of silicon [21].

seen for particles below 50 MeV. For higher energies, the relativistic rise is quite flat in the restricted model due to the energy taken away by $\delta$ electrons and the effective MIP energy (or momentum) rises.

The ionization energy loss is statistically distributed around its mean value. The distribution is Gaussian for thick absorbers, but develops an asymmetry and a tail towards high energies for decreasing thicknesses. Ideally, it becomes a *Landau distribution* for very thin absorbers [22]. In probability theory, the Landau distribution is defined as the complex integral

$$p(x) = \frac{1}{2\pi i} \int\limits_{c-i\infty}^{c+i\infty} e^{s \log s + xs} \, ds \tag{3.18}$$

where $c$ is a positive real number. For numerical purposes it is more convenient to use the following equivalent form of the integral:

$$p(x) = \frac{1}{\pi} \int\limits_{0}^{\infty} e^{-t \log t - xt} \sin(\pi t) \, dt. \tag{3.19}$$

The measured energy loss distribution of MIP particles is shown in figure 3.10 for a thin silicon detector. The fitted curve is a convolution of a Landau distribution describing the signal and a Gaussian caused by electronic noise and statistical detector fluctuations. The long upper tail is called *Landau tail* and is due to rare, but highly energetic $\delta$ electrons and extends to infinite energies
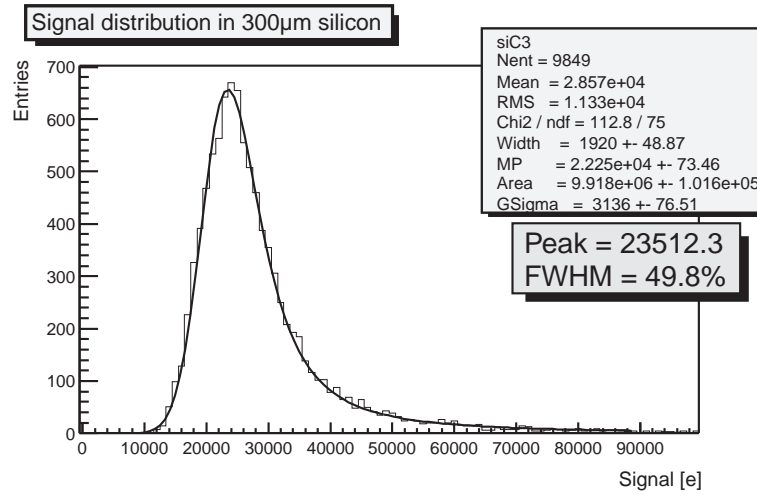
**Figure 3.10:** Measured MIP signal distribution in a silicon detector of a thickness of 300 μm [21]. The *most probable*
(MP) value is the peak of the distribution at 23.512 electrons, where the mean value is 28.570 electrons.
This results in a ratio of 1.22 between mean and peak values.

in theory, which implies an infinite mean value. In reality, a mean value of the distribution exists
but it is not identical with the *most probable* (MP) as a result of its asymmetry. The MP represents
the peak of the distribution and is typical lower than the mean value by a factor of about 1.2 to
1.3.

### 3.3.5 Recombination

Recombination of electrons and holes is a process by which both carriers annihilate each other: elec-
trons occupy - through one or multiple steps - the empty state associated with a hole. Both carriers
eventually disappear in the process. The electron energy released due to any type of recombina-
tion can be emitted as photon (radiative recombination) for direct or by multiple phonon scatterings
(non-radiative recombination) for indirect semiconductors.

The recombination rate is proportional to the concentrations of electrons in the conduction band
(n) and of holes in the valence band (p). In thermal equilibrium, recombination ($R$) and thermal
generation $G_{th}$ rates are equal and are proportional to the product of electron and hole concentration
$\beta np$. But if excess carriers are introduced, e.g. by illuminating silicon with light, the net recom-
bination rate $U = R - G_{th}$ and the light-induced creation rate $G_L = \frac{\Delta n_L}{\tau_p}$ are equal. This leads to a
recombination rate of

$$U = \frac{p - p_0}{\tau_p} \tag{3.20}$$

where $\tau_p = \frac{1}{\beta n_0}$ denotes the charge carrier lifetime and $n_0$ and $p_0$ are the intrinsic charge carrier
densities calculated in formula 3.7 and 3.8.

For silicon, the dominant recombination process is indirect transition via discrete energy states in
the energy gap. These traps act as stepping stones between conduction and valence bands. The
discrete energy states are caused by the presence of a foreign atom or a structural defect. Once

the trap is filled it cannot accept another electron. The electron occupying the trap, in a second step, moves into an empty valence band state, thereby completing the recombination process. This process is also called *Shockley-Read-Hall* (SRH) recombination.

Auger recombination is a process in which an electron and a hole recombine via the SRH mechanism, but the resulting energy is given off to another electron or hole. The involvement of a third particle affects the recombination rate such that Auger recombination needs to be treated differently from SRH recombination.

Near the surface of a semiconductor there are dangling bonds which introduce additional states within the band gap region. These states cause an increased recombination rate compared to the pure SRH process rate.

## 3.4 pn-Junctions

A combination of *p*- and *n*-type silicon material forms a *pn*-junction. The voltage, current, and capacitance characteristics of such devices depend on the polarity of the applied electric field. The majority charge carriers in the connection zone of the n-type and the p-type silicon diffuse into the neighboring regions and recombine there. The resulting region of ionized acceptors and donors is named *space charge region* (SCR). The electrical potential evolved in the SCR, called *built-in voltage $U_{bi}$*, is calculated

$$U_{bi} = \frac{1}{q_e}(E_i^p - E_i^n) = \frac{k_B T}{q_e} \ln\left(\frac{N_A N_D}{n_i^2}\right) \tag{3.21}$$

and is in the order of 0.1–0.5 V. The width of the SCR is made up of the width in the *n*- and in the *p*-type material and is given by [16]:

$$W_{\text{SCR}} = W_p + W_n = \sqrt{\frac{2\varepsilon_0 \varepsilon_r U_{bi}}{q_e (N_A + N_D)}} \left(\sqrt{\frac{N_A}{N_D}} + \sqrt{\frac{N_A}{N_D}}\right) = \sqrt{\frac{2\varepsilon_0 \varepsilon_r (N_A + N_D) U_{bi}}{q_e N_A N_D}} \tag{3.22}$$

When an external reverse bias voltage $U_{\text{bias}}$ is applied to the device, the width of the SCR becomes:

$$W = W_p + W_n = \sqrt{\frac{2\varepsilon_0 \varepsilon_r (U_{bi} - U_{\text{bias}})}{q_e N_a (1 + N_a/N_d)}} + \sqrt{\frac{2\varepsilon_0 \varepsilon_r (U_{bi} - U_{\text{bias}})}{q_e N_d (1 + N_d/N_a)}} \tag{3.23}$$

$$= \sqrt{\frac{2\varepsilon_0 \varepsilon_r}{q_e}(U_{bi} - U_{\text{bias}})\left(\frac{1}{N_d} + \frac{1}{N_a}\right)} \tag{3.24}$$

Since in practice the operation voltage is much higher than the built-in voltage ($U_{\text{bias}} \gg U_{bi}$), this equation can be simplified to:

$$W \approx \sqrt{2\,\varepsilon_0 \varepsilon_r\, \mu\, \rho\, |U_{\text{bias}}|} \tag{3.25}$$

where $\mu$ is the mobility of the majority charge carriers in the lower doped region and $\rho$ is the resistivity of the lower doped material as described in equation 3.13.

In reality, merging two differently doped semiconductor materials forming a *pn*-junction is technically complicated. Therefore, a thin silicon wafer already doped during production (e.g. to *n*-type material) is used as base material. Ion implantation is then used to create areas of the complementary material (e.g. *p*-type) into the wafer forming a *pn*-junction. Since the depth of the ion implantation is only in the order of a few microns, the implantation dose must be relatively high, forming regions called $p^+$. Because of diffusion and other processes, the *pn*-junction is not sharp but a rather smooth transition between the two doping regions. Thus, all formulae have to be considered as approximation.

### 3.4.1 Full Depletion Voltage

When applying an external voltage $U_{\text{bias}}$ across a *pn*-junction, the built-in voltage $U_{bi}$ has to be substituted by $U_{bi} - U_{\text{bias}}$. A bias voltage with positive potential on the p-side and negative potential on the n-side is called *forward bias* and the contrary polarity *reverse bias*, respectively.

The voltage at which the SCR reaches the borders of the device is called *full depletion voltage $U_{\text{depl}}$*. It is given by:

$$U_{\text{depl}} = \frac{q_e d^2}{2\,\varepsilon_0 \varepsilon_r} |N_D - N_A| \tag{3.26}$$

with $d$ as the thickness of the device (e.g. the silicon wafer). The expression $|N_D - N_A|$ is also called effective doping concentration $|N_{\text{eff}}|$. In real silicon detectors, the *pn*-junctions are segmented into strips or pixels. Therefore, the electrical field is not linear in the device and the depletion zone does not grow homogeneously. The correction factor between a non-segmented diode and a segmented device is discussed in section 4.1.4.

With the previous equation, we obtain for the resistivity $\rho$:

$$\rho = \frac{1}{q_e \, \mu \, N_{\text{eff}}} \tag{3.27}$$

where $\mu$ is the mobility of the majority charge carriers. Combining the two previous equations, the important correlation between resistivity $\rho$ and $U_{\text{depl}}$ becomes

$$\rho = \frac{d^2}{2\,\varepsilon_0 \varepsilon_r \, \mu \, U_{\text{depl}}} \tag{3.28}$$

### 3.4.2 Capacitance Characteristics

The capacitance versus reverse bias voltage is depending on the effective doping concentration and thus on the full depletion voltage. Using 3.25, 3.27 and the capacitance $C$ of a parallel-plate capacitor

$$C = \varepsilon_0 \varepsilon_r \frac{A}{d} \tag{3.29}$$

we get for *n*-type bulk material:

$$C = A\sqrt{\frac{\varepsilon_0 \varepsilon_r q_e N_D}{2U_{\text{bias}}}} \qquad \text{for} \quad U_{\text{bias}} \leq U_{\text{depl}} \tag{3.30}$$

and

$$C = A\frac{\varepsilon_0 \varepsilon_r}{d} \qquad \text{for} \quad U_{\text{bias}} > U_{\text{depl}} \tag{3.31}$$

where A is the active area of the diode. Figure 3.11 shows the theoretical CV curve for a silicon detector. In the y-axis $1/C^2$ is plotted instead of C to better visualize its behavior.
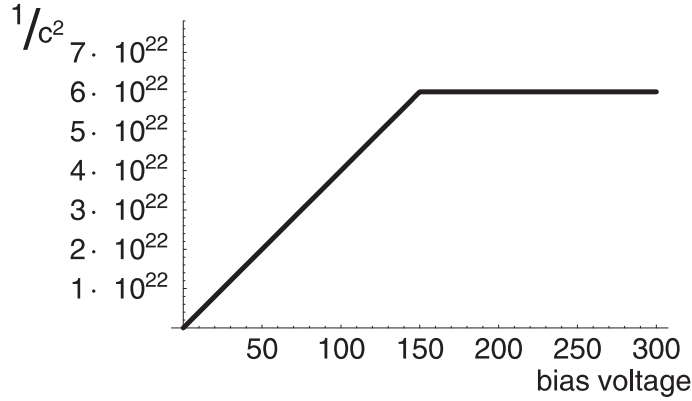


**Figure 3.11:** Theoretical CV curve for a silicon detector. The y-axis shows $1/C^2$ in arbitrary units to better show the kink of the curve at the full depletion voltage $U_{\text{depl}} = 150\text{V}$.

For the total capacitance at depletion, similar geometrical considerations for segmented devices apply as in the previous section. The total capacitance per strip length depends on the sensor thickness $d$, the strip pitch $p$ and the function $\mathbf{f}(w/p)$ (see equation 4.4) according to the following equation [23]:

$$C_{\text{tot}} = \varepsilon_0 \varepsilon_r \frac{p}{d + p\mathbf{f}(w/p)} \tag{3.32}$$

### 3.4.3 Current Characteristics

The total current $J_{\text{tot}}$ in a reverse-biased silicon detector is the sum of the thermal current in the depleted region $J_{\text{th}}$ and the diffusion current of the *pn*-junction $J_{\text{tot}}$:

$$J_{\text{tot}} = J_{\text{th}} + J_{\text{diff}} \tag{3.33}$$

The thermal current can be expressed [17] as

$$J_{\text{th}} = \frac{n_i e}{\tau_g} \cdot W \tag{3.34}$$

using the intrinsic carrier density $n_i$ at room temperature, the depletion layer depth $W$ and the generation lifetime of the majority charge carriers $\tau_g$. This lifetime was measured to be $4300\mu\text{s} <$

$\tau_g < 6500\,\mu s$ [24]. The thermal current component is proportional to the width of the depletion zone $W$ and thus scales with $\sqrt{V_{\text{bias}}}$.

The second fraction of the total current, the diffusion current, can be calculated using the *Shockley equation*:

$$J_{\text{diff}} = J_{\text{diff sat}} \left( \exp\left( \frac{q_e U_{\text{bias}}}{k_B T} \right) - 1 \right) \tag{3.35}$$

with the saturation diffusion current $J_{\text{diff sat}}$ for reverse bias given by:

$$J_{\text{diff sat}} = q_e \left( \frac{n_{p0} D_n}{\sqrt{D_n \tau_{r,n}}} + \frac{p_{n0} D_p}{\sqrt{D_p \tau_{r,p}}} \right) \quad . \tag{3.36}$$

In this equation $D_n$ and $D_p$ are the diffusion constants for electrons and holes, respectively. They can be calculated using Einstein's relations:

$$D_n = \mu_n \frac{k_B T}{q_e} \tag{3.37}$$

$$D_p = \mu_p \frac{k_B T}{q_e} \quad . \tag{3.38}$$

The parameters $n_{p0}$ and $p_{n0}$ are the minority charge carrier densities in $p$ and $n$ type materials in thermal equilibrium. Their values can be derived from equation 3.10 which leads to

$$n_{p0} = \frac{n_i^2}{N_A - N_D} \tag{3.39}$$

for holes and similarly for electrons.

The Shockley equation defines three regions

- In *forward bias mode* ($U_{\text{bias}} > 0$) the current rises exponentially with the bias voltage.
- For *reverse bias* ($U_{\text{bias}} < 0$), but larger than $\approx 4k_B T/e$, the exponential term can be neglected and the current is limited to the saturation value ($J_{\text{diff}} = J_{\text{diff sat}}$).
- In real diodes, avalanche effects cause a *breakthrough* when the bias voltage exceeds a certain threshold ($U_{\text{bias}} > U_{\text{break}}$). The high electrical field causes an energy transfer to electrons which are moved from the valence to the conduction band. The reverse current rises instantly. This process is not described by the Shockley equation.

Two mechanisms can cause breakdown, namely avalanche multiplication and quantum mechanical tunneling of carriers through the bandgap. Neither of the two breakdown mechanisms is destructive. However thermal stress caused by large breakdown currents at high breakdown voltages cause the diode to be destroyed unless sufficient heat sinking is provided or the current is limited, e.g. by a shunt resistor.

Breakdown in silicon at room temperature can be predicted using the following empirical expression for the electric field at breakdown [25]:

$$|E_{br}| = \frac{4 \times 10^5}{1 - \frac{1}{3} \log(N_{\text{eff}}/10^{16})} \text{ V/cm} \tag{3.40}$$

Assuming a one-sided abrupt *pn*-junction, the corresponding breakdown voltage can then be calculated as:

$$|V_{br}| = -U_{bi} + \frac{|E_{br}|^2 \varepsilon_0 \varepsilon_r}{2 q_e N_{\text{eff}}} \qquad . \tag{3.41}$$

The total leakage current in silicon detectors is temperature dependent according to

$$J_{\text{tot}} \propto T^2 \exp\left(-\frac{E_g}{2 k_B T}\right) \quad , \tag{3.42}$$

where T is the temperature.

## 3.5 Silicon-Metal Junctions

A contact between a semiconductor like silicon and a metal is called *Schottky barrier*. Similarly to a *pn*-junction, this junction can also be explained in the band model. Since the metal acts as a conductor, it has a partially filled conduction band and the Fermi energy level is inside the conduction band. Furthermore, the electric field in a metal can be considered as zero with surface charges on the outside boundary of the metal responsible for the interaction with the surrounding material. Since the Fermi levels on the junction have to line up, a built-in voltage

$$U_{bi} = \Phi_m - \Phi_s \tag{3.43}$$

occurs. $\Phi_m$ and $\Phi_s$ are the work functions of the metal and the semiconductor, respectively. On the metal side, a surface charge will develop which compensates the positive space-charge in the semiconductor boundary region. This creates a barrier, with the height of $q\Phi_m - q\chi$, where $q\chi$ is the difference between the edge of the conduction band and the vacuum level. This difference is an intrinsic property of the specific semiconductor, independent of doping, and is called *electron affinity*. Therefore, the height of the Schottky barrier remains unchanged if an external voltage is applied.

The current-voltage characteristic of such a junction must be considered taking majority carriers into account. The electron flow from the metal to the semiconductor is constant and only dependent from the barrier height. For the opposite direction, the flow from the semiconductor is expected to be proportional to the carrier concentration at the interface and thus depends on the applied voltage. With this assumptions and similar considerations like for the *pn*-junction, the relationship between voltage *U* and current *J* becomes [16]:

$$J = A^* T^2 \exp\left(-\frac{q(\Phi_m - \chi)}{k_B T}\right) \left[\exp\left(\frac{qU}{k_B T}\right) - 1\right] \tag{3.44}$$

with the effective Richardson constant $A^* = 110 \, \text{AK}^{-2} \text{cm}^{-2}$ for *n*-type silicon [17]. This equations consider thermal emission of electrons to be the main source of the current.

For very high doping concentrations at the silicon edge region ($> 10^{19} \text{cm}^{-3}$), the width of the potential barrier becomes so small that tunneling processes become important [17]. Then, the characteristic resistance becomes very small and the silicon-metal junction is called *ohmic contact*.

## 3.6 MOS Structures

MOS structures are formed when a metal is coupled to a semiconductor using a dielectric layer, like silicon dioxide ($SiO_2$). The most important parameter to characterize such a structure is the flatband voltage $V_{fb}$. It corresponds to the voltage which, when applied to the metal, yields to a flat energy band in the semiconductor. If there are no charges present in the oxide and at the oxide-semiconductor interface, the flatband voltage simply equals the difference between the metal work function $\phi_M$ and the semiconductor work function $\phi_S$:

$$V_{fb0} = \phi_M - \phi_S \tag{3.45}$$

For an aluminum metal layer and n-type silicon with a doping in the range of $10^{11} - 10^{12}$ cm$^{-3}$, the intrinsic flatband voltage $V_{fb0}$ is around $-0.5$ V.

The flatband voltage of real MOS structures is affected by the presence of charge in the oxide or at the oxide-semiconductor interface. For a charge $Q_i$, located at the interface between the oxide and the semiconductor, and a charge density $r_{ox}$, distributed within the oxide, the flatband voltage is given by:

$$V_{fb} = V_{fb0} - \frac{Q_i}{C_{ox}} - \frac{1}{\varepsilon_{ox}} \int_0^{t_{ox}} \rho_{ox}(x) x \, dx \tag{3.46}$$

where $\frac{Q_i}{C_{ox}}$ is the voltage across the oxide due to the charge at the oxide-semiconductor interface and the last term is due to the charge density inside the oxide.

The capacitance of an MOS structure is obtained using the same assumptions as those listed in section 3.4.2. The MOS structure is treated as a series connection of two capacitors: the capacitance of the oxide and the capacitance of the depletion layer.

We can identify three regions (see fig. 3.12):

**accumulation region ($V_{gate} > V_{fb}$):** Free electrons are accumulated beneath the gate. The measured capacitance is the oxide capacitance $C_{ox}$ only. Therefore, the oxide thickness can be extracted from this value.

**depletion region ($V_{gate} \leq V_{fb}$):** Lowering the gate voltage, the Si region underneath the gate depletes of free electrons. The MOS capacitance is obtained from the series connection of the oxide capacitance and the capacitance of the depletion layer. In a theoretical situation (as shown in the figures), this happens close to zero: $V_{fb} \approx 0$V. The shift of the flatband voltage measures the trapped positive charge in the oxide, which is the main parameter of practical interest.

**inversion region ($V_{gate} << V_{fb}$):** Holes accumulate beneath the metal gate. The capacitance becomes independent of the gate voltage. The low frequency capacitance equals the oxide capacitance since charge is added to and removed from the inversion layer. The high frequency capacitance is obtained from the series connection of the oxide capacitance and the capacitance of the depletion layer (see figure 3.13.)
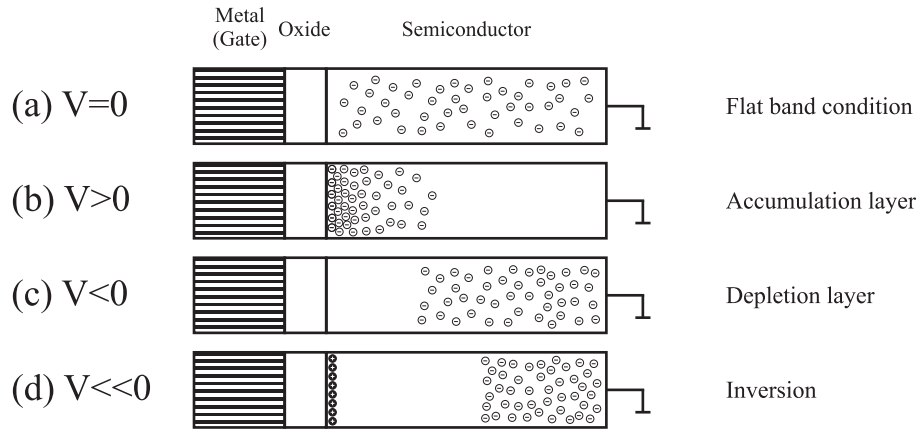
**Figure 3.12:** States of an "ideal" ($V_{fb} = 0$) *n*-type MOS structure: thermal equilibrium (a); accumulation (b); depletion (c); inversion (d).
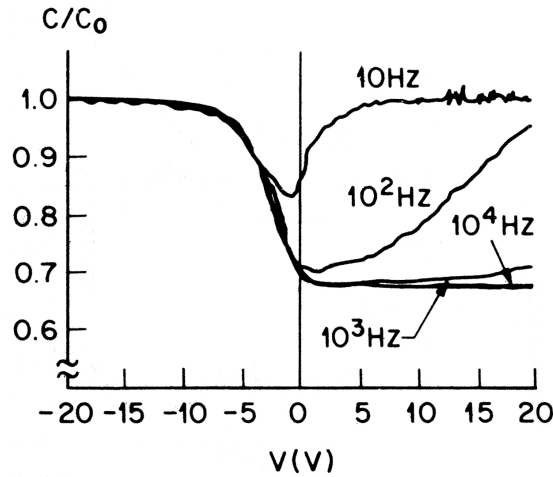


**Figure 3.13:** Diagram showing capacitance versus voltage (CV curve) on a MOS structure for different measurement frequencies [17].

## 3.7 Poly-Crystalline Silicon

Ohmic resistors are necessary in silicon detectors to connect the strips to the bias line. The most reliable option for those resistors is poly-crystalline silicon. It is fabricated by deposition of a poly-crystalline silicon layer of very fine grain size upon an insulator surface like silicon oxide, followed by ion implantation of boron (or phosphorous). The implant dose of the dopant is within the range from $5 \cdot 10^{14}$ to $10^{16}$ ions/cm$^2$. This ion implantation is normally done using a screen silicon dioxide surface layer. The structure must be annealed afterwards to control the grain size of the poly crystalline silicon layer and homogenize the distribution of implanted ions throughout the entire film thickness. Normally, just the value of the resistance is defined and it is the decision of the sensor producer which kind of poly crystalline silicon and doping is used.

## 3.8 Silicon Detector Working Principle

A highly doped thin $p^+$ region on a very lowly doped $n$ substrate forms a large-area *pn*-junction. The back side of the substrate consists of a highly doped $n^+$ region and is called *backplane*. When a reverse bias voltage is applied between backplane and $p^+$ region which is above the full depletion voltage of the device, the SCR ranges across the whole detector. The device is then called *over-depleted*.

When a charged particle traverses the detector, energy is deposited in the detector material, leading to the generation of electron-hole-pairs along the particle's track (see section 3.3.4). These electron-hole-pairs are separated by the electric field and move towards the electrodes, electrons towards the $p^+$ and holes to the backside $n^+$ region. The speed of their movement is known as carrier drift velocity $v$ which is proportional to the electric field up to a saturation level. The proportional constant is called carrier mobility $\mu$ and is $\mu_n = 1450\ \mathrm{cm^2/Vs}$ for electrons and $\mu_p = 450\ \mathrm{cm^2/Vs}$ for holes, respectively [1].

The number $n$ of created charges is the quotient of the total energy loss $E_{\mathrm{loss}}$ of the incident particle and the energy necessary for pair production (ionization energy $E_{eh}$),

$$n = \frac{E_{\mathrm{loss}}}{E_{eh}} \quad . \tag{3.47}$$

In silicon, $E_{eh} = 3.6\ \mathrm{eV}$, which results in a most probable charge of about $n = 23{,}000$ pairs for a MIP in a standard silicon detector of 300 μm thickness.

A charge moving inside the detector bulk induces a current, no matter whether the carriers eventually reach the electrodes or not. According to Ramo's Theorem [26], this current $j$ is proportional to the sum of both carrier velocities,

$$j = \frac{e}{d} \left( \sum v_e + \sum v_h \right) \tag{3.48}$$

with the elementary charge $e$, the detector thickness $d$ and the carrier drift velocities $v_e$ and $v_p$ for electrons and holes, respectively. The integrated current gives the total collected charge $Q_c$, which can be measured by integrating amplifiers,

$$Q_c = \frac{e}{d} \int \left( \sum v_e + \sum v_h \right) dt \quad . \tag{3.49}$$

To measure the position of the incident particle, the area of the $p^+$ region is usually segmented into many small regions (strips or pixels) which are read out separately. The measured precision depends mainly on the strip spacing and the method of readout. As long as only digital information is used (taking the center position of the strip as the measured coordinate) and effects arising from track inclination and charge diffusion during collection are neglected, the measurement precision is given for the strip pitch $p$ by

$$\langle \Delta x^2 \rangle = \frac{1}{p} \int_{-p/2}^{p/2} x^2 dx = \frac{p^2}{12} \tag{3.50}$$

This means that the root-mean-square deviation from the true coordinate is

$$\sigma_x = \sqrt{\langle \Delta x^2 \rangle} = \frac{p}{\sqrt{12}} \quad . \tag{3.51}$$

The measurement precision is substantially improved with analog readout, so that the signal charge is collected on more than one strip and the coordinate is found by interpolation, e.g. by the center-of-gravity of the signal. If this method is used, the expected resolution can be calculated by using

$$\sigma_x \propto \frac{p}{\text{SNR}} \tag{3.52}$$

with SNR being the signal-to-noise-ratio of the system (see below).

## 3.9 Noise Sources

A *silicon detector system* is meant to be the silicon detector itself plus its associated readout electronics. The noise in such a system has a significant contribution to its performance, since the measured signals are very small. Especially for strip detectors, many effects affect the system noise like the readout line impedance, the strip capacitance, the dark current and the bias resistor. It is important to know the contributions of each effect in detail to optimize not only the design of the detector but of the whole system.

The noise is expressed as Equivalent Noise Charge (ENC) using *electrons* as unit. Thus, the signal-to-noise ratio (SNR) can easily be calculated by dividing the number of electrons generated by a particle traversing the detector (see section 3.3.4) by the ENC:

$$\text{SNR} = \frac{\text{signal}}{\text{ENC}} \tag{3.53}$$
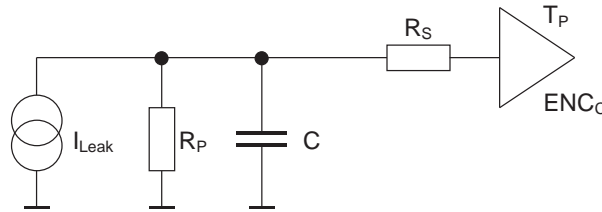


**Figure 3.14:** Noise sources in a silicon detector and the readout amplifier.

The different sources for noise in a silicon detector and a readout amplifier are shown in figure 3.14, comprising for contributions:

$$\text{ENC}^2 = \text{ENC}_C^2 + \text{ENC}_J^2 + \text{ENC}_{R_p}^2 + \text{ENC}_{R_s}^2 \tag{3.54}$$

The noise contribution of the capacitive load $C$ of a single readout strip connected to an input channel of the readout chip is approximated by:

$$\text{ENC}_C = a + bC \tag{3.55}$$

where $a$ and $b$ are constants which are defined by the design of the readout chip. The capacitance $C$ is actually composed of a network of capacitances including the coupling capacitance $C_{ac}$, the inter-strip $C_{int}$ and the backplane capacitance $C_{back}$.

The contribution of the sensor's dark current to the noise can be expressed by

$$\text{ENC}_J = \frac{e}{2}\sqrt{\frac{J_{\text{leak}}\, t_p}{q_e}} \approx 107\sqrt{J t_p} \tag{3.56}$$

where the dark or leakage current $J_{\text{leak}}$ is in nA and the shaping time of the readout chip $t_p$ is expressed in µs. The factor $e$ is Euler's number ($e \approx 2.71828$).

The thermal noise of the poly-silicon resistor, $\text{ENC}_{R_p}$, is given by

$$\text{ENC}_{R_p} = \frac{e}{q_e}\sqrt{\frac{k_B T\, t_p}{2R_P}} \approx 772\sqrt{\frac{t_p}{R_P}} \tag{3.57}$$

where $R_P$ is expressed in MΩ and $t_p$ in µs.

The contribution of the serial line noise $ENC_{R_s}$ is dominated by the resistance of the aluminum readout strips and can be calculated using

$$\text{ENC}_{R_s} = \frac{e\,C}{q_e}\sqrt{\frac{k_B T\, R_s}{6 t_p}} \approx 0.395\,C\sqrt{\frac{R_s}{t_p}} \tag{3.58}$$

with Ω as unit of $R_S$, pF for the detector capacitance $C$ and µs for the shaping time $t_p$.

Each of these noise contributions and the total ENC noise calculated according to formula 3.54 can be plotted individually versus the shaping time of the readout chip. This is shown for the CMS SST in figure 3.15 (left) together with the signal-to-noise ratio calculated from these numbers.
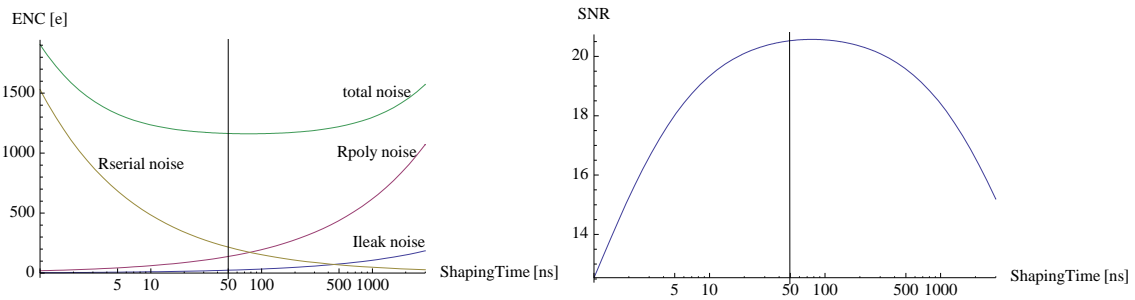


**Figure 3.15:** Noise sources (left) and signal-to-noise ratio (SNR; right) in the CMS detector-readout system versus the integration time of the readout chip. The vertical lines in both diagrams indicate 50 ns, which is the integration time for the APV25 readout chip used in CMS.

## 3.10 Radiation Damage

Operating a silicon detector in a HEP experiment like the LHC induces changes in the semiconductor properties because of irradiation. At the expected annual irradiation level of up to several $10^{14}$ hadrons/cm$^2$ during ten years of operation, these changes cannot be neglected. They are degrading the performance of the detector and thus are called *radiation damage*. Many changes are neither stable with temperature nor with time due to so called *annealing effects*. Microscopic effects of the radiation damage are

- an effective doping change of the bulk material, including type inversion of the original *n*-type silicon to *p*-type after a certain fluence
- an increase of resistivity of undepleted bulk material
- introduction of many energy levels within the band gap because of impurities incorporated into the silicon lattice
- charge trapping and thus the reduction of signal
- a change of oxide charge

Macroscopically, these effects change the electrical properties of the sensor by

- increase of the leakage current,
- change of the full depletion voltage,
- change of the flatband voltage and surface current

Irradiation effects must be separated into two parts, bulk and surface damage.

### 3.10.1 Bulk Radiation Damage

The bulk damage in silicon detectors caused by hadrons or highly energetic leptons is primarily due to displacement of lattice atoms out of their position. The first lattice atom hit by an incident particle is called *Primary Knock-on Atom* (PKA). The threshold energy for this process is around 25 eV. Such single displacements result in a *Frenkel pair* of interstitials and vacancies (see figure 3.16). While incident particles of higher energies can create clusters of Frenckel pairs, low energy particles are responsible for single fixed point defects.

In addition, nuclear interactions like neutron capture and nucleus transmutation, secondary processes from highly displaced lattice atoms and defect clusters from cascade processes cause changes to the silicon lattice, thus creating additional levels in the band gap. All these defects have severe effects on the detector performance, depending on their concentration and energy levels. All those defects are responsible for the effects on the detector parameters described later.

The Non-Ionising-Energy-Loss (NIEL) hypothesis is used to compare the damage induced by different particle types and particle energies [27, 28]. It relies on the assumption that the amount
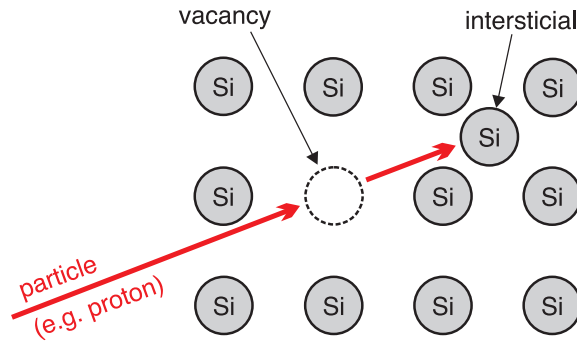
**Figure 3.16:** Schematic view of a Frenckel pair production. If the incoming particle exceeds a certain energy level, a lattice atom is being displaced from the lattice to the surroundings. The empty lattice site forms a vacancy, while the additional atom in between the lattice is called interstitial.

of damage scales linearly with fluence. Radiation damage in silicon bulk material can be described by the *displacement damage cross-section D*, which is normally quantified in [MeV mb] and which is proportional to the NIEL, usually given in given in [keV cm$^2$/g]. For silicon the relation between D and NIEL is defined as $100\,\text{MeV mb} := 2.144\,\text{keV cm}^2/\text{g}$ [27]. The common way to compare radiation damage is to scale all fluences to an equivalent fluence $\Phi_{eq}$. The reference particles are neutrons with an energy of 1 MeV [28]. The displacement damage cross-section for 1 MeV neutrons is thus set as a normalizing value: $D_n(1\,\text{MeV}) := 95\,\text{MeV mb}$. Figure 3.17 shows the normalized NIEL values plotted as a function of the energy for neutrons, pions and protons.



**Figure 3.17:** Non-ionizing energy loss (NIEL) for different particles versus the particles energies [27].

One effect of the irradiation of n-doped semiconductor devices is the removal of donors and the generation of acceptor-like defects. This effect reduces the effective bulk doping concentration

$$N_{\text{bulk}} = |N_D - N_A| \tag{3.59}$$

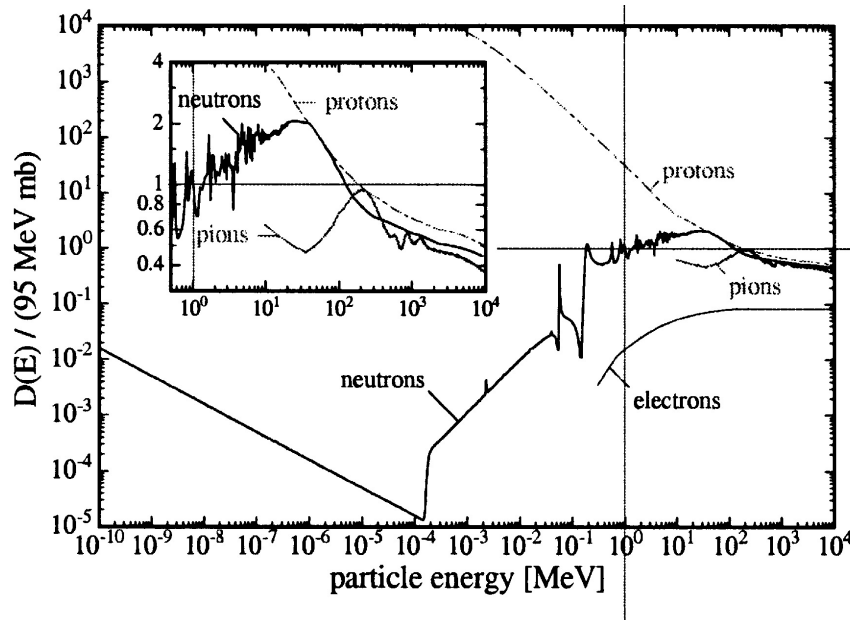until the doping concentration is zero and the device behaves like an intrinsic semiconductor. This state is called *inversion point*. With further irradiation, acceptors dominate and the bulk material acts like a *p*-type semiconductor. This effect is called *type inversion*. As the depletion voltage scales with the bulk doping concentration (see equation 3.26), the bias voltage has to be adjusted with fluence level to ensure operation of the device above the full depletion voltage (see figure 3.18). Initially the depletion voltage decreases until it theoretically reaches zero in the inversion point.
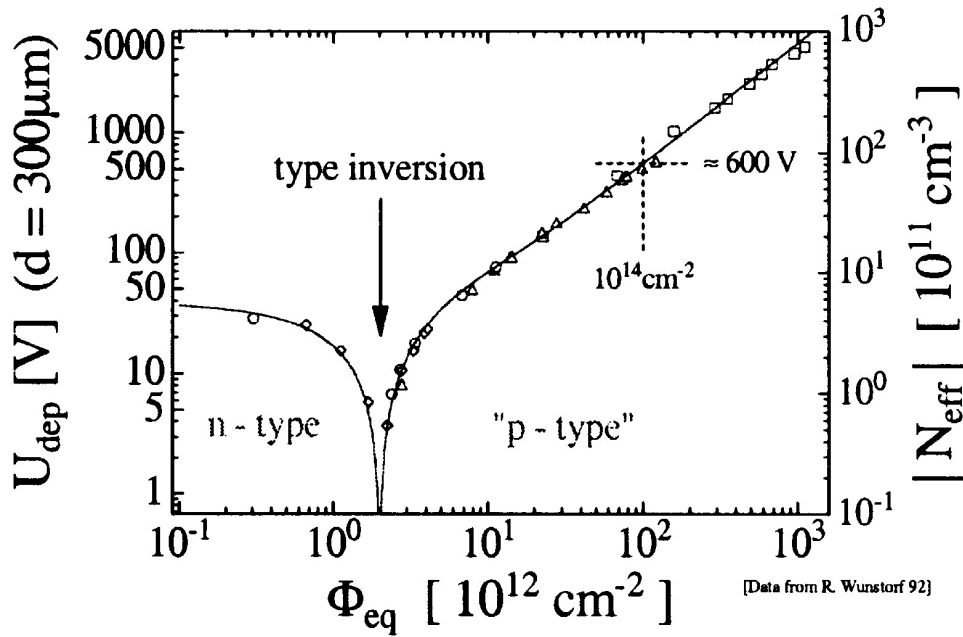


**Figure 3.18:** Evolution of the full depletion voltage $U_{\text{dep}}$ versus the equivalent fluence $\Phi_{\text{eq}}$. The detector bulk material is *n*-type before and *p*-type after the inversion point [29].

After that, the depletion voltage rises proportionally to the fluence. The level of fluence needed for type inversion depends on the initial number of donors. High resistivity sensors have a low initial donor density and reach the inversion point with less fluence than sensors with low resistivity.

In addition, radiation als introduces defects in the silicon bulk material which act as charge traps and recombination centers. This leads to a reduction of the *charge collection efficiency*. The probability of charge trapping is proportional to the drift time. Thus a higher bias voltage has to be applied which results in shorter drift times to reduce this effect.

Moreover, radiation damage causes an increase of the detector leakage current $J_{\text{leak}}$, which is proportional to the equivalent fluence $\Phi_{\text{eq}}$ and the sensitive volume $V$ [27],

$$\Delta J_{\text{leak}} = \alpha \, \Phi_{\text{eq}} V \tag{3.60}$$

where $\alpha$ is the type-independet *current related damage rate*[5]. At room temperature, values between 4 and $10 \cdot 10^{-17}$ A/cm are given in literature, depending on measurement conditions (e.g. annealing). This parameter scales with the temperature like the leakage current (eq. 3.42) and thus is reduced approximately by a factor of 15 for a temperature of $-10°$C compared to room temperature. Besides the fluence dependence, the radiation induced current $\Delta J_{\text{leak}}$ evolves, since the damage factor $\alpha = \alpha(t)$ decreases with time. This time-dependence is initially exponential, but changes to a logarithmic scale for long observation times [30].

### 3.10.2 Surface Radiation Damage

For discussing radiation damage effects in the surface one needs to dissect the term *surface* more precisely into regions like the *dielectric bulk* material, which consists of silicon oxide and silicon nitride. Another part is the *border region* between the oxide bulk and the silicon bulk material. This region of roughly 30 Å thickness is characterised by high mechanical stress, which increases the defect sensitivity. Underneath this region, the very thin (few nanometers) *Si/SiO$_2$ interface* is located.

Thermally grown silicon oxide always contains various kinds of intrinsic defects with a relatively low concentration. Often foreign atoms of hydrogen play a decisive role since they passivate dangling bonds by attaching to them. Most defects act on the donor levels. Because of that the net oxide charge density is always positive[6]. Like for the silicon bulk, irradiation causes removal of donors and generation of acceptor-like defects in the oxide. But since the oxide acts like a insulator, the charges are stuck and cause an additional shift of the net oxide charge density. This can be measured by a CV curve on a MOS structure (see section 3.6).

Radiation induced effects by ionizing particles, either at the border region or at the Si/SiO$_2$ interface, lead to a charge accumulation at the silicon-oxide interface, resulting in a decrease of the inter-strip isolation. This causes unwanted signal charge sharing between neighboring strips. Additionally it leads to an increase in the inter-strip capacitance, which is a major contribution to the noise of the system (compare section 3.9). Also an increase of the surface current has been observed after irradiation, attributed to the creation of additional surface states which act as generation centers. The capacitive coupling between a strip and its neighbors is dominated by the quality of the oxide at the interface, which is process-dependent, and by the ratio of strip width to strip pitch $^w/_p$. It is possible to reduce the damage-induced coupling by substantially over-depleting the device. This results in high electric fields on the strip borders and restricts the oxide charge in the region between the strips, thus reducing the capacitance. However, all these surface effects tend to saturate after some time, because the concentration of oxide charges does not exceed a certain limit [31].

---

5. This is assumptions are only valid for silicon, but independently of type, resistivity and production method (float zone, Czochralski,...).

6. However, there are two mechanisms related to oxygen contamination of the oxide possible which are causing a negative charge density: The high electron affinity of interstitial oxygen is causing acceptor level defects and the non-bridging oxygen can complete its outer shell by accepting a bond electron, leaving a hole behind.

### 3.10.3 Annealing

Defects caused by radiation can propagate in the silicon lattice, which leads to unstable conditions. Two effects, annealing and reverse annealing, with different time behavior and temperature dependence, take place.

With time constants in the range of a few days, a decrease in the radiation induced changes occurs soon after irradiation. This is called *beneficial annealing* since it is considered to have good impact on the detector parameters like decreasing number of defects and decreasing leakage current.

On a longer timescale (e.g. weeks), the irradiation introduced doping concentration increases again. This effect is called *reverse annealing* and deteriorates the detector performance again. It can be suppressed by cooling the detector and by minimizing the maintenance periods of the silicon detectors at room temperature.

Figure 3.19 shows the annealing behavior of the effective doping concentration after irradiation, with both beneficial and reverse annealing shown.
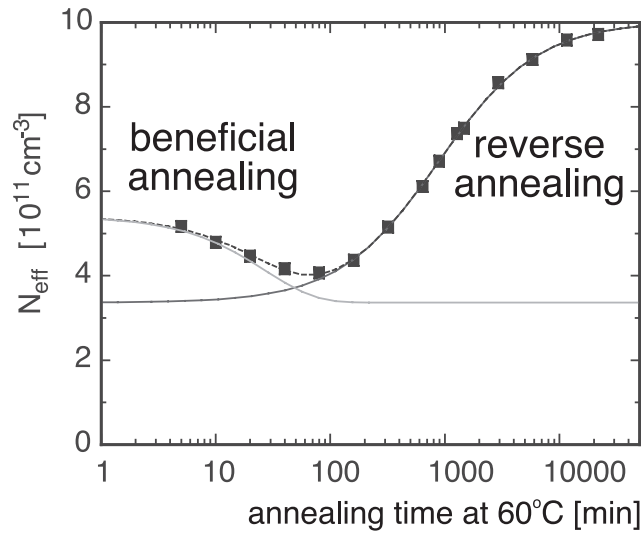


**Figure 3.19:** Annealing behavior of the effective doping concentration after irradiation versus annealing time. The beneficial (decrease) and reverse (increase) annealing are clearly visible [30].

# 4 Silicon Detectors for CMS

## 4.1 Sensor Specifications

The CMS sensors are single-sided silicon sensors with $p^+$ strip implants on n-bulk float zone material, with poly-crystalline bias resistors and AC coupling [32]. The special features of these sensors are: operation beyond the type inversion, metal overhang design and use of <100> lattice orientation. These features as well as the electrical and mechanical properties of the sensors are described in detail in this chapter.

### 4.1.1 Thickness and Resistivity

The CMS Tracker consists of 10 barrel layers (TIB and TOB), two times three inner disks (TID) and two sets of nine endcap disks (TEC), as discussed in chapter 2.3 and shown in figure 2.7. From another point of view, the Tracker can also be divided into two regions of different sensor properties: the inner and the outer part. TIB, TID and four innermost rings of the TEC are forming the inner region while TOB and the three outermost rings of TEC makes up the outer region. For the inner region each detector module is built with one silicon sensor of 320 μm thickness, while the outer region uses two daisy-chained sensors of 500 μm thickness. The higher signal there is compensated by higher system noise introduced by the daisy-chained sensors.

The full depletion voltage is proportional to the square of the sensor thickness and the effective doping concentration of the bulk material (see equation 3.28) and varies with radiation dose (fluence). In order to keep it within a practically manageable range, the sensors were produced at *n*-type silicon substrate. With this material, the full depletion voltage decreases with fluence up to the type inversion point and increases afterwards. The best scenario is the one where the full depletion voltages are on the same level before and after irradiation [11]. This can be seen in figure 4.1. Together with an acceptable signal to noise ratio (SNR), the following parameters were defined for the two regions of the tracker.
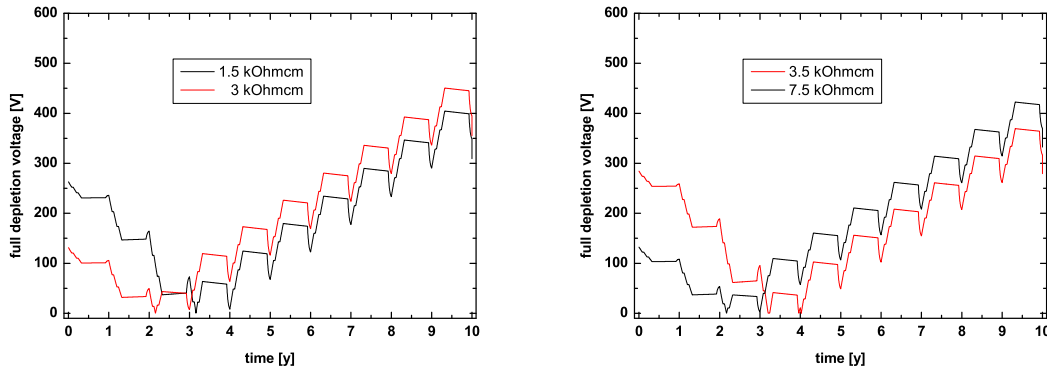
**Figure 4.1:** Evolution of the full depletion voltages for thin (left) and thick (right) sensors versus the LHC operating time in years (equivalent to fluence or integrated luminosity). These plots are following theoretical considerations called "Hamburg model" and are calculated using standard CMS annealing assumptions [11]. The "dips" of the graphs are caused by the warm maintenance period once a year.

## Inner Region

All of the inner detectors were fabricated using wafers with a thickness of 320 µm and a resistivity between 1.5 and 3 kΩ cm according to the technical specifications [32][1]. According to equation 3.28 the depletion voltage for these sensors is expected to be between 105 and 270 V. These sensors are called "thin".

## Outer Region

Two sensors are daisy-chained via wire bonding to build up one module in the outer region to reduce the number of readout channels. These modules have different electrical characteristics form the inner region since the strips are approximately twice as long as for single-sensor modules. This fact increases the aluminum and $p^+$ strip impedance. Moreover, the effective value of the polysilicon resistor is reduced by a factor of two since the resistors of the sensors are connected in parallel. Additionally, the long strips result in higher capacitive load for the readout chip. These effects increase the electronic noise of those modules. To achieve a similar signal-to-noise ratio as for the inner region, the thickness of the sensors was increased to 500 µm. Hence those sensors are called "thick". By using wafer material with a resistivity between 3.5 and 7.5 kΩ cm, the depletion voltage is almost identical to the one for thin sensors in the inner region. Table 4.1 shows the correlation of resistivity, thickness and full depletion voltage for both regions.

---

1. During production, the specifications have been relaxed and wafers with a resistivity between 1.25 and 3.25 kΩ cm were accepted.

|                |                        |                                                          |
|----------------|------------------------|----------------------------------------------------------|
| inner region:  | nominal thickness:     | 320 μm (*"thin"*)                                        |
|                | effective thickness    | $300 < d < 340$ μm (variation $\pm 20$μm)               |
|                | resistivity:           | $1.5 < \rho < 3.0$ kΩ cm                                |
|                | full depletion voltage:| $105$ V $< V_{\text{depl}} < 270$ V                      |
|                |                        |                                                          |
| outer region:  | nominal thickness:     | 500 μm (*"thick"*)                                       |
|                | effective thickness:   | $480 < d < 520$ μm (variation $\pm 20$μm)               |
|                | resistivity:           | $3.5 < \rho < 7.5$ kΩ cm                                |
|                | full depletion voltage:| $107$ V $< V_{\text{depl}} < 270$ V                      |

**Table 4.1:** Specified sensor thicknesses, bulk resistivities and expected full depletion voltages for the two different regions.

## 4.1.2 Mechanical Specification of the Wafer

Both, the 320 μm "thin" and the 500 μm "thick" silicon sensors were fabricated using 6" technology, with the standard planar process usually employed in the semiconductor industry. One single detector is produced from each wafer and it must be placed within a fiducial circle of about 13.5 cm diameter. The variation of the wafer thickness must not exceed ± 20 μm. The vendors were asked to dice the sensor out of the wafer and the surrounding test structures with an accuracy of better than ±20 μm. The quality of the cut edges shall be such that there are no chips grater than 40 μm and no cracks. The sensors must have a flatness of $< 100$ μm without any stress applied [32]. The quality assurance scheme of CMS required that every sensor had to be visually inspected with a microscope to fulfill these specifications [33].

## 4.1.3 Crystal Orientation

The main strategies to ensure the radiation hardness of the silicon sensors are: a) reducing the surface damage, b) delaying the bulk type inversion and c) use a special design of the guard ring and the metal overhang structure to allow excellent HV stability. To minimize the surface damage, CMS has decided to use silicon material with <100> crystal orientation in contrast to the "standard" <111> material. This material has less dangling bonds in the interface layer between silicon bulk and oxide and thus has a smaller number of charge carriers present in this interface. This is shown in figure 4.2.

Since the mobility of charges in silicon oxide is very low, these carriers are often called "fixed oxide charges". Irradiation raises the number of positive charge carriers in the silicon dioxide, increasing the interstrip capacitance and lowering the interstrip resistance. Both values influence the noise behavior of the detector and readout electronics. Thus, the initial number of positive charge carriers must be kept on a very low level. They can be measured either using dedicated MOS test structures or by probing the interstrip capacitance and resistance directly on the sensor [34].
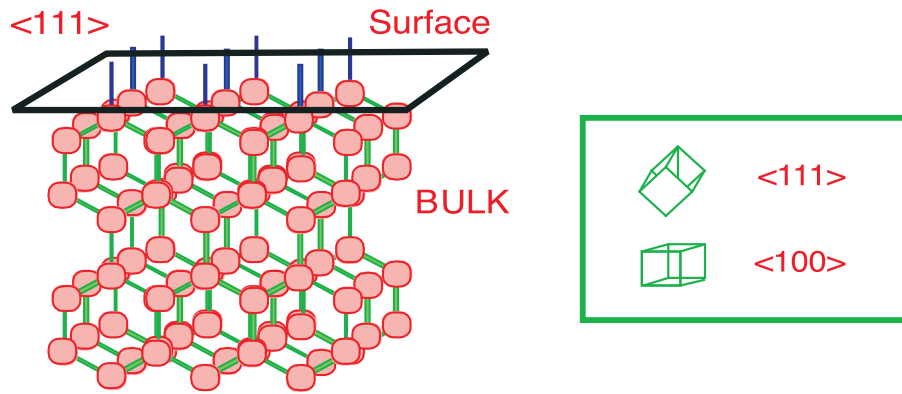
**Figure 4.2:** Silicon crystal and dangling bonds (blue) on the silicon-to-silicon-dioxide interface. The number of free
dangling bonds is $10^{11}$ for <111> silicon and $10^{10}$ for <100> silicon.

### 4.1.4 Strip Implantation

Strips are formed by implanting acceptors into the $n$-type bulk material forming $p^+$ regions. Both together represent a $pn$-junction, which is essential to build a depletion zone in the bulk volume. The specifications require a sheet resistivity below 400 $\Omega$/square [32], while CMS internal measurements showed that the actual values are between 140 and 175 $\Omega$/square [34].

The ratio between strip width and strip pitch $w/p$ is 0.25 for all sensor geometries. This is the result of a comprehensive study [35] done on multi-geometry detector prototypes where various $w/p$ ratios between 0.13 and 0.5 were evaluated. Measurements before and after irradiation of those prototypes have demonstrated that the interstrip capacitance can be parameterized by the following approximation:

$$C_{int} = 0.1 + 1.5 \cdot \frac{w + 20\mu m}{p} \quad \text{pF/cm} \tag{4.1}$$

and the total capacitance by

$$C_{tot} = (0.8 + 1.6 \cdot w/p) \quad \text{pF/cm.} \tag{4.2}$$

For the chosen value of $w/p = 0.25$, this leads to $C_{tot} = 1.2 \text{pF/cm}$.

Due to the strip segmentation, the electrical field is not homogeneous in the device. A correction factor for the full depletion voltage between a planar diode and a segmented detector device must be taken into account [23]:

$$\frac{U_{\text{depl segmented}}}{U_{\text{depl diode}}} = \left(1 + \frac{2p}{d} \mathbf{f}\left(\frac{w}{p}\right)\right) \tag{4.3}$$

with the strip pitch $p$, the strip width $w$, the thickness of the device $d$ and the function $f\left(\frac{w}{p}\right)$ a numerical approximation of the poisson equation for the non-linear field:

$$\mathbf{f}(x) = -0.00111x^{-2} + 0.0586x^{-1} + 0.24 - 0.651x + 0.355x^2 \tag{4.4}$$

For the constant width-over-pitch ratio $w/p = 0.25$, the function's value is $f(0.25) = 0.3161$ for all sensor geometries. As a consequence, the correction factor beween diode and segmented strip varies

between 1.15 and 1.3, depending on the strip pitch and sensor thickness. For better understanding, figure 4.3 shows the result of equation 4.3 as a function of $w/p$, while keeping the strip pitch $p$ constant. For $w/p = 1$ the factor becomes 1 as this is the planar diode case.
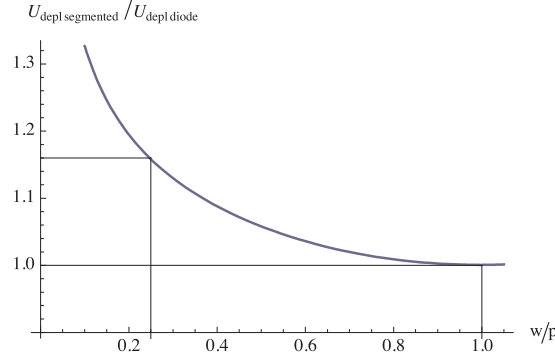


**Figure 4.3:** Diagram showing the correction factor $\frac{U_{\text{depl segmented}}}{U_{\text{depl diode}}}$ from equation 4.3 for varying width-over-pitch ratios $w/p$. In this example, the strip pitch is $p = 80\mu m$ and the sensor thickness is $d = 320\mu m$. For $w/p = 0.25$, the excess factor becomes to 1.16.

## 4.1.5 Dielectric Layer

The dielectric layer between the $p^+$ strip implants and the aluminum strips forms an integrated capacitor which results in AC coupling between the biasing circuit and the readout circuit of the detector. The dielectric layer itself is a sandwich design consisting of silicon oxide ($SiO_2$) and a thinner silicon nitride ($Si_3N_4$) layer separated by a very thin layer of poly crystalline silicon. Measurements showed that the $SiO_2$ layer is about 2000 Å and the nitride layer about 750 Å thick [34]. The thickness of the poly-silicon layer is estimated to be thinner than 60 Å.

## 4.1.6 Aluminum Metallization and Metal Overhang

Aluminum is deposited on top of the p$^+$ strip implantation and the dielectric sandwich-layer. This layer was specified to have a resistivity below $18\,m\Omega/\text{square}$ and a thickness of at least $1.5\,\mu m$ [32]. CMS-internal measurements showed that this value is very hard to achieve and thus the limit was extended to $30\,m\Omega/\text{square}$. The average value measured on HPK test structures was $23\,m\Omega/\text{square}$, while for STM the value was slightly above the limit for the first deliveries, but dropped to $19\,m\Omega/\text{square}$ after an intervention by CMS.

HV stability with respect to high bias voltages is ensured by a method called *metal overhang*. This technique uses metal strips which are 4 μm wider than the $p^+$-strips below the dielectric layer. Figure 4.4 shows the principle of this design. If the aluminum strip has the same width as the implant, the maximum electric field density is around the edges of the implant. The metal overhang design moves that maximum to the metal strips, while the field is now penetrating the dielectric layer. There, a breakthrough is not possible because of the small number of free charge carriers. Hence, the HV stability is significantly improved by this technique.
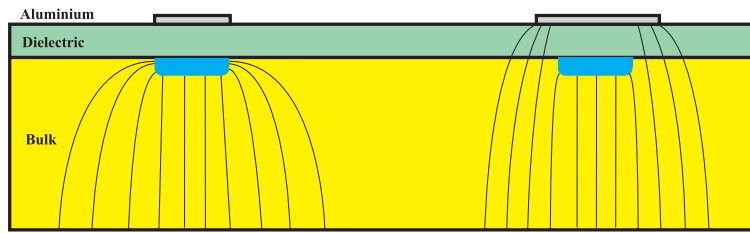
**Figure 4.4:** Electrical field lines in an AC coupled silicon strip detector without (left) and with (right) metal overhang.

### 4.1.7 Guard Ring

The guard ring has to adjust the electric field configuration towards the sensor edges. Consequently, the metal overhang was applied to bias and guard ring as well. While the design is similar for the bias ring, the metal overhang is much larger on the outer side of the guard ring. This is shown in drawing 4.5. Usually, HV is applied to the back side of the sensor, while the
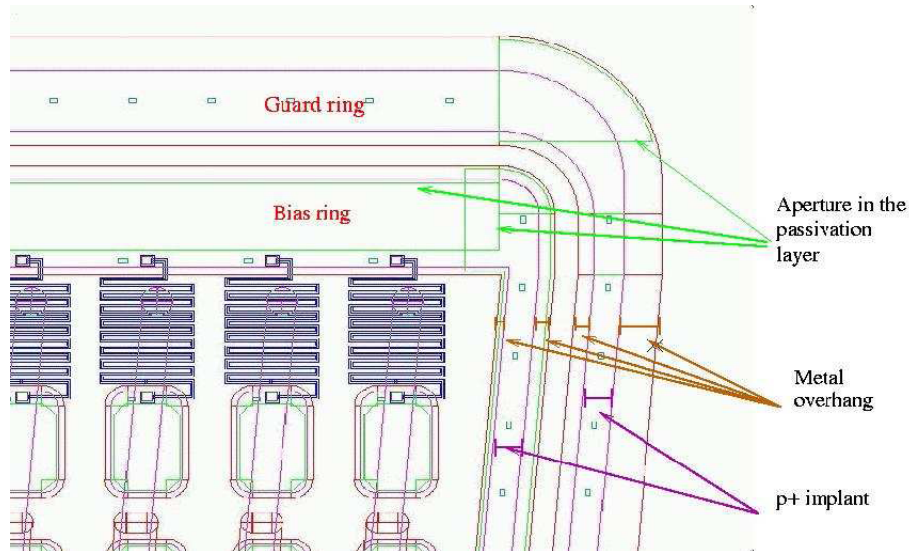


**Figure 4.5:** Layout of the metal overhang design of the guard ring. The latter has a large overhang on the outer side.

bias line is grounded. The outer $n^+$ implantation (see next section) follows the HV potential on the sensor's backplane. The guard ring is kept floating, hence it smoothly adjusts the potential from GND on the bias ring to HV on the outer $n^+$ ring, preventing HV breakdown on the sensor edges.

### 4.1.8 Outer $n^+$ implantation

A ring of $n^+$ material is implanted around the guard ring to the cutting area of the sensor. It is connected by vias to the aluminum layer, which contains alignment marks and strip numbering (see figure 4.6). The ring itself is floating like the guard ring, but as it is made of highly-doped $n^+$
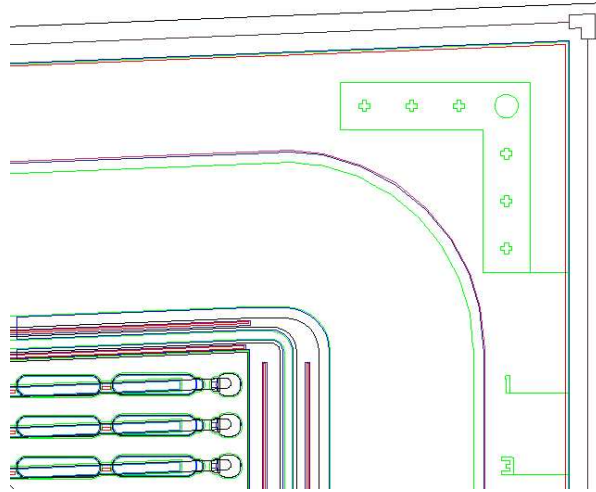
**Figure 4.6:** Outermost sensor region with n+ layer and aluminum layer. The alignment marks and strip numbers on odd strips are shown.

material, its potential follows the $n^+$+ backplane. This means that HV applied to the backplane propagates to the front side of the sensor by this ring. This technique helps to reduce dark currents and minimizes the chance of HV breakdown since it avoids surface currents from the backplane through the cut region into the active inner area of the sensor.

### 4.1.9 Backplane

The uniformly metallized backplane is located on the back side of the bulk substrate, opposite of the strips of the detector. It is made of approximately 2 µm thick aluminum-silicon-alloy and its task is to provide electrical connection to the bulk material to apply the HV bias voltage. Between this metal layer and the silicon bulk material, a several µm thick, highly-doped $n^{++}$ layer is located providing ohmic contact. This layer also acts as a *pn*-junction after type inversion. In that case, the bulk material is of *p* type and the $n^{++}$ region forms the junction which acts as seed for the SCR or depletion zone. This implies that sensors after type inversion cannot be operated under-depleted as the depletion zone – and thus also the signal charge – does not reach the front-side strips anymore.

### 4.1.10 Biasing

To form a depletion region in the sensor, a reverse bias voltage has to be applied between the back-plane and the junction side of the detector. Thus, a positive HV is applied to the sensor backplane, while the bias line is connected to ground (GND). An ohmic connection is necessary from the bias line to each p$^+$ strip to maintain this potential on the strips. For this purpose, poly-crystalline sil-icon is deposited on the sensors forming a so called *poly-silicon* resistor or, shorter, *poly resistor*. The cross-section of a detector utilizing this biasing technique is shown in figure 4.7 and the elec-

tric schematics of an AC coupled silicon sensor vs. a DC coupled device is shown in figure 4.8.
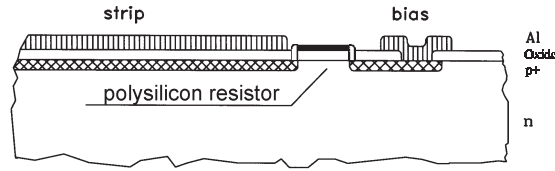


**Figure 4.7:** Sensor Profile. The strips are made of implanted $p^+$ material on n-type bulk. The polysilicon resistors connect each of these strips with the common bias ring. The $p^+$ strip is covered by the metallization layer separated by the dielectric oxide layer, forming the coupling capacitor.
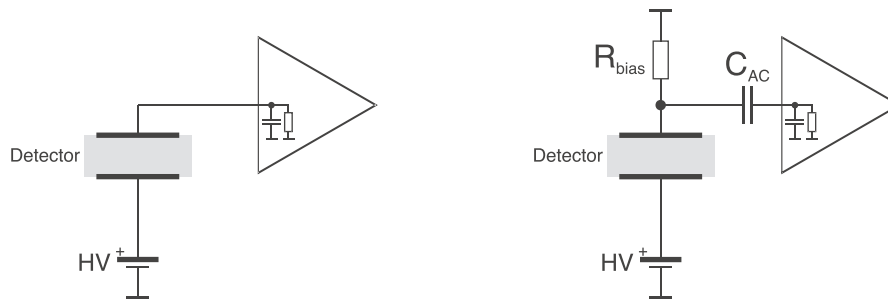


**Figure 4.8:** Biasing schemes of a silicon sensor with DC coupled (left) and AC coupled (right) readout [21]. AC coupling was chosen for the CMS sensors.

The poly-resistor is usually meander-shaped resulting in longer lines and thus increased resistor value (see also figure 4.5). For CMS, $1.5 \pm 0.5 M\Omega$ was specified [32] and values between 1 and 2.3 M$\Omega$ were actually measured on the devices with an average value exactly at 1.5 M$\Omega$ [34]. Only few sensor batches exceed the upper limit of 2.0 M$\Omega$. Those batches were accepted by CMS in agreement with the producer and were installed in regions of the tracker where this excess is not of critical importance.

### 4.1.11 Passivation Layer

The uppermost layer of the sensor is called *passivation* or *overglass*. Its purpose is to protect the sensor surface from (limited) mechanical damage and from chemical reactions with air moisture. In principle, it is another silicon dioxide layer with a thickness of around 1 µm. The passivation layer is etched at areas where an electric contact to the underlying metal layer is necessary, i.e. the connection pads of the strips and dedicated contact regions of the bias and the guard ring.

## 4.1.12 Bond and Probe Pads

Contact areas are foreseen to connect the strips to the readout chips. These areas are called *bond pads*, as the electrical connection is done using aluminum wire-bonding technique. The pads should be large enough that even several bonding wires fit onto. Thus, the CMS specifications request two bonding pads with 400 μm distance on each side of the strip. Each pad needs to have a bondable area of $60 \times 300 \, \mu m^2$ [32].

For testing purposes, it is also mandatory to have direct access to the $p^+$ strip implants by so called *probe pads*. Since these pads will only be used with probing needles, their size is $60 \times 100 \, \mu m^2$ only. They are located only on the bias-resistor side of the strips.

The layout of the strip region showing bonding and probe pads is given in figure 4.9.
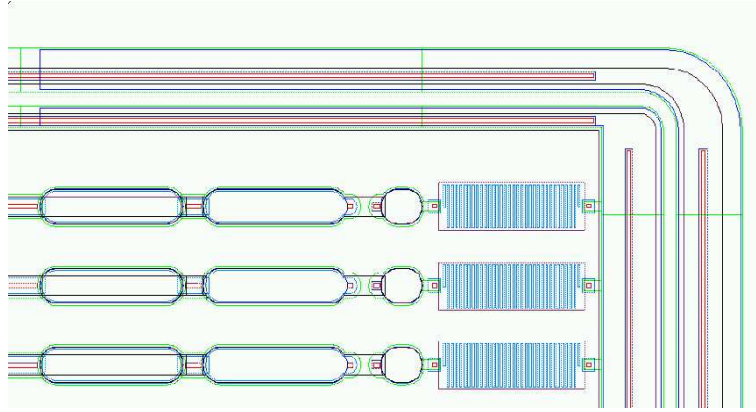


**Figure 4.9:** Layout of the region where the bonding and probing pads are located. Two bonding pads are on the left, the probe pad (center) and the meander-shaped poly silicon resistor (right) can clearly be identified along the strips. More detailed drawings of this region for the different sensor types can be found in [36].

## 4.1.13 Identification

Strips are labeled by consecutive numbers written inside the metal layer of the outermost $n^+$ ring for easy identification. Depending on the sensor geometry and the available space, either every or every second strip (as shown in figure 4.6) is labeled.

In addition, each sensor can be identified by a row of scratch pads, also located in the outermost ring. The scratch pad region consists of six blocks with four pads each. Each block is used to store one numerical character by using Binary Coded Digital (BCD) code. Starting from the left, four blocks are used to indicate the batch number, while the right two blocks are displaying the number of individual sensors within one batch. A picture of a scratch pad area is shown in figure 4.10.
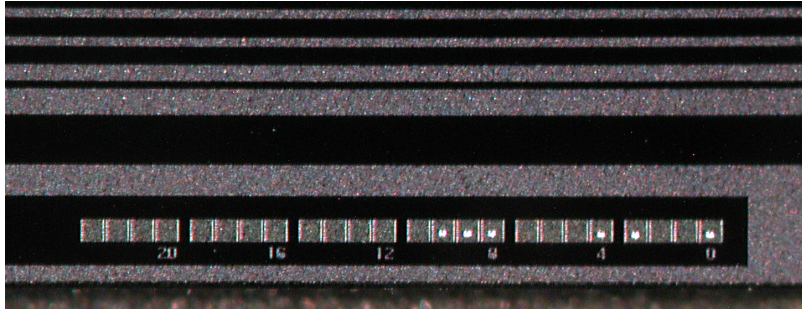
**Figure 4.10:** Scratch pads region in the outer $n^+$ ring of a sensor. In this picture, the code stored in the scratch pad area corresponds to batch 7, sensor 19. Apparently, not all pads of the batch number were scratched.

### 4.1.14 Sensor types and geometries

For the CMS Tracker, 15 geometrically different sensor layouts were designed. Two layouts of the inner barrel (IB) utilizing "thin" sensors, and the two types of "thick" sensors for the outer barrel (OB) are rectangular. The sensors of the seven rings in the forward region (TID and TEC) are wedge-shaped (W1-W7). TID and TEC share two sensor layouts for ring 2 and 3, but need a different design for ring 1. Thus, 11 sensor layouts were necessary for the discs and end-caps.

Furthermore, there are two additional sensor types which are geometrically identical to W4 and W6B sensors, but with special purpose. They are part of the Tracker's internal laser alignment system, which requires that they are transparent to infrared laser light of a wavelength of around 1060 nm [37]. For this purpose, the sensors have a hole of 1 cm diameter in the aluminum backplane metallization and a thinner passivation layer on the front side to reduce the reflection. However, it was shown that these measures were not sufficient and therefore, an additional treatment of the hole on the backside with an anti-reflective coating was enforced [37].

The geometrical dimensions, the strip pitch, the number of strips per sensor and the total number of required sensors for each sensor type are shown in table 4.2.

### 4.1.15 Test Structures

Since the sensors are produced on circular wafers, some cut-off space is available, where additional test structures (TS) are located. These structures allow the measurement of parameters which are not accessible on the main sensor or would require destructive measurements. The knowledge of these parameters helps in monitoring the stability of the manufacturing process and the compliance with specifications. The TS are also perfectly suited for irradiation tests, avoiding radiation damage of the main sensors. They are optimized in a way that one parameter is measured on one dedicated structure. Thus, a set of test structures is necessary to get a complete picture of the overall quality and to determine all interesting parameters.

| type | thickness [µm] | length [mm] | height [mm] | pitch [µm] | average active strip length [mm] | number of strips | quantity |
|---|---|---|---|---|---|---|---|
| IB1 | 320 | 63.3 | 119.0 | 80 | 116.885 | 768 | 1536 |
| IB2 | 320 | 63.3 | 119.0 | 120 | 116.885 | 512 | 1188 |
| OB1 | 500 | 96.4 | 94.4 | 122 | 91.571 | 768 | 3360 |
| OB2 | 500 | 96.4 | 94.4 | 183 | 91.571 | 512 | 7056 |
| W1 (TEC) | 320 | 64.1–87.9 | 87.2 | 81–112 | 85.1 | 768 | 288 |
| W1tid | 320 | 63.6–93.8 | 112.9 | 80.5–119 | 110.858 | 768 | 288 |
| W2 | 320 | 88.1–112.2 | 90.2 | 113–143 | 88.16 | 768 | 864 |
| W3 | 320 | 64.9–83.0 | 112.7 | 123–158 | 110.66 | 512 | 880 |
| W4 | 320 | 59.7–73.2 | 117.2 | 113–139 | 115.16 | 512 | 1008 |
| W5A | 500 | 98.9–112.3 | 84.0 | 126–142 | 81.169 | 768 | 1440 |
| W5B | 500 | 112.5–122.8 | 66.0 | 143–156 | 63.198 | 768 | 1440 |
| W6A | 500 | 86.1–97.4 | 99.0 | 163–185 | 96.136 | 512 | 1008 |
| W6B | 500 | 97.5–107.5 | 87.8 | 185–205 | 84.936 | 512 | 1008 |
| W7A | 500 | 74.0–82.9 | 109.8 | 140–156 | 106.926 | 512 | 1440 |
| W7B | 500 | 82.9–90.8 | 98.8 | 156–172 | 94.876 | 512 | 1440 |
| | | | | | total number of sensors: | | 24244 |

**Table 4.2:** Dimensions of the silicon strip sensors [32, 38].

Nine test structures (called *standard half moon*) were defined by CMS [32] and measured by three *Process Qualification Centers* (PQC). More than 4500 half moons were tested by these centers during the sensor production time [34]. Many problems which would not have been discovered on the main detectors were pointed out by those measurements [38].

The individual test structures on the "standard half moon" shown in figure 4.11 are described in the list below, starting from left to right.
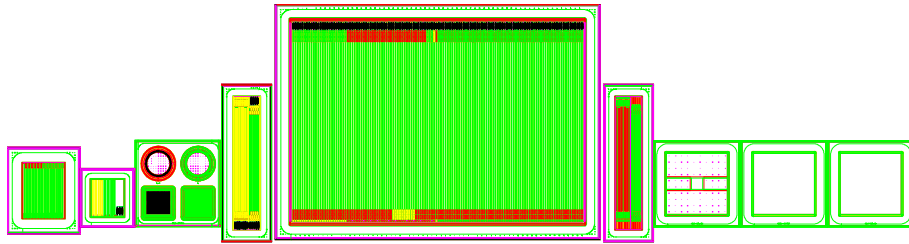


**Figure 4.11:** Standard half moon containing nine test structures, which are called (from left to right): TS-CAP, sheet, GCD, CAP-TS-AC, Baby, CAP-TS-DC, Diode, MOS1 and MOS2.

**TS-CAP:** An array of 26 AC coupled strips, characterized by the same dielectric composition as the main detector but with direct connection to the bias ring without any bias resistor. This structure is used to measure the coupling capacitance.

**Sheet:** A structure consisting of three implant strips, three aluminum strips and three poly-silicon resistors, each of different width. All of these strips have a contact pad on one side and a

common connection to a bias ring on the other. They are used to determine the resistivity of each layer.

**Gate Controlled Diode (GCD):** a set of four GCDs, where only one was used to determine the surface current in the silicon-oxide interface. This structure consists of comb-shaped $p^+$ strips intertwined with comb-shaped MOS strips.

**CAP-TS-AC:** A device of nine strips with the same structure like the sensor, which is used to measure the inter-strip capacitance. For this purpose, the three outermost strips on each side are shorted through their metallization and connected to ground. This improves the accuracy of the measurement done on between the central and the neighboring strips to the left and the right.

**Mini Sensor:** This sensor is a small replica of the main detector, but with 192 strips only. The strip pitch is 120 μm. It is used to measure the bulk breakdown voltage by applying high voltages.

**CAP-TS-DC:** Geometrically identical to the CAP-TS-AC structure, but since the poly-silicon resistors are missing such the the strips are completely isolated. This feature was used to measure the inter-strip resistance between two neighboring strips.

**Diode:** A simple pin diode was used to determine the full depletion voltage of the device by CV measurements.

**MOS1 (inner):** Metal-Oxide-Semiconductor structure with the same dielectric composition as the thick oxide layer that is present in the inter-strip region of the main detector.

**MOS2 (outer):** For HPK, this structure is completely identically to MOS1. For STM, the dielectric layer is the same as underneath the strips with a thicker silicon oxide and a thinner silicon nitride layer.

## 4.2  Quality Assurance Scheme

Due to the large number of sensors a quality assurance procedure was developed by the *CMS Tracker sensor working group* to ensure the full compliance of all delivered sensors with the technical specifications [33, 38, 39]. To qualify all testing procedures and capabilities of the potential vendors, CMS decided to schedule the production in three steps:

1. **Milestone 200 (M200):** Procurement of 400 sensors to build 200 modules (40 TIB, 80 TOB and 80 TEC). The purpose of this step was to evaluate the manufacturing process of the vendors together with a verification of the quality assurance measurements within the CMS collaboration.

2. **Pre-Series:** Five per cent (5%) of full delivery was foreseen to be produced at the full delivery throughput to check if the producers and the CMS test centers can cope with the rate at a high quality level.

3. **Full production within 2.5 years:** During full scale production the sensors were sample-tested according to the experience gathered during M200 and pre-series phases.

The sensors were produced by two commercial vendors, Hamamatsu Photonics Company (HPK) in Hamamatsu-City (Japan) and ST Microelectronics (STM) in Catania (Italy). All sensors had been

delivered to the *Distribution Center* at CERN, where they were distributed to five *Quality Test Centers* (QTC) located in Rochester, Pisa, Perugia, Vienna and Karlsruhe. Each of them was responsible for the qualification of the sensors and performed sample tests on the sensors itself. The measurements done at QTC Vienna are described in detail in the following section.

To gather additional information about the sensors' quality, a small number of approximately 1% of the sensors and 5% of the standard half moon test structures were sent from QTCs to two *Irradiation Qualification Centers* (IQC) at Karlsruhe and Louvain-la-Neuve for radiation hardness inspection. There, the sensors and test structures were irradiated with neutrons (Louvain-la-Neuve) and protons (Karlsruhe) up to a fluence equivalent to the one after 10 years of LHC operation. The IQC did measurements on the sensors and test structures before and after irradiation and compared the results to ensure the stability of different parameters regarding radiation damage [11].

Another 5% of the test structures were sent to Pisa and Strasbourg for wire-bonding tests. There, test bonds were made and pull forces at which the bonds lifted off were recorded. This was necessary to prove the ability to reliably place wire bonds on the sensors in order to connect the strips with the readout electronics. Since this is a destructive measurement, it was performed on test structures only.

Almost all remaining test structures were sent to the *Process Qualification Centers* (PQC) at Strasbourg, Vienna and Florence, where the uniformity of various process parameters was tested [34]. In addition, about 5% of sensors were operated at high bias voltages to investigate their long-term stability by monitoring the total leakage current. The minimum test duration was 72 hours, but several batches were tested up to 1,000 hours (approximately 42 days). A schematic diagram of the logistics procedures is shown in Figure 4.12.

By examining all measurement results, the responsible persons at QTC had to judge about the qualification of a group of sensors called *batch*. It was either accepted and sent to the *module assembly centers* or rejected and thus returned to the producer.


## 4.3  Quality Test Hardware Setup

As mentioned in the previous section, five Quality Control Centers (QTC) performed measurements on the silicon sensors including strip-by-strip scans. While the electric setup at each center was different, the measurement procedures, the results obtained and the output format of the data were identical. This was proven by cross-checking results of the same sensors, which were measured at several centers [40]. In this section, the setup developed in Vienna will be presented, while the results from all centers are shown.

The setup consists of a light tight box where the sensor rests on a vacuum support. It is mounted on a motorized XYZ-table. This table can be moved either "semi-manually" using a joystick or completely automatized by a computer system. A sensor resting on this table is shown in figure 4.13 (right). Two micro positioners, holding one needle each, are used to connect the bias line. These
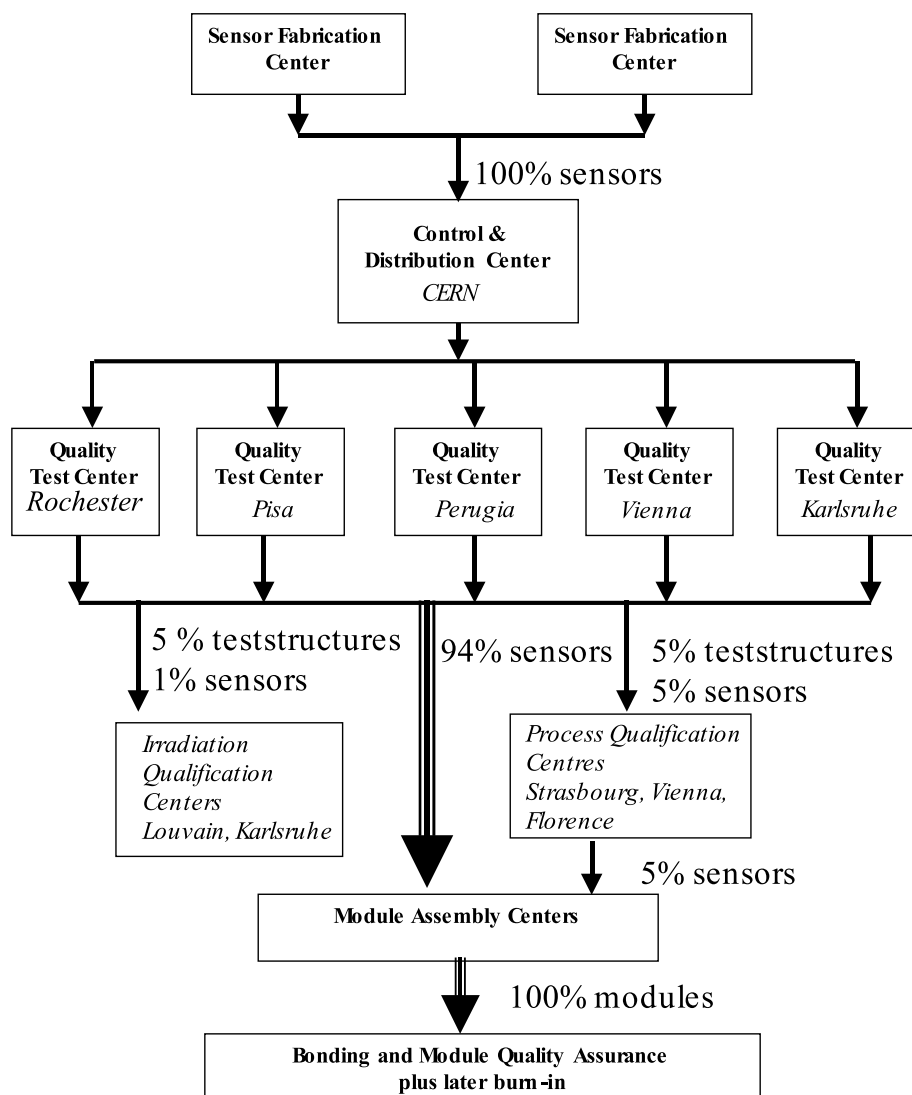
**Figure 4.12:** Diagram showing the quality assurance and logistics scheme of the CMS silicon sensor production.
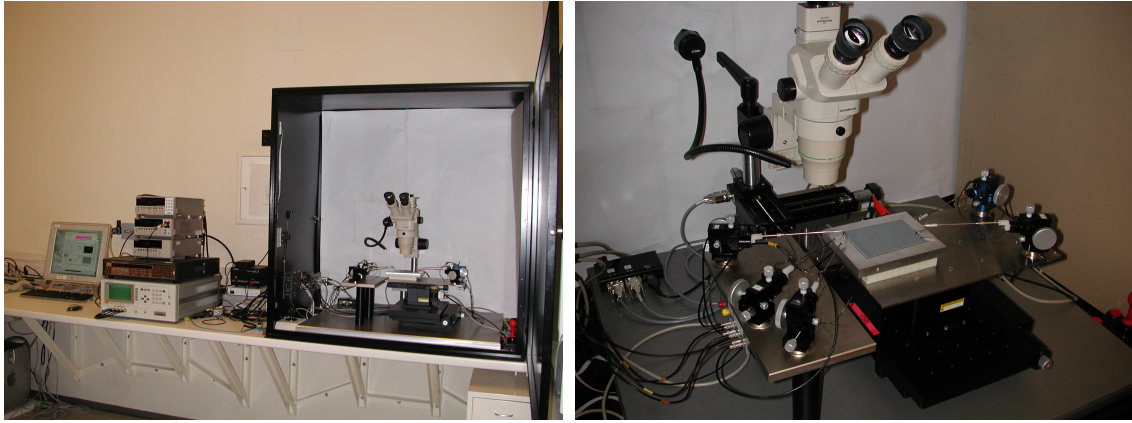
**Figure 4.13:** Pictures of the QTC setup in Vienna. The whole setup is shown on the left with the computer running Labview (left), instruments (middle) and light tight box (right). The content of this box is shown in detail on the right picture. The sensor can be seen in the middle resting on the vacuum support carried by the XYZ-Table. Two bias needles on the right and three needles on the left can be seen.

positioners are located on the XYZ-table together with the sensor, so that they always remain in the same position relative to the sensor. This allows movement of the sensor while the bias connection is maintained. Two bias needles are used in parallel to minimize the possibility of losing contact to the bias ring for a short time during acceleration or deceleration of the table. This can easily happen if only one needle is used and would cause burnt holes on the sensor because of high current transients [41]. In the following schematics this fact is taken for granted and only one bias connection is shown.

On the left side of the sensor, three needle positioners are placed which rest with respect to the light-tight box. Their contact needles are used to connect the bonding pad (*AC pad*) of one strip, while a second needle contacts the probe pad (*DC pad*) of the same strip. The third needle is used to contact the DC pad of the adjacent neighboring strip. For instance, if both AC and DC pads of strip #25 are connected by the needles, the third needle contacts the DC pad of strip #26.

Using the motorized table, the sensor is moved from one position to the next, allowing to perform a scan over all strips [42]. The table stage performs three steps to move from one strip to the adjacent one: it moves the sensor down (losing needle contact), performs an XY movement to the next strip and lifts the table again to re-establish contact with the pads of the next strip.

The electric circuit of the probe station setup is designed for voltages up to 1000 V and current measurement precisions in the range of few pA. Thus, good shielding and insulation of all components is essential. For this purpose, most connections are made using Triax cables and connectors[2]

---

2. Triax cables are similar to coaxial cables, but contain a second shielding – called *guard* – between the core and the outer shielding. The core and the guard are kept at the same potential, thus the leakage current between them is zero for all practical purposes, despite the imperfections of the insulation. Instead, the leakage occurs between the inner and outer shields, which does not matter, because it is the core that is connected to the device under test and the core current is being measured.

Unfortunately, this concept is not consistent applied in this setup because of limitations of the instruments.

The test bench is controlled by a computer using the Labview measurement program (Version 6.0) and communicates with the motor controller for the XYZ-table and the measurement instruments utilizing the IEEE488 (GPIB) interface bus. The instruments used in the setup are listed below and a picture of them while connected to the setup is shown in figure 4.14:

- Primary source measure unit (SMU): Keithley 237

- Secondary source measure unit (SMU2): Keithley 2410

- Electrometer (EL): Keithley 6514

- High frequency (HF) capacitance meter (LCR): Agilent 4284A with self made decoupling box. This box basically contains a high-pass filter to separate DC bias voltages from the inputs of the LCR meter (see detailed description below).

- Quasi-static capacitance meter (QCV): Keithley 595

- Switching matrix frame: Keithley 7001 equipped with two 7153 matrix cards ($5 \times 4$ contacts)
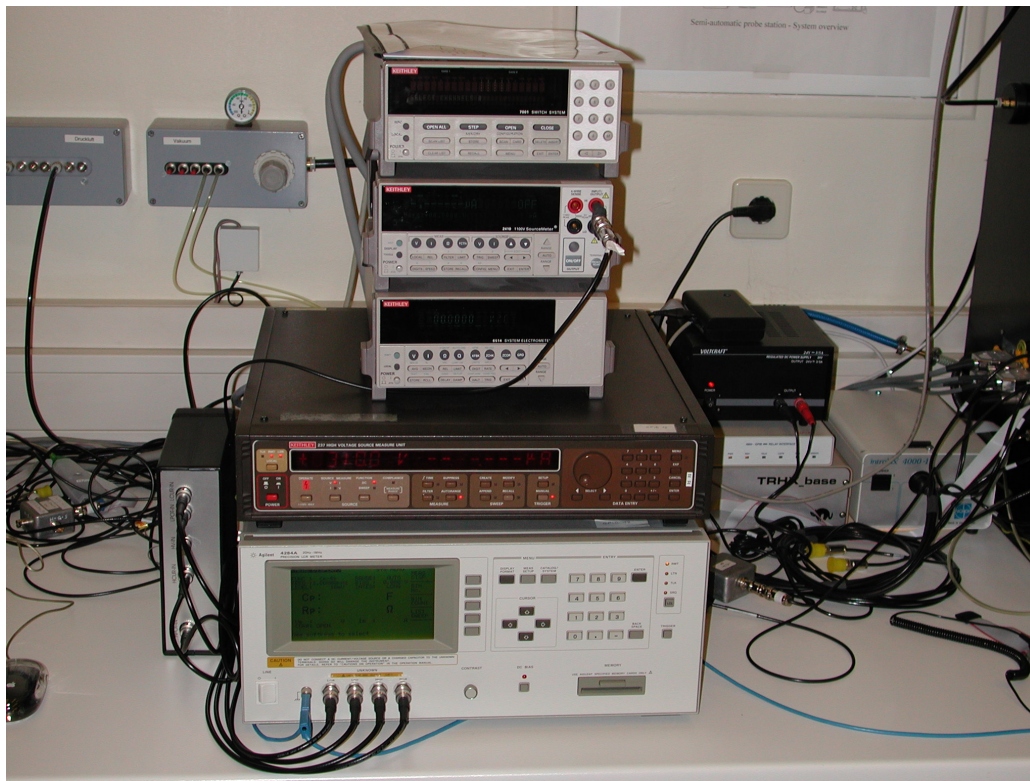


**Figure 4.14:** Instruments used for the QTC setup. From top to bottom: Keithley 7001 switching frame, Keithley 2410 SMU, Keithley 6514 Electrometer, Keithley 237 SMU, Agilent 4284A LCR-Meter. The small silver/black box to the left is the decoupling box. The devices on the right are a power supply for the microscope stages in the box (black), the GPIB I/O box for remote discharge of the decoupling box, a TRHX system and a light source for the microscope in the measurement box.

The heart of the electric setup is the switching matrix system. Its purpose is to connect the instruments to the needles in a flexible way. It needs to be re-configured for each measurement.

Since this has to be done while HV is constantly applied to the sensor to maintain its depletion, each switching operation must be performed on lines with (almost) the same potential only. Otherwise, high equalizing currents can flow which can easily destroy the contacts of the switching relays.

The primary source measure unit (SMU) is used to determine current versus voltage (IV) behavior and – together with the HF LCR meter – also capacitance versus voltage (CV) characteristics of the sensors. It is further used to apply bias voltage across the sensors during the strip scan.

For each strip the dark current is measured by the electrometer, while the coupling capacitance of the dielectric can be determined either by the HF or the quasi-static LCR meter. The SMU2 device is used to measure both the poly-silicon resistance and the current through the dielectric.

In addition to the measuring instruments, several utility devices are used in the setup as well:

- The TRHX system [43] is used for monitoring temperature and humidity in the measurement box.

- A cold-light source with fiber optics to illuminate the area where the sensor is manually contacted by the needles.

- GPIB relay box for controlled discharge of the capacitors of the decoupling box.

- LED box indicating a measurement in progress. When the red LEDs are flashing, the box must not be opened since a measurement is currently in progress. The LEDs are driven by the GPIB relay box.

- A motorized microscope XY stage with power supply, control box and operation joystick to allow the positioning of a microscope above the sensor inside the box.

Besides the manual alignment of the sensor in the beginning, the system performs all measurement tasks automatically, controlled by the Labview software. Just after its start, an IV and CV curve are recorded, before the strip scan is performed. There, four electrical parameters for each strip are measured, which are described in more detail below. The characterization is fully automatic and takes 2.5 hours for a sensor equipped with 512 strips. Once completed, the results are compared against the specified limits and are written to disk using an XML-compatible format (see section 5.3.2). The resulting file is then transferred to a Linux server, on which a Java application called BigBrowser is used (in command-line mode) for insertion of the measurement results into the *Tracker Construction Database* (TrackerDB), which is described in more detail in chapter 5.

## 4.4 Quality Test Measurements

In this section, the switching scheme for each type of measurement performed on the sensors is described, together with histograms showing results from these measurements. The histograms

have been produced by querying the Tracker construction database using a tool called *visualDB* (see [44] and section 5.4.2) and the following database tables:

|  |  |
|---:|:---|
| IV curve: | ivtest_1_sen_ |
| CV curve: | cvtest_1_sen_ |
| single strip current ($I_{\text{strip}}$) : | istrip_1_sen_ |
| poly-silicon resistor ($R_{\text{poly}}$) : | rpoly_1_sen_ |
| coupling capacitance using the LCR meter at 100Hz ($C_{\text{ac}}$): | cac100Hz_1_sen_ |
| coupling capacitance using the quasi-static CV meter ($C_{\text{ac}}$): | cacquasi_1_sen_ |
| dielectric current ($I_{\text{diel}}$): | idiel_1_sen_ |

### 4.4.1 Current versus Voltage (IV) Characteristics

The primary *source measure unit* (SMU) is used to deplete the detector and to measure the total current during an IV curve. While the high terminal of the SMU is directly connected to the sensor backplane, the switching matrix has to be configured to connect the bias ring to the SMU low terminal (Contact @1,1,1) as shown in figure 4.15. The SMU uses a shunt resistor in its high line
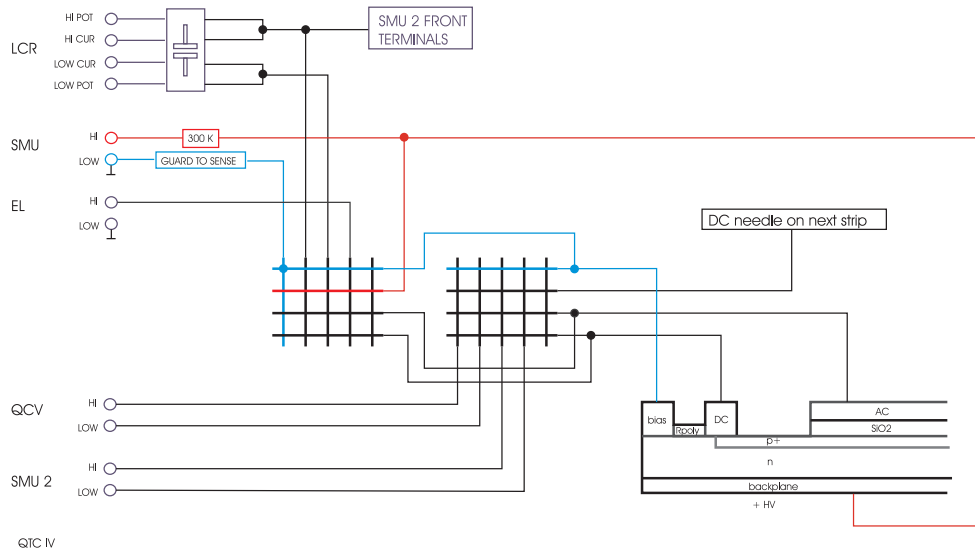


**Figure 4.15:** schematics IV

and a small converter box in the low line. The shunt resistor (300 kΩ) is used to limit the current in case of a short, with the drawback of creating a voltage drop which cannot be neglected for high sensor currents. While the voltage drop is a negligible 0.3 V for 1 μA current, it becomes 30 Vfor 100 μA! The converter box is necessary as the SMU can perform 4-wire measurements. In that mode, the guard wire is used as the current output and the core wire acts as a sense wire only. Since the setup is designed for 2-wire measurements only, the box translates the core wire of the SMU to the guard line of the triax cable.
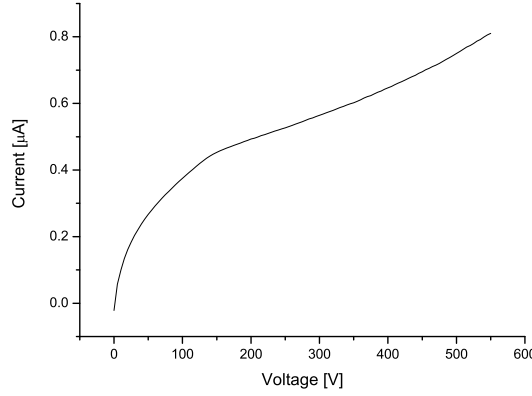
**Figure 4.16:** Current versus voltage (IV) curve on a CMS W2 detector. The voltage is ramped up to 550 V in steps of 5 V. On each step the dark current is measured after a certain delay time.

An example IV curve of a HPK W2 detector can see seen in figure 4.16. For the IV curve measurement, the SMU voltage source is usually increased in steps of 5 V and the current is measured after a delay time of 2 s. The delay before the current measurement is important, since there is a compensation current after each voltage jump, which must be taken into account:

$$I = \frac{dQ}{dt} = C\frac{dU}{dt} \tag{4.5}$$

The shut resistor and the poly-silicon bias resistor together with the detector capacitance $C$ act as a $RC$-network with a time constant $\tau = RC$. It can be considered that $C$ is charged to more than 99 % after $t_l = 5\tau$. For a typical detector capacitance of $C = 2.5\text{nF}$, $t_l$ becomes approximately 4 ms. However, this consideration is only valid if the compensation current is not limited, which is not the case. In our setup, the current compliance function of the SMU is typically set to 20 µA to prevent irreversible damage of the detector by high currents in case of a breakthrough. Thus the settling time is increased significantly. In addition to the current limitation by the SMU, the acquisition software switches the HV off if an breakthrough is detected.

## 4.4.2 Capacitance versus Voltage (CV) Characteristics

The total capacitance of the detector is measured versus the applied bias voltage to determine the depletion voltage and the bulk resistivity. Before the measurement is actually started, the switching matrix is configured in a way that the LCR meter is connected in parallel to the SMU (see figure 4.17). However, the LOW terminal of the SMU must not be connected via the switching matrix but through the external ground connection. Otherwise, it would create a short in the LCR meter and the SMU would become unstable when trying to compensate the AC voltage applied by the LCR meter (see below). The external ground connection shorts the LOW terminal of the SMU and electrometer with the "chassis" pin of the LCR meter by bypassing the switching system.
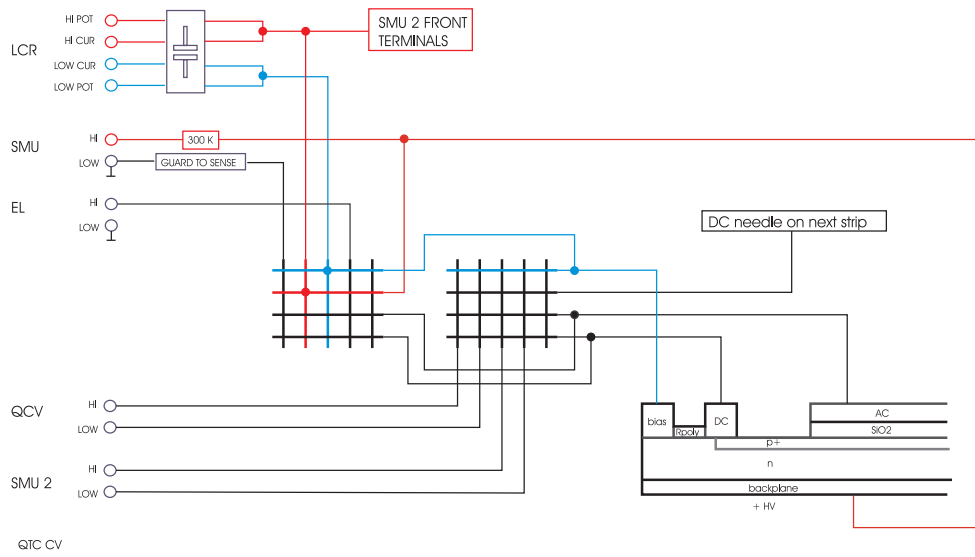
**Figure 4.17:** schematics CV

The LCR meter determines the capacitance by applying a small AC voltage while measuring the phase of the current. The signals across the DUT [3] are [45]

$$V_{\text{DUT}} = \frac{Z_x}{R_{so} + Z_x} \times V_{\text{Osc}} \tag{4.6}$$

$$I_{\text{DUT}} = \frac{V_{\text{Osc}}}{R_{so} + Z_x} \tag{4.7}$$

with the oscillator voltage level $V_{\text{Osc}}$ of the LCR meter, the source resistor $R_{so}$ of the LCR meter (100 Ω), voltage and current levels $V_{\text{DUT}}$ and $I_{\text{DUT}}$ of the DUT and the impedance $Z_x$ of the DUT. Knowing the impedance, the capacitance can be calculated using this equation, where $i$ is the imaginary unit:

$$Z_x = R_p + iX = R_p - i\frac{1}{2\pi f C} \tag{4.8}$$

The LCR oscillator voltage $V_{\text{Osc}}$ used during these measurements is 100 mV at a frequency of 1 kHz. Since we measure small capacitances, the mode selected in the LCR meter is $C_p$-$R_p$ according to the recommendations in the operations manual [45].

The Agilent LCR meter is not built for measuring capacitances using cables longer than 2 meters between instrument and DUT. Thus, we are using the *long* integration time setting of the device to get more accurate results and do not use the built-in correction function to compensate stray capacitances, but simply subtract a pre-recorded measurement of this number from the obtained result[4].

The maximum DC voltage level on the input terminals of the LCR meter is 40 V. To protect these terminals from the (much) higher bias voltage provided by the SMU (up to 1100 V), a decoupling

---

3. DUT: Device Under Test
4. This is only true for the capacitance measurement during the global CV measurement. When measuring coupling capacitances, the instruments internal correction (in both "open" and "short" modes) is being used, though.

box is used which acts as a high-pass filter to the AC voltage of the LCR meter but keeps the bias voltage away from the instrument. As it consists of large capacitors which can store large amounts of energy, we must take precautions when opening or closing contacts of the switching matrix when the capacitors are charged. Since we had damaged some relays of the switching matrix several times during software development, it was necessary to implement a controlled discharge function for those capacitors. This was realized by the GPIB relay box, connected to a discharge circuit comprising a shut resistor.

To speed up IV and CV measurements, we developed a method to gently switch between IV and CV measurement during a single voltage ramp. After such a combined voltage ramp, the discharge circuit is closed and the capacitors are discharged across the shunt resistor. To test whether the discharge was successful, the voltage at the decoupling box is being measured at the front terminals of SMU2 and the software reports an error if the voltage after discharge exceeds 5 V.

The result of combined IV-CV measurements are shown in figure 4.18. By plotting $1/C^2$ instead
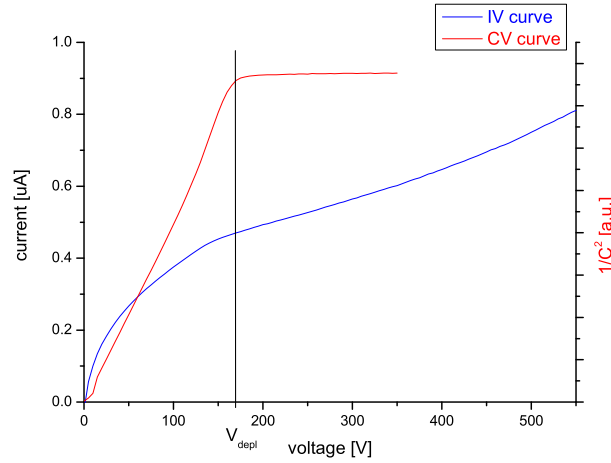


**Figure 4.18:** Example of a combined CV and IV measurement. The capacitance is shown as $1/C^2$ to see the kink better which represents the full depletion voltage $V_{\text{depl}}$.

of the pure capacitance $C$ versus the voltage $V$, one can determine the full depletion voltage of the detector as the voltage, where the linear capacitance increase kinks to a horizontal line. Using this value of the full depletion voltage $V_{\text{depl}}$ and the total capacitance at depletion $C_{\text{tot}}$ it is possible to calculate the "active" detector thickness $d$ by using the equation for a parallel plate capacitor (equation 3.29). The resistivity of the silicon bulk material can be then determined using equation 3.28.

### 4.4.3 Single Strip Measurements

Upon completion of the combined voltage ramp to measure CV and IV, the strip scan is started. For this purpose, the SMU is ramped from the end voltage of the IV-CV-measurement (usually 550 V or 800 V) down to 400 V. At this bias voltage, four measurements are performed on the first strip of the

sensor. When done, the motorized XYZ-table is moving down (-Z) to disconnect the DC- and AC-needles on this strip and moves in XY-direction until the DC and AC pads of the next consecutive strip are underneath the needles. Finally, the table moves up again (+Z) until the previous height is reached to re-establish contact of one DC and two AC needles. Then, the measurements of the second strip are performed. This procedure is repeated for all strips.

An initial alignment has to be performed before the measurement is actually started to know the distance and direction of the XY movement. During this procedure, the geometry of the detector is read from a *pad file*, but the absolute position of the first and of last strip must be manually assigned by the operator.

The electrical measurements performed on every single strip are the single strip current, the poly silicon resistor, the coupling capacitance and the current through the dielectric. The results of a strip scan measuring these quantities are shown in figure 4.19.
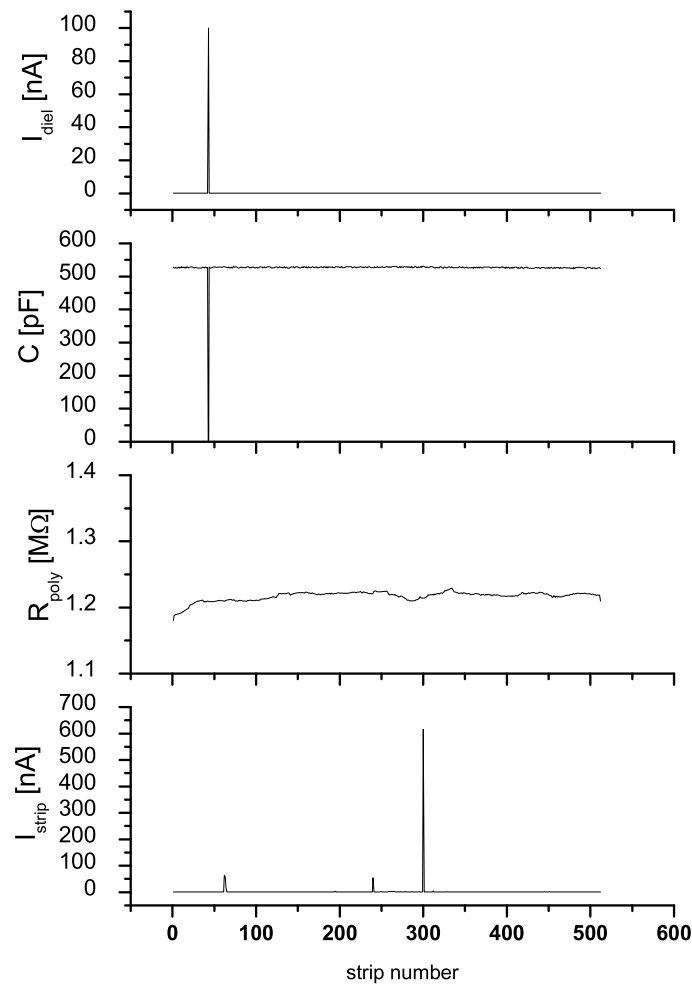


**Figure 4.19:** Example of a strip scan on a sensor with 512 strips. One pinhole at strip 43 (high dielectric current and zero capacitance) and one strip with high leakage current at strip 300 can be identified.

**Single strip current**

The single strip leakage current is measured by configuring the switching matrix in a way such that the strip DC pad is directly connected to the electrometer (see figure 4.20). This device measures
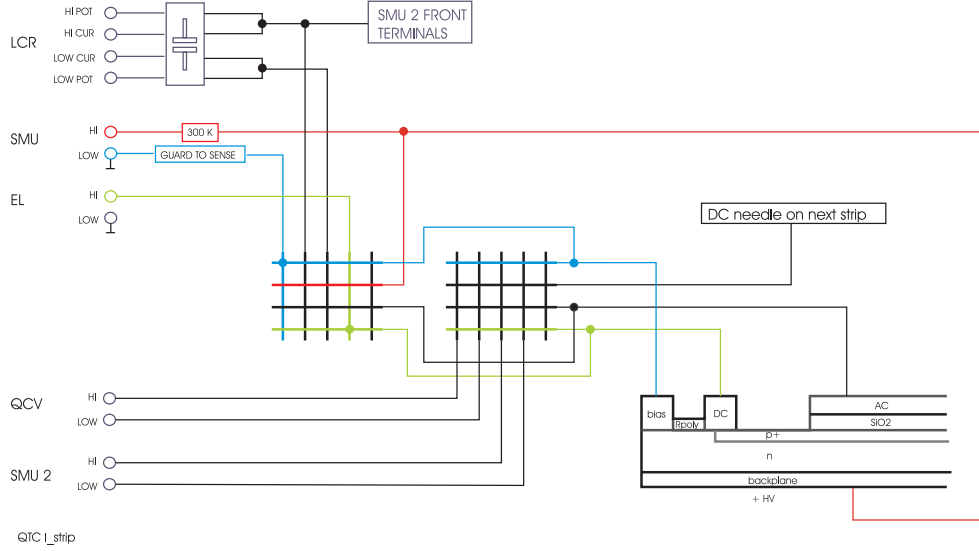


**Figure 4.20:** Schematics of the $I_{\text{strip}}$ measurement.

the current against the external ground, thus by-passing the normal current path through the poly-resistor. Typical current values are around 100 pA for CMS detectors. Scratches or other impurities induced during production can cause a higher current. Such strips are called *noisy* and can cause problems in the APV25 readout chip. The limit defined by the CMS sensor working group for this parameter is $50\,\text{pA} < I_{\text{strip}} < 100\,\text{nA}$.

The results of measurements done on 9,071 silicon sensors from both producers in all five QTC centers are shown in the histograms in figure 4.21. The left histogram contains every single strip measured on these detectors, while the histogram to the right shows the average of the single strip currents of each sensor.

**Poly silicon resistor**

The poly silicon resistors are used to connect each strip to the bias line. The limits are specified as $1\,\text{M}\Omega < R_{\text{poly}} < 2\,\text{M}\Omega$ [32]. The SMU2 device is connected via the switching matrix between DC pad of each strip and the bias line to test if this requirement is fulfilled. The instrument is configured to measure the resistance directly in $\Omega$ mode. The system setup during this test is shown in figure 4.22. The measurement results from 8,956 sensors from both producers performed in all QTC centers are shown in the histograms in figure 4.23. Again, the left histogram contains values of every single strip, while the histogram to the right shows the averaged data per sensor. The average distribution shows a clear peak around 1.5 MΩ. However, the single strip histogram features a
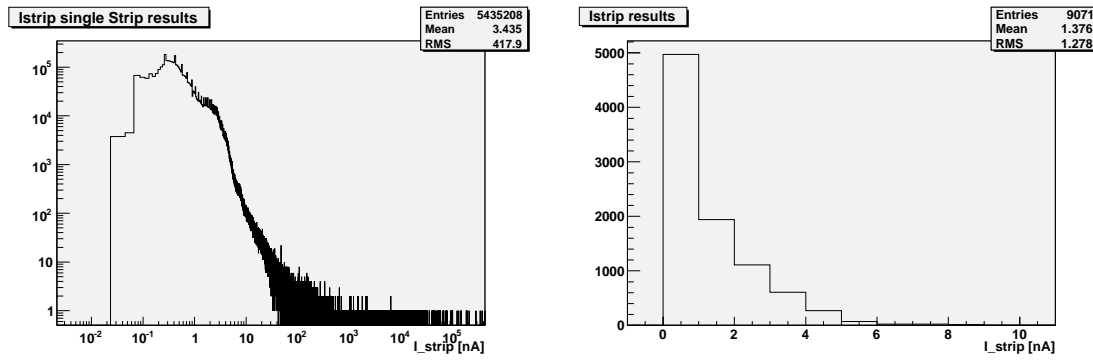
**Figure 4.21:** Results of $I_{strip}$ measurements on 9,071 silicon detectors. In the left histogram, every single strip is shown, while on the right an average value for each sensor was calculated before filling the histogram.
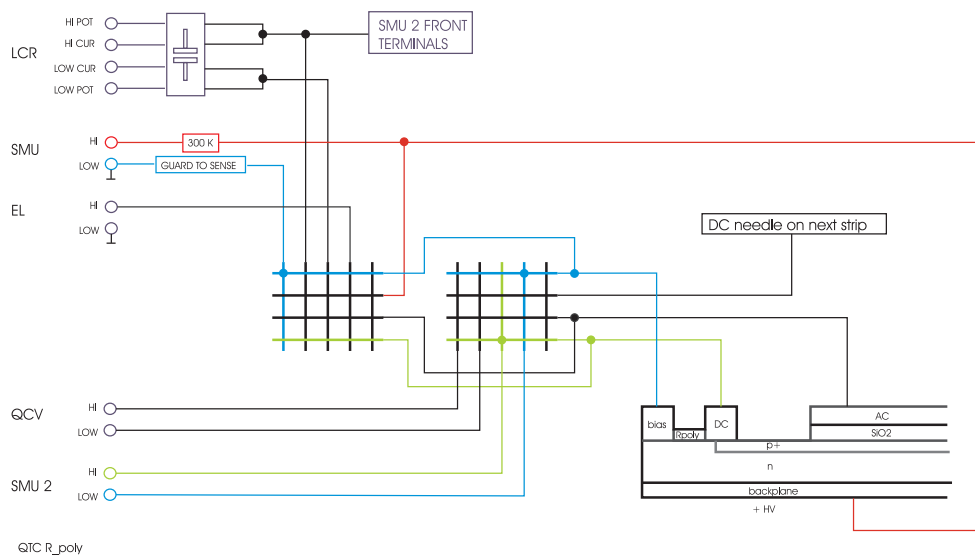


**Figure 4.22:** Schematics of the poly-silicon resistor ($R_{poly}$) measurement.

second peak around 100 MΩ. This peak is very likely related to bad contacts, e.g. "opens", during the measurement.

### Coupling capacitance

The coupling capacitance is defined as the capacitance between $p^+$ implant and aluminum strip across the dielectric layer of oxide and nitride. This parameter is measured by connecting the LCR meter between DC and AC pads of each strip. In addition, the DC needle is shorted with the DC pad of the next strip in consecutive order (called "DC2" pad). This measurement allows to electrically determine single strip failures like *opens* or *shorts*. An *open* decreases the effective area of a strip and thus reduces the measured capacitance. This is most likely caused by the separation of the strip metallisation into two parts, e.g. caused by scratches. Then, the second part further away from the connection pads is not sensitive anymore. Shorts between two or more consecutive strips can be
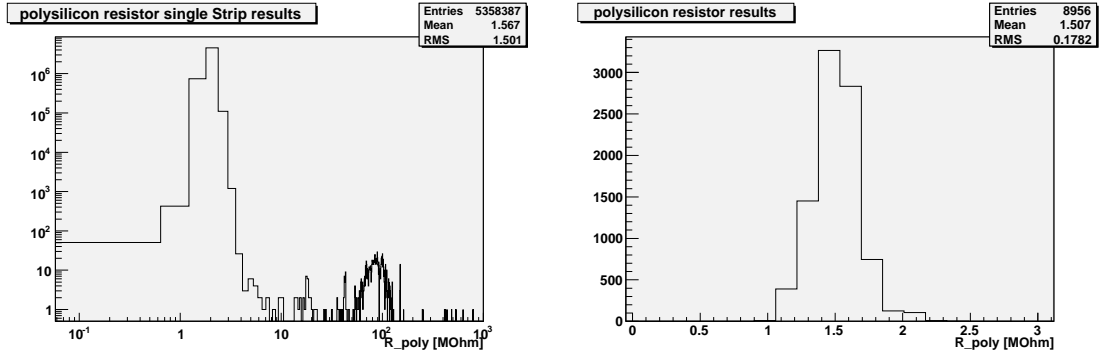
**Figure 4.23:** Measurements results of the polysilicon resistor of 8956 detectors. The left histogram shows the values of every single strip, while the histogram to the right shows the averaged data per sensor.

detected by an increased capacitance. The number of shorted strips can be determined by dividing the measured capacitance by the average single strip capacitance. Microscope photos of such sensor failures are shown in figure 4.24.
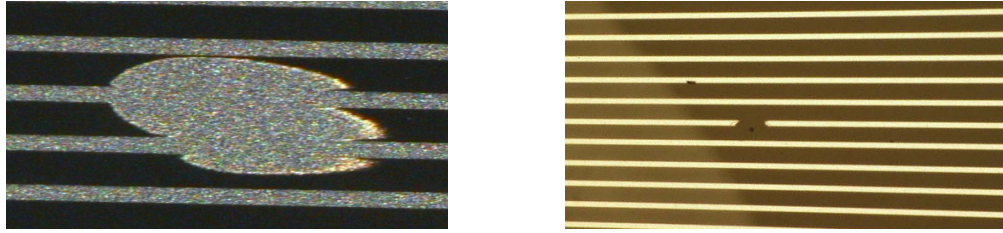


**Figure 4.24:** Examples for single strip failures on sensors. A *short* between two strips is shown on the left and an *open* aluminum line on the right.

Both capacitance sensitive instruments, the Agilent LCR meter (schematics in figure 4.25) and the Keithley quasi-static LCR meter (schematics in 4.26) were tried for this measurement. However, the use of the quasi-static CV meter was abandoned after a certain time and only the high-frequency measurement method utilized by the Agilent device became the standard meter for this purpose.

The limits are defined individually for each sensor type since strip dimensions and pitches vary. The calculated limits for each sensor type are listed in table 4.3. Taking the active strip length and strip width into account (see table 4.2), a normalized value of the capacitance $C_{ac}$ per implanted strip area can be calculated. This was done for 3,760 HPK sensors and the results are shown in table 4.4. The average capacitance of all sensors is 1.3135 pF/cm/μm, which is well above the requested minimum of 1.2 pF/cm/μm [32].
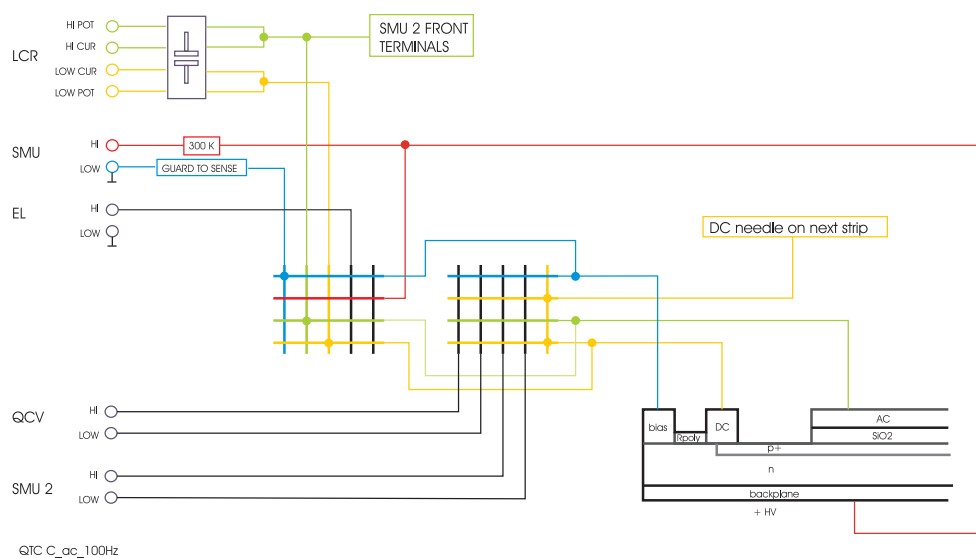
**Figure 4.25:** Schematics of the coupling capacitance measurement using the Agilent LCR meter at 100Hz oscillator frequency ($C_{ac\,100Hz}$).
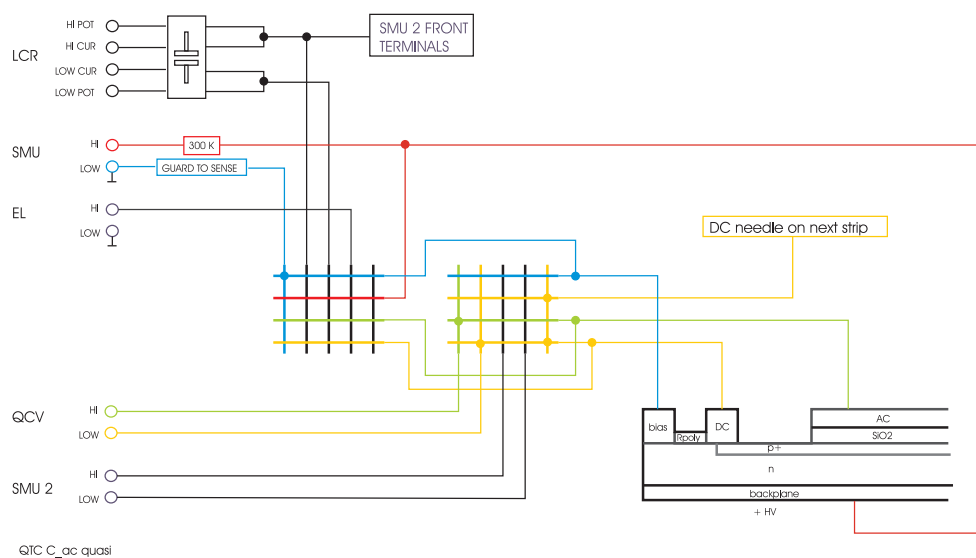


**Figure 4.26:** Schematics of the coupling capacitance measurement using the quasi-static LCR meter Keithley 595 ($C_{ac\,quasi}$).

| Type | $C_{ac\ min}$ | $C_{ac\ max}$ |
|------|------|------|
| IB1 | 229 | 343 |
| IB2 | 343 | 515 |
| OB1 | 277 | 415 |
| OB2 | 415 | 650 |
| W1 | 207 | 311 |
| W2 | 277 | 416 |
| W3 | 382 | 573 |
| W4 | 355 | 533 |
| W5A | 271 | 407 |
| W5B | 237 | 356 |
| W6A | 413 | 620 |
| W6B | 412 | 618 |
| W7A | 390 | 585 |
| W7B | 390 | 585 |
| W1tid | 207 | 311 |

**Table 4.3:** Table showing the limits of the coupling capacitance $C_{ac}$ for all sensor types.

| sensor type | number of tested sensors | average $C_{int}$ [pF] | Standard deviation [pF] | active strip length [cm] | $p^+$ strip width [µm] | normalized pF/cm/µm |
|------|------|------|------|------|------|------|
| IB1 | 446 | 322.972 | 5.702 | 11.6885 | 20 | 1.3816 |
| IB2 | 566 | 465.01 | 6.513 | 11.6885 | 30 | 1.3261 |
| OB1 | 616 | 373.898 | 52.543 | 9.1571 | 30.5 | 1.3387 |
| OB2 | 1084 | 563.781 | 61.102 | 9.1571 | 46 | 1.3384 |
| W1 | 21 | 272.045 | 3.853 | 8.51 | 24 | 1.3320 |
| W1TID | 36 | 367.607 | 4.762 | 11.0858 | 25 | 1.3264 |
| W2 | 103 | 370.397 | 6.094 | 8.816 | 32 | 1.3129 |
| W3 | 29 | 497.035 | 30.993 | 11.066 | 35.125 | 1.2787 |
| W4 | 97 | 473.253 | 8.15 | 11.516 | 31.5 | 1.3046 |
| W4S | 43 | 450.737 | 97.584 | 11.516 | 31.5 | 1.2425 |
| W5A | 111 | 358.373 | 14.431 | 8.1169 | 33.5 | 1.3180 |
| W5B | 106 | 310.79 | 5.075 | 6.3198 | 37.5 | 1.3114 |
| W6A | 123 | 541.698 | 19.429 | 9.6136 | 43.5 | 1.2953 |
| W6B | 127 | 532.115 | 9.234 | 8.4936 | 48.5 | 1.2917 |
| W6BS | 24 | 529.573 | 38.247 | 8.4936 | 48.5 | 1.2856 |
| W7A | 109 | 523.861 | 15.508 | 10.6926 | 37 | 1.3241 |
| W7B | 119 | 513.745 | 16.329 | 9.4876 | 41 | 1.3207 |
|  |  |  |  |  | Average: | 1.3135 |
|  |  |  |  |  | Stddev: | 0.02854 |

**Table 4.4:** Measurement results of the coupling capacitance $C_{ac}$ for all sensor types including the alignment sensors (W4S and W6BS).

**Dielectric current**

A pinhole is the most severe damage of a strip. It is defined as a short of the coupling capacitor and hence an ohmic connection through the dielectric. In general, it should be sufficient to measure the capacitance either using the LCR or the quasi-static CV meter to determine a pinhole by is exceptional capacitance. However, in some cases that test was passed undetected yet the strip was actually dead when it was connected to the readout chip later. This effect is caused by 'hidden' pinholes which only become visible when a certain voltage is applied to the capacitor. The measurement amplitude of 100 mV used by LCR and CV meters is too low to reveal such a pinhole. Thus, a dedicated measurement was introduced applying 10 V across the dielectric using SMU2 while measuring the current. The electric setup is shown in figure 4.27. A normal strip exhibits currents less
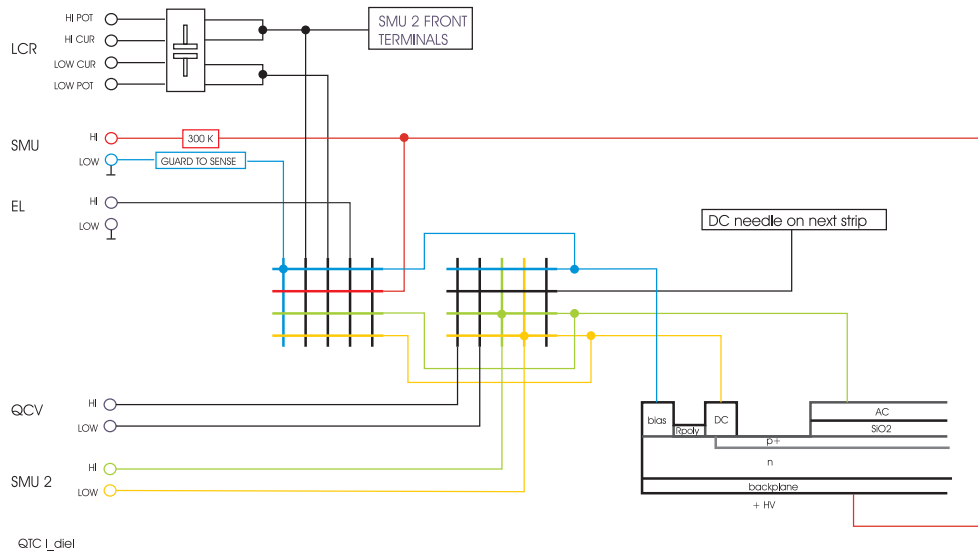


**Figure 4.27:** Schematics of the $I_{\text{diel}}$ measurement.

than 100 pA, while a pinhole drives the SMU2 into compliance, which is set to 100 nA during this measurement (for the Vienna setup). Figure 4.19 presents a pinhole at strip 43, which was identified by both, the LCR meter and the test of the dielectric current.

Figure 4.28 shows statistical results of $I_{\text{diel}}$ measurements. In the histogram showing all strips individually (left), two distinct peaks around 100 nA and 1 mAare clearly visible together with a distribution around 30 µA. These three regions represent the compliance values of the SMU2 instruments at three different QTC station while measuring a strip with pinhole.

## 4.5 Long-term stability tests

The technical specification of the sensors [32] and the specification for the CMS sensor quality control [33] require leakage current stability test performed on a sample basis. The sensors must work stably for at least 24 hours, both at room temperature ($21 \pm 1^{\circ}$C) and at operating temperature
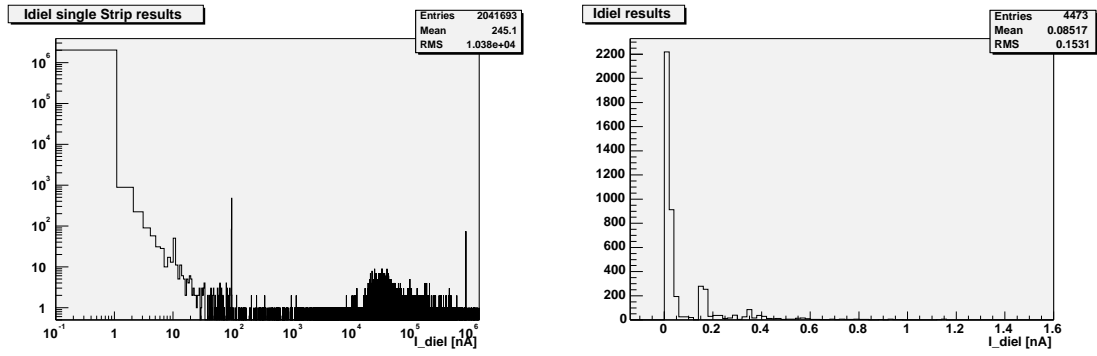
**Figure 4.28:** Results of $I_{diel}$ measurements. The left histogram includes values of every single strip, and the right histogram shows the averaged data per sensor.

$(-10 \pm 1°C)$, with a relative humidity below 30 %, and a bias voltage in the range from 450 V to 550 V in order to pass the test. During this time, the total leakage current must not increase by more than 30 % of the initial value.

The setup developed for this task in Vienna consists of a light-tight box containing ten sliding plates with conducting surface [46]. The sensors are placed onto these slides where a conducting mat ("rubber") provides backplane contact. The bias ring of each sensor is connected to a pad via wire bonding. HV is provided between that pad and the conducting mat by a Keithley 2410 source measure unit. The current of each sensor is measured as the voltage drop across individual shunt resistors using a scanning Voltmeter (Keithley 2700 with 40-channel multiplexer card model 7702). An electric schematic of the setup is shown in figure 4.29. All tested HPK sensors passed this test, while some of the STM sensors failed. The evolution of the dark current of a failing STM sensor is visualized in figure 4.30. More about these tests as well as results from tests at operation temperature $(-10°C)$ can be found in [34].
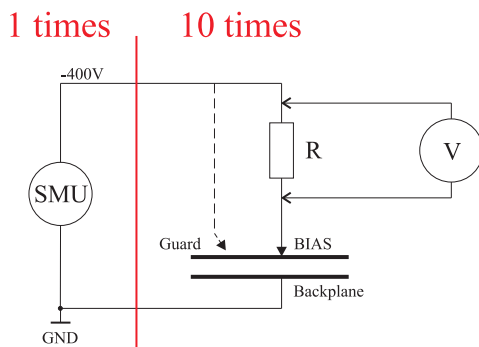


**Figure 4.29:** Schematics of the longterm measurement setup. One SMU is connected to ten sensors with individual shunt resistors. The guard connection is optional and not used in the current configuration.
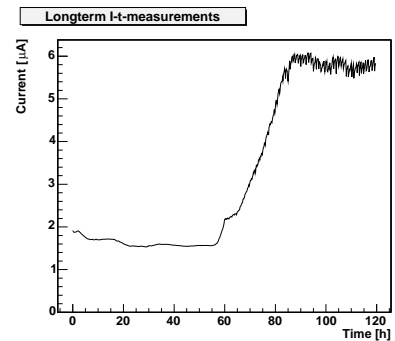


**Figure 4.30:** Behavior of an unstable sensor. The current typically stabilizes at a certain high level where fluctuations due to humidity cycles occur.

## 4.6 Corrosion

Despite of the dark current instabilities, some STM sensors developed dark shades at the aluminum edges after the longterm tests. Standard QTC procedures [33] include optical inspection before any electrical tests, where such shades were not observed. Thus, these dark stains must have evolved afterwards. This effect triggered an intensive investigation about the cause of the problem. Long-term measurements were extended up to three months to see the time response of this effect, while parameters like bias voltage, humidity or temperature were varied systematically to study their effects.

After analysis of the data we concluded that both HV bias voltage and humidity are necessary to develop stains and dots on the sensors metallization (see figure 4.31). Testing at $-10°C$ still showed a stain development but on a reduced rate.
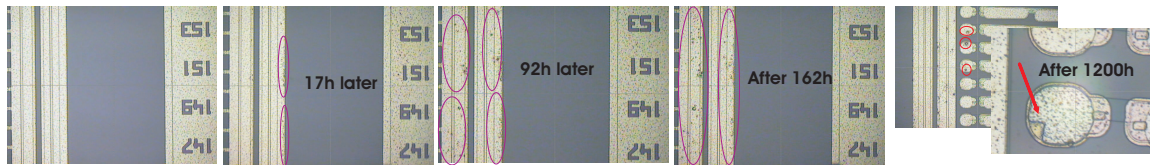


**Figure 4.31:** Stain development under bias voltage in a humid environment. The first picture on the left shows a detail of the original sensor without any stains, followed by snapshots taken after 17, 92 and 162 hours, respectively. The rightmost picture reveals corroded pads after 1200 hours (50 days) in the same environment.

Samples of those sensors where studied using an *environmental scanning electron microscope* (ESEM). It was shown that pure aluminum of the bias ring was reduced to 72 % by weight in the affected region, while the rest contained 24.3 % oxygen, 1.7 % silicon, 0.2 % phosphorus, 0.45 % sulphur and 0.8 % potassium. One part of the oxygen molecules started to form $SiO_2$, while the other lead to 20% alumina ($Al_2O_3$). It is assumed that potassium acts as catalyst for this reaction together with oxygen from the air or air moisture, respectively [47].

# 5 Tracker Construction Database

> Make everything as simple as
> possible, but not simpler.

*(Albert Einstein)*

A relational database was introduced to efficiently store the large number of measurement results obtained during characterization of the CMS silicon detectors for future reference (see chapter 4) and to trace their way through different laboratories. Eventually, this database handled all data relevant for the assembly, construction and commissioning of the CMS Tracker and all its components.

This *CMS Tracker Construction Database* (TrackerDB) is a relational database management system (RDBMS) based on the commercial product *Oracle*[1]. It is operated by the central computing center of IN2P3[2] in Lyon (France) and provides various interfaces for data input and output using the *Structured Query Language* (SQL). These interfaces are described in the following sections.

Using this database was (and still is) mandatory for almost all production steps of the CMS Tracker, starting with "atomic" objects such as sensors or hybrids up to complex cabling information. By the help of this system, it is possible to trace the history of each component through various assembly and testing steps, starting with the initial producer, while monitoring the conformance to the specifications. The TrackerDB will be available during the whole lifetime of the experiment.

## 5.1 Design Considerations

A database is called *relational* when it is based on tables and the tables are itself linked to each other (relations) [48]. Each table consists of columns. *Constraints* are a way of providing restrictions on the kind of data that can be stored in the cells. A *key* is special constraint which requires that the object, or critical information about the object, isn't duplicated. One of the columns of each table is defined as *primary key* for the table. It uniquely identifies each row in a table. No other cell in this table can have the same value in the primary key column. Depending on its design, a table may have many *unique keys* but only one primary key.

---

1. Oracle Database 10g Enterprise Edition Release 10.2.0.3.0 - 64bit Production With the Partitioning, Real Application Clusters, Oracle Label Security, OLAP and Data Mining Scoring Engine options.
2. Institut National de Physique Nucléaire et de Physique des Particules, Centre de calcul (CC-IN2P3), 69622 Villeurbanne Cedex, Lyon, France, `http://cc.in2p3.fr/`

A *foreign key* is a relationship or link between two tables which ensures that data is consistent. The foreign key is set up by matching columns in one table (the *child*) to the primary key in another table (the *parent*). The concept of foreign keys (and other related problems) is visualized in figure 5.1.

| ARTIST | |
|---|---|
| **artist_id** | artist_name |
| 1 | Queen |
| 2 | The Police |
| 3 | U2 |

| ALBUM | | |
|---|---|---|
| *artist_id* | **album_id** | album_name |
| 3 | 1 | War |
| 4 | 2 | Eat the rich |
| 3 | 3 | Rattle & Hum |

**Figure 5.1:** Principle of foreign keys: In this example, there is a foreign key (artist_id; shown in red) in the album table that references a non-existent artist – in other words there is a foreign key value with no corresponding primary key (bold) value in the referenced table. What happened here was that an artist with artist_id of "4" was deleted from the artist table. However, the album "Eat the Rich" referred to this artist. The Relational Database Management System (RDBMS) enforces referential integrity, either by deleting the foreign key rows as well to maintain integrity, or by returning an error and refusing deletion.

Each object stored in the TrackerDB is given a unique number, called *object_id*. This number is used to identify objects in different tables and to allow traceability of these objects and consistent data submission into the action tables. The object_id is a 14 digit number and its scheme is agreed among all four LHC experiments and the accelerator groups. Figure A.1 in the appendix shows how the object_id is constructed using a silicon sensor as example. The first digit always denotes the experiment (or accelerator), while the meaning of further digits varies hierarchically depending on the content of the previous digits.

## 5.2 Main Tables

The TrackerDB incorporates more than 400 tables in total. Despite from *action tables* containing data (e.g. measurement results), there are some tables which are necessary to make the database scheme work properly. These important tables are described in detail below. Figure 5.2 shows the relationship between the main tables of the TrackerDB. Since each of them appears in almost any query, their knowledge is mandatory for understanding the database scheme.

The central table is called *history* and represents a "logbook" of all activities. When two or more objects are combined to a composed object, e.g. 2 sensors plus hybrid are forming a module, the table *object_assembly* table is used. Information about the devices, (e.g. how many sensors fitting on which module type, can be extracted from the table *object_assembly_description*. Although it sounds similar, the table *object_desciption* has a different task. It stores verbose, descriptive information about each object, e.g. the correspondance of an type number to a certain module geometry. Finally, the table *transfers* stores shipment data.
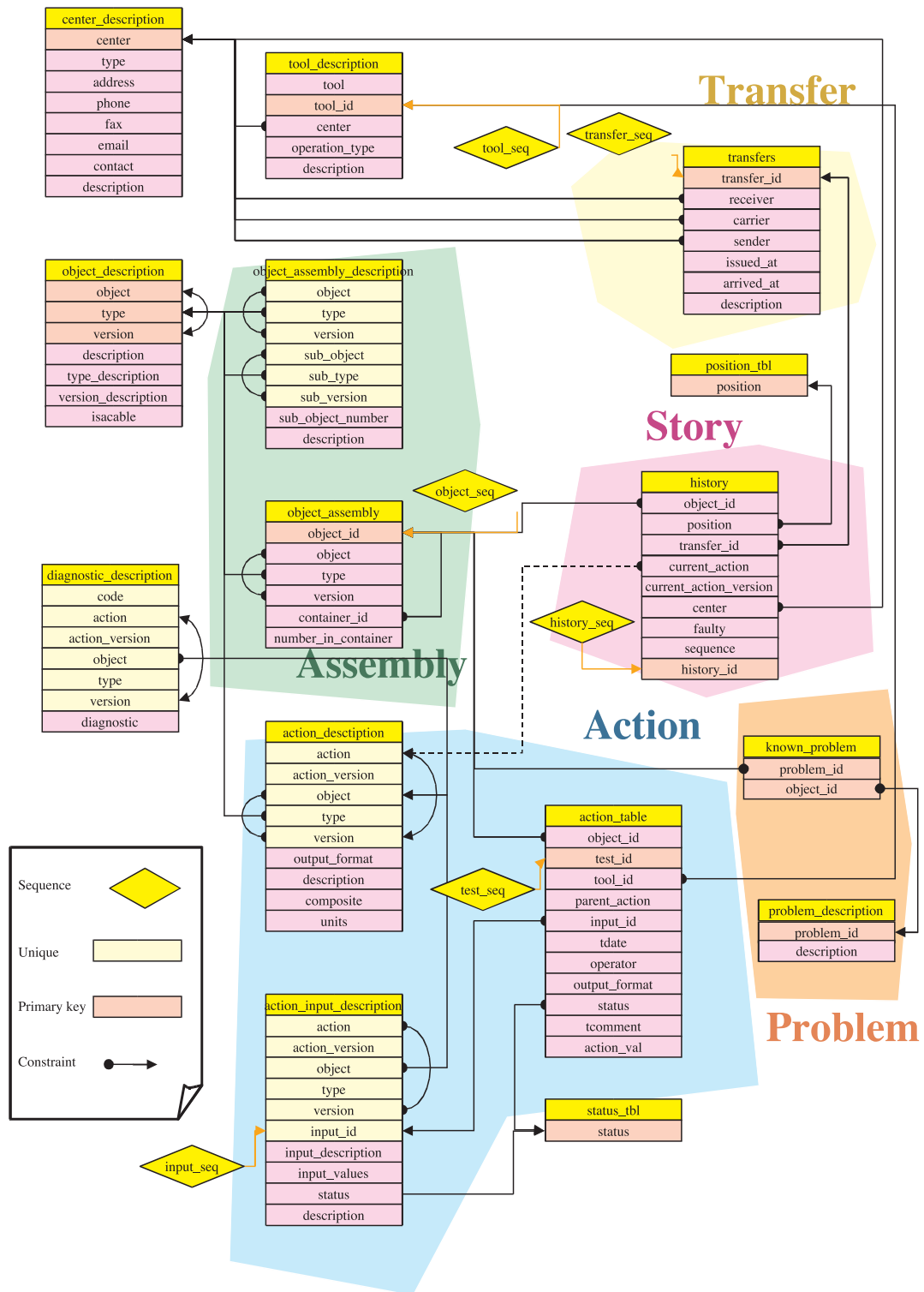
**Figure 5.2:** Main tables and their relationships (constraints or foreign keys) of the TrackerDB. The tables are grouped according to its purpose for assembly, history, transfer, problem and action. The table name *action_table* is a placeholder for more than 300 different action tables containing various kinds of data (measurements, results, comments, . . . ).

### 5.2.1 Table "history"

For every event or action happening to an object (described by its object_id), one line is added to the history table, containing the date and time of the entry and what actually happened, e.g. a transfer, an assembly action or data submission into action tables. The list of columns in the table and their meaning is given in table A.2 in the appendix. The very first mandatory action for every object_id is its registration.

The full history of an object can be simply retrieved by querying the table by its object_id:

```
select * from history where object_id=30200020026989
```

This will show the history for a particular object, e.g. a module represented by the object_id 30200020026989. Table A.1 in the appendix shows the result of this query.

### 5.2.2 Table "object_assembly"

The table *object_assembly* contains information about the assembly status of the objects. A description of each column is shown in table A.3. Each object_id can have a parent object (represented by the container_id), on which it is assembled onto/into. For instance, a module (parent) houses one or two sensors and the FE hybrid ('childs'). A query like

```
select object_id, number_in_container from object_assembly
where container_id=30200020016210;
```

results in three lines showing the components of the module with the given object_id. Since an object can have more than one child of the same type, the table incorporates an column *number_in_container* giving an unique number to each child. The two sensors of a module are represented by number_in_container=1 and 2. There is an additional table called *object_assembly_description* which stores information about the number, type(s) and version(s) of child objects which a parent item is allowed to consist of.

### 5.2.3 Table "object_description"

The table *object_description* lists verbose information for every object (see column "description" in the table A.4). By linking the tables object_assembly and object_description with the columns OBJECT, TYPE and VERSION, a unique mapping between an object_id listed in the object_assembly table and its verbose description is given. A SQL query like this:

```
select oa.object_id, od.type, od.type_description, od.version,
 od.version_description from object_assembly oa,
object_description od where oa.object=od.object and
oa.version=od.version and oa.type=od.type and
oa.object_id=30200020016210
```

results in *EC_R7P.4U* for the type_description. This translates to a module for TEC ring 7 with 4 APV chips.

In another example, the query

```
select distinct type,type_description from object_description
where object='SEN' and version=1;
```

would list the type_descriptions of all sensor types.

### 5.2.4 Table "object_assembly_description"

The table *object_assembly_description* stores information about type and number of child objects for parent object_id's. This means that the data in this table describes the hierarchy of the Tracker. Each object, whether single modules or large sub-systems like TEC are described by this table. To better visualize its purpose, a SQL statement like this is used to produce the output given in table 5.1:

```
select * from object_assembly_description where object='MOD'
and type='2.13.26.23'
```

| OBJECT | TYPE | SUB_OBJECT | SUB_OBJECT TYPE | SUB_OBJECT NUMBER |
|--------|------|------------|-----------------|-------------------|
| MOD | 2.13.26.23 | HYB | 2.1.1.700 | 1 |
| MOD | 2.13.26.23 | SEN | 13.2 | 1 |
| MOD | 2.13.26.23 | SEN | 14.2 | 1 |

**Table 5.1:** Result of a query for a particular module type on the object_assembly_description table. This example shows the module type EC_R7P.4U (type 2.13.26.23) and its child objects, a hybrid (type 2.1.1.700) and two sensors (type 13.2 and 14.2). The field SUB_OBJECT_NUMBER says that only one child of each type is allowed.

### 5.2.5 Table "transfers"

The last entry of any object in the history table tells about its current location (field *center*). This property can be used to generate inventory lists for centers. To move an object from one center to another, the 'transfer' functionality has been established. The table *transfers* contains information about shipments which can be treated as "meta information" of the history table updates. See table A.5 for a description of its fields.

To query the 'meta' information like issuing and receiving centers about a particular shipment, a query like this could be used:

```
select sender, receiver, carrier from transfers where
transfer_id=30299990010696;
```

However, to get the list of transferred object_ids, the *history* table must be queried using the same transfer_id:

```
select object_id from history where current_action='shipping'
and transfer_id=30299990010696;
```

A transfer is updating the history table twice, once when issued (the object now belongs to the "virtual" center given in the CARRIER field of the transfers table, e.g. "COURIER") and once when the reception is acknowledged. After the acknowledge, the last entry in the history table belongs to the new (receiver) center and the transfer is complete.

### 5.2.6  Action Tables

Tables storing data (mostly measurement results, but also quality flags or comments) are called *action tables*. These tables are mostly nested in two hierarchies. A *composite table* links to other *elementary tables*. For sensors, e.g. there is a composite table called *VALIDATION_1_SEN_* consisting of several elementary tables, each storing results of a dedicated test:

- IVTEST_1_SEN_
- CVTEST_1_SEN_
- ISTRIP_1_SEN_
- CAC100HZ_1_SEN_
- RPOLY_1_SEN_
- IDIEL_1_SEN_

The table name consists of the action name itself (e.g. ivtest), the action version (1) and the object this action applies to (SEN). The contents of an action table are listed in table A.6. The table *action_description* defines the relationship between composite and elementary action tables.

Normally, each measurement result is inserted with the flag *reference* in the column *STATUS*. If there are already data to the same object_id and measurement type (the same action table), the new data is inserted with the status *reference*, while the status of the old data is automatically switched from *reference* to *valid*. This means that there is only one data row to a particular object_id which has a status *reference* and that this line is the one representing the most recent data inserted to this object_id. To get only the latest measurement results from action tables, an SQL query must always include the restriction on the column *STATUS*. This example shows the correct use of this mechanism to get the most recent full depletion voltage for a sensor:

```
select v_depl_v from cvtest_1_sen_ where
object_id=30211333710919 and status='reference'
```

Omitting the status restriction would give (for this example) three different measurements of the full depletion voltage, one done by the vendor and two done in Vienna.

There is another table related to actions which is called *action_input_description*. This table is intended for storing parameters for the measurements ("input data") the action refers to. This means that, e.g. for sensors, the stop voltage and the step size of the voltage ramp for the IVTEST is

described there together with limits which can be used as cuts. However, this concept was not commonly followed by all subdetector groups.

## 5.3 Data Submission

Submitting data into the TrackerDB means adding content to tables. For security reasons, any submission of data is only and exclusively possible via a dedicated application, called *Big Browser*. It is a standalone Java application developed by different people and the only way for a user[3] to perform SQL INSERT or UPDATE statements on the TrackerDB. However, certain operations can be automized using XML files. Data is never deleted by the application, thus the concept of *reference* and *valid* status was introduced for action tables. While the Big Browser applications is executed locally, a TCP/IP connection to the Oracle servers in Lyon is established to perform the requested database operations online. A screenshot of this application is shown in figure 5.3.
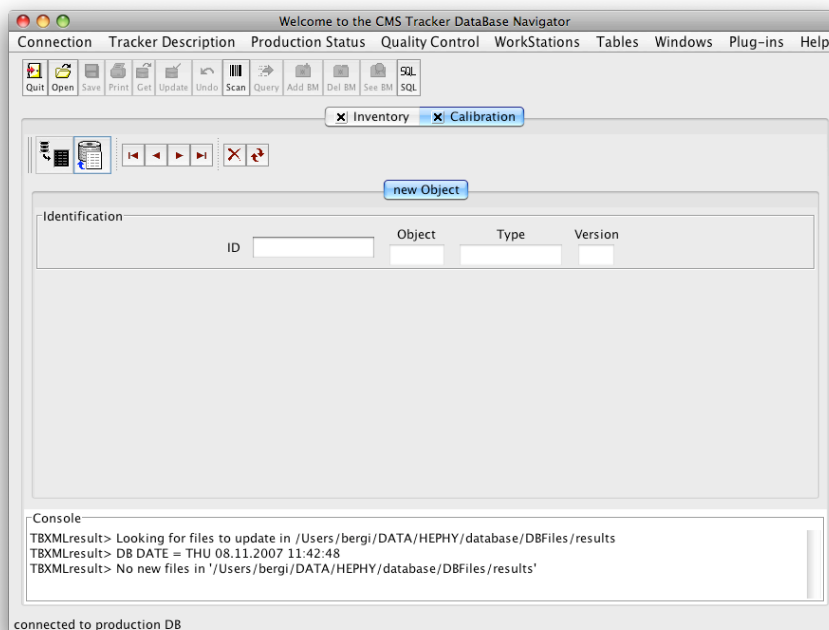


**Figure 5.3:** User interface of the Big Browser Java application showing the "calibration" panel, which is used to insert mesurement data into the TrackerDB.

---

3. This means not a database administrator

### 5.3.1  Big Browser

The main duties of the Big Browser are handling registrations, transfers, assemblies of objects and data submission into action tables. Despite the restriction for data submission to this single application, there are still two ways to use this program: interactively and in batch mode. Using interactive mode means using the mouse to initiate some activity, while in batch mode a special XML file is uploaded (which must have been prepared before) by a command line tool without Graphical User Interface (GUI). Except for submitting data into action tables (this is only possible via XML files), all other tasks can be performed in either way.

The tasks mostly done interactively are object registration, assembly or transfer (issuing and acknowledging the reception). For this, the corresponding panel must be opened from the pull-down menu item called *workstation*.

- For *Registration*, the object must be selected from the pull-down menu, followed by type and version. The center should be already pre-selected from the value chosen in the preferences. After that, the object_id should be entered, preferably automatically by reading the number with a barcode reader. This can be repeated several times, until the *UPDATE* button in the toolbar is pressed and the database is updated immediately.

- The *Assembly* panel allows the assignment of child objects to a parent object. For this purpose, the barcode of the parent object must be entered after the button "Add card" has been pressed. Now, after pressing the "Add/Remove Component" button, a new input field appears and new child object_ids can be added together with the "position" number. After committing the change with the *UPDATE* button the changes are updated immediately to the DB. Deleting a child object works similar but instead of entering an new object_id, an object_id of an existing child can be given and the "remove" checkbox can be marked.

- A dedicated panel also exists for issuing and receiving *Transfers*. Here, it is possible to issue a new transfer by clicking on the "Add card for transfer" button, followed by an unique, but not already consumed, transfer_id number. The object_id's foreseen for the shipment can be entered in the input box and by pressing the *UPDATE* button the transfer is entered into the database tables. In contrast, for acknowledging the reception of a transfer one has to press the *GET* button and enter the (existing) transfer_id. The main window will show the list of object_ids which can be compared to the real contents of the shipment, before the *UPDATE* button closes the transfer and updates the database accordingly.

### 5.3.2  XML Files

For data submission into action tables, XML files containing e.g. measurement results are parsed by the Big Browser and converted into the corresponding SQL statements. A typical XML file for data submission is shown below. In this example, the composite table is called *validation*. It can consist of more than one elementary table, but here only *IVtest* is listed. Together with the version and the object_name, the TrackerDB table belonging to this statement will be IVTEST_1_sen_. The name/value pairs given in the tag <results> are directly converted to SQL statements, with the *name* as column name and the *value* as data for that column.

```xml
<?xml version="1.0" encoding="UTF-8"?>
<DBFile xmlns:xsi="http://www.w3.org/2001/XMLSchema-instance"
xsi:noNamespaceSchemaLocation="TrackerDB.xsd">
<unit>
<object id="30222051800602"/>
<composite>
<action_description input_id="32" name="VALIDATION" object_name="SEN"
version="1"/>
<action>
<action_description input_id="26" name="IVTEST" object_name="SEN" version="1"/>
<result name="Test_center" value="Vienna"/>
<result name="Parent_action" value="Validation"/>
<result name="input_file" value="Sensor_v_1.5"/>
<result name="Tdate" value="2006-02-15_07:21:00"/>
<result name="Duration_minutes" value="5.00"/>
<result name="tool_id" value="1"/>
<result name="Temp_start" value="0.00"/>
<result name="Humidity_start" value="0.00"/>
<result name="Temp_end" value="0.00"/>
<result name="Humidity_end" value="0.00"/>
<result name="I_tot_V1_nA" value="191.77"/>
<result name="I_tot_V2_nA" value="204.27"/>
<result name="V_break_V" value="552.00"/>
<result name="IVtest_val" value=":0:"/>
<result name="Status" value="reference"/>
<result name="Operator" value="Thomas_Bergauer"/>
<result name="Voltage_V" value="0_50_100_150_200_250_300_350_400_450_500_540"/>
<result name="I_tot_nA" value="15.22_130.18_156.68_171.6_180.7_186.78_191.77_
196.51_200.35_204.27_207.62_210.5"/>
</action>
</composite>
</unit>
</DBFile>
```

On the computer running the Big Browser application, a directory usually called *DBfiles* must exist, which has to be configured in the preferences settings of Big Browser. XML files are stored in another directory called *results* below *DBfiles*. In parallel, there must be other directories as well: *registration*, *assembly*, *transfer*, *parameters*, *error* and *indb*. The last two directories are treated specially since each XML file is either moved from its source directory to *error* or to *indb*, depending on the success of the database insertion.

For batch processing, there is also a possibility to invoke the application without Graphical User Interface (GUI). This mode is especially handy for automatic data submission and was used for submission of the sensor characterization results.

## 5.4 Data Retrieval

There are several ways for retrieving data. One possibility is the Big Browser itself, which is only efficient for simple queries. For more complicated and challenging tasks like plotting different results in statistical ways, more convenient tools will be presented below.

### 5.4.1  Big Browser

Big Browser can be also used for data retrieval. It provides a possibility to submit free SQL queries, but provides also basic plotting functionality, accessible via the pull-down menu items "Production status" and "Quality Control".

The most useful panels in the menu item "Production status" are "Inventory" and "View transfers". In the first one, information about objects and their history can be printed or lists of objects currently belonging to one institute can be produced. The lists can be restricted to match certain conditions, e.g. that objects are not faulty, not assembled or not affected by a problem from the *known_problem* table. This panel is basically an interface to the history table for the unexperienced user, who is not able to write own SQL queries. See figure 5.4 for a screenshot of this panel.
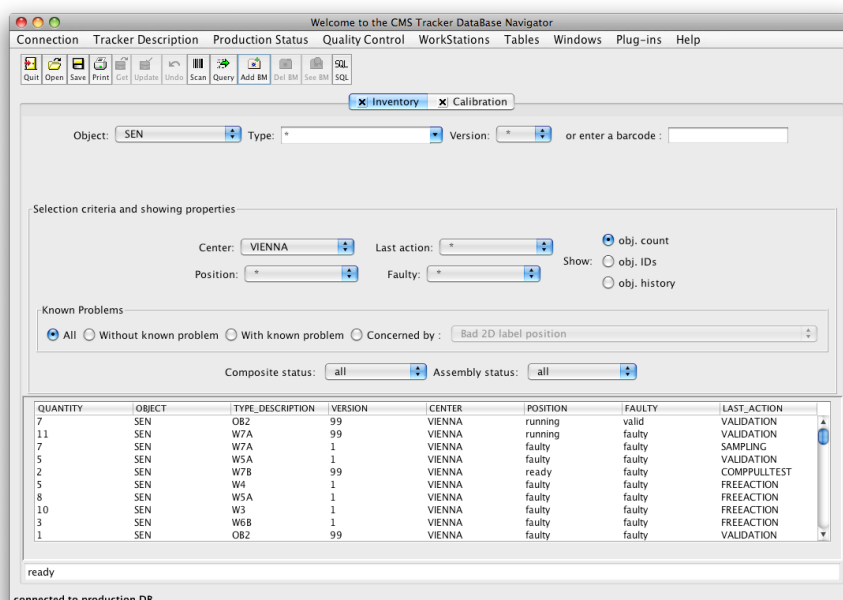


**Figure 5.4:** User interface of the Big Browser Java application showing the "inventory" panel.

The purpose of the "View Transfers" panel is similar. While the "Inventory" shows the history table in a user friendly way, "View transfers" does the same for the transfers table. It lists open transfers with the possibility to restrict the list to dedicated centers. By right-clicking on a transfer_id number it shows all objects belonging to this transfer.

### 5.4.2  Relay Application

For advanced SQL queries and simplified result processing, another interface to the TrackerDB was established. It is called *relay application* and provides an easy way to retrieve data without the need

of a GUI and Java. This program acts at a server daemon waiting for incoming TCP connections on the host `cmstrkdb.in2p3.fr`[4] (port 3615), redirects SQL commands to the Oracle servers and returns the answer to the connected client. The SQL statement must be enclosed by an opening and closing XML tag. An example query would look like this:

```
<select db="prod">
 sysdate from dual
 </select>
```

which sends the enclosed statement to the database servers:

```
select sysdate from dual
```

The answer from the database is itself encapsulated by the relay application in XML tags. The answer of the above query would be

```
<?xml version="1.0" encoding="UTF-8"?>
<answer>
<status>200 DBQuery: OK</status>
<row><column>SYSDATE</column><value>2007-11-04 20:56:51.0</value></row>
</answer>
```

In the following, two programs are presented which are using the relay application interface to access the TrackerDB.

**relay.pl**

*relay.pl* `http://relay.hephy.at` is a command line utility written in the PERL programming language, allowing an easy, fast and reliable access to the TrackerDB via the relay application. It uses the PERL module *XML::Parser*[5] to parse the XML output and to print it on *standard out* (STDOUT) as simple list, with columns separated by tabulators. This tool can be easily integrated into other or other program code.

To execute a query, the SQL code has to be XML-encapsulated and must be available as a file, which is then given as option to the script. Several other parameters are available, which are summarized in table 5.2.

| | |
|---|---|
| -v | verbose. print query and db status. |
| -h | no header. suppress column name in answer. |
| -s | read query from stdin and not from file. |
| | (example: cat file.sql \| relay.pl -s) |
| -t | set timeout for answer in seconds. |

**Table 5.2:** Optional parameters for the relay.pl perl script.

---

4. There is another server available as backup running on host `lyopc72.in2p3.fr`.

5. *XML::Parser* (`http://search.cpan.org/dist/XML-Parser/`) is a Perl extension interface to the XML parser *expat*. It requires at least version 5.004 of PERL and release 1.95.0 or greater of *expat* installed. Expat can be downloaded from `http://sourceforge.net/projects/expat/`.

**VisualDB**

Another client application of the relay interface was implemented using Root [49] and is called
*visualDB* [44]. It allows a very easy way to plot data from the TrackerDB's action tables using
the Root framework. Similar to relay.pl, it reads a file containing the SQL query, sends it to the
relay application and fills the result into a Root histogram. The columns, which shall be plotted, are
configured by an additional header in the XML file. It is treated as comment by all other programs
(similar to a C pre-compiler directive) and also defines the plot type. A screenshot of the program
showing the plotted result of a query is given in figure 5.5.
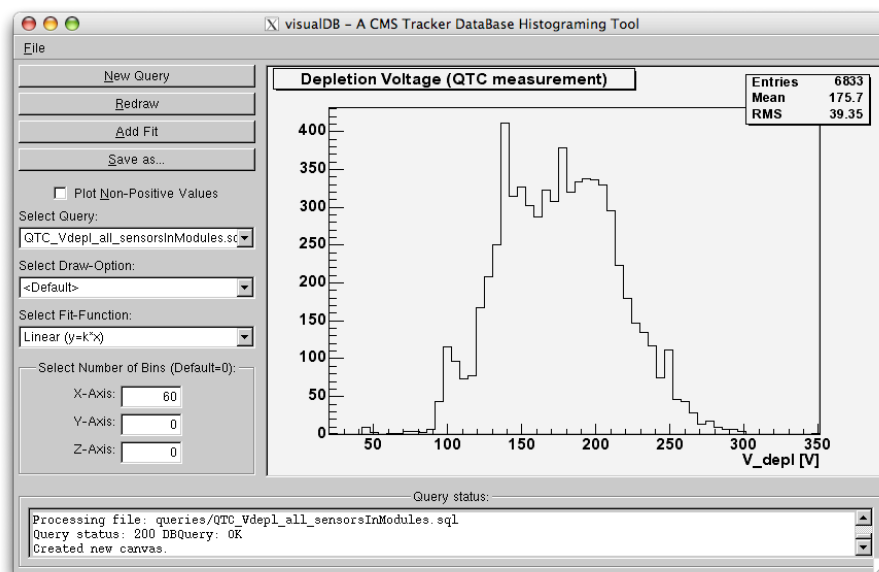


**Figure 5.5:** Screenshot of the visualDB application showing a histogram with the full depletion voltage of all silicon
sensors for CMS which have been tested at the CMS-internal (QTC) test setups.

### 5.4.3  Oracle Client

The supervision and steering of the CMS module production required a more sophisticated data
retrieval tool than using the relay application. For this purpose, a direct connection to the database
servers via Oracle's own client drivers and *SQL\*NET*[6] was established. The credentials to connect
to TrackerDB using this method are described in a file called *tnsnames.ora*, which is listed in ap-
pendix A.4. When using this connection method, each table name must be preceded with with word
*cmstrkdb*. This means that e.g. the name for the table *history* becomes to *cmstrkdb.history*.

The correctly installed and configured Oracle client drivers are then used by the Perl database in-
terface modules *DBI* and *DBD::Oracle*. DBI (previously called DBperl) is a database independent

---

6. SQL\*Net is an Oracle network interface usually running an SQL\*Net Listener on TCP port 1521 or 1526 of the Oracle
   server. Clients can connect to this network ports using Oracle's client driver or third-party products.

interface module for Perl. It defines a set of methods, variables and conventions that provide a consistent database interface independent of the actual database being used. DBD::Oracle is the Oracle specific module for DBI. This method was used to fill tables in a local mySQL[7] database with data from the TrackerDB (see section 6.5.3).

For Windows PCs, a third-party product[8] was used to provide ODBC drivers for the connection to TrackerDB using SQL*Net. This mechanism enables a convenient way to create *Visual Basic for Applications* (VBA) code within Microsoft Excel to submit queries and to fill Excel tables and charts using the resulting data. This technique was used for the CMS module production supervision (see section 6.5).

## 5.5 Other DB Interfaces

In addition to the previously mentioned possibilities to submit and retrieve data to and from the TrackerDB, other interfaces – each for very dedicated purpose – were developed as well. This section describes generic tools only, while in section 6.5 specific tools developed for the module production supervision and steering are presented in detail.

### 5.5.1 Sampling

The silicon sensors for the CMS Tracker were tested twice, first at the sensor producers and later in the CMS quality assurance framework (see section 4.2 for details). While 100% of the sensors were tested at the vendors, the CMS tests were performed on samples of approximately 5-10%. However, the data of all sensors must be available within TrackerDB for production purposes, e.g. during the bonding process of the modules, information about bad strips must be available. Thus, the results from measurements at the companies (called *vendor data*) are uploaded into the corresponding TrackerDB action tables using a special flag *valid* in the status columns (see section 5.2.6 for details). After the decision whether to accept or reject a sensor batch, a dedicated Java program called *Sampling Application* was available to switch the status from *valid* to *reference* to give the vendor data associated with the sensor batch the same significance as CMS-internal measurement results.

### 5.5.2 Bonding Interface

In the previous section the Big Browser application was presented as the only possibility to submit data to the TrackerDB. This is correct, however, data submission can be centralized. This was

---

7. *mySQL* is an Open Source project to provide a relational SQL database management system. http://www.mysql.com/

8. *Datadirect Connect for ODBC 5.0 SP1* using "'Oracle wire protocol'", http://www.datadirect.com/products/odbc/

realized for the *Bonding Interface*[9]. Wire bonding of the modules for the CMS Tracker was done at several centers (see section 6.3). A web application was used to avoid local installation of the Big Browser and additional applications for creating XML files with the measurement results on every laboratory PC. It was installed on a central server in Catania or locally[10] and provided dynamic web pages via a web server. The interface provides the bonding operator information about bad channels, which must be skipped because of sensors problems. *relay.pl* was implemented in this code for the data extraction. On the other hand, the web application allows submission of bonding results, e.g. pull tests values. In that case, the Big Browser application was run on the web server machine utilizing the command-line mode.

### 5.5.3 Tracker Navigator and Little Browser

Two other applications are available for data retrieval and data monitoring. Both were written in Java and have to be installed on a local computer, but can share the *Java Runtime Environment* (JRE) with the Big Browser.

The *Tracker Navigator*[11] is a generic tool to query the TrackerDB for any object_id available. It prints the status, its current location, the history of any object_id and can also be used to retrieve measurement data by clicking on history entries. It provides a fast method to browse between different parent and child objects in a very convenient way. A screenshot of this application is shown in figure 5.6.

*Little Browser*[12] was explicitly developed to quickly view all relevant plots and data for silicon sensors. It was later extended to plot module data as well. Little Browser retrieves all elementary action tables for a given object_id and allows to plot the data found in the vector fields and prints the values in scalar (string, float) fields. However, it does not provide any possibility for querying history data or parent/child relationships of the objects.

9. The Bonding interace has been developed by S. Costa in Catania (Italy). http://cms.ct.infn.it/bonding/
10. http://dbserver.hephy.at/~bonding/ (HEPHY-internal access only)
11. Tracker Navigator was written by Simone Paoletti (INFN Firenze). The most recent version 2.5 is available at http://hep.fi.infn.it/CMS/testres/trkNavigator/.
12. *Little Browser* was developed by INFN Pisa.
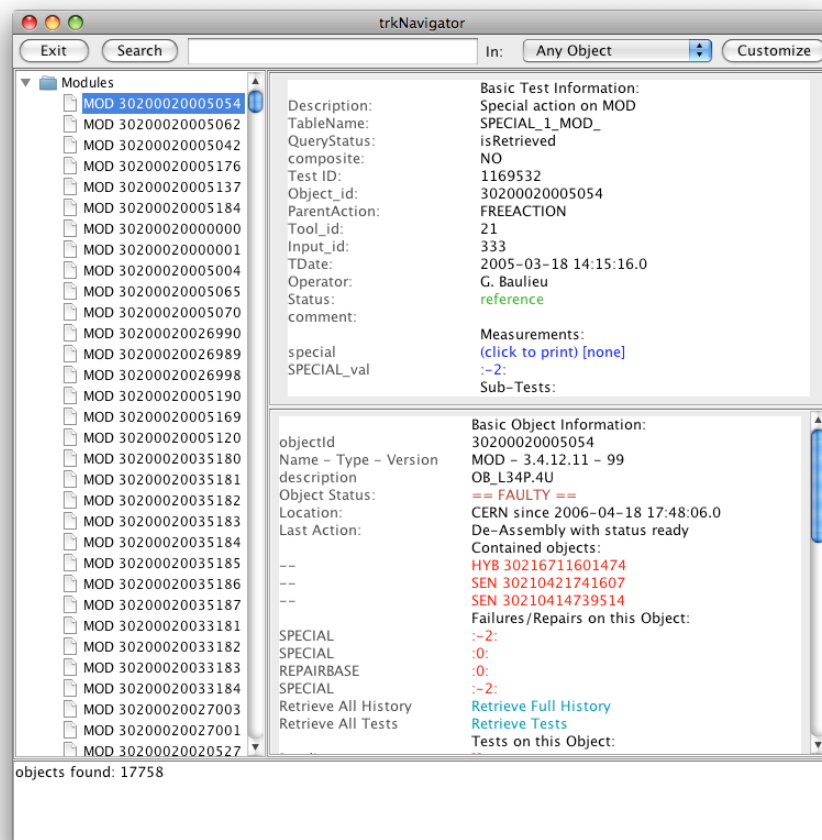
**Figure 5.6:** Screenshot of the Tracker Navigator Java application showing information about a specific module.

# 6 Module Production

> Consistency is better than truth.
>
> *(Unknown Source)*

The CMS Silicon Tracker consists of 15,148 detector modules. Each of these modules is made up of a carbon fiber support structure (called *frame*), a front-end hybrid circuit, and one or two silicon microstrip sensors. Modules in the inner and outer barrel region (TIB and TOB) are of rectangular shape, built with strips aligned along the beam direction (z-axis), and have a constant pitch along the sensor. In the forward region (TID and TEC), modules are wedge-shaped with the strips along the radial direction; thus the pitch varies along the strips. Only TEC modules are discussed in this chapter, as some of them were built at HEPHY Vienna.
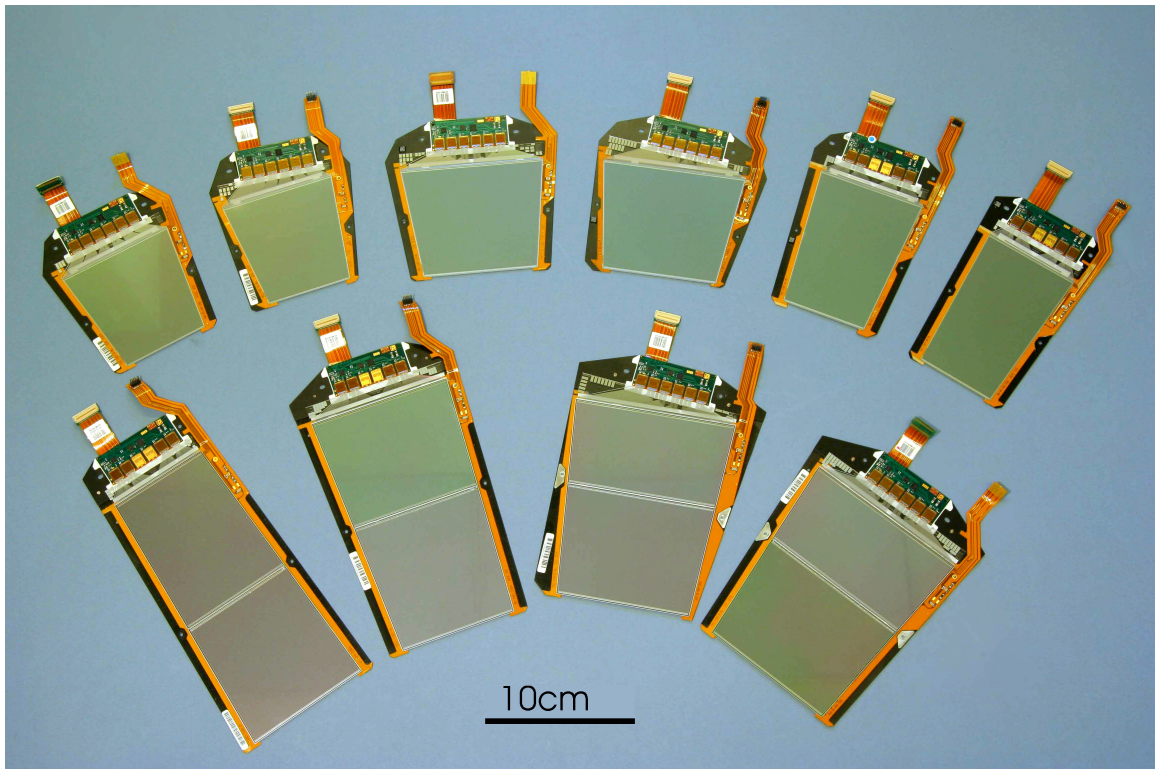


**Figure 6.1:** Picture of the ten different TEC module geometries. Clockwise from top left, the modules are: R1N, R1S, R2N, R2S, R3N, R4N, R5N, R5S, R6N, R7N. The characters N and S refer to *normal* and *stereo*. For stereo modules, the sensor is tilted w.r.t. the hybrid.

Both tracker endcaps comprise 6,400 modules of ten different mechanical geometries (which are shown in figure 6.1) and two additional types which are mechanically identical, but contain different

silicon sensors for the Tracker's internal laser alignment system. In total – including spares – more than 7.200 TEC modules were built by 16 institutes in Europe and the United States. This was a more challenging task than it appeared to be initially. In this chapter, the module components are described in detail first, before the different production steps are listed and the overall logistics and quality assurance is discussed.

## 6.1  Module Components

Each module consists of a support structure called *frame*, which carries one or two silicon sensors (depending on the module geometry) and the front-end (FE) hybrid housing the readout electronics. A picture of a module can be seen in figure 6.2.
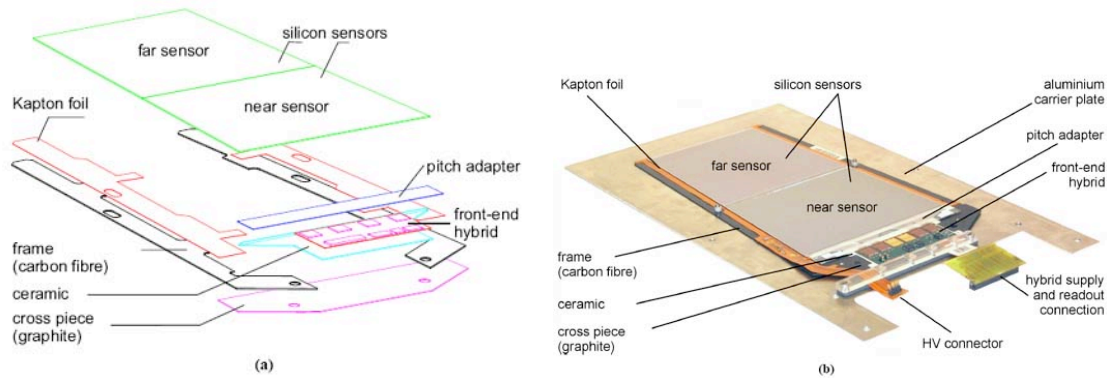


**Figure 6.2:** Exploded drawing (a) and photo (b) of a real TEC module for ring 6. The photo shows the module mounted onto its aluminum carrier plate used during transport.

### 6.1.1  Module Frame

For two-sensor-modules the frame is formed of two carbon fiber legs glued onto a graphite cross piece, while the frame of single-sensor-modules consists of just one single U-shaped piece of graphite. Both materials were chosen because of its high stiffness at low mass and its excellent heat removal capacity, while having similar thermal expansion coefficients than silicon. Another important property is their good radiation hardness.

During transportation, storage, testing and even bonding of the electrical connections between hybrid and sensor, the module rests on an aluminum plate, the so called transport plate, which eases transport and handling and helps to avoid damage of the modules. The plate can be seen in figure 6.2 (b).

The carbon fiber or graphite frames house several precision holes which are used to precisely align the frame during automatic assembly of the FE hybrid and the sensors using a so called *gantry system* (see section "Assembly" below).

To provide extra stability to the silicon sensors during the wire bonding process, one or two ceramic rigidifiers serve as supporting structure underneath pitch adapter and sensor(s).

## 6.1.2 Kapton Foil

A layer of Kapton foil[1] is used to insulate the electrically conducting module frame and the backplane of the silicon sensors (which is at HV potential of up to 600 V). It is being glued on the frame with an epoxy resin glue and the sensors are glued to the foil using a silicone glue. The Kapton foil is metallized on one side to electrically connect the HV bias voltage to the backplane of the sensors via an integrated low-pass filter element called *T-filter*, whose schematics is shown in figure 6.3.
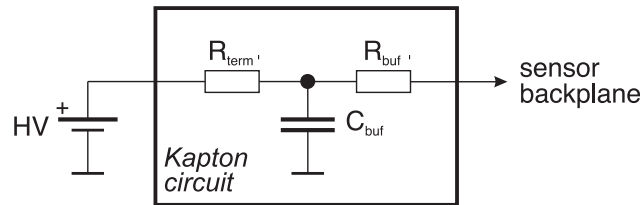


**Figure 6.3:** Schematics of the RC-filter used on the Kapton to block the propagation of high frequencies in both directions. The values are $R_{\text{term}} = 2\text{k}\Omega$, $C_{\text{buf}} = 100\text{nF}$ and $R_{\text{buf}} = 8\text{k}\Omega$.

The connection from the Kapton metallization to the sensor backplane is done by both, gluing and wire bonding. Initially, only conductive glue (EPO-TEK EE129-4) was used, but since it was shown that thermal stress decreases the quality of this connection (increasing resistance) [50], wire bonding was introduced as additional connection method. Figure 6.4 shows a glued and wire-bonded connection.
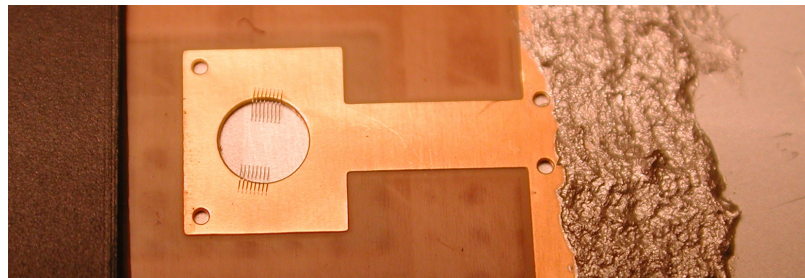


**Figure 6.4:** Detailed view of the backside of a silicon module. The black bar on the left is part of the module frame, while the Kapton with the gold-plated metallization is visible in the center. Wire bonds are placed in the hole, connecting the metallization with the sensor backplane. On the right side, the craggy area is the (reinforced) conductive glue providing a second connection between Kapton and sensor backplane.

---

1. Kapton is a polyimide film which remains stable in a wide range of temperatures. It is a registered trademark of DuPont. http://www.dupont.com/kapton/

### 6.1.3 Front-end Hybrid

The board made of multi-layer Kapton is called *hybrid* and is shown in figure 6.5. It is housing
the front-end (FE) electronics. The main device is the APV25 readout chip, which collects the
electrical charges from the strips, converts it to voltages, amplifies them and serialises the signal
from all channels on its analog output. The outputs of two APVs are multiplexed together using the
APVMUX chip. The PLL chip handles triggers and timing and the DCU chip is used to monitor
temperatures, currents and voltages. All chips on one FE hybrid can be programmed and read
out via an $I^2C$ interface sharing the same bus, but addressed separately by sending data packets to
hard-coded $I^2C$ addresses.
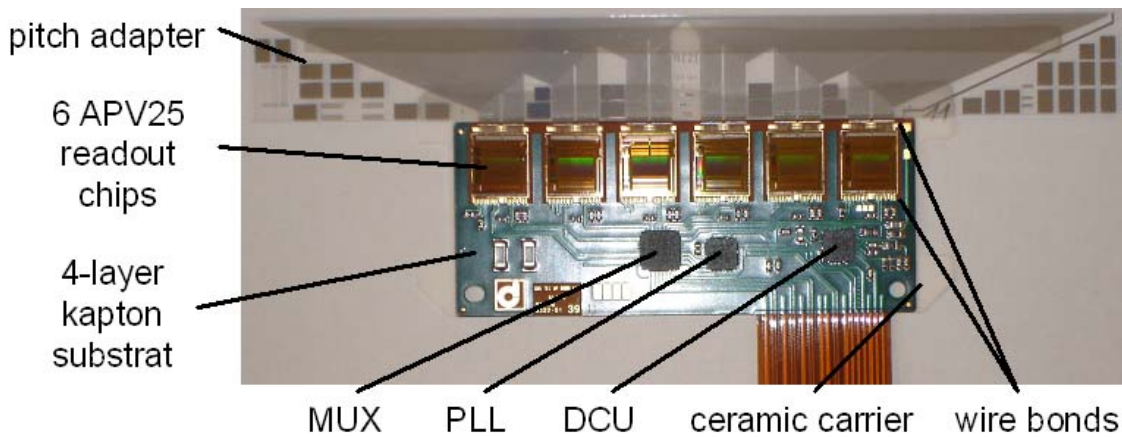


**Figure 6.5:** Front End Hybrid PCB and associated pitch adapter. The PCB contains usually four or six APV chips
together with APVMUX, PLL and DCU.

**APV25 Readout chip**

The electronics responsible for the amplification and shaping of the silicon sensor signals is the
*Analogue Pipeline Voltage* (APV) chip, a custom designed ASIC built with the radiation-tolerant
IBM deep sub-micron (0.25 μm) technology [21, 51, 52]. Thus, the full abbreviation for this
chip is APV25 to distinguish it from its predecessor APV6, made with Harris AVLSIRA 1.2 μm
CMOS process. In this case the number 6 does not refer to the technology, but was a sequential
number.

The schematics of a single channel of the APV25 readout chip is shown in figure 6.6. The AC
strip of the silicon sensor is directly connected with the integrating preamplifier. Its output signal
polarity can be optionally changed by inserting an inverter. The shaper with an adjustable peaking
time defaulting at 50 ns is in CR-RC configuration. Its output is sampled with 40 MHz(synchronous
to the LHC beam bunch crossing frequency) and fed into an analog pipeline (ring buffer) with 192
cells. Upon request by a L1A trigger pulse, the signals are extracted from the pipeline. An optional
switched capacitor filter (analog pulse shape processor; APSP) is available to implement a so-called
*deconvolution*, which calculates a weighted sum of three consecutive signals. If not used, the simple
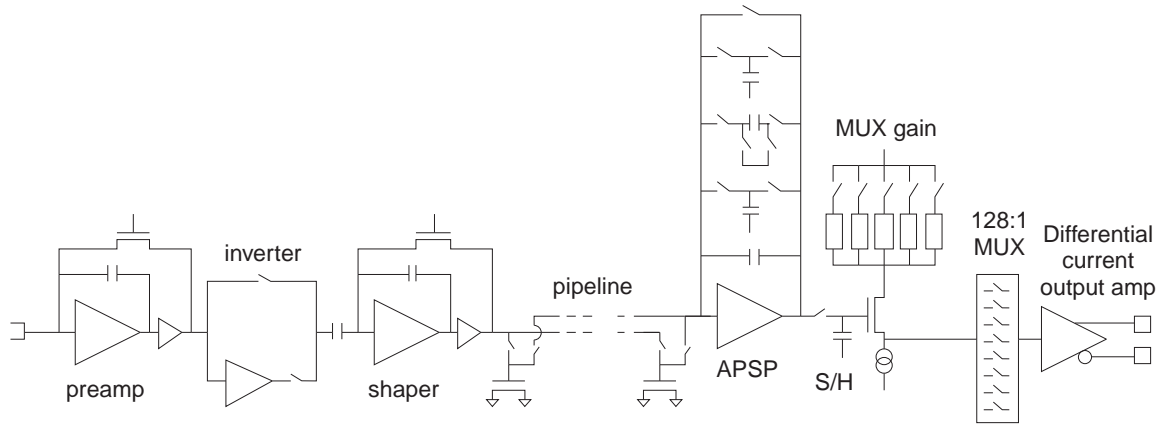
**Figure 6.6:** Block diagram of the APV25 chip for a single channel. The blocks shown to the left of the MUX are implemented 128 times in the chip.

*peak mode* uses just one single signal sample to feed into a sample/hold (S/H) stage, followed by an amplifier with programmable gain. The signals of all 128 channels are multiplexed onto a single line, but – due to the tree structure of the multiplexer – not in consecutive order. If $n$ is the order in which the channels (starting at 0,1,2,...) appear on the output, then the physical channel number can be optained by

$$\text{physical channel no.} = 32\,(n \bmod 4) + 8 \operatorname{int}\left(\frac{n}{4}\right) - 31 \operatorname{int}\left(\frac{n}{16}\right) \tag{6.1}$$

Finally, the multiplexed signal is sent to the outside by a differential current output amplifier. The analog data are preceded by a digital header including the pipeline address of the event and an error bit, as shown in figure 6.7. The chip also delivers a synchronization pulse, often called *tick*
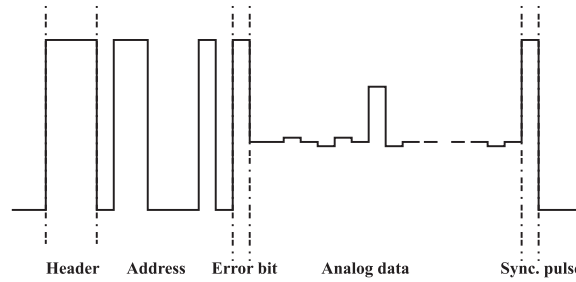


**Figure 6.7:** APV output data frame of one event. The digital part containing header, address and error bit is followed by the multiplexed analog data. It is terminated by a synchronization pulse, called *tick mark*.

*mark*, every 70 clock cycles when there is no data to read out. This helps subsequent readout electronics to stay synchronized with the chip and to adjust offset and gain settings in the signal path.

The deconvolution mode implemented with the APSP filter helps to distinguish signals coming from different bunch crossings by mathematically narrowing the signal in time at the cost of increased noise. The signals of three consecutive pipeline cells are combined with individual weights according to

$$x_{\text{deconv}} = 0.4463\,x_{k-2} - 1.4715\,x_{k-1} + 1.2131\,x_k \tag{6.2}$$

Two particles, each producing a signal in consecutive bunch crossings, cannot be recognized in the raw shaper output (e.g. peak mode), but easily after deconvolution. Diagram 6.8 shows the APV output for both, peak and deconvolution mode.
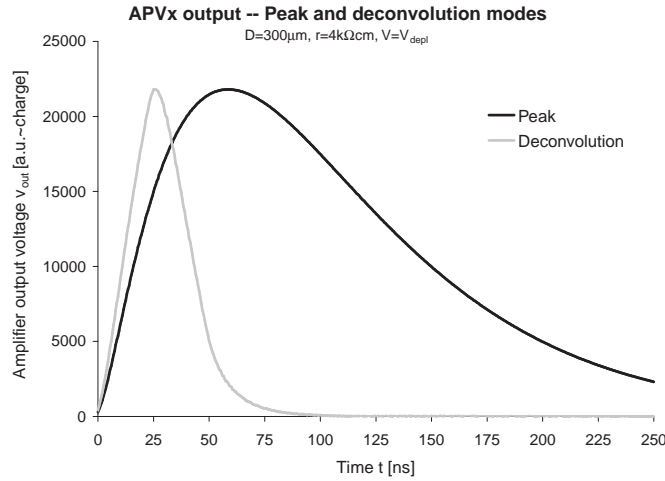


**Figure 6.8:** APV output for peak (black line) and deconvolution mode (grey line) [21].

In deconvolution mode, the noise figures for the APV chip are higher than the ones in peak mode according to table 6.1.

| mode | a $[e^-]$ | b $[e^-/\text{pF}]$ |
|---|---|---|
| peak | 250 | 36 |
| deconvolution | 430 | 61 |

**Table 6.1:** Noise figures for the two operation modes of the APV readout chip. The constants $a$ and $b$ are contributing to the EMC noise according to equation 3.55.

The APV25 chip incorporates a command register to adjust various settings of the chip by I$^2$C commands, e.g. the operation mode (peak or deconvolution mode) can be adjusted by modifying the MODE register. The full list of registers and their meanings is given in table 6.2. The command registers must be programmed after powering up and prior normal operation.

The APV25 includes an internal calibration pulse generator, which allows to check the functionality of each channel. When used, it applies a voltage step pulse $\Delta V$ to a series capacitor $C$ which is connected to the preamplifier input. The injected charge can be calculated using $\Delta Q = C \Delta V$. The calibration pulses can be applied to one (or more) out of eight groups, each connected to 16 input channels of the amplifier.

A single APV25 chip containing 128 channels needs 2.5 V for its digital and additionally 1.25 V for its analog part, consuming $355(\pm 36)$ mW, depending on the APV settings, in total [53] (compare to $\approx 25$ mW/APV for the Analog Opto Hybrid and $\approx 33$ mW for the DCU chip; see below).

| Register | Meaning |
|----------|---------|
| IPRE | Preamp Input FET Current Bias |
| IPCASC | Preamp Cascode Current Bias |
| IPSF | Preamp Source Follower Current Bias |
| ISHA | Shaper Input FET Current Bias |
| ISSF | Shaper Source Follower Current Bias |
| IPSP | APSP Current Bias |
| IMUXIN | Multiplexer Input Current Bias |
| ISPARE | Not Used |
| ICAL | Calibrate Edge Generator Current Bias |
| VFP | Preamp Feedback Voltage Bias |
| VFS | Shaper Feedback Voltage Bias |
| VPSP | APSP Voltage Level Adjust |
| CDRV | Calibrate Output Mask |
| CSEL | Calibrate Delay Select |
| MODE | Mode of Operation of Chip |
| LATENCY | Delay Between Write and Trigger Pointers |
| MUXGAIN | Sets Gain of Multiplexer |
| ERROR | Holds Error Flags |

**Table 6.2:** APV25 command register names and their meanings [52].

**Multiplexer**

The APV25 clock is 40 MHz, but its output is clocked at only 20 MHz. The APVMUX chip is a 2:1 multiplexer which combines the output of two APV chips to a single output at 40 MHz in order to minimize the number of readout channels. The chip includes an $I^2C$ interface for configuring built-in termination resistors.

**PLL chip**

The PLL (phase locked-loop) chip generates clock and trigger signals for the APV chip from a single line containing both signals in a mixed way. This line propagates the clock signal (*CLK*), but omits one clock pulse for a trigger signal (*TRG*). Logically, the signal line is composed of $CLK \& \overline{TRG}$, which is shown graphically in figure 6.9.

**DCU chip**

The *Detector Control Unit* (DCU) monitors environmental parameters like the silicon sensor temperature using an external Negative Temperature Coefficient (NTC) resistor and the hybrid temperature using an internal temperature sensor. Moreover, the sensor leakage current is determined by the voltage drop of a small resistor connected in series to the ground connection of the sensor bias line.
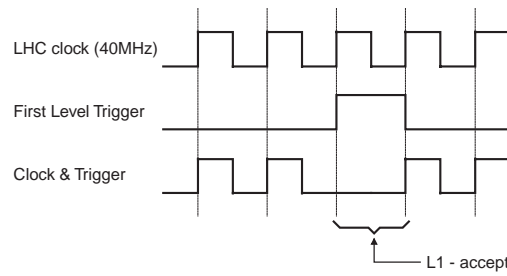
**Figure 6.9:** LHC clock and first level trigger signals are propagated to the FE hybrid sharing a single line, which omits a clock pulse for a trigger signal.

Furthermore, the levels of the two low voltage lines $V_{1.25}$ and $V_{2.5}$ are monitored internally using a multiplexer followed by a single-slope rail-to-rail analog-to-digital converter.

Another important task of the DCU is to provide an unique ID number which can be read out using its I$^2$C interface. This 24 bit identifier is hard coded into the chip to allow the identification of each module inside the Tracker. A correlation table between DCU ID and and object_id of its associated hybrid is stored in TrackerDB in the table *fhitproduction_1_hyb_* and the correlation to the module id can be found in the table *modulbasic_2_mod_*.

### 6.1.4 Pitch Adapter

In order to connect the readout strips of the silicon sensors to the APV readout chips, a *pitch adapter* (PA) needs to adapt the different strip pitch of the sensor to the staggered pads of the APV chip of 44 μm pitch. It is made of glass substrate with aluminum strips of 1.5 μm thickness on a Cr/Ni coating layer. In addition, alignment marks, bond test areas and a broader bias strip are incorporated in the PA as well. There are 24 different designs and the substrate dimensions, precise to $\pm 50$ μm, vary between $64 \times 9$ mm$^2$ and $123 \times 21$ mm$^2$. The substrate material used in connection with "thin" sensors is 300 μm thick borosilicate glass (CORNING 1737F), while for TOB and "thick" TEC sensors 550 μm thick Schott D263 glass is used [54].

All pitch adapters were manufactured by two companies, Reinhart[2] and Planar[3].

## 6.2 Assembly

Before the components were assembled into modules, each component – sensors, frames, hybrids plus associated pitch adapter – were tested electrically and mechanically at their production sites or at CMS-interal test centers similar to the sensors' QTC centers described in the previous chapter.

At the module production centers, each part was visually inspected prior to the actual assembly procedure. The assembly itself is performed automatically by a so-called *gantry robot* in five different centers [55], while in Vienna a fully manual procedure has been established [50].

The basic element of the automatized assembly is a robotic positioning system called *gantry*[4] which provides a large movement range for a working head, equipped with various tools and operated in four coordinates (x,y,z and $\phi$ rotation). A sensor platform, assembly platform, pick-up tools and a glue dispensing system had been designed at CERN using vacuum to hold the pieces to be assembled and pressurized air to dispense the glue. The system used a CCD video camera system with pattern recognition to precisely find and align the components, which all had to be equipped with alignment marks. The system has been tested before being commissioned to reach a relative placement accuracy of better than $1.5\,\mu m$ and a similar reproducibility. The absolute accuracy turned out to be well within the design goal of $< 5\,\mu m$ [56].

The module assembly in Vienna was performed manually. A 3D coordinate measuring machine[5] was used for positioning in order to achieve a comparable resolution to the automatic gantry system. The actual assembly took place on three precision tables, which are geometrically identical but had been replicated for quasi-parallel work. These tables were designed and built in the HEPHY workshop and contain a cavernous material, where vacuum is applied to attach the module parts during glue curing. Directly after assembly and gluing a first position measurement took place, which was repeated several hours later when the glue was hardened. The following glues were used for distinctive parts of the module:

- EPO-TEC EE129-4 conductive glue for the HV backplane connection of the silicon sensor to the HV line of the Kapton foil.

- Araldite 2011 Expoxy AW 106 to attract the stiffener and the hybrid to the frame.

- Dow Croning 3140, RTV coating: A flowable, non-corrosive silicone rubber glue, used to glue the silicon sensors to the frame allowing some movements of the sensors since this type of glue does not fully stiffens.

The maximum allowed deviation from the nominal sensor position in respect to the frame was set to $\pm 39\,\mu m$ for shifts perpendicular to the strips and $\pm 65\,\mu m$ along the strips. The maximal angle deviation was specified by $\pm 0.03\,°$. The mounting precision achieved by the "manual" method performed in Vienna is compatible to the figures of the automated gantry robot [50].

## 6.3 Bonding

After module assembly and glue curing, the wire bonding was performed to electrically connect the strips of the sensors with the FE hybrid. Ultrasonic wire bonding is a cold welding technique, using an aluminum/silicon-alloy wire (1 % of silicon) of $25\,\mu m$ thickness. For CMS, various bonding machines in 12 different laboratories were availabe. In Vienna, a fully automatic wire bon-

---

4. The automatic positioning robot is based on the system AGS 10000 by Aerotech. `http://www.aerotech.com/`
5. The 3D coordinate measurement machine is a model Euro-C apex 776 by Mitutoyo, `www.mitutoyo.de/`

der[6] was used to perform the bonding of more than 650 modules or approximately 500,000 single bonds.

A destructive pull test was foreseen on test bonds using a bond pull tester[7] to prove the quality of the wire bonds. This machine uses a hook to pull on a bond wire until it breaks or one of the two bond feet lifts up from the bond pad. The force necessary to break the bond, expressed as mass $m$ in grams, which the bond wire can resist, is recorded. In the beginning of the production, every 50th bond of the readout channels was pulled as well. Since this test did not reveal any problem, it was skipped for the subsequent mass production. The average pull force for bonds between sensor and pitch adapter was 11 grams, which is well above the specified minimum of 6 grams [57].

In addition to the wire bonding of the readout strips, the connection of the sensor backplane to the Kapton foil had to be bonded. As mentioned in section 6.1.2, this measure was introduced after tests of the initial procedure (conductive glue only) showed increased resistance after several cooling cycles between +20 °C and -10 °C and affected around 10 % of the connections [50].

## 6.4 Testing

After bonding, the module is mechanically ready and needs to be tested electrically to check its functionality. These tests were performed using the *APV Readout Controller* (ARC) system, which was developed explicitly for this purpose [58] and was commonly used by every institute involved with the CMS module production. The uniformity of the test results was ensured by using identical testing systems with the same hardware and software versions at all sites and by the help of cross-calibration using a module whose test results at all test stations were compared.

The test setup hardware used in Vienna was composed of the following elements: a light-tight, shielded box containing the module (*device under test* [DUT]), an electronics crate connected to a power supply and a personal computer. The electronics modules of this setup are shown in picture 6.10.

The light-tight box consists of aluminum which acts as Faraday cage and houses the DUT, a front end adapter electronics board and an array of 16 infrared light emitting diodes (LEDs) used to generate signals in the silicon sensors. The crate uses a 50-wire flat ribbon cable as backplane to communicate with the other modules and the personal computer using the so-called PCMIO bus protocol, which is an adaptation of the ISA bus protocol. The main module is the *ARC board* with the ability to readout two hybrids or modules at the same time. Clock and trigger signals are generated internally common to both front-ends. The ARC board is connected by a 26 pin twisted pair cable to the front end adapter board located in the light-tight box. The *Depletion Power*

---

6. Fully automatic rotary head wedge bonder model 6400 by F&K Delvotec http://www.fkdelvotec.at/. The accessible work area is $150 \times 200$ mm and 25 mm in height.
7. A Microtester 22 by Dage was used for this purpose in Vienna.
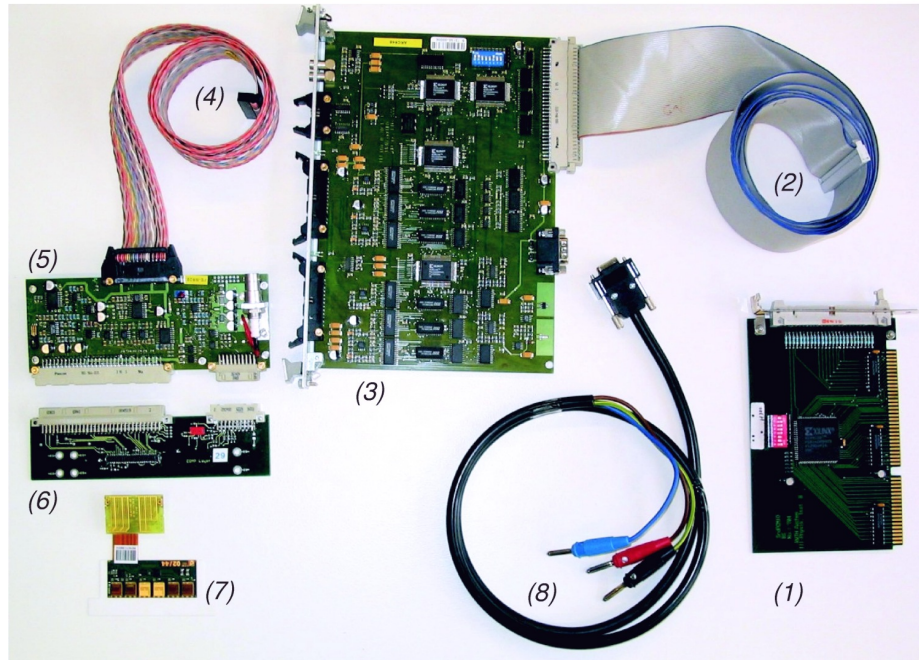
**Figure 6.10:** Components of the ARC system [58]. It consists of a PC ISA board (1) which connects to the main ARC board (3) by a 50-wire flat ribbon cable (2). Another flat ribbon cable with twisted pairs (4) connects the front end board (5) to the ARC board. The next board (6) is the Hybrid-to-VUTRI adapter card, necessary to connect the front-end hybrid (7) to the system. The black cable (8) supplies power to the ARC board.

(DEPP) board provides high voltage of up to 600 V to bias the silicon sensors and to measure its dark currents. Another dedicated module called *LEP16* located in the PCMIO crate is used to drive the infrared LED array.

The *APV Readout Controller Software* (ARCS) is a Labview 6i application that serves as graphical user interface to the hardware test setup. It is able to configure all registers of the FE hybrid chips via the $I^2C$ bus, to run several measurements on the module, to interpret the results and to write these results into an XML file. The software provides the opportunity to run a *Fast Test* or a *Deep Test* where most of the individual tests are performed automatically. A detailed description of the ARCS Software can be found in [59].

A fully working module was given a grade A when the following tests had been passed successfully: Fast Test, IV test (leakage current at 450 V less than 6 μA for one-sensor or less than 12 μA for two-sensor modules), pedestal & noise test, pulse shape test, pinhole (LED) test, pipeline test and less than 1 % bad channels. When the number of bad channels exceeded 2 % and/or the dark current at 450 V was above 10 μA (20 μA for two-sensor modules), the module was considered as faulty and hence not used for the CMS Tracker.

# 6.5 Logistics, Monitoring and Production Steering

Monitoring and steering of the TEC module production was under responsibility of HEPHY and took advantage of information from the TrackerDB. It was used to get current production data on one hand, and provided a future working plan on a weekly updated website to all involved institutes. Defect analysis of faulty modules was done using a local mySQL database mirroring some of the TrackerDB's tables but extending it with additional tables with defect data. These tools are presented in this section.

## 6.5.1 Production Monitoring

The TEC module production was shared by 16 institutes in Europe and the United States (see table 6.3). A software was developed using *Visual Basic for Application* (VBA) – the programming

| Geometry | Target value | Assembly center | Bonding center |
|----------|-------------|-----------------|----------------|
| R1 | 152+152 | Lyon | Hamburg |
| R2 | 303+303 | Vienna | Vienna |
| R3 | 680 | Bari, Brussels, Lyon | Bari, Catania, Hamburg, Karlsruhe, Padova, Pisa |
| R4 | 610 | Bari, Lyon | Bari, Catania, Padova, Pisa, Zürich |
| R4A | 460 | Lyon | Zürich |
| R5 | 760+760 | Brussels, Santa Barbara | Aachen, Karlsruhe, Santa Barbara |
| R6 | 920 | Brussels, Santa Barbara | Aachen, Santa Barbara, Zürich |
| R6A | 156 | Brussels | Aachen |
| R7 | 1525 | FNAL, Lyon, Santa Barbara | FNAL, Hamburg, Santa Barbara, Strasbourg, Zürich |

**Table 6.3:** TEC Module types and the centers where each type was assembled and bonded. The column *target values* gives the number needed to build the Tracker plus 6 % contingency. For R1, R2 and R5, the two numbers represent normal and stereo modules. The module types R4A and R6A are the special modules with a hole in the backplane needed for the Laser Alignment System.

language included with Microsoft's Office suite – to oversee this distributed production. It allows to query the TrackerDB using the ODBC driver for Oracle described in section 5.4.3. It prints the delivered bare hybrids, the bonded and tested hybrids together with the assembly and bonding rate at every institute on a weekly basis in an Excel file called *TEC-Org*. A screenshot of a part of this huge table can be seen in figure 6.11. The graphical representation of these numbers is shown in figure 6.12, demonstrating the good progress and effective production within the TEC community.
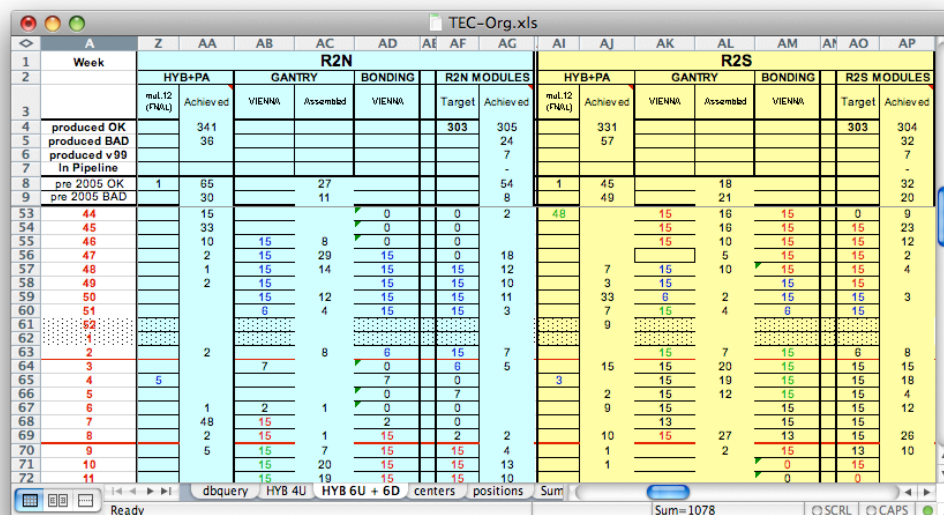
**Figure 6.11:** Screenshot showing part of the Excel spreadsheed which was used to oversee the TEC module production. These tables contain the numbers of the weekly TEC module production queried from TrackerDB by VBA programs and the weekly target values which are given to the institutes using dynamically generated webpages.
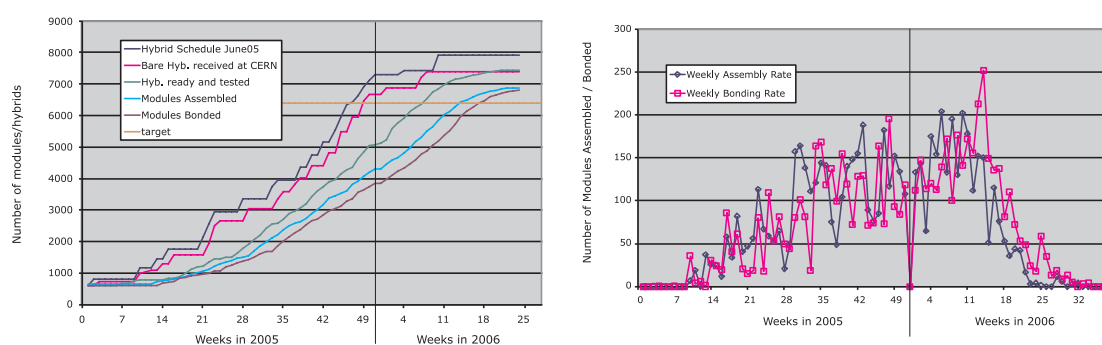
**Figure 6.12:** Cumulative production (left) and weekly production rate (right) for module assembly and bonding.

### 6.5.2 Module Production Monitor

The weekly production data extracted from TrackerDB was then used as basis to prescribe target values for each institute for the coming weeks by writing these numbers into additional columns of the TEC-Org spreadsheet file. The target values were uploaded into a local mySQL database by another part of the VBA program stored together with the data in the file TEC-Org. A Perl script executed automatically every day (via cron-job) was used to dynamically create webpages like the one shown in figure 6.13 using data from this database[8]. The numbers on these pages show to each institute their target values for the forthcoming weeks together with the material (e.g. hybrids, sensors) which should be in stock or arriving soon.
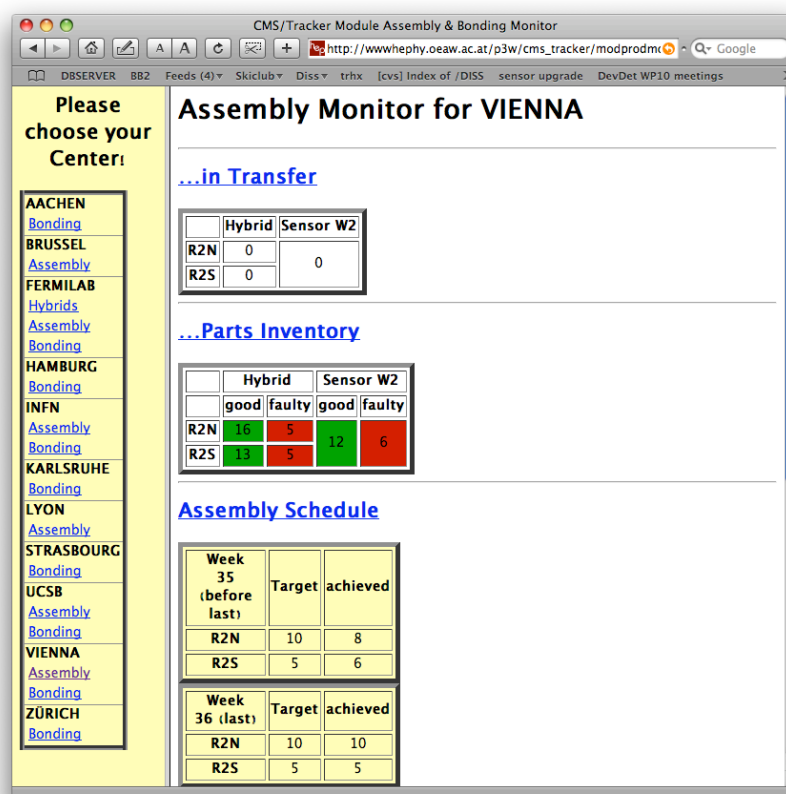


**Figure 6.13:** Screenshot of the Module Production Monitor webpage showing the data for Vienna.

### 6.5.3 Faulty Modules Database

Additional tables of the mySQL database were used to store all available data about each faulty module in order to better diagnose and repair broken modules. For this purpose, some information was queried from the TrackerDB and mirrored locally like the module history, parts of the

---

8. This website is found at `http://cms.hephy.at/modprodmon/`

object_assembly table and others. All this information was then used to manually and interactively judge each module and to classify it into one of 15 different problems. This was performed using a self-developed PHP frontend to the mySQL server.

Additionally, another flag called *category* was introduced as overall classification of the severity of the fault. By using this flag, the modules had either a *minor problem*, was *repairable*, required *sensor recuperation* or *hybrid/frame recuperation* or was *lost* completely. For details about these categories and problems, see [50] (page 81ff). Sensor recuperation means that a module consists of one or two good sensors but a broken frame, hybrid or other component on the module. In that case, it was disassembled in Vienna and the sensors were subsequently shipped – after detailed tests – back to the module production centers to re-use them. Statistics about disassembly yield can also be found in [50]. The output of the classification of faulty modules resulted in detailed information about the reason of the fault, as shown in figure 6.14.
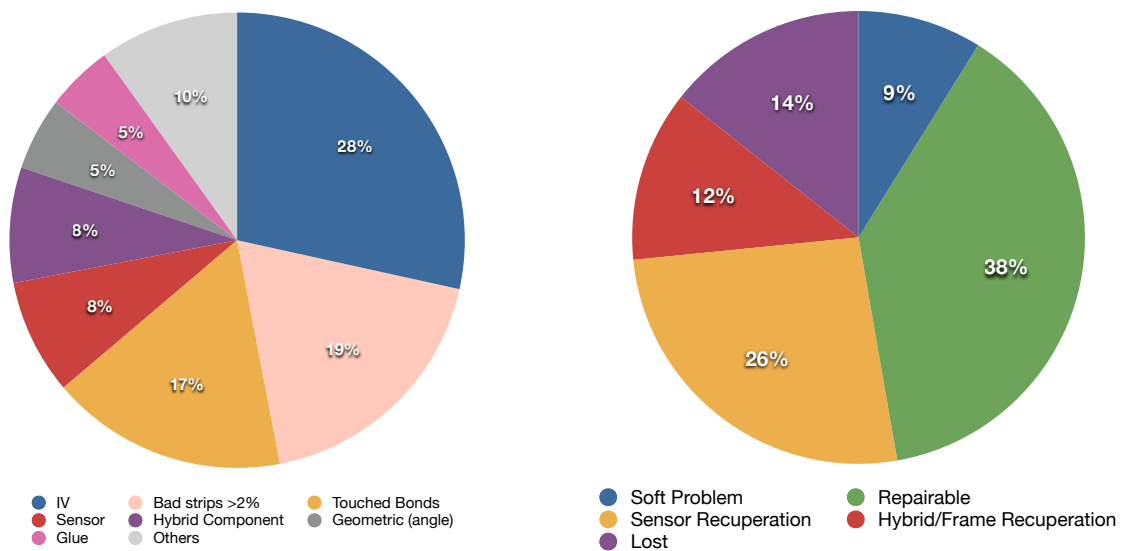


**Figure 6.14:** Distribution of faulty modules by problem (left) and by category (right). These numbers were extracted from the local mySQL database after the module production finished (October 2006).

# 7 Petal Production

Substructures of the Tracker Endcaps (TEC) are called petals. In total, eight different petal types exist which can be grouped by two mounting forms, *front* and *back*. While front petals are installed facing the intersection point, pack petals are placed in the opposite direction.

## 7.1 Petal Components

A petal has trapezoidal shape and consists, of about 20 to 30 silicon modules depending on the petal type, together with further control and readout electronics. These elements are placed on large printed circuit boards (PCBs) called *Interconnect Board* (ICB). The petals incorporate integrated cooling pipes for heat dissipation, which are also responsible to keep the sensors on their operating temperature of -10°C.

### 7.1.1 Mechanics and Cooling

A carbon fiber structure with hexagonal form is the support for a petal in which two approximately 3.50 m long and 6 mm thick cooling pipes made of titanium are embedded. Special cooling manifolds are used for connecting them to external cooling circuits. Perfluorohexane ($C_6F_{14}$), a perfluorocarbon which is known as a greenhouse gas, is used as cooling liquid. Because of its high volatility, each cooling loop is tested for tightness using pressure tests with air or helium before being filled with the coolant.

The main sources of heat on the petal are the APV chips on the module's front-end hybrids. The cooling system has to dissipate up to 75 W of power for a fully equipped petal [60]. Titanium cylinders called *inserts* are used to achieve a fast heat transfer from the modules to the cooling pipes. For a good thermal contact, radiation-hard thermal grease is placed on the inserts before the modules are installed. This ensures a fast heat dissipation from the chips to the coolant.

### 7.1.2 Interconnect Board

The first element to be installed on the carbon fiber support structure is the *interconnect board* (ICB). It is a multi-layer PCB made of woven fiberglass and epoxy (FR4[1]) and provides connectors for all other components which are installed onto it. The ICB consists of up to five different parts in total, depending on the petal type. For outer discs, e.g. the petals are shorter in length and thus the outermost parts of the PCBs are omitted. Picture 7.1 shows a carbon fiber petal support with the ICB already installed.
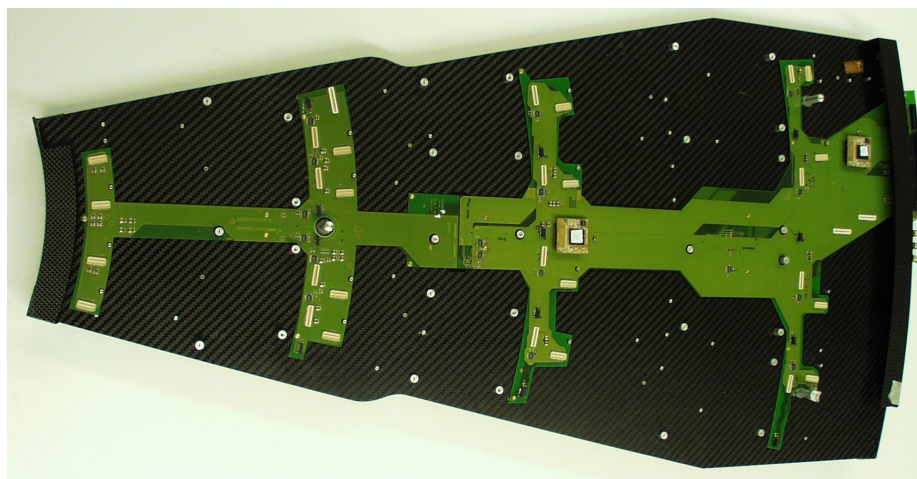


**Figure 7.1:** Picture of a carbon fiber (CF) petal support structure (grey) with the components forming the ICB (green). The small metal cylinders in the CF are the inserts for cooling of the modules.

The ICB contains electrical lines to distribute high and low voltages as well as trigger, control and clock signals to all modules and other components of a petal. Since all signals from and to the petals are transmitted via optical links, the ICB houses digital optical transceivers (DOHs) and analog optical transmitters (AOHs) to convert optical to electrical signals. While these elements are only converters, there are also dedicated cards mounted on the ICB which are responsible for communication and control, the CCU modules (CCUM; see below). These components are described in detail below. Moreover, temperature and humidity sensors are welded directly onto the ICB which are read out via MSC and LIC cables.

### 7.1.3 Digital Opto-Hybrid

The control signals from the *front-end controllers* (FEC) are transmitted from the service cavern to the Tracker via optical links. The *digital opto-hybrid* (DOH) installed on the ICB is responsible for converting the light pulses to electrical signals of the LVDS[2] standard and vice versa. This is done by InGaAsP/InP laser diodes with a wavelength of 1310 nm and semiconductor photodiodes acting as receivers [13].

---

1. FR4, an abbreviation for Flame Retardant 4, is a common material used for making high-end electronics PCBs.
2. Low Voltage Differential Signaling

The optical fibres transmit the LHC clock and CMS Level-1 trigger signals using the *Timing, Trigger and Control* (TTC) system [61] at 80 Mbit/s, together with control signals at 40 Mbit/s to and from the Tracker front-end. These signals are, once converted to electrical, transmitted via copper lines on the ICB to the CCU modules (see below). There are 8 optical link channels per control ring. Four channels are required to communicate the TTC and control signals. The four other links are part of a redundancy scheme in case of component failures in the control ring system.

## 7.1.4 Communication and Control Units

The *Communication and Control Unit* (CCU), a PLL chip and a LVDS fanout ASIC make up the *CCU module* (CCUM). The CCU receives the data from the FEC via the DOH and relays it to the front-end chips on the silicon modules via $I^2C$ protocol (see figure 7.2), plus provides dedicated lines for clock, trigger (TTC) and reset. Each CCU can control up to 16 silicon modules.
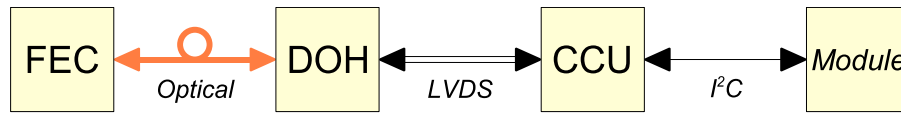


**Figure 7.2:** Data path of the communication between *Front-End Controller* (FEC), *Digital Opto-Hybrid* (DOH), *Communication and Control Unit* (CCU) and the front end chips in the modules. The FECs located in the service cavern are approximately 100 m away from the other parts located in the detector itself, hence the optical links.

Each petal houses two CCUMs, one responsible for the modules of ring 1 to 4, and the other for ring 5 to 7. A front petal together with a back petal form a so-called *control ring*. The ring operates a token ring architecture, where one token is passed between the four CCUMs on the petals and a FEC located 100 meters away in the service cavern (see figure 7.3).
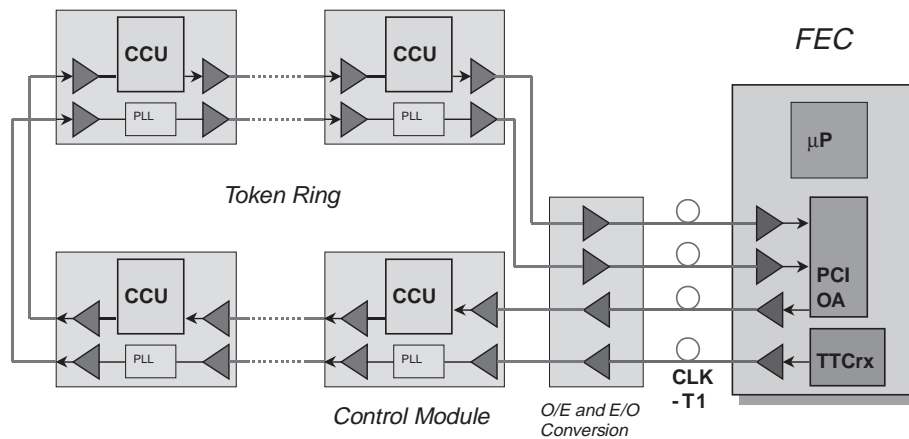


**Figure 7.3:** Schematics of a control ring. The token ring architecture passes a token between the FEC and the four CCUs sitting on Control Modules (CCUM).

Each CCU has two inputs and two outputs, called *default* and *alternative*, to implement connection redundancy. Upon power-up the *default* input and output are selected. To switch outputs from *default* to *alternative* a command is sent to the CCU node via the token ring, changing the proper bit in its Command Register. To switch the input, the command must be sent through the same port one wants to activate. Any other command sent to a port which is not active is ignored.

Apart from the control and configuration of front-end chips, the CCUM receives the combined clock and trigger signal (TTC) from the DOH and passes it to the PLL, which distributes it via the LVDS fanout.

### 7.1.5 Silicon Sensor Modules

The fundamental elements of each petal are the silicon modules containing the actual sensors. The modules are mounted ring-wise on the petal, with ring numbers counting from one to seven. The even rings (2, 4 and 6) are mounted away from the intersection point (IP), and the odd rings towards the IP (1, 3, 5 and 7). Table 7.1 lists the number of modules needed for each petal type. Altogether, there are 3,200 modules on 144 petals necessary to build one full Tracker Endcap. Since the whole tracker consists of two endcaps, these numbers must be doubled to get the grand total.

### 7.1.6 Analog Opto Hybrid

Once a *level 1 trigger accept* (L1A) signal is sent via the TTC and the digital optical link to the front-end electronics, the analog data stored in the pipeline of each APV chip must be read out. Analog optical links are used for purpose. They transmit the multiplexed APV output data to the service cavern, where they are digitized and processed by the *front end drivers* (FEDs).

A dedicated *Analog Opto-Hybrid* (AOH) is installed on the ICB for each silicon module. It houses an amplifying laser driver ASIC together with two or three laser diodes. Depending on the number of readout channels (strips) on the silicon module, its associated AOH module needs two (512 strips) or three (768 strips) laser diodes.

The AOH receives the analog signals from the APVMUX chip (see section 6.1.3) and converts them to light. Since the optical output power of semiconductor lasers is zero below a certain threshold, the laser driver adds a programmable bias current to the input related current. The bias current is typically set slightly above the threshold. Additionally, four different gains of the amplifier can be selected via its $I^2C$ interface. Since radiation induced effects increase the threshold of the laser diodes with time, it must be adjusted accordingly.

| module / petal | F-D13 | B-D13 | F-D46 | B-D46 | F-D78 | B-D78 | F-D9 | B-D9 |
|---|---|---|---|---|---|---|---|---|
| R1P | 2 | 1 | 0 | 0 | 0 | 0 | 0 | 0 |
| R1S | 2 | 1 | 0 | 0 | 0 | 0 | 0 | 0 |
| R2P | 2 | 1 | 2 | 1 | 0 | 0 | 0 | 0 |
| R2S | 2 | 1 | 2 | 1 | 0 | 0 | 0 | 0 |
| R3 | 3 | 2 | 3 | 2 | 3 | 2 | 0 | 0 |
| R4 | 4 | 0 | 4 | 0 | 4 | 0 | 4 | 0 |
| R4-A | 0 | 3 | 0 | 3 | 0 | 3 | 0 | 3 |
| R5P | 2 | 3 | 2 | 3 | 2 | 3 | 2 | 3 |
| R5S | 2 | 3 | 2 | 3 | 2 | 3 | 2 | 3 |
| R6 | 4 | 2 | 4 | 2 | 4 | 2 | 4 | 2 |
| R6-A | 0 | 1 | 0 | 1 | 0 | 1 | 0 | 1 |
| R7 | 5 | 5 | 5 | 5 | 5 | 5 | 5 | 5 |
| modules per petal | 28 | 23 | 24 | 21 | 20 | 19 | 17 | 17 |
| multiplicity of petals | 24 | 24 | 24 | 24 | 16 | 16 | 8 | 8 |
| total number of modules | 672 | 552 | 576 | 504 | 320 | 304 | 136 | 136 |

**Table 7.1:** Number of silicon modules per petal. The petal types are listed horizontally. E.g. F-D13 means front petal for the discs one to three. Vertically, the module types are given, separated by the ring. An character P appended the the ring number means *normal* modules, while S means *stereo* (for rings with double-sided modules). Character A means *alignment* and refers to modules which consist of sensors with a hole in the metallization to allow laser light to go through.

## 7.2 Logistics and Petal Production

### 7.2.1 Logistics

Because of its complexity, the petal production had been divided into three steps: manufacturing of the mechanics, AOH integration, and finally module integration [62]. Due to the large number of petals, the work was shared between six institutes.

Aachen-1[3] produced the mechanics of all petals, which included the installation of the cooling pipes and the ICBs on the petal frames. The quality tests performed there consisted of metrology measurements and tightness tests of the cooling loops.

In a next step, the AOH integration took place in Hamburg[4]. Since the routing of the optical cables is a very delicate operation in terms of breaking the fragile fibres, a well trained team carried out this task. After installation of the AOHs and the cables, each fiber transmission line was tested (50 fibres per petal in average).

---

3. I. Physikalisches Institut B, RWTH Aachen.
4. Institut für Experimentalpysik, Universität Hamburg

The final module integration was performed by six institutes, namely Aachen-3[5], Brussels[6], Karls-ruhe[7], Louvain[8], Strasbourg[9] and CERN. The cumulative production of petals at these centers is shown in figure 7.4.
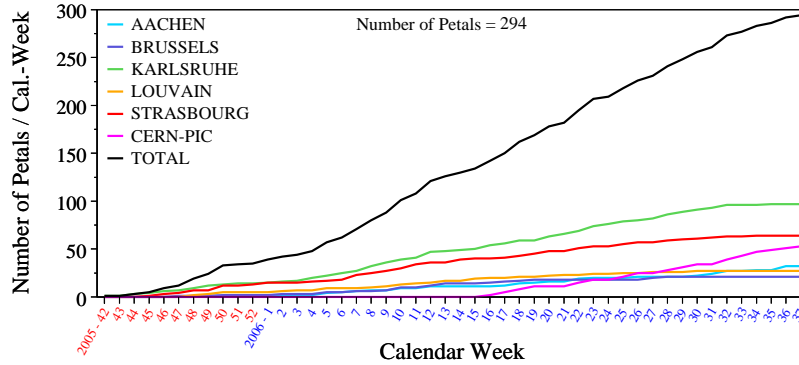


**Figure 7.4:** Cumulative petal production rate per week for each institute involved in the final module inte-gration [63]. In total, 288 petals are installed in the CMS Tracker, while 294 were built in total including spares.

In this operation, the modules are mounted closely to each other and there is a high risk to damage parts of it or to touch the wire bonds on the modules. In some positions, two modules – one *normal* and one *stereo* – were mounted back to back to get 2D position information. During integration, the communication between each module and its associated AOH was checked. This integration test was followed by a deeper test afterwards. A dedicated assembly guidance software was developed due to the large number of spacers and screws of different types to be mounted on a petal. The main purpose was visual help, but the initial test was also included into it. Moreover, all main parts of a petal, like modules, AOHs, CCUs, ICB and petal mechanics were individually entered into TrackerDB by the help of this program.

### 7.2.2  Module Pairing

Each power group of the end cap receives high voltage for the silicon modules from two indepen-dent high voltage channels. Each of the two channels is split into four parallel HV lines at the back board of the PSU. Nevertheless, two or three silicon modules share a single power line. For this reason, the modules were paired together in terms of depletion voltage. To manage this task, an-other software program was used which queries the TrackerDB for the modules depletion voltages. Since different depletion voltages are expected after irradiation for modules with different sensor thicknesses and at different regions of pseudorapidity, pairing is only possible for modules of the same type.

---

5. III. Physikalisches Institut B, RWTH Aachen
6. Vrije Universiteit Brussel
7. Institut für Experimentelle Kernphysik, Universität Karlsruhe
8. Universite Catholique de Louvain-la-Neuve
9. Institut de Recherches Subatomiques de Strasbourg

## 7.2.3 Petal Testing

During petal integration, each component on the petals was tested. Nevertheless, a full test at operation temperature was necessary to prove the stable operation of each petal. For that purpose, a longterm test setup had been developed which was used extensively to grade all petals.

The longterm petal test took place in a light-tight refrigerator, which cooled the petal to its operation temperature of $-10°C$ via an external cooling circuit. Moreover, the petal cooling loops were filled with the coolant liquid and were connected to a chiller. Dry air was blown in to avoid condensation. All modules were powered and read out in parallel by FEDs, while one FEC provided the control signals. The final configuration was used for the AOH–FED link, while the control link was established by a FEC prototype card with electrical input and output and hence without using the DOHs.

Various tests were performed on each petal. During the *opto-scan* the quality of the optical connections was determined by varying the AOH bias and gain settings. The *timetune-test* was used to set correct timing and delay values. Since the cable lengths on the petals are different for individual module types, each module must be set to an optimal delay. After that, a *pedestal-run* was started which measured the common mode noise of each strip of the silicon modules at several HV bias voltages. This test allows a judgment of each strip from its noise figure. Low or high noise in respect to the average strip noise of an APV shows either dead, e.g. not connected strips, or shorts, pinholes or strips with high leakage current. Additionally, a *calibration pulse test* was made to better evaluate the reason of the fault (open, short or pinholes). Moreover, an *IV scan* of all modules on the petal was performed, which was then compared to the results of the same test in the ARC setup during module production (see previous chapter, section 6.4 and figure 7.5).
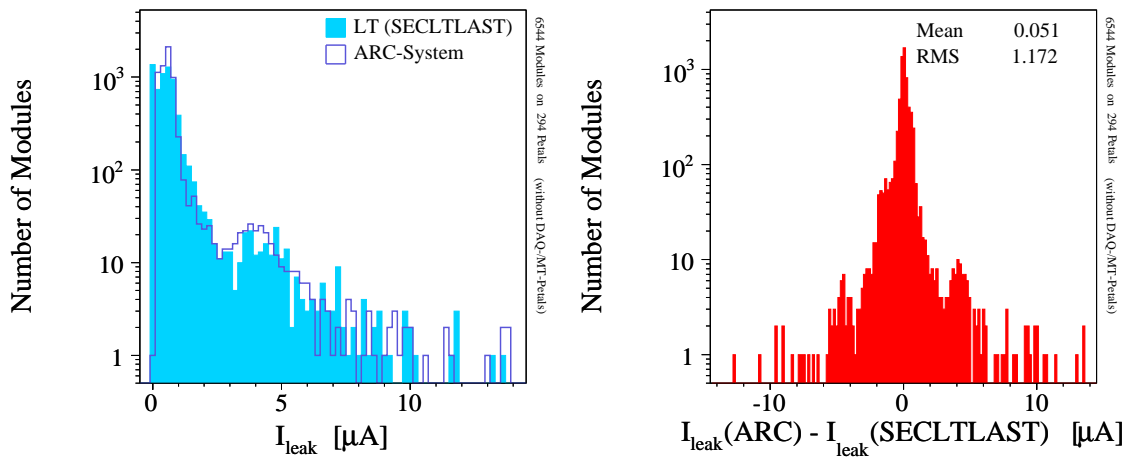


**Figure 7.5:** Comparison of the dark currents of 6,544 silicon modules between measurements taken during module assembly (ARC test) and petal longterm test (SECLTLAST). 99 % of measurements agree within $\pm 5\,\mu A$. Each current value was taken at a bias voltage of 450 V [63].

## 7.3 Petal Integration

After all petals had been built and tested, they were shipped to Aachen-3 and CERN[10] for integration into the TEC support structures, called TEC+ and TEC- for the endcap of the positive and the negative $z$ direction, respectively. Tables B.1 and B.2 in the appendix show the final list of petal object_id's integrated into TEC+ and TEC-.

### 7.3.1 Reception Test

After receiving the petals at these centers, two final tasks had to be performed on each petal: DOHM board and humidity sensor[11] installation. After this step, a final test called *reception test* was performed on all petals. Its purpose was to exclude any damage introduced during shipping and to test the final assembled parts on the petals. During this test, the petals were fully read out at room temperature to test the communication with all front end devices and the integrity of the optical links. The test was not intended to provide an in-depth qualification of the petals, but a fast possibility to prove their functionality [64].

### 7.3.2 Integration

Once the petals had passed the reception test, they were ready for integration into the TEC+ and TEC- support structures. This task can roughly be divided into two steps. First, the installation of the petals on the support structure was performed. Thanks to its construction, the installation of a petal into the TEC support structures requires only very few step: The petal was mounted onto the carbon-fiber discs with three fixations. Once it was mechanically placed, the AOH fibers were connected to the fiber mechanics and the multi-service cables (MSC) – providing HV and LV power and carrying the temperature and humidity readout signals – were connected. Moreover, the cooling loop of the petal was connected to cooling manifolds on the TEC support. Because of the weight and size of a petal, a safe assembly was only possible with the discs in a horizontal position. Figure 7.6 shows the drawing of one disc with the petals installed.

In a second step, all these integration steps had to be verified by subsequent tests of all components. Detailed results and a description of the procedures can be found in [64] for TEC+ and [65] for TEC-.

---

10. Even though the TEC- assembly took place at CERN it was performed and supervised by technicians and physicists from Lyon.
11. The humidity sensors are of type HMX2000 by Hygrometrix.
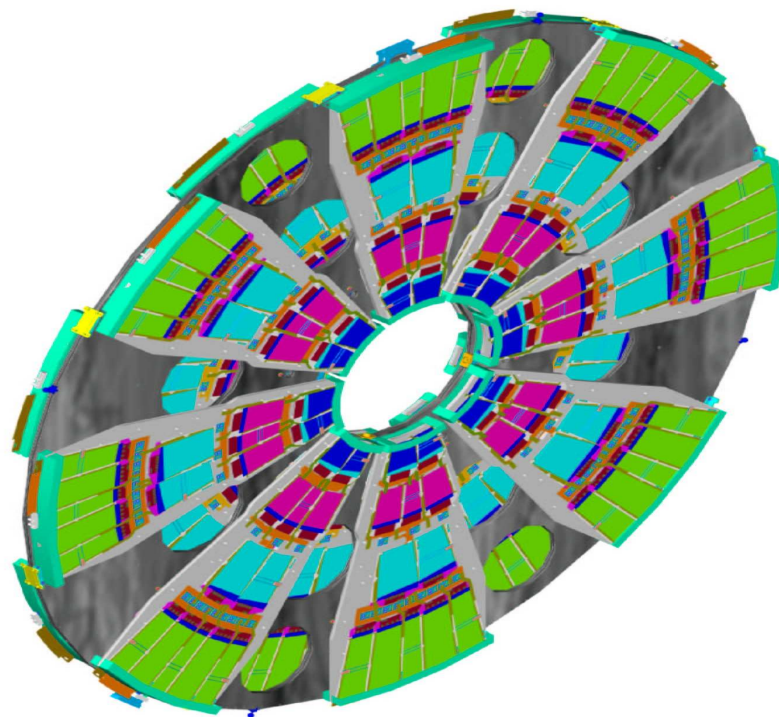
**Figure 7.6:** One disc of the Tracker endcaps. The 8 front petals of type F-D13 are clearly visible, while the back petals B-D13 are hidden behind the support structure (grey).

# 8 Tracker Slice Test

What hasn't been tested doesn't work.

*(Trapnell's Law.)*

After successful integration of all petals into the Endcaps, they both were installed into the *Tracker Support Tube* (TST), in which TIB and TID had been integrated before. The TOB subdetector was assembled directly in the TST since its support structure had been installed in the TST before TOB assembly.

The tracker integration was performed in a dedicated clean room at CERN, the *Tracker Integration Facility* (TIF). A picture of the TIF with TOB, TEC+ and the TST is shown in figure 8.1. After the integration was completed, an extensive testing phase started in November 2007. Its aim was to read out a *slice* of the cylindrical detector, and thus the test was called *slice test*. This chapter presents tools and methods necessary for operation of the Tracker, discusses test procedures and shows results from the slice test.
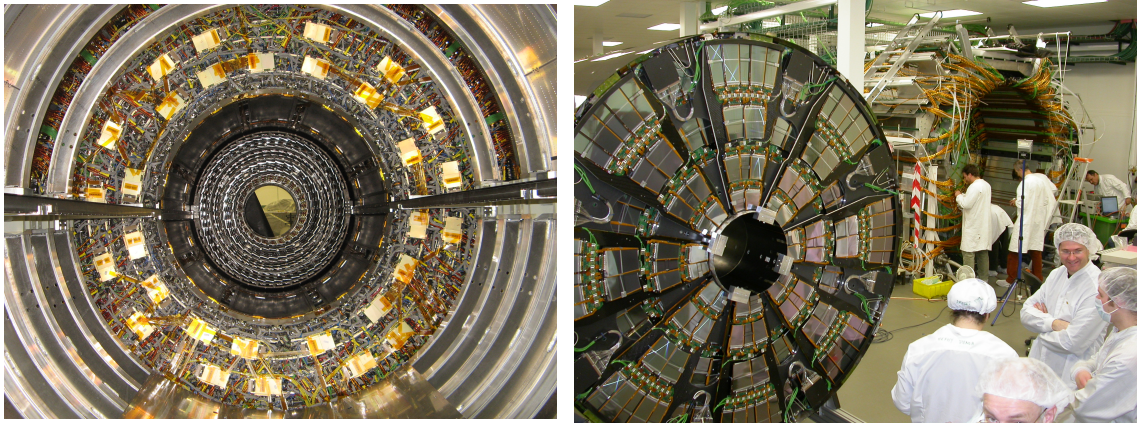


**Figure 8.1: Left:** View into the Tracker Support Tube (TST) showing the TOB and one part of the TIB subdetector (TIB+), prior to TIB- integration.
**Right:** Picture of TEC+ with the petals of disc 1 visible, shortly before its integration into the TST, which can be seen in the background. Both pictures have been taken on 25. January 2007.

First experience of operating the tracker hard- and software had already been gained during summer 2006, when a small fraction of Tracker was operated at room temperature in a comprehensive test called *magnet test and cosmic challenge* (MTCC) together with various other CMS detector parts, like the muon chambers and the superconducting solenoid, which was then ramped up to its nominal magnetic field of 4 T for the first time. At that time, the Tracker setup con-

sisted of only 133 silicon modules, corresponding to less than 1 % of the total electronic channels and an active area of 0.75m$^2$. More than 25 million cosmic muons traversing the detector and the other prototype sub-systems of CMS were recorded using the muon chambers as trigger [66].

## 8.1  Hardware Setup

During March to July 2007 parts of the different sub-systems were connected to power and readout electronics to measure noise behaviour and to collect large samples of cosmic ray data. This was done at five different temperature points. Scintillators on top and below the TST were used as trigger for the cosmics. More than 4.7 million events were recorded and subsequently used to verify the cluster finding and track reconstruction software as well as for alignment exercises.

### 8.1.1  Tracker Geometry

Eventually, 2,168 silicon modules were operated during the slice test. For its readout, 65 FEDs and 8 FECs were used, corresponding to 14.3 % of the final system. Despite the initial goal to test 25 %, the effort was an outstanding success. Table 8.1 shows the total number of active modules split up into the different subdetectors, while figures 8.2 and 8.3 show graphical visualizations for barrel and endcap regions, respectively.

| Subdetector | Number of Modules | Percentage of Final System |
|:---:|:---:|:---:|
| TIB | 444 | 16 % |
| TID | 204 | 25 % |
| TOB | 720 | 14 % |
| TEC | 800 | 13 % |
| total | 2168 | 14.3 % |

**Table 8.1:** Overview of the Tracker sub-systems participating in the slice test.

### 8.1.2  Slow Control

The Tracker has to work at -10°C and in very low relative humidity environment. These conditions as well as low voltages and leakage currents are permanently monitored during data taking by more than 100,000 individual measurement channels by the DCUs on the silicon modules (see section 6.1.3). These data are handled by the *Data Acquisition System* (DAQ), being read out together with the physics data. In addition, approximately 3,000 temperature sensors and around 1,000 sensors for relative humidity are installed inside the tracker volume to provide environmental data independently from the run mode. These channels are read out using dedicated wires in
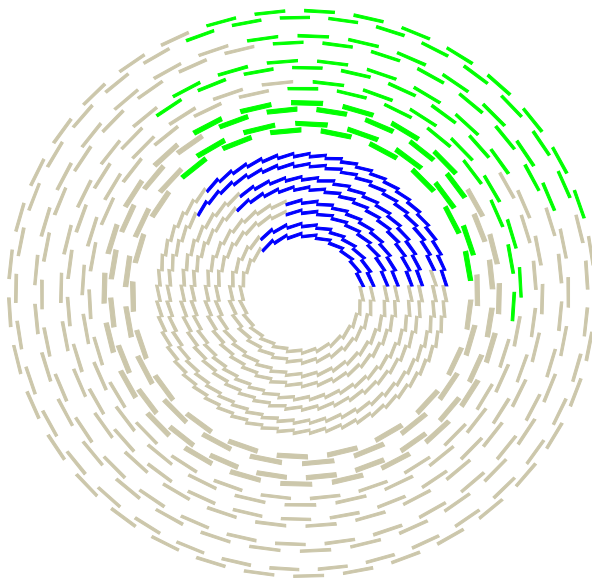
**Figure 8.2:** View of the Tracker Barrel. For the TIB, the strings shown in blue are connected to the electronics and thus participating in the slicetest, while for TOB the active rods are shown in green.
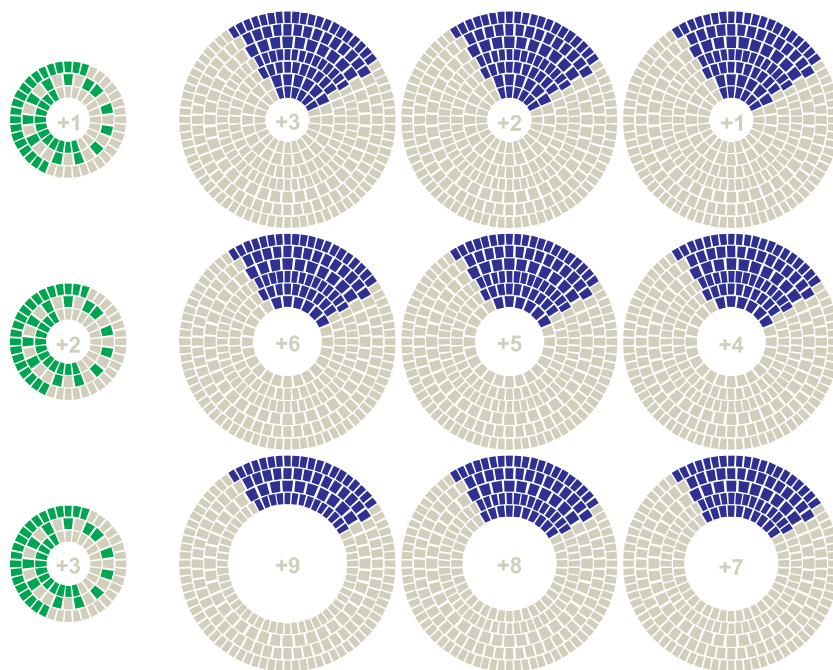


**Figure 8.3:** View of the Tracker Inner Disks (TID; left) and Endcaps (TEC; right) of the positive side ($+z$) involved in the slice test.

the MSC and LIC cables [67], routed via the power supplies directly to the Tracker Safety System.

## Tracker Safety System

The task of the *Tracker Safety System* (TSS) is to keep the detector in a healthy state and to react on technical problems or critical environment conditions which could damage the detector in the worst case. The TSS is made of an interlock system, which is completely separated from the software and hardware used for operations. Its central elements are *Programmable Logic Controllers* (PLC) called *Simatic*[1]. Those units are used to read out the hardwired temperature and humidity sensors. PT1000 probes, thermistors and humidity probes are connected to the PLC via conditioning cards, which transform the measured voltages and currents into PLC-compatible values. The calibration constants are stored in a database and are uploaded into the conditioning cards using dedicated software.

Together with other information like the the radiation levels, temperatures of the cooling fluids, the status of the cavern, the other CMS detector systems and the accelerator, the TSS is designed to switch off all power supplies through an interlock mechanism and bring all components to a safe state in case of an emergency. This is done once certain thresholds are exceeded.

## Tracker Control System

While the TSS is designed to react in emergency situations only, the *Tracker Control System* (TCS) is used for everyday operation. Its main task is to run and control the detector, while it also reacts on certain abnormal conditions before the TSS needs to take action. It communicates with the TSS using Simatic's native protocol S7 to retrieve the environmental data from the hardwired probes. Furthermore, it can communicate with the DAQ system using SOAP[2] messages. This allows access to the data transmitted via the analog optical link from the DCUs to the FEDs. Moreover, the TCS retrieves additional information about the status of the cooling system, the thermal screen, the dry air system and the *Beam Conditions Monitor* (BCM) via S7 links. The TCS uses all this information together with the operation commands from the experiment control to drive the power supplies via OPC[3] commands to the CAEN power supply main frame SY1527.

The interplay of TCS, TSS, the DAQ system with its supervisor RCMS[4], the power supplies and other different subsystems is shown in figure 8.4.

The TCS is implemented as a *finite state machine* (FSM). This means that there is a finite number of well defined states, transitions between those states, and actions. Depending on the hardware

---

1. *Simatic* is a PLC series and trademark of Siemens.
2. The *Simple Object Access Protocol* (SOAP) is used to exchange status informations between different systems using Web Services.
3. *Object-Linking and Embedding for Process Control* (OPC), is an open standard for real-time data exchange between control devices from different manufacturers.
4. The *Run Control and Monitoring System* is the top level experiment control system of CMS.
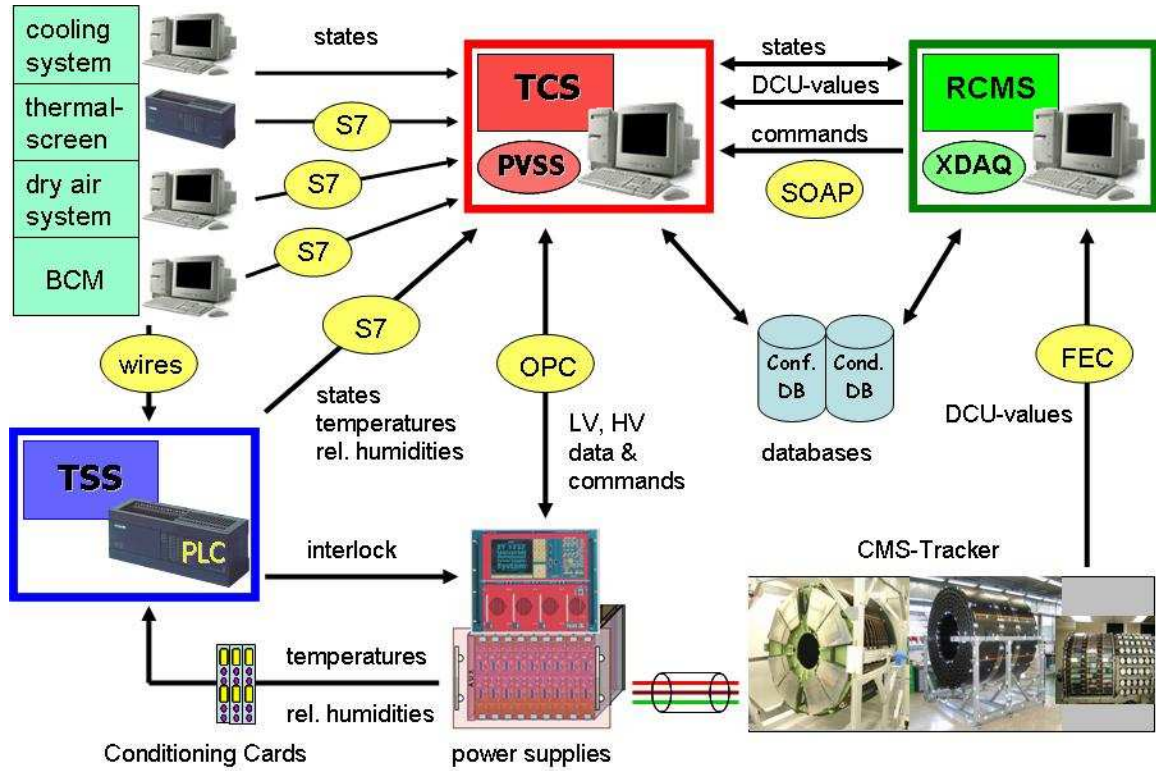
**Figure 8.4:** Schematics and data flow of the Tracker Control and Safety Systems. An explanation of all abbreviations is given in the main text.

status, specific actions are taken. The actions are mostly signals to the power supplies. The main states can be either *OFF*, *ON_CTRL*, *ON_LV* and *ON* (LV and HV on). In the first step of powering the detector, the state is switched from OFF to ON_CTRL, which means that during the transition phase the control power supplies are switched on via OPC communication. In this first step, the DOHMs and CCUMs are powered and communication between FECs and CCUs is established. Once this state has been reached, the next transition powers all low voltages, i.e. all APV chips, leading to the ON_LV state. After that, the command *ON* can be issued which triggers the ramp-up of all HV channels. Feedback signals are sent back to the TCS via OPC, reporting success or failure of each operation. In addition to the four main states mentioned above, there are also some temporary states like HVRAMPING during ramp up and down of the high voltage channels and error states like HV_ON_LV_OFF or LV_ON_CTRL_OFF, which cannot be chosen manually from the operator panel but reached in case of errors.

During the slice test, 380 LV channels, 780 HV channels and 70 control voltage channels were operated, while the full setup when the Tracker will be operated in the CMS experiment will consist of 1944 LV, 3888 HV and 356 control voltage channels [68].

The FSM is implemented using a professional SCADA[5] software (*PVSS II* Version 3.6 by ETM[6]) which also provides front panels for user interactions. PVSS was chosen by CERN as a common

---

5. SCADA is an acronym for *Supervisory Control And Data Acquisition* and refers to a large-scale, distributed measurement and control system
6. ETM was founded in 1985 as an Austrian company and is now a Siemens subsidiary.

LHC framework and was extended to meet the project's needs. It includes an internal database to store values like voltages and currents from the power supplies and temperatures and humidities locally. In order to have information available later for offline use, data is archived to an Oracle database called *ORCON* (Off line ReConstruction ONline subset). Each value is updated once it changes more than 2% of its value. This allows an efficient way of compressed data storage, avoiding excessive database traffic with redundant data at every time stamp.

### 8.1.3  Data Acquisition System

The subsystem used to gather the signals from the FE electronics and process these data online is called *Data Acquisition System* (DAQ). It can roughly be divided into two parts, a hardware and software related part. The former is discussed below, while the software part will be described in section 8.2.

The DAQ hardware consists of VME crates containing FED and FEC boards used to communicate with the front end electronics via optical fibers. When the global trigger and DAQ systems will be used in the future final setup, the FEDs forward their data packets to the CMS *event builder* (EVB) and online computing farm via *S-link* connections [69]. For stand-alone operation of the tracker during the slice test, data is read out via the VME backplane to local PCs.

The main task of the DAQ system is handling and processing *event data*. These data are read out from the APV chips upon reception of a trigger signal (L1A), and subsequently processed in the FED boards and in the computing farm. However, there is another data stream coming out of the DAQ system with a much lower rate than the event data. This additional stream is called *non-event data*. It contains mostly slow control information such as temperatures, FE voltages and HV currents read out by the DCU chip. These data are also stored in the ORCON database.

Using the DAQ slow control data queried from the ORCON database, figures 8.5 and 8.6 show the distributions of low voltages and temperatures, respectively, as measured by the front-end DCUs during the slice test.

### 8.1.4  Cosmic Trigger

The CMS trigger system [70] distributes trigger and clock signals from the *Global Trigger Controller* (GTC) to the various sub-detector control and readout components via the TTC system [61]. In addition, the *Local Trigger Controller* (LTC) can be used to operate a sub-detector individually in a stand-alone data-taking mode for debugging and commissioning purposes. In that case, trigger signals have to be generated locally. As the aim of the slice test was taking cosmic muon data, the trigger signals for the LTC were generated by a set of scintillators.
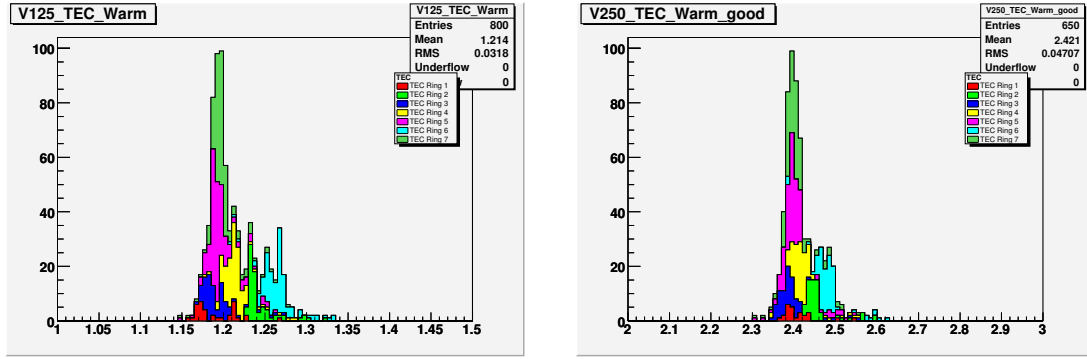
**Figure 8.5:** Histograms showing the actual low voltages of the 1.25 V (left) and 2.5 V (right) lines arriving at the hybrids of the 800 TEC modules participating in the slice test. Each color represents a particular module ring [68].
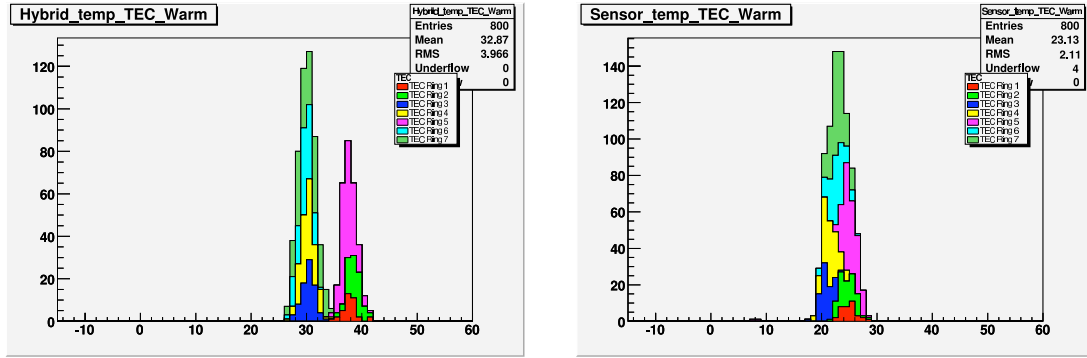


**Figure 8.6:** Histograms showing the temperatures of the FE hybrid (left) and the silicon sensors (right) for the modules of different rings, each represented by a different color. The two distinct peaks in the left figure are caused by the different thermal power of hybrids with four or six readout chips, respectively. These temperatures were measured in a "warm" condition with a cooling liquid temperature of $15°$C [68].

Six scintillators, called *A* to *F*, each equipped with a photomultiplier, were placed onto the scaffolding above the Tracker. Their positions are shown in figure 8.7. Another scintillator called *G* was located below the tracker, resting on a moveable carriage. Three dedicated positions were used during the slice test (see figure 8.8). The signals from all counters were transmitted to a NIM[7] crate where they were logically combined. First, the top counters *A* to *F* were combined using a logical OR (symbol $\cup$) operation. The OR output and the signal from the bottom counter *G* was used as input of a coincidence unit to build the logical AND (symbol $\cap$). The signal from scintillator *G* was delayed by 23 ns before fed into the coincidence unit to take the flight time of the muons and the delay of the OR unit into account. The resulting signal *TRG* is represented

---

7. The Nuclear Instrumentation Module (NIM) standard defines mechanical and electrical specifications for pluggable electronics modules used in experimental particle and nuclear physics.
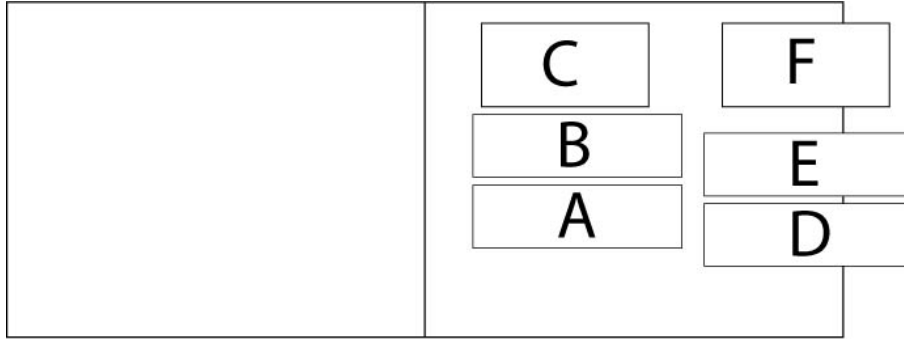
**Figure 8.7:** Position of the six scintillators above the positive side of the Tracker (bird's view). The central vertical line represents the center of the Tracker at $z = 0$.

by

$$TRG = (A \cup B \cup C \cup D \cup E \cup F) \cap G \tag{8.1}$$

and reached an average rate of 5 Hz, while the frequency of each individual top counter was approximately 90 Hz and the larger bottom counter fired at approximately 230 Hz.

Scintillator $G$ was covered by a 5 cm thick plate of lead to achieve a momentum cut for the cosmic muons. The lead plate absorbs muons with an energy below 200 MeV such that those do not generate trigger signals. Low momentum muons had to be excluded because of their excessive high multiple scattering, which would spoil track reconstruction and alignment algorithms.

By using the scintillators as trigger, the Tracker was used to record tracks of cosmic muons through it. This allowed to generate a hit map of the scintillators by extrapolating the track to the plane of the top or the bottom scintillators, which is shown in figure 8.9. One can clearly see that only scintillators $A$, $B$ and $C$ were powered on the top (black) and scintillator $G$ (red) on the bottom. The bar-shaped agglomeration of points on the right side of the bottom scintillator shows nicely the shape of the photomultiplier which was used for its readout.

## 8.2 Software Setup

### 8.2.1 Conventions

The CMS software code uses the following conventions: Energy in is measured in units of GeV, thus momentum and mass are given in GeV/c and GeV/c$^2$, respectively. Distance and positions are in centimeters (cm), while time is denoted in nanoseconds (ns). The magnetic field in measured in Tesla (T) and the orientation of the coordinate system is such that the solenoidal B field is along the z axis. The electric charge q in measured in units of the elementary charge $|e|$.
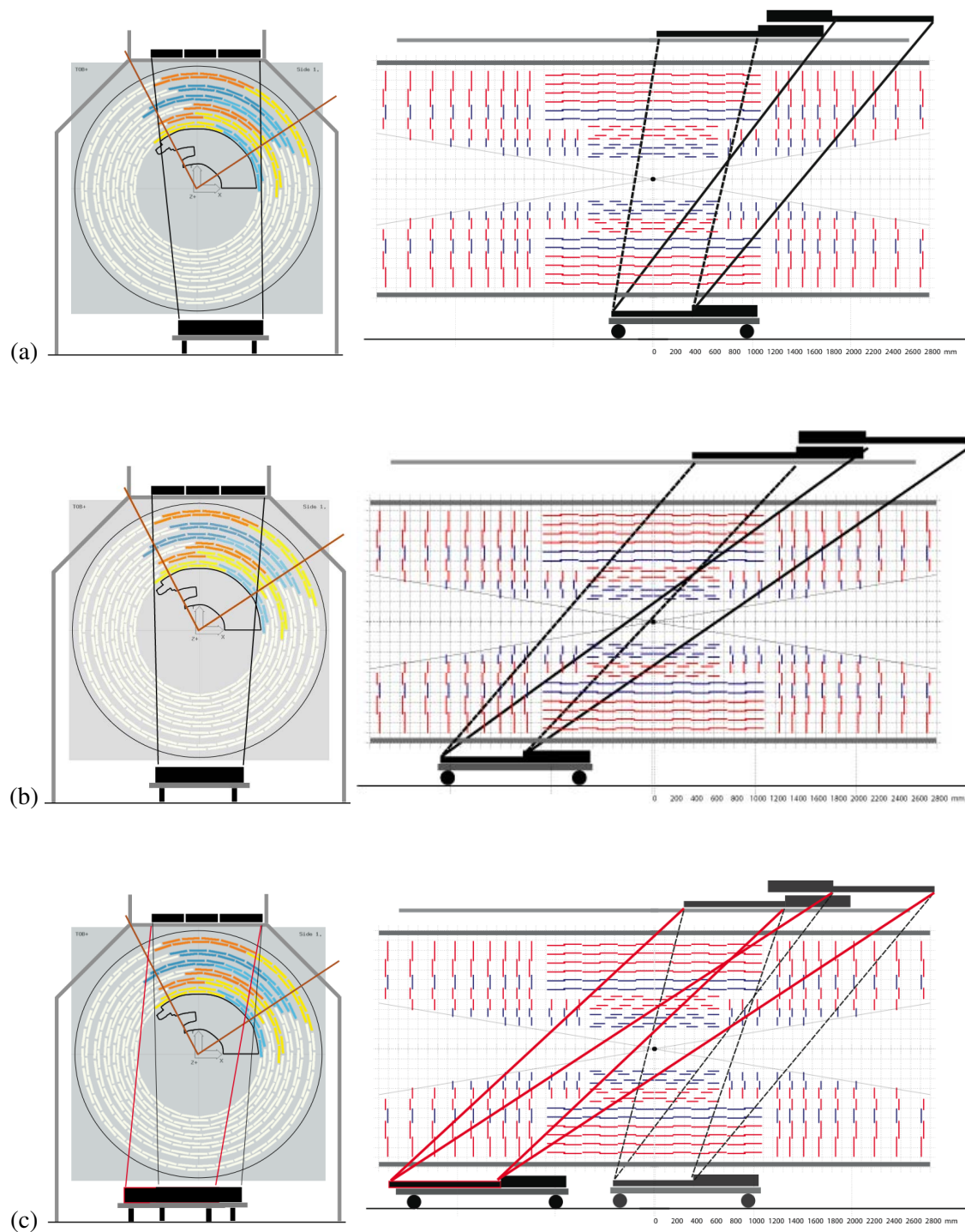
**Figure 8.8:** Layout of the trigger scintillator positions used during the slice test. The left and right views show *xy* and *rz* cross-sections, respectively. The straight lines connecting the active areas of the top and bottom scintillators indicate the acceptance regions in which possible muon tracks could be recorded.
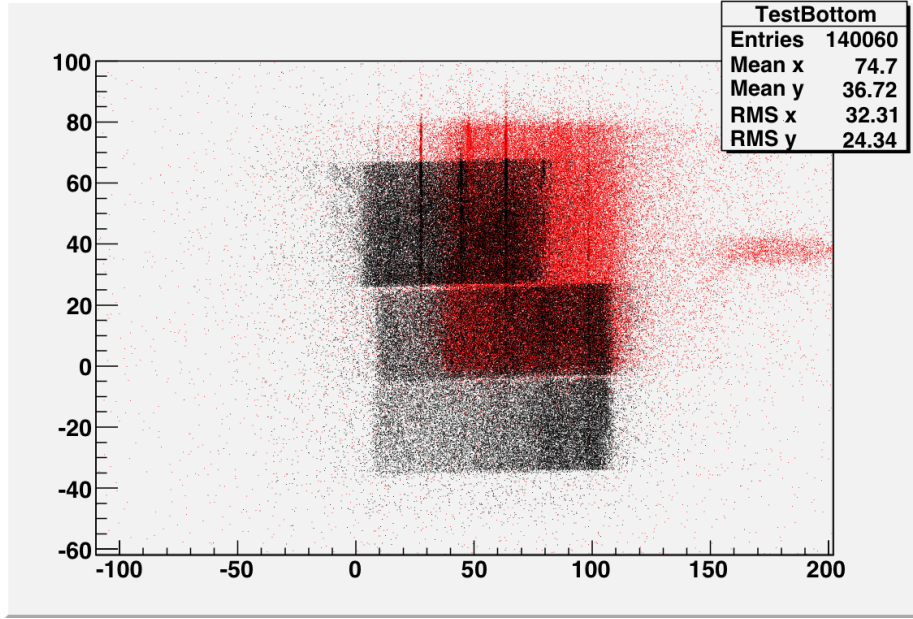
**Figure 8.9:** Hit map of the scintillators above (black) and below (red) the Tracker (run 6215) [71].

The coordinate system adopted by CMS has the origin centered at the nominal collision point in the center of the experiment, the *y*-axis pointing vertically upward, and the *x*-axis pointing radially inward towards the center of the LHC ring (south). Thus, the *z*-axis points along the beam direction towards the Jura mountains pointing west of LHC Point 5.

Angles are measured in radians, with $\theta$ being the polar angle between $0 \leq \theta \leq \pi$. The positive *z* axis is represented by $\theta = 0$, while for the negative *z* axis $\theta = \pi$. Usually, the polar angle is given as pseudorapidity $\eta$ with

$$\eta = -\ln\tan\frac{\theta}{2} \qquad . \tag{8.2}$$

This means that $\eta = 0$ is +y axis (upwards), while $\eta = +\infty$ coincidences with the positive *z* direction. The azimuthal angle $\phi$ is measured in the $x/y$ plane and is defined as

$$\phi = \arctan\frac{y}{x} \tag{8.3}$$

It is in the range of $-\pi < \phi \leq +\pi$, with $\phi = 0$ corresponds to the +*x* axis and $\phi = \pi/2$ identical with the positive *y* axis.

## 8.2.2 Software Frameworks

Many services required by the DAQ software are provided by the two official software frameworks developed for the CMS experiment, called XDAQ and CMSSW.

**XDAQ**

XDAQ [72] is the online software framework for the CMS DAQ system and provides a set of services and tools, including a fast communication protocol for peer-to-peer messaging between processes registered within the framework; a slower communication protocol for configuring processes; a finite-state machine; event builder applications and memory management tools [73]. XDAQ processes control the trigger system, maintain hardware configurations by uploading configuration parameters to the front end electronics, and are used for event building and data analysis. The finite state components allow to automatically run sequences and acquisition loops.

**CMSSW**

The *CMS Software Framework* (CMSSW) is the offline software package used for event reconstruction, High-Level Trigger (HLT), calibration, monitoring and physics analysis. It incorporates the CMS *Event Data Model* (EDM) scheme [9], which is centered around single *events*. An event object contains all data that was taken during a triggered physics event as well as all data derived from the measured data. Additional information needed to process an event is accessed via the *EventSetup*. Events are processed by passing the object data through a sequence of software modules. This allows independent development and verification of distinct elements of the reconstruction and analysis chain. Each module is configurable by *ParameterSets* defined in a configuration file together with the list and order of modules to be executed. This is done using the CMS framework executable *cmsRun* with the configuration file as argument.

**Interplay with Hardware**

During the slice test, all DAQ processes were hosted on local computing resources, more precisely PCs which were connected to the VME crates housing the off-detector electronics (FEDs, FECs, trigger cards, etc). The raw data from the FEDs were accessed via the VME backplane and event fragments were built at the level of single VME crates. Standard tools of the XDAQ framework were then used to build complete events from these fragments.

Event building was distributed across several crate PCs to allow parallel event processing. The software was replicated for each PC connected to a FED crate and comprisd the following XDAQ applications:

- One *FED supervisor* per FED (this means up to 16 per VME crate) that controls and configures the FEDs and handles the data capture and readout.

- One Fragment builder per VME crate, which receives the data from each FED supervisor and builds the event fragments

- Each crate PC also hosts additional applications (Readout Unit, Builder Unit and Filter Unit), which are used to build complete events from the fragments.

- One database client application per PC to access the configuration database.

Each PC connected to a FEC crate (a crate housing FEC cards) comprises

- One *FEC supervisor* per FEC (typically 11 per VME crate) used to control all front-end devices via the FEC and the digital optical link.

- One database client application per PC for the same purpose as described above.

Special PCs connected to the trigger crate via VME hosted applications used to control the trigger when operating in stand-alone mode. These applications were the *LTC supervisor* and the *TTC supervisor* to define and control trigger patterns. One *event builder manager* was used to handle trigger tokens from the LTC supervisor and control the event building. On top of all applications, one *tracker supervisor* application communicated with all other processes and steered the data acquisition. The whole setup is shown in figure 8.10.
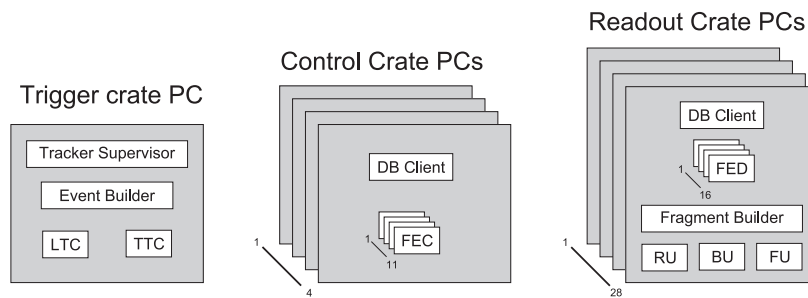


**Figure 8.10:** Scheme of the Tracker data acquisition software. The grey boxes represent the PCs, each connected to a VME crate, while the white boxes symbolize the software processes running onto these PCs.

### 8.2.3  Data Formats

The FEDs receive analog data from the front-end electronics, which is digitized, processed, and formatted before being forwarded to the global DAQ or processing in local computing resources takes place. The FEDs can operate in one of four readout modes as described below:

**Zero-Suppressed:** This is the default mode for proton-proton collisions. The raw detector data is processed on the FEDs using firmware algorithms implemented within FPGA devices, so that only useful signal information is transmitted upstream to the computing farm. The algorithms have to perform data reordering and pedestal and common-mode subtraction before cluster finding (see below) takes place.

**Processed Raw:** The data are pedestal-subtracted and reordered to reflect the detector strip order (this is not the case for the raw APV25 data streams). However, the data are not zero-suppressed. This mode is foreseen for heavy-ion collisions where high occupancies are expected which might exceed the capabilities of the FED firmware.

**Virgin Raw:** In this mode, the FED performs no processing and only formats the raw detector data. This mode is intended for use during detector commissioning and also facilitates debugging. Almost all data during the slice test was taken using this configuration.

**Scope mode:** In this mode, the FEDs simply capture the APV data streams observed within a given time window (of configurable size). This mode can again be used during detector commissioning and is useful for system debugging.

### 8.2.4 Commissioning Procedures

Commissioning procedures are required to bring the detector into an operational state suitable for physics data-taking [74]. They consist of several dedicated runs to configure, calibrate and synchronize the different parts of the readout systems with the detector. All data belonging to commissioning runs are stored in the online configuration database. During the slice test, these special runs were often performed to debug off-detector hardware, software, the detector itself and its connections. During the operational phase, the procedures will be performed between periods of physics data-taking, e.g. during LHC beam fill, in order to guarantee optimal detector performance. Usually, the commissioning runs have to be performed in a well-defined order, in which they are described below. When starting up from scratch, e.g. after a power cut, all steps have to be performed. Subsequently, only higher level runs have to be performed, but the given order must always be observed to get conclusive results.

The first step in establishing the data-taking mode from scratch is creating a new *partition* within the XDAQ framework, which hosts all calibration data for a given configuration. A partition could be e.g. when the TEC sub-detector is running alone with local trigger for debugging purposes.

#### Crate Scan

The *FEC crate scan* is started first to establish communication of the VME-PCs with the FECs housed in VME crates. The *FED crate scan* performed afterwards works in close connection with *TrimDAQ*, an application used to determine the pedestal levels of the FED channels, creating an initial FED configuration. All front end devices must be off for this run.

#### Connection Scan

The connection scan establishes connection between front-end and off-detector electronics and thus needs the TCS in the state *ON_LV*, to have the FE electronics powered. The AOHs are switched on by biasing each laser individually in sequential order. A trigger signal is sent for every laser driver and by reading out all FEDs in parallel, the FED input channel observing "light" from the currently active laser can be found. Thus, the result of this scan is a mapping of AOH lasers to FED input channels. This run also helps debugging weak or faulty optical connections by simply measuring the amount of light received in the FED.

**Timing Run**

Due to different cable and fiber lengths, trigger signals would not arrive synchronously at all APVs and its data would not sampled by the FEDs synchronously. For this run, the FEDs are operated in scope mode and are forced to capture the APV tick marks. In a loop, the delay parameter of the PLL chip is set in steps of 1.04 ns ($25/24$) until all tick marks are lined up at the FEDs. The delay parameter for each channel is then stored in the configuration DB.

**Gain Scan**

In this procedure, the optimum working points of the AOHs is determined. Each AOH is equipped with two or three laser diodes and a single laser driver ASIC. The laser driver provides a bias current for the lasers which is typically chosen slightly above the laser threshold. A current proportional to the input voltage is added to the bias current. The optical gain of the whole readout chain is defined to be 1 when the input voltage of the laser driver is the same as the output voltage of the photo receiver in the FED. The gain is therefore given with as $V_{out}/V_{in}$. During the slice test, a gain of 0.8 $V_{out}/V_{in}$, corresponding to a tick mark amplitude of 640 ADC counts, was used.

The optical gain of the lasers can be selected from four discrete values which are chosen together with the bias current such that both the base line and the maximum of the tick marks of the APV output frame reside well within the linear (non-saturating) range of the optical chain end at the ADC. Figure 8.11 (left) shows the distribution of achieved gains for TEC-, separated for each of the four discrete gain settings. As it is evident from the gain distribution with the second curve
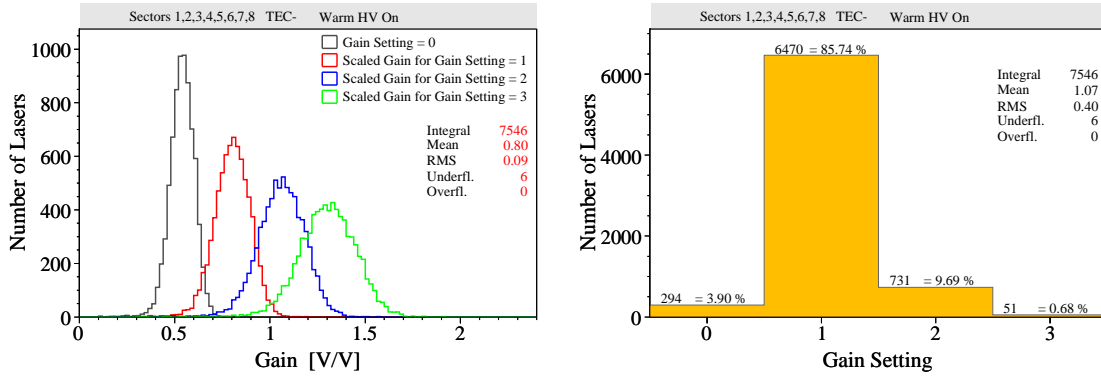


**Figure 8.11: Left:** Distribution of the actual AOH gains for different gain settings in TEC- during integration [63].
**Right:** Gain setting for these laser drivers to achieve an optical gain as close to 0.8 as possible.

peaking around 0.8, gain setting 1 fits best for most channels. Only a small fraction of channels, which reside in the tails of the distributions, require a different setting. During the gain scan run, each AOH laser driver is scanned for all four gain settings, and the optimum setting is recorded. Figure 8.11 (right) shows the distribution of those optimum settings for the TEC- sub-detector. Since the laser light emission degrades with irradiation, the gain and bias current settings will

need to be adjusted accordingly. Moreover, the gain is temperature dependent. Typically, a second timing run is performed with the new gain settings after the gain scan has been completed successfully.

### VPSP Scan

The VPSP register of the APV can be used to adjust the analog base line level between the two digital signal levels, representing the minimal value at logic level 0 and maximum at logic level 1. In this run, the DAQ measures the baseline level for the different values of the VPSP register and selects a VPSP value which places the analog baseline to approximately $1/4$ of the APVs output range.

### Pedestal Run

The result of the *Pedestal Run* is information about noise and pedestal level of each single strip. During the run, triggers are sent to the modules and FEDs are switched to Virgin Raw data mode (see section 8.2.3). All analog frames from the modules are acquired and for each channel both the average value and the RMS noise are computed, together with common mode correction.

After the run is finished, the data are stored in the online database and will be uploaded into the FEDs so that they can perform pedestal subtraction themselves when running in zero-suppression mode. Even if data is later recorded in virgin raw mode, the pedestal data stored in the DB can be subtracted by a software module.

### Calibration Run

Pulses injected via the APV's internal calibration circuit can be used to test their pre-amplifier input stage and subsequently the whole readout chain. Since these pulses generate signals on the APV inputs similarly to real particles traversing the silicon detector, the run comes very close to the real data taking and is thus the last test in the commissioning chain. It requires all other commissioning runs successfully passed and also relies on pre-recorded pedestal and noise data.

The amount of charge to be injected can be selected by changing the ICAL register of the APV via $I^2C$ commands. The delay between charge injection and readout can be shifted by adjusting two more APV registers (CDRV and CSEL). In a calibration run that delay parameters are scanned, while the APV output is recorded by the FEDs operated in Scope Mode. Thus, the whole time response of APVs to a charge pulse can be reconstructed (figure 6.8 was obtained this way). Similar to all other runs of the commissioning procedure, the results of the calibration run are stored in the databases for future reference.

### 8.2.5  Raw Data Treatment

After the analog data have been received by the FEDs, they are converted into digital numbers by analog-to-digital converters. Then, the fist processing task – performed by FPGA chips located on the FED boards – is data re-ordering such that the data stream reflects the physical channel numbers of the APVs according to equation 6.1 and corresponds to the sensor strip numbering.

Then, the systematic pedestal value of each strip, which was determined before during a *pedestal run*, is subtracted from the signals and the common mode noise of each APV is being calculated and subtracted from the signals in a 2-pass procedure [15].

#### Cluster Finding

Cluster Finding takes place in the FEDs (when running in zero-suppression mode) or within a CMSSW software module and is called *clusterization*. Its purpose is to find a set of adjacent strips with a signal above noise $\sigma$. Clusters are reconstructed by searching for a seed strip with a signal to noise ratio *SNR* above a certain threshold, e.g. $\mathrm{Th}_{\mathrm{seed}} > 3\,\sigma$. Neighboring strips are included in the cluster if they satisfy another threshold, e.g. $\mathrm{Th}_{\mathrm{neigh}} > 2\,\sigma$ (see figure 8.12). The total signal size of the cluster must exceed a third threshold, e.g. $\mathrm{Th}_{\mathrm{cluster}} > 5\sigma$. This method is usually referred to as *3-Threshold algorithm*.
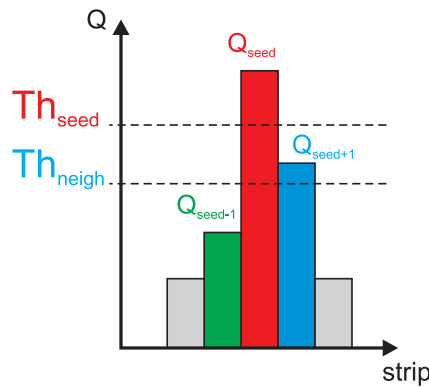


**Figure 8.12:** Description of a cluster. This diagram shows the charge $Q$ stored for a single event and a range of consecutive strips ($x$-axis). The seed strip (red) is surrounded by a neighbor, whose charge exceed the corresponding threshold.

The cluster position is usually determined from the centroid (a.k.a. barycenter) of the signal heights by a center-of-gravity (COG) assumption [75]. It can be determined by

$$x_{\mathrm{COG}} = \frac{\sum Q_i\, x_i}{\sum Q_i} \tag{8.4}$$

where $x_i$ is the position of the *i*th strip included in the cluster and $Q_i$ the signal on that strip. The sums are over all the strips included in the cluster. For a cluster consisting of only two strips $x_L$ and $X_R$ and for small local track angles, the previous equation becomes to

$$x_{2\text{strips}} = x_L + \frac{Q_R}{Q_L + Q_R} p \tag{8.5}$$

A diagram of a signal cluster with charge shared almost equally by two strips and thus a cluster center inbetween those two strips is shown in figure 8.13.
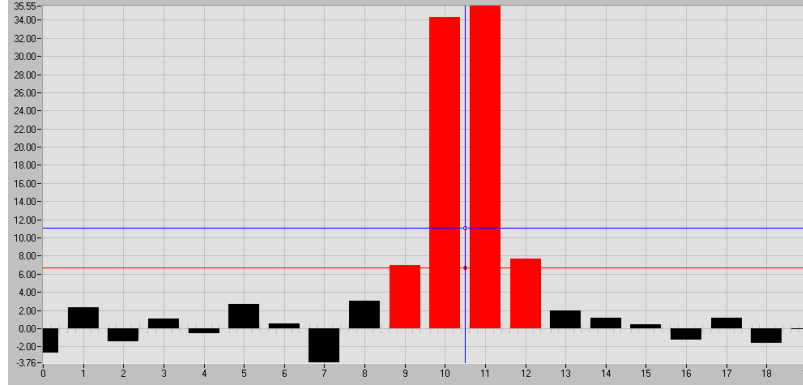


**Figure 8.13:** Diagram showing the strip signal expressed as ADC counts (y-axis) versus adjacent strips [76]. The horizontal blue and red lines represent the cuts for the seed ($5\sigma$) and neighboring ($3\sigma$) strip, respectively. The vertical blue line represents the weighted cluster position, calculated according to equation 8.4.

The reconstruction chain starts with the raw data. Zero-suppressed data are called *Digi*. These data are used for the cluster finding algorithm (CMSSW module *SiStripClusterizer*). Finally, the module *SiStripRecHitConverter* creates *RecHits*, which are space points determined by the cluster position, its amplitude and the centroid of the signal. The position resolution is parameterized as a quadratic function of the projected track width on the sensor in the plane perpendicular to the strips. Deviations from the ideal geometry (called *misalignment*) are taken into account by adding an *Alignment Position Error* (APE), i.e. an additional uncertainty on the module positions, to the hit errors. The size of the APEs was estimated from survey data [77]. The data flow is visualized here:

$$\text{RawData} \Longrightarrow \text{Digi} \Longrightarrow \text{Cluster} \Longrightarrow \text{RecHits} \ (\Longrightarrow \textit{Tracks})$$

## 8.2.6 Track Reconstruction

As its name indicates, the main purpose of the CMS Tracker is to record tracks of charged particles being created during proton-proton collisions of the LHC. In an uniform solenoidal magnetic field, charged particles are bent in $xy$ ($r\phi$)-view but not in $z$-view (see figure 8.14). In that case, the particles' transverse momenta can be determined from their bending radii (see equation 2.3). During the slice test, no magnetic field was present. Thus, the cosmic muons recorded during this test traversed the tracker on straight paths.

There are three algorithms available to reconstruct cosmic muon tracks:
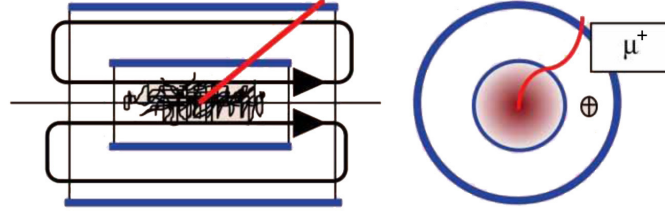
**Figure 8.14:** Track of a charged particle in CMS. In *z*-view (left), its path is not bent by the solenoidal magnetic field. In *xy* ($r\phi$)-view (right) the particle (a positive muon $\mu^+$) describes a curvature to one side inside the coil and to the other side outside the coil, where the return flux affects the particle. The Tracker is located inside the coil of the magnet.

- Cosmic Track Finder
- Combinatorial Track Finder (CTF)
- Road Search Algorithm (RS)

All three algorithms successfully reconstruct cosmic muon tracks, and its up to the user to decide which algorithm suits the needs best. For proton-proton collisions, the standard algorithms will be CTF and RS, since the Cosmic Track Finder is a specialized algorithm for the reconstruction of single-track cosmic events. The differences between the two standard methods are visualized in figure 8.15.
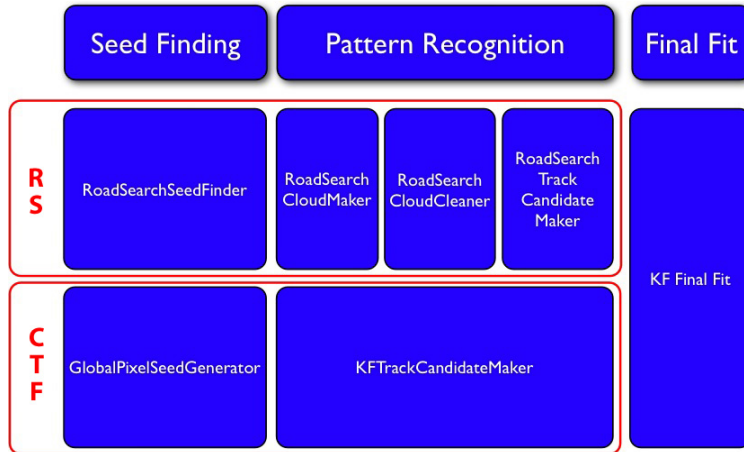


**Figure 8.15:** Differences of the two track reconstruction algorithms *Road Search* (RS) and *Combinatorial Track Finder* (CTF) for the three stages of the track reconstruction [78].

The reconstruction of charged tracks is done in three stages [79]. The principle reconstruction chain is visualized here:

$$(recHits \Longrightarrow) \text{ SeedGenerator} \Longrightarrow \text{Pattern Recognition} \Longrightarrow \text{Final Fit}$$

First, the *SeedGenerator* provides seeds for further reconstruction, based on pairs of hits which are compatible with the geometry and which comply with a lower cut in the transverse momentum,

taking multiple scattering into account. For proton-proton-collistions, the pixel detector will provide the best seeding because of its fast and efficient pixel selection, its low occupancy and the real 2D position information. Without the pixel detector, the seeds are searched in the inner layers of the TIB sub-detector. For cosmic data taking during the slice test, the SeedGenerator had to accept seeds in the TOB as well.

The second stage (Pattern Recognition) uses a first estimate of the track parameters, calculated from the seed, to collect the full set of hits for a charged particle track. It is based on a set of pre-calculated paths for RS and on a combinatorial Kalman filter approach [80] for the CTF. There, the trajectory is extrapolated with the current parameters to the next layer and compatible hits based on the $\chi^2$ between the predicted and measured positions are selected. The Kalman update of the predicted parameters with each of these hits provides a new set of trajectory candidates.

In the third stage a least-square fit is performed in the form of a Kalman filter for the final estimation of the track parameters. It consists of two fits of opposite direction. A "forward" fit going outwards from the interaction point minimizes the approximations used in the second stage. The "backward" fit maintains the track parameters in the inner region. The combination of both results in the final track [79].

## 8.2.7 Data Quality Monitoring

The online *Data Quality Monitoring* (DQM) system is designed to ensure that data of good quality is recorded and detector problems are spotted very early and efficiently [81]. It is based on a common CMS framework for online data monitoring [82] and consists of three parts: *Producer* (DQM Source), *Collector* and *Consumer* (DQM Client). The histograms or *Monitoring Elements* (MEs) are defined and filled with relevant event information by the Producer. The MEs for the Tracker can be subdivided according to the tasks at different levels (commissioning, zero-suppression, digi, reconstructed hits, tracking....) and also according to the geometrical structure of the Tracker (whole tracker, TIB, TOB, TEC, TID, layer, disc, rod, string, detector module).

The MEs are fetched by the Collector, which performs further analysis on them and creates summary MEs. Those are compared to reference histograms and the Collector generates alarms in case of discrepancies. The summary plots are extremely important as it is impossible to check each of the huge set of MEs in the Tracker. Cuts are applied on both the elementary and the summary MEs and alarms (*Ok*, *Warning*, *Error*) are generated.

The DQM Client, which is based on XDAQ, acts as a web server. A web browser is sufficient to connect to the client in order to access the MEs, view histograms and alarm states. Different views for shifters and different expert levels are available which provide sets of predefined MEs to check the overall performance of the detector and debug problems quickly and easily.

## 8.3 Cosmic Data Taking

During integration and commissioning of the Tracker, stable operating conditions were only achievable during weekends. It was chosen to bring all systems to run conditions each Friday noon at latest and to record cosmic data from Friday, 4pm to Monday, 8am. During those weekends, about 5 million cosmic muons were recorded. This section documents the results obtained from the slice test for the major run periods as defined largely by the chiller coolant temperature and the position of the scintillator trigger. The chiller temperature ranged from room temperature down to $-15°C$ and the scintillators were arranged in three positions, called *A* to *C* (see fig. 8.8). Table 8.2 shows the run numbers for the various environmental conditions.

| scintillator position | temperature [°C] | run number |
|:---:|:---:|:---:|
| A | +15°C | 7277 – 7296 |
| B | +15°C | 7635 – 8055 |
| C | +15°C | 9255 – 9341 |
|   | +10°C | 10145 – 10684 |
|   | -0.5°C | 10848 – 11274 |
|   | -10°C | 11316 – 11915 |
|   | -15°C | 12045 – 12585 |
|   | +14°C | 12599 – 12656 |

**Table 8.2:** TIF run numbers in the configuration TIB+TOB+TEC, listed for the three different scintillator positions and for several temperatures.

The high voltage channels of the silicon sensors were set to a bias voltage of 290 V for TIB and TID, while TEC always had 250 V; TOB HV had been at 250 V before run 9200 and was at 300 V later.

The APV parameters were taken from laboratory studies [83] at each hybrid temperature and for the silicon geometries of the TIB and TOB. For the TID and the TEC, the APV parameters had not been optimized for each geometry, so the TID copied the TIB parameters, and the TEC used parameters very close to those of the TOB. Starting with run 10609 the optimization of the VPSP parameter became part of the commissioning procedure. This parameter controls the level of the analog baseline. Before this run, VPSP was set to 35 for all TOB APVs and to 37 for all TIB, TID, and TEC APVs (the larger the VPSP value the lower the baseline). Afterwards, it was individually optimized [68].

For each run, summary information was manually entered into the electronic logbook called *TIF elog* [84]. These data, together with information automatically recorded for each run and accessible via the *Run Summary* page [85], provide basic information like the run type (cosmic, pedestal,...), the number of recorded events, the APV mode (peak or deconvolution), the temperature of the cooling plant, firmware versions of the FECs and FEDs, the partition, state and system name and the list of ROOT files storing the data. Slow control information can be retrieved using a utility called *DcsLastValue* [86] that provides information about the HV, LV settings for each run

and information about temperatures and humidities. This tool extracts the data from the ORCON database.

### 8.3.1  Data Flow

During a run, the PCs attached to the VME crates housing the FED and FEC boards are collecting event data. During the slice test, these machines were also used for the Builder Units (BUs) and Filter Units (FUs). In the final setup this task will be performed by the dedicated Filter Farm which works together with the CMS *High Level Trigger* (HLT). All FUs forward their (L1-accepted) events to the CMSSW StorageManager [87]. From there, the data stream is distributed in parallel to the visual online event monitoring using *Interactive Graphics for User Analysis* (IGUANA) [88], the online *Data Quality Monitoring* (DQM) and the local disk storage, where it is written to binary files known as *streamer* files. These files contain the raw FED buffer data and a small number of header words which define the data structure. The local disk buffer is located on a dedicated server (*cmstkstorage.cern.ch*), equipped with 2.8 TB of disk capacity. This allows local caching for about 10 days of data taking without the need for a remote storage [89].

Once a file is not accessed for one hour (which means that either the run is finished or that the file size limit was reached and further data is written into a new file), it is converted from the raw streamer format to *Event Data Model* (EDM) compatible format. Both data files are then automatically copied to CASTOR[8] by a cron job.

As soon as new data are available on CASTOR, the files are registered and transferred to remote sites in order to make them officially available to the CMS community. First, the EDM data files are registered within the *Dataset Bookkeeping System* (DBS)[9]. When a run is finished, the block of files is *closed*, which means that no further file could be added to the same block in the future. This ensures data consistency. The location of such block of files (a.k.a. data run) is then registered in the *Data Location System* (DLS)[10].

Once a set of files is registered in DBS and DLS, it is ready to be transferred to remote sites using the CMS data movement tool PhEDEx[11]. The injection to PhEDEx is handled by the ProdAgent tool. To access the data from remote sites (Tiers), the data must be subscribed remotely, which triggers the transfer of the dataset. At the end of the transfer and after a check whether it was successful, the copy of the dataset is itself registered in DLS as a new location for these data.

This data flow was used during the slice test and is visualized in figure 8.16 , while figure 8.17 shows the equivalent for the final setup in the CMS experiment.

---

8. CASTOR is the *CERN Advanced STORage manager*, a hierarchical storage management system used to store physics production files. With December 2007, there are 10.5 petabyte of simulated and test data stored in CASTOR.
9. *Dataset Bookkeeping System* (DBS) is a database and user API that indexes event-data for the CMS Collaboration. http://cmsdbs.cern.ch/
10. The DLS system uses the LCG (LHC Computing Grid) file catalog technique to store information about file blocks in a database.
11. The PhEDEx project provides the data placement and the file transfer system for the CMS experiment. The project name is an abbreviation of *Physics Experiment Data Export.*

**Figure 8.16:** Overview of the data flow during the CMS Tracker slice test. The data collected from the detector are distributed by the Storage Manager to Data Quality Monitoring (DQM), event visualisation (IGUANA) and further storage in CASTOR, where data are distributed via DBS and PhEDEx to Tier 1 and 2 centers around the world for further reconstruction.



**Figure 8.17:** Overview of the data flow for the CMS experiment taking advantage of the grid and its Tier 1 and 2 centers (T1 and T2).

## 8.3.2 Reconstruction

Tracks of cosmic muons were reconstructed from the data by two different manners, called *FNAL* and *standard* reconstruction.

### FNAL Reconstruction

The FNAL reconstruction is a dedicated reconstruction effort carried out at *Fermi National Laboratory* (FNAL), Batavia, Illinois (USA). It uses a development version of ProdAgent that allows to include non-release code in the data processing. This enables the use of the latest code changes, e.g. patched geometry or latest algorithm changes to get the highest efficiencies. Since only cosmic runs are reconstructed, the main focus is tracking development and tracker alignment studies.

Several passes were performed:

- The Pass 0 reconstruction was the initial reconstruction using a pre-release version of CMSSW 1.3.0 (pre5). The results are now outdated.

- Pass 1 was an intermediate reconstruction pass using CMSSW 1.3.2. Like the previous pass it is now outdated.

- Pass 2 was the next step using CMSSW version 1.3.3. It uses different cluster reconstruction thresholds than the previous passes (2/3/5 for seed/neighbor/cluster) and implements a cluster filter. This filter discards so-called *hi-multiplicity events* with more than 1000 clusters per event.

- Pass 3 uses CMSSW software version 1.3.6 and applies different cuts, e.g. the hi-multiplicity cut is reduced from 1000 to 300 clusters per event. In addition, different bugs of the three track reconstruction algorithms which were found in the previous passes [90], are fixed.

- Pass 4 is a new re-processing campaign of the data using the most recent CMSSW version available (1.7.3). This pass is dedicated to test the efficiency of tracking and alignment algorithms [68].

All reconstructed runs were registered in DBS. Each run is a separate data set. For pass 3, the data can be found there using the following information:

```
Application: /CMSSW_1_3_6/Reco/cmsRun
Primary Dataset: TAC-XXX-RecoPass3
Data tier: RECO
```

where `XXX` is either `TIB`, `TOB`, `TIBTOB` or `TIF` for the TIB+TOB+TEC configuration. Figure 8.18 shows how the number of reconstructed events for passes 2 and 3 follow the raw data closely. Detailed information about the different reconstruction passes, the CMSSW versions and individual file tags used can be found in [90].
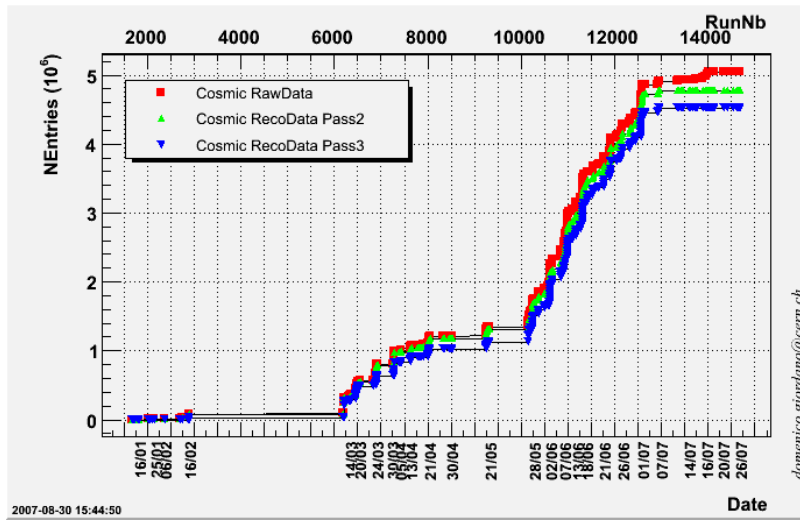
**Figure 8.18:** The numbers of processed events for two reconstructions (pass 2 and 3) follow the raw data closely.

### Standard Reconstruction

The standard reconstruction uses a defined (pre-)release of CMSSW (version 1.3.0-pre6). Since only release code is used, no changes in the form of additional or modified packages are allowed. Thus, the efficiency and quality of the tracks is lower than for the FNAL reconstruction. All data runs – independent of type – are reconstructed and can be accessed via DBS using the following parameters:

```
Application: /CMSSW_1_3_0_pre6/DIGI-RECO/cmsRun
Primary Dataset: TAC-TIBTOB-120-DAQ-EDM
Dataset: CMSSW_1_3_0_pre6-DIGI-RECO-Run-00XXX-SliceTest_TIBTOBTEC
Data tier: RECO
```

### 8.3.3  Track Visualisation

The visualization system in the CMSSW project is called IGUANA (*Interactive Graphics for User Analysis*). It provides an interactive application for track reconstruction and allows to display CMS events and geometry to debug algorithms and code which produce them. The system is based on OpenGL, a toolkit of 2D and 3D graphics and user interface components. It needs the same CMSSW configuration file as used for track processing, to reconstruct each event before it is being displayed. A cosmic muon visualized using IGUANA and traversing the TEC and TID sub-detectors is shown in figure 8.19.

A plot summarizing all events of a given run into one three dimensional overlay plot if given in figure 8.20. It shows the acceptance regions of the scintillators used for the cosmic trigger, similarly to the scintillator hit map shown in figure 8.9.
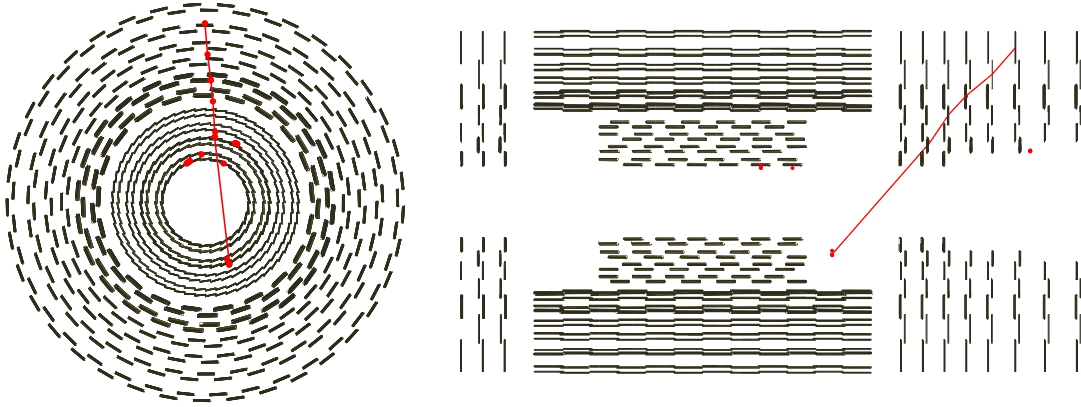
**Figure 8.19:** First reconstructed cosmic muon traversing the positive Tracker Endcap, seen in *xy*- (left) and *z*-view (the TEC and TID subdetectors are not shown). It was recorded on March, 31st, 2007 in run 7286 (event #30).
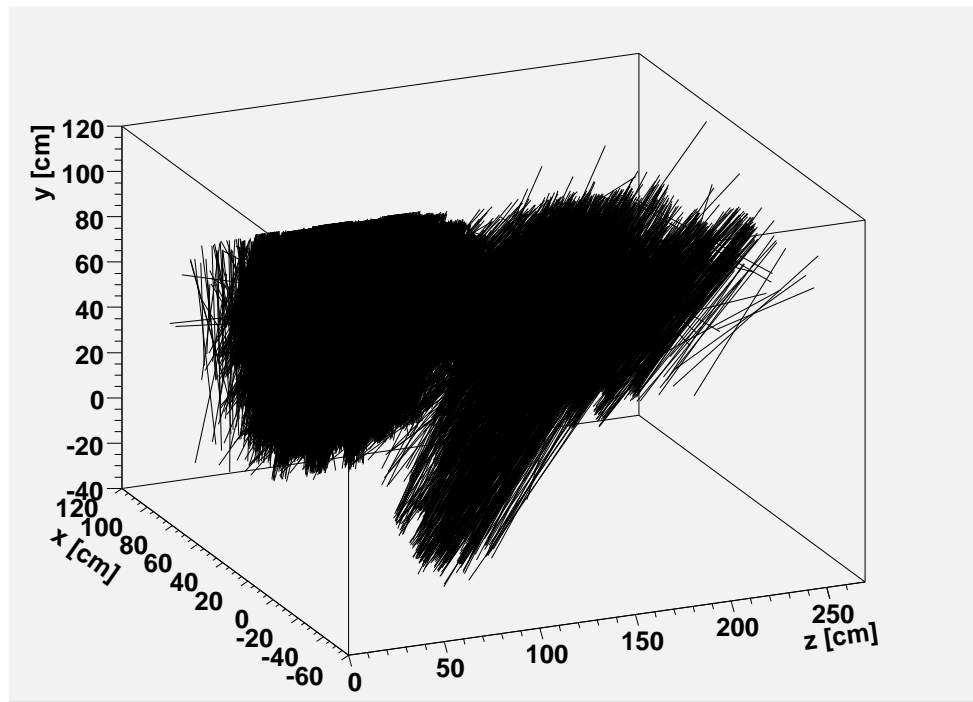


**Figure 8.20:** Three dimensional overlay plot showing all tracks of run 10215 (scintillator position C, -0.5°C) in the slice test [91]. Two type of tracks can clearly be separated: straight tracks traversing TOB only (left) and diagonal tracks traversing TEC and TID.

A specialized tool called *Tracker Map* was developed using the IGUANA framework for monitoring purposes [92]. It allows collections of data associated with individual Tracker modules (strip and pixel) to be viewed in a single 2-dimensional image. This image shows all modules arranged in their mechanical structures: disks for the endcaps and flattened layers for the barrels. Modules from stereo layers are not displayed as rectangular blocks but represented by two adjacent triangles forming a rectangle of the same shape together. The data which can be visualized by different colors are any parameters accessible via the data quality monitoring, e.g. sensor dark current, noise or any APV settings. The Tracker Map can be used in an interactive mode providing zoom functionality in order to get the visual impression of the status of a single parameter for all modules very quickly.

## 8.4 Conclusions

Probably the most important outcome of the slice test is the experience gained in operating such a complex system and the knowledge of the bottle necks for scalability. Thus, many important changes to the system were made to improve all parts of the system.

### 8.4.1 Slow Control

For the TCS, one of the main lessons learned was to identify the bottle neck of the OPC communication between the SY1527 power supply mainframe and the PVSS servers. This protocol was initially applied in polling-mode. It was discovered that the transfer of several thousand sensor values degrades network performance and thus reduces the reaction speed of the PVSS user interface panels. In the worst case, it took several minutes after an *ON* command was issued until all power supply were actually switched on and reported their status back into PVSS. This issue was first addressed by using a dedicated network link between the OPC server and the power supply mainframe, which reduced the problem but the real cause remained. To solve this problem completely, a new OPC server was necessary which incorporated event-driven communication to reduce the load on both the network and the servers.

Another result was the understanding to introduce a majority-voting system for the finite state machine (FSM). Usually, all power supplies must be in the state *ON* that this state is reported upwards to the experiment control system. It happened several times that one power supply tripped and the whole system switched into an error state which consequently aborted the data taking run. Since it can always happen that some power supply channels are not operational for whichever reason, the FSM was modified such that a certain percentage of faulty channels does not affect the current state. This allows a fraction of LV or HV channels being off without interrupting data taking by not reporting these states upwards.

## 8.4.2  Data Acquisition

From the DAQ point of view, the system was heavily debugged and continuously developed during the whole slice test. The most important change was the integration of the commissioning tools within the CMSSW framework. Before, the commissioning was done using custom tracker-specific software (known as RootAnalyzer). The utilization of CMSSW has the advantage of transparent use of both stand-alone and global operating modes for commissioning and data taking, due to the identical software architecture.

The online *configuration database* stores all parameters that are downloaded to hardware registers in the FEDs, FECs and FE electronics during initialisation. It was discovered that a large fraction of these data is also needed offline during event reconstruction. Because of security and performance reasons, standard reconstruction tasks and user analysis code are not allowed to access this database, not even in read only mode. However, a dedicated offline *conditions database* exists, which stores all information needed for event reconstruction (except the actual event data). Thus, a large fraction of the information in the configuration database is copied into the conditions database. This necessitates an Online-to-Offline (O2O) transfer tool that copies data between those two databases and a mechanism that defines an *Interval Of Validity* (IOV) range for all conditions data with respect to the event data.

Another important development is the *Error Diagnostics System* (EDS). The Strip Tracker is a hugely complex detector with many potential sources of problems. The EDS handles both configuration and runtime error conditions like hardware failures or abnormal detector states. It provides immediate diagnostic feedback to the user, together with failure analysis and will eventually incorporate automized recovery procedures. The central component called *error dispatcher* collects and processes error messages from XDAQ applications. It has various communication possibilities with other error dispatchers, with monitoring frameworks and with a dedicated CMS *errors database*. This allows to store the most common error patterns collected by EDS. Since data from the conditions and configuration databases will also be needed, the O2O transfer tool will be used to provide that information.

## 8.4.3  Detector Noise Performance

An important experience made during the slice test is the impression about the quality of the detector itself. Although only 13 % of the whole tracker was read out, it represented the largest silicon tracking device ever operated at that time. Many interesting effects could be studied on such a large, complex system.

### Strip Noise Studies

The noise of silicon modules is dominated by the capacitive load on the input of the readout chip. In such a complex system like the CMS Tracker, there are several other possibilities of noise sources.

In particular, there could be ground loops, cross-talk effects from neighboring modules or noise introduced through cabling or from power supplies. The overall noise behavior was studied during the slice test depending on various settings and at different temperatures.

The noise is very sensitive to parameters like the gain settings of the APVMUX and AOH, thus the commissioning procedures – where these settings are optimized – play an important role for noise studies.
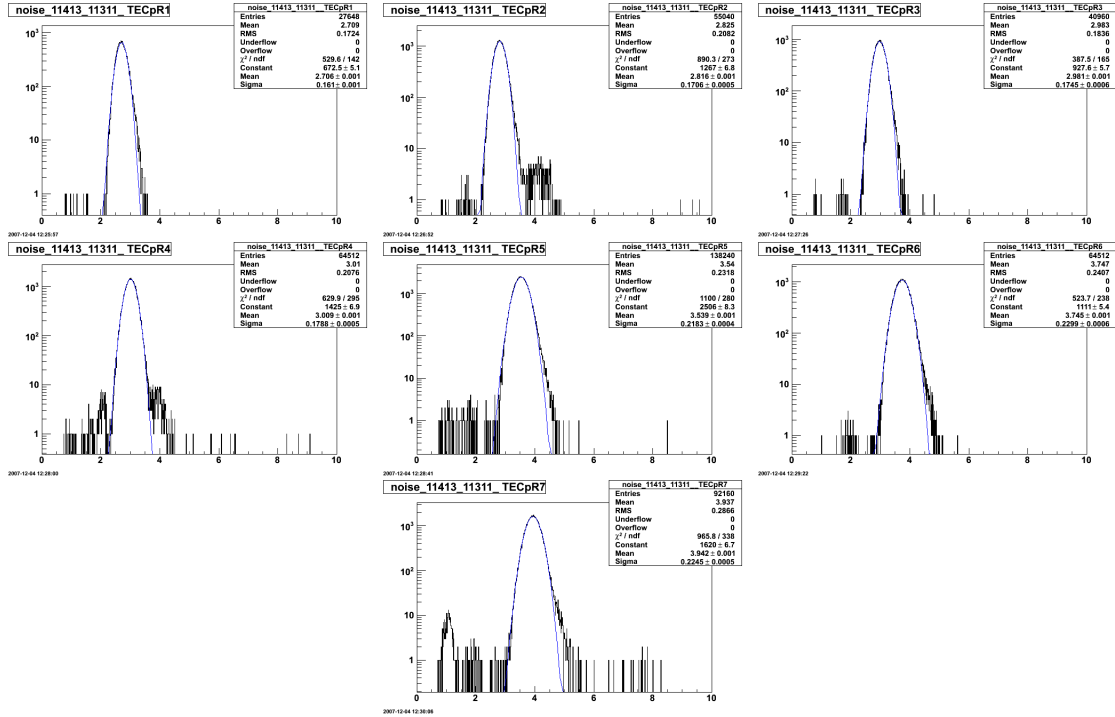


**Figure 8.21:** Noise histograms for individual TEC rings from ring 1 (top left) to ring 7 (bottom center). The data was taken during pedestal run 11413 at -10°C. Increasing strip lengths cause rising mean noise, which can be seen as shift of the distributions to higher ADC values. A Gaussian fit for each plot is shown in blue [68].

As for the capacitance increase, the noise scales with the strip length, which is different for modules of different TEC rings. The histograms in figure 8.21 show the strip distributions for each ring. A Gaussian fit was applied to each histogram. The noise is generally well described by the fit, with small non-Gaussian tails for ring 2, 4, 5 and 7. These tails represent dead and noisy strips for tails on the left and right sides of the distribution, respectively. The mean values essentially scale linearly with the length of the active strips for each ring, as shown in figure 8.22. This result demonstrates that the noise is indeed dominated by the strip capacitance and not by external noise pickup of the system. Results taken at different temperatures show also a linear dependence, but with a different slopes caused by temperature dependence of various APV parameters.

In order to get comparable results for different rings, the noise needs to be scaled. This was done in figure 8.23, which shows the noise of all TEC rings superimposed into one single histogram. The noise is scaled to ring 1 using the results of the fit shown in figure 8.22. Ignoring known bad
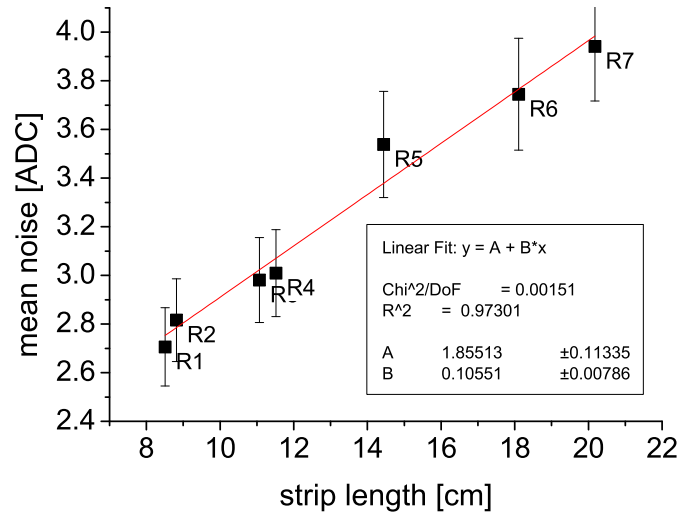
**Figure 8.22:** Mean strip noise as shown in figure 8.21 versus the active strip length for each TEC module type. As the noise is mainly dominated by the strip capacitance, a linear fit describes the noise dependence on the strip length.
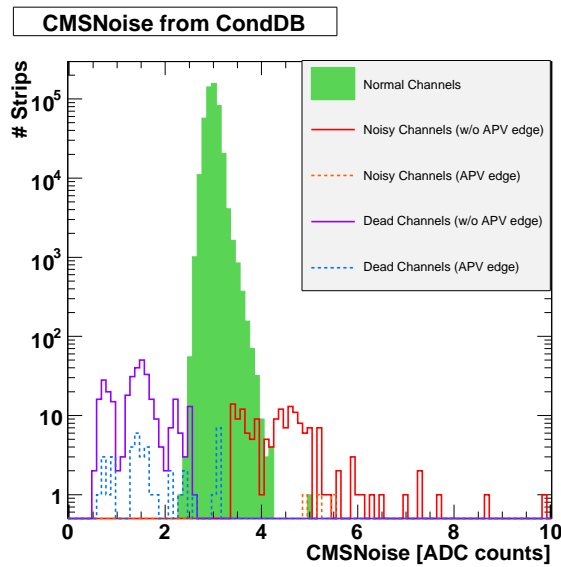


**Figure 8.23:** Histogram showing the noise of each strip of the Tracker Endcap modules participating in the slice test, scaled to ring 1. Bad AOH lasers and bad APVs are not included in this plot [91].

APVs and optical links, the data in the diagram can be used to deduce the overall quality of the silicon sensors since the channels with low noise ("dead channels") represent open strips, which e.g. were left unbonded because of pinholes. The channels with high noise represent strips with e.g. high single strip current. In total, 335 dead and 164 noisy channels were found during the slice test (omitting bad APV edge channels, which are known for intrinsic excess noise). This corresponds to the excellent number of 0.1 % bad strips.

Larger defects listed in table 8.3 are the cause for additional defective channels. In the two tested sectors of the Tracker Endcap 2,944 channels were affected by such problems, corresponding to approximately 0.6 % of all channels.

| Position | Defect | Comment |
|---|---|---|
| S3 BP4 2.1/0 | bad tick marks | known before slice test |
| S3 BP1 5.3/0 | low tick marks | weak laser |
| S3 BP5 7.3 | two bad APVs | known since integration |
| S3 BP3 4.3 | one bad APV | known since integration |
| S2 FP3 1.4/0 | laser with bad noise in deconv. mode | not conclusive because of low statistics in deconv. mode |
| S2 FP7 5.4 | PLL not working | whole module lost |
| S2 BP6 2.1/2 | laser with bad noise | working at and below $-10°$C |
| S2 FP8 3.2/1 | laser with high noise | working at and below $-10°$C |
| S2 BP2 7.5/0 | laser with low noise/pedestal | only at $-15°$C |
| S3 BP4 7.2/1 | very high base line; saturated | only at $-15°$C |

**Table 8.3:** Table showing the defects of the two sectors of TEC+ tested during the slice test. The information in the *Position* field is explained for the first item in the list: S3: Sector 3; BP: back petal; 2.1: module position within petal; /0: laser number 0 of AOH (0/1/2).

For TIB, TID, and TEC the noise behavior was as low as expected from previous tests of sub-structures of the detector. For TOB, however, external noise was absorbed by the system, caused raising noise figures towards the APV edges. This characteristic profile is often referred to as *wing noise* and must not be mixed up with the increased noise of APV *edge channels* (channel #1 and #128), which can be observed on almost all modules. The TOB modules which suffer most from this problem are located closest to the CCU board and the *multi-service cable* MSC cable (containing the power lines) on each rod. High noise increases the strip occupancy because of fake noise clusters. Since the modules' signal-to-noise ratio remains sufficiently high, the thresholds for the cluster finding algorithms can be increased to preserve the signal and to retain the excellent TOB tracking performance. However, some concern exist about even more noise pickup in the final setup in CMS. During the slice test, various grounding scenarios were tested in order to minimize noise pickup. The main conclusion was that it can be significantly reduced by grounding the shielding of the TOB power cables (either LIC or MSC) at the *patch panel 1* (PP1), which connects the external LIC power cables to the Tracker's internal MSC cables [93].

**Noise versus Temperature**

Figure 8.24 shows the noise of all rings versus the run number. Both arithmetic average and mean value of a Gaussian fit are displayed as solid and open symbols, respectively. Bad modules were removed from the analysis. For constant coolant temperature the noise is stable to better than $\pm 0.5$ %. APV parameters were optimized for each temperature. Since run 10609 (at 10°C), the VPSP scan had become part of the commissioning procedure. The consequence of introducing this tuning measure was not clearly visible in the noise plot due to changes of other APV parameters (ISHA and VFS) at the same time [94].
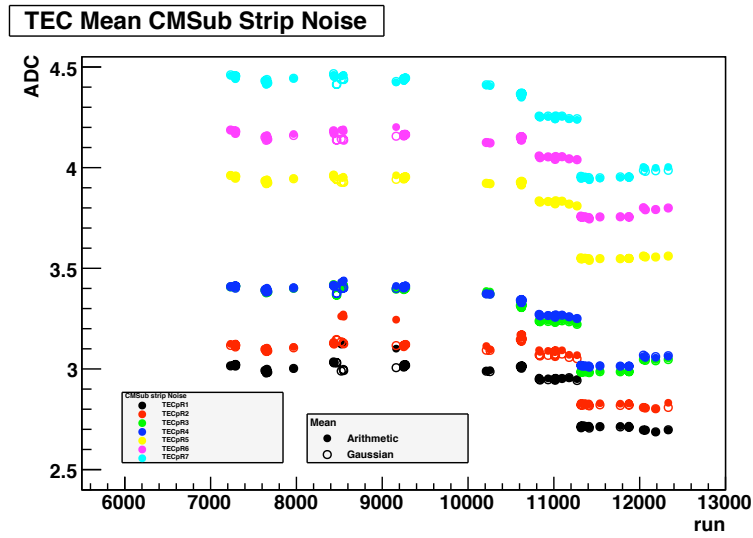
**Figure 8.24:** Noise versus run number for TEC discs [68]. The lower noise figures correspond to lower temperatures.

The decrease of noise with decreasing temperature is very nicely visible and implies an increase of the signal-to-noise ratio (SNR) by the same factor, if non-linearities caused by temperature effects can be neglegted. A diagram showing the evolution of the SNR versus the run number is given in figure 8.25. This plot shows excellent numbers for the SNR ranging from 26 to almost 40. However, it must be taken into account that these numbers were achieved using the APVs in Peak Mode. For the default run mode during proton-proton collisions (Deconvolution Mode), the SNR values will be lower than the ones given here.
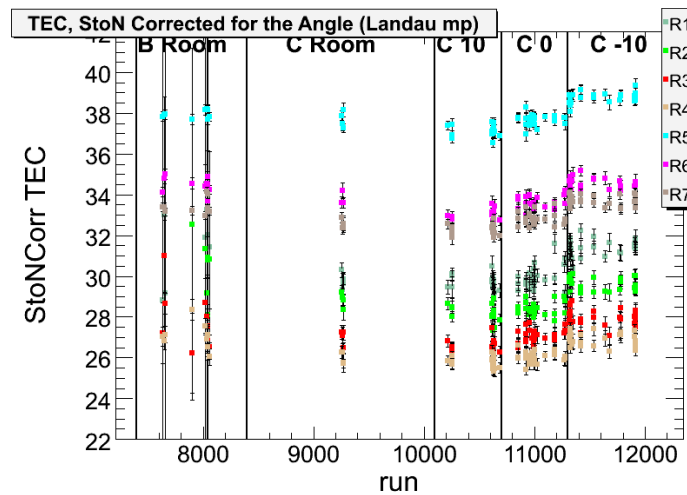


**Figure 8.25:** Signal-to-noise ratio of the TEC modules (in Peak Mode) versus the run number. An increase of the SNR can be seen for runs at lower temperatures [68].

### 8.4.4 Cluster and Tracking Performance

**Cluster and Hit Reconstruction**

The first stage in track reconstruction is cluster finding. This is performed by the 3-Threshold algorithm (see section 8.2.5), whose results are RecHits. Figure 8.26 (left) shows the mean number of hits in each event (which corresponds to a trigger signal) versus the run number. It is clearly visibly that the performance was very stable during the runs at $+10°$C, $0°$C and $-10°$C. The runs at $-15°$C have less hits per event because of limited cooling power, where some parts of the system had to be switched off to achieve this low temperature.

An analysis of hit efficiency and hit resolution is currently ongoing [68], using a sample of well reconstructed events. The track sample contains events with exactly one track reconstructed by the CTF, reconstructed from hits in at least three stereo layers (matched hits), one hit in the first TIB layer and in one of the two last TOB layers. The efficiency was measured by asking for an intersection of a module with the interpolated track and checking for the presence of a hit. It exceeds 99.8 % for all measured layers [95].

The hit resolution depends on local track angles (with respect to the silicon sensor) and cluster widths. It was studied using a sample of events with at least six reconstructed hits in the barrel region, exactly one track found by the CTF and a local angle of less than $30°$ between $x$ and $z$ plane. It was shown that the hit resolution is qualitatively well understood as a combination of the uncertainty in the predicted position largely due to misalignment, and the uncertainty in the hit position. For TIB layers the predicted position uncertainty dominates the total measured cluster width, while for TOB layers the uncertainty due to alignment has a smaller contribution to the total cluster width. This means that TIB suffers more from misalignment than TOB [77].

**Track Reconstruction**

Three tracking algorithms, which were described in section 8.2.6, were applied to the data acquired during the slice test. In contrast to the Cosmic Track finder, CTF and RS algorithms are able to reconstruct more tracks per event. Hence it is expected that the number of single track events will be higher for the Cosmic Track Finder in contrast to the others. Figure 8.26 shows the distribution of hits and tracks per event, split up for the different tracking algorithms for a data sample taken at $-10°$C temperature in trigger position $C$.

To monitor the stability of the track reconstruction algorithms versus different operating temperature, plots showing various parameters versus run number are useful. For each run, the mean of the parameter under study was calculated and plotted as a function of the run number. It is expected that the number of tracks per event do not vary with temperature. However, different scintillator positions cause varying number of modules in the acceptance region and hence a different mean number of hits per event. This behavior can be seen in figure 8.27, where the number of hits and reconstructed tracks is shown versus the run number. For the temperatures of $+10°$C, $0°$C and $-10°$C the parameters were almost stable. At $-15°$C, parts of the detectors had to be switched off
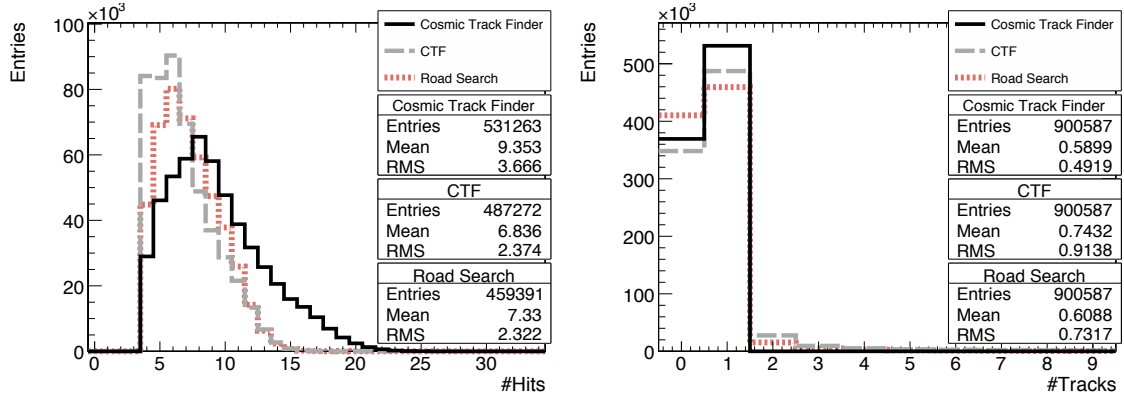
**Figure 8.26:** Number of hits (*left*) and reconstructed tracks (*right*) per event, split up for the three different track reconstruction algorithms. The data was taken at $-10°C$ in trigger position $C$ (run 11316-11915) [95]. The Cosmic Track Finder algorithm reports more hits since it treats matched RecHits (coming from stereo layers) independently in contrast to CTF and RS.

in order to maintain cooling at the desired temperature, because of limited cooling power of the TIF chiller. Hence, the results obtained there are not comparable to the other temperature regimes.
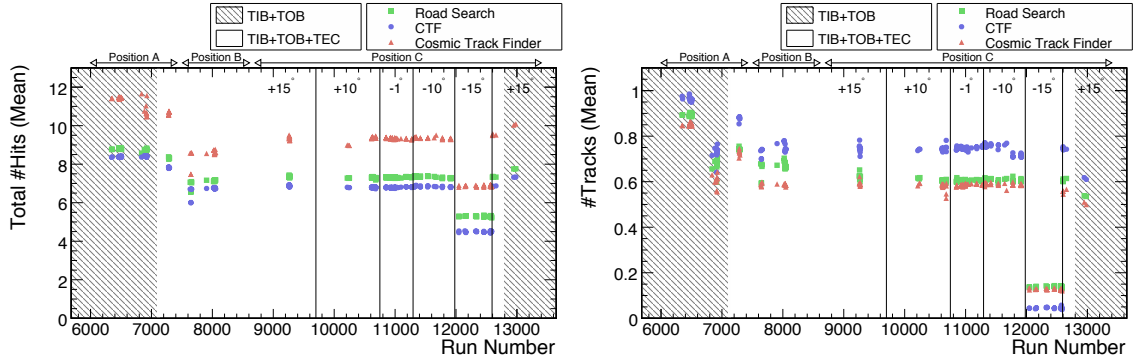


**Figure 8.27:** Plots showing the mean number of hits (*left*) and reconstructed tracks (*right*) versus the run number. A stable behavior is apparent in the period between $+10°C$ and $-10°C$. At $-15°C$, parts of the setup needed to be switched off and thus multiplicities are not comparable to the other temperature ranges.

The majority of the TIF data has been taken in Virgin Raw mode of the FEDs, using a dedicated CMSSW software module performing the zero suppression offline. However, around 100,000 events were collected in Zero Suppression mode at room temperature with scintillator position $A$ using data from TIB and TOB sub-detectors. These data was used to compare the tracking results of both readout modes, demonstrating an excellent agreement [95].

Since the TIF data was recorded without external magnetic field, it is difficult to select precise, high-momentum tracks. However, the lower trigger scintillator was equipped with a lead plate to absorb muons with very low momentum (see section 8.1.4). Even with this countermeasure, muons below $20\,\mathrm{GeV}/c$ degrade the quality of track-based alignment studies [95]. Thus, an analysis was

performed using the tracking algorithms in order to obtain the momentum of each track. This was done be re-fitting the tracks with the momentum as an unknown variable by taking multiple scattering into account. The result was compared with simulation data and results obtained from energy spectra measurement using a balloon experiment [96]. There is generally a good agreement.

### 8.4.5 Tracker Alignment

TIF cosmic data can be used for track-based alignment of the CMS Tracker. This method uses the fact that the measured and trajectory impact points of a track are systematically displaced if the module position is not known correctly. This results in track *residuals* $\varepsilon$, which should be minimized. Taking these residuals, which are part of the Tracker's *calibration data*, into account for future track reconstruction, the efficiency and quality of track reconstruction can be increased.

#### Laser Alignment System

Before using track-based alignment, data from the tracker's internal *Laser Alignment System* (LAS) is used for rough estimation of movements and deformations of the Tracker support structures. This system uses infrared laser light at a wavelength of 1060 nm to penetrate special silicon sensors and generate signals in them [37]. These act as normals signals coming from charged particles traversing the Tracker, and are read out through the standard DAQ readout chain. The system consists of ten fibers guiding laser light into the Tracker, where it is distributed in two regions using beam splitters: one light path traverses the modules of ring 6 of the endcaps, while the other laser path traverses the TEC on the height of ring 4 modules, providing signals also for TIB and TOB via additional beam splitters (see figure 8.28).
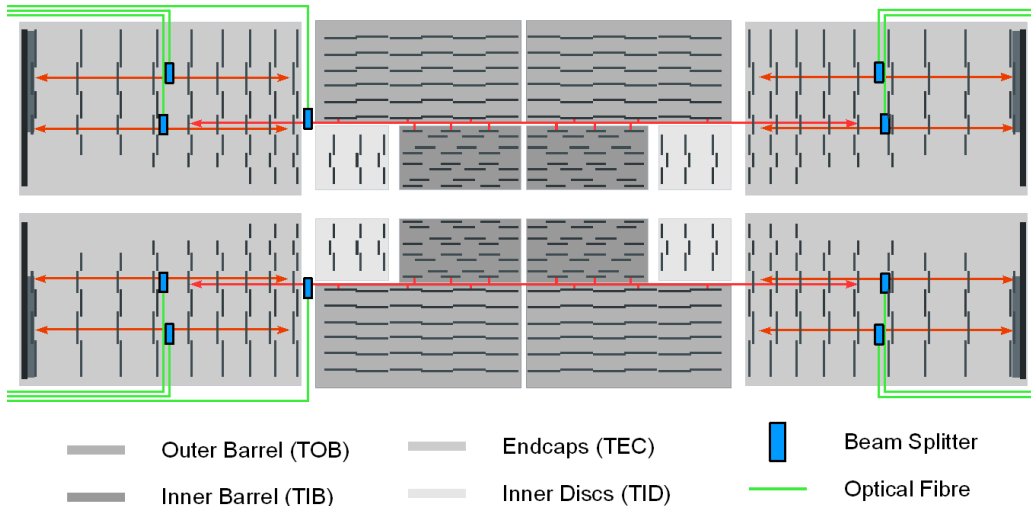


**Figure 8.28:** Layout of the CMS Tracker Laser Alignment System [77]. The laser beams traverse the tracker on two radii, namely at TEC ring 4 and ring 6. The former also provide signals for TIB and TOB.

For proper function, the full LAS ($2\pi\,\phi$-range of the tracker) needs to be operated, which was not the case during the slice test. This means that no complete picture of the Tracker alignment could be achieved. However, the data taking was useful to verify the proper function of the laser system (lasers, fibers, beam splitters) and the DAQ system during LAS runs. Some limited conclusions can be drawn from the obtained data as well as the influence of operation temperature on the support structures [77]. Moreover, LAS data taken during TEC integration in Aachen can be compared to slice test data to see if handling, transport and insertion of the endcaps caused any mechanical shifts in the system.

**Survey Information**

Another alignment information source is data from the *optical survey* of the Tracker and its components. Information about the relative position of modules within detector sub-structures (e.g. petals) had been recorded using data from coordinate-measuring machines during integration of these sub-structures and stored in TrackerDB. Later, an optical survey analysis using photogrammetry was performed on the sub-structures during or after these parts were integrated in the Tracker (e.g. TIB+/- with respect to TOB). For TIB and TID both data from TrackerDB and survey information is available for alignment studies, while for the outer detectors (TOB and TEC), module survey was just used for mounting precision monitoring and only optical survey of high-level structures was used in alignment analysis.

**Track-based alignment algorithms**

Track-based alignment in the CMS Tracker takes advantage of three different algorithms, (i) the *Hits and Impact Points* (HIP) local iterative method, (ii) a Kalman filter based fit method and (iii) the *Millipede II* global minimization method. All methods use a common definition of module coordinates taken into account for alignment. A module is assumed to be a rigid body, meaning that three shifts and three rotations are sufficient to express its degrees of freedom [77].

(i) The *HIP method* minimizes the sum of the residuals of each aligned object, independently from the others. Since the track fit, which predicts the impact point, is biased by misalignment, this procedure is repeated iteratively until convergence is achieved [97].

(ii) The *Kalman alignment algorithm* is based on the Kalman Filter [80]. It is an iterative method where the alignment parameters are updated immediately after a track is processed. Since it would be too slow to update the alignment parameters of all modules, the update is limited to modules with significant correlations to the ones in the current track. To keep track of the correlations, some bookkeeping is required. For this purpose, a list containing all the correlations for each module is stored. This list is updated for all modules crossed by the current track. The metric distance between two different modules $d(i,j)$ is defined to determine which alignables have significant correlations and should therefore be included in the list. Only if this distance is small enough, a module's correlation list is updated (see figure 8.29).
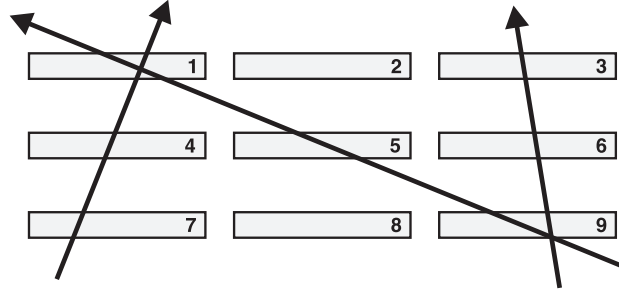
**Figure 8.29:** Example of the metric distance $d(i, j)$ between modules hit by different tracks: $d(1,9) = 1$, $d(5,6) = 2$ and $d(3,7) = 3$ [98]. These values are used by the Kalman alignment algorithm to calculate the correlation between different modules.

(iii) The principle of the *Millipede II* algorithm is the minimization of a objective (cost) function, simultaneously taking track and alignment parameters into account [99]. Being interested in $n$ alignment parameters only, the problem is reduced to the solution of a matrix equation of size $n$. The algorithm provides fast methods to solve this equation for up to $n = 10^5$, together with other tools like hit outlier rejection and the inclusion of survey measurements.

## Alignment using TIF data

First alignment studies of TIF data started recently and are ongoing [77]. The studies include the investigation of differences between the three track-based alignment algorithms, the verification of survey and LAS data and monitoring the stability of the Tracker support structures with variation of stress and temperatures in the whole slice test temperature range. Preliminary results obtained with the Kalman alignment algorithm are shown in figure 8.30. These plots demonstrate the shift of the actual module position w.r.t. the nominal position. The modules of the Inner Barrel (TIB) sub-detector ($R < 55$ cm) show a larger shift than the ones in the Outer Barrel (TOB) detector with $R > 55$ cm. The typical achieved precision on module position measurement in the global $x$ coordinate is 500 µm in the TIB and 150 µm in the TOB.
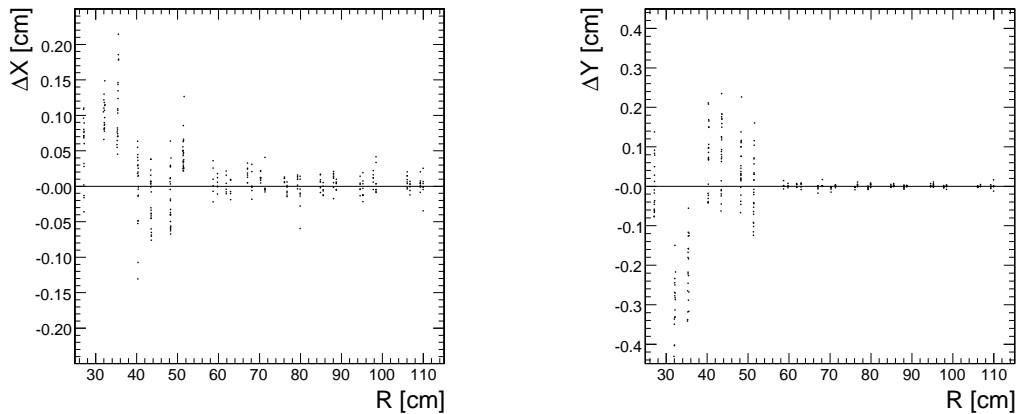


**Figure 8.30:** Deviations of module positions from their nominal values (shifts) for global $x$- (left) and $y$-coordinates (right) versus the radius $R$ in the barrel part of the Tracker [71, 77].

# 9 Plans for an International Linear Collider

> No one wants to learn from mistakes, but we cannot learn enough from successes to go beyond the state of the art.

*(Henry Petroski)*

Caused by the point-like structure of leptons, an $e^+e^-$ collider is the better choice for precision measurements than a proton-proton collider like the LHC. Because of that, the *International Linear Collider* (ILC) is foreseen as the next large high energy particle accelerator intended to verify and to review the possible discoveries of the LHC.

## 9.1 Machine

The ILC accelerator is based on cold superconducting radio-frequency (SCRF) accelerating cavities. This technology was recommended by the International Technology Recommendation Panel (ITRP) and later endorsed by the International Commitee for Future Accelerators (ICFA) in favour of the non-superconducting room-temperature technology. The current ILC baseline defined in the *Reference Design Report* [100] assumes an average accelerating gradient of 31.5 MV/m in the cavities to achieve a center-of-mass energy of 500 GeV in the first stage with a later upgrade to 1 TeV. The collision energy will be tunable to any energy starting with 200 GeV. The nominal design luminosity will be $2 \cdot 10^{34} \, \mathrm{cm}^{-2} \, \mathrm{s}^{-1}$.

Figure 9.1 shows the basic layout of the ILC accelerator complex. The particles are created by a polarized high-current electron source and an undulator-based positron source, driven by the 150 GeV main electron beam. In the center of the ILC complex, two 5 GeV damping rings for electrons and positrons with a circumference of 6.7 km will be installed. A beam transport system will deliver the particles to the main linacs, each of which will be 11 km long, utilizing the SCRF cavities. A 4.5 km long beam delivery system will bring the two beams into collision with a 14 mrad crossing angle at a single interaction point (IP). This IP will be shared by two experiments in a push-pull solution. The electron source and the dampling rings will be centrally located around the IP. The upgrade of the machine to 1 TeV would require an extension of the main linacs and the beam transport system by another 11 km each. The total footprint of the site is approximately 31 km (plus additional 22 km after a upgrade to 1 TeV in a second stage). The location of the site is not yet decided, although some obvious proposals already exist.
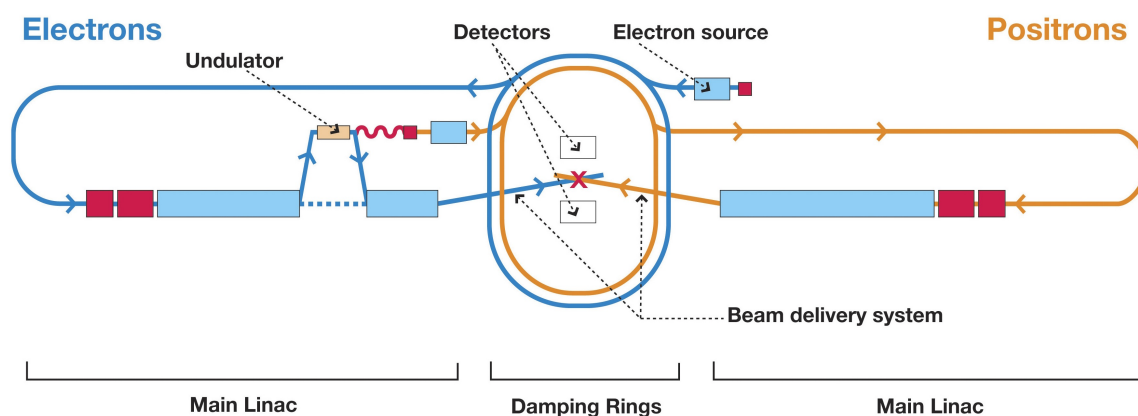
**Figure 9.1:** Footprint of the International Linear Collider accelerator complex.

### 9.1.1 Beam Parameters

Table 9.1 shows the basic design parameters for the ILC for the start-up center-of-mass energy of 500 GeV. The time structure of the beam is defined by pulses with a frequency of 5 Hz, or a repetition rate of 200 ms. In each pulse, thousands of bunches are emitted very rapidly, also called *bunch train*. Figure 9.2 shows the beam time structure.

| Parameter | Unit | Value |
|---|---|---|
| Center-of-Mass energy range | GeV | $200 - 500$ |
| Peak luminosity | $\text{cm}^{-2}\,\text{s}^{-1}$ | $2 \cdot 10^{34}$ |
| Pulse rate | Hz | 5.0 |
| Beam current in pulse | mA | 9.0 |
| Number of bunches per pulse | | $1000 - 5400$ |
| Accelerating gradient | MV/m | 31.5 |
| RF pulse length | ms | 1.6 |
| Beam power (per beam) | MW | 10.8 |
| Typical beam size at IP ($h \times v$) | nm | $640 \times 5.7$ |
| Total AC power consumption | MW | 230 |

**Table 9.1:** Basic design parameters for the ILC start-up with a center-of-mass energy of 500 GeV.
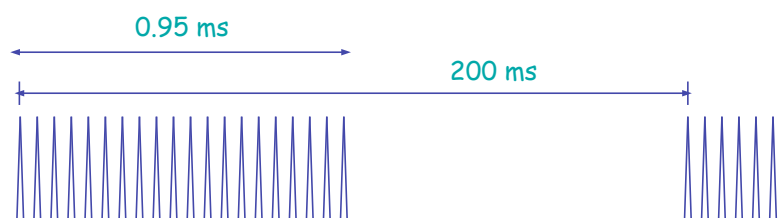


**Figure 9.2:** Time structure of the ILC beam. A bunch train contains 1000-5000 single bunches and is repeated every 200 ms.

### 9.1.2 Electron Source

The ILC electron source must generate the required bunch train of polarized electrons with more than 80 % polarization. This is done by a laser illuminating a photocatode of a DC gun. Two independent laser systems provide redundancy. The beam leaves the source with 140 keV. The first stage of acceleration up to 76 MeV is performed by a normal-conduction linac, after which the beam is accelerated to 5 GeV in a superconduction linac. Before injection into the damping ring, superconduction solenoids are used for spin rotation and energy compression of the beam. The electron source and the pre-accelerators are located on the positron-side of the damping rings.

### 9.1.3 Positron Source

The positron source takes advantage of pair-production to generate positrons. A 150 GeV electron beam coming from the first stage of the main linac is fed to an helical undulator for $\gamma$ production. The undulator will be 150 m long and will contain a vacuum chamber with 6 mm inner radius. The photons with an energy of approximately 10 MeV are then directed onto a rotating Ti-alloy target, generating a beam of electron and positron pairs. This target needs to be 1.4 cm thick and will have a diameter of 1 m. Its outer surface must rotate at a speed of 100 m/s in vacuum to dissipate the heat created by the photon beam.

After the target, the electrons and remaining photons are separated and the positrons are selected by a magnet, pre-accelerated first to 400 MeV and transported 5 km through the rest of the electron main linac tunnel. Before they are injected into its damping ring, a linac with super-conducting cavities is used to accelerate the positrons to 5 GeV, and spin rotation and energy compression takes place like for the electrons.

For commissioning or when the high-energy electron beam is not available, a low-intensity auxiliary positron source (called *keep-alive source*) is provided. This source uses a 500 MeV electron beam directed onto a heavy-ion target for producing approx 10 % of the nominal positron beam intensity.

### 9.1.4 Damping Rings

The two damping rings are needed to damp incoming longitudinal and transversal beam jitter and provide highly stable beams for the main acceleration stage. The two rings, one for electrons and one for positrons, operate at a beam energy of 5 GeV. Both rings, each 6.7 km in circumference, are housed in a single tunnel near the center of site. In its center, the primary IP from the main linacs is located. To avoid interference between particles in the main linacs and the damping rings, both are separated by approximately 10 m in vertical direction. This layout allows access to the IP and other parts of the site while the synchrotron radiation produced in the damping rings is shielded. The damping ring must be equipped with very fast kicker magnets for single bunch injection and

extraction in the ring together with a RF system and superconducting wigglers for momentum and bunch compression.

## 9.1.5 Main Linacs

The two main linear accelerators (linacs) accelerate the electron and positron beams from 5 GeV to a maximum energy of 250 GeV at an average gradient of 31.5 MV/m over a combined length of 23 km. The linacs comprise 560 superconducting RF units, each equipped with a stand-alone RF source (modulator, clystron). In the center of each RF unit, superconducting correction magnets (quadrupoles) are placed. Liquid helium is supplied from 10 cryogenic plants, each with an cooling power of approximately 20 kW, to operate the cavities at 2 K. The main linacs follow the average Geoid to simplify the liquid helium transport and distribution.

The main linacs are housed in tunnels typically hundreds of meters underground and are connected to the surface via vertical shafts. The components are separated in two separate tunnels, an accelerator and a service tunnel. For better access and for radiation protection, the RF sources are housed mainly in the service tunnel as shown in figure 9.3.
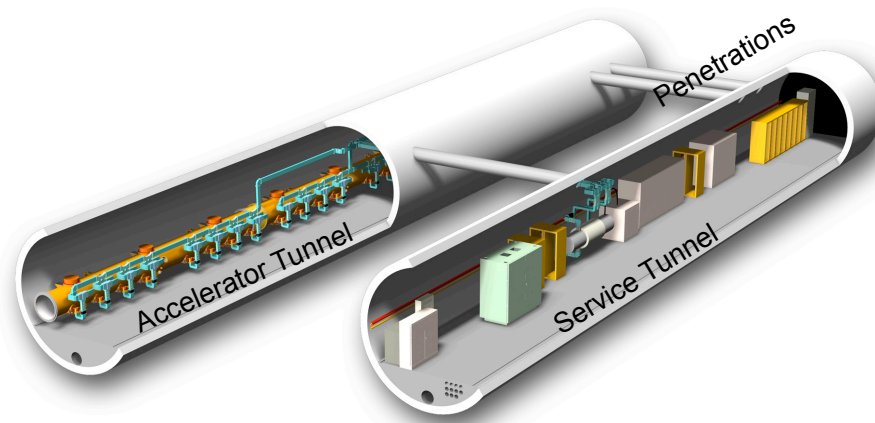


**Figure 9.3:** Accelerator and service tunnel of the International Linear Collider [100].

## 9.1.6 Beam Delivery System

The *Beam Delivery System* (BDS) is responsible for the transportation of both electron and positron beams from the exit of the linacs to the intersection point of the experiment and subsequently guiding the remaining particles to the beam dumps. It must also bring the beams into final focus ready for collision. Since the beam IP will be under a 14 mrad crossing angle, there is space for separate focusing elements and beam dumps, but requiring crab cavities for effective head-on collisions.

## 9.2 Possible Sites

The ILC Reference Design Report [100] lists several possible locations where the machine could be built. A sample site for each region was developed taking care of local requirements and characteristics in geology, topography and local standards. The sites are

- The US site is located near Fermilab in Illinois. The tunnels will be sitting 3-100 m below the surface in a continous dolomite rock.

- The Asian sample site at a unspecified region in Japan is located in a mountainous region, with tunnel depths ranging from 40 m to 600 m in granite. Because of this special terrain, the access tunnels from the surface do not need to be vertical but can be horizontal with some slopes, like in a mine.

- In Europe, the site is located near CERN in Geneva (Switzerland/France) and runs in parallel to the Jura mountain in the *Molasse*, a local impermeable sedimentary rock at a typical depth of 370 m.

Apart from these 'official' design sites, there are also a second European site near DESY in Hamburg (Germany) and a proposal for a site near JINR[1], Dubna (Russia), under discussion. While the first three sites are so called *deep-tunnel* solutions, the latter two are examples of *shallow* sites with a depth of 25 m only.

## 9.3 Detector Concepts

The physics goals of the ILC accelerator and its detectors are understanding the mechanisms of mass generation and electroweak symmetry breaking. This implies precision measurement of the Higgs boson and the search for supersymmetric particles and their detailed study, if they are found. The experimental conditions of an lepton collider like the ILC provide an ideal environment for that, since they offer well defined initial conditions for the collisions. Because of that, irradiation problems like they exist the LHC experiments do not play a large role for the ILC detectors. However, precision measurements have other challenges, like a very high precision of momentum measurements from the beam energy down to very low values over the full solid angle. This requires minimum material in the detectors, since multiple scattering spoils the precision of that effort.

### 9.3.1 Push-Pull Solution

Four detector concepts are being studied as candidates for the ILC. From these, only two will possibly be realized. In the current design [100], the two detectors are required to move on and off the beam line quickly and reproducibly. This is called *push-pull* solution and enables two experiments to share the single intersection point of the ILC. The detectors must be calibrated and

---

1. JINR is the *Joint Institute for Nuclear Research* in Dubna (Russia), http://www.jinr.ru/.

aligned each time a detector is moved into the beam before actual data taking can start. This requires reinforced mechanics for the support structures of the experiment together with a reliable possibility to connect/unconnect all service lines, cables, fibers and pipes. A possible layout of two experiments sharing a single IP is shown in figure 9.4. Another alternative, avoiding the push-pull solution and comprising a second beam delivery system, was abandoned because of cost issues.
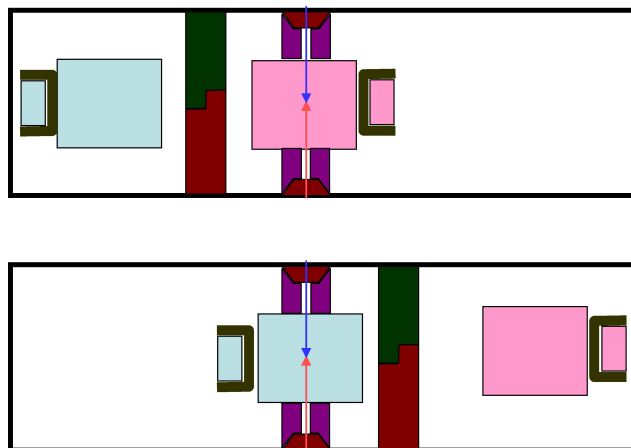


**Figure 9.4:** Possible Layout of the intersection region of the ILC showing the push-pull solution for two experiments. One experiment is in the beamline (shown in pink in the top figure), while the other one is in stand-by (blue), separated by a concrete wall for shielding.

### 9.3.2 Detector Concepts

There were four detector concepts proposed, each by a different community. Three of them can clearly attributed to the large scientific regions in the world: Europe, the United States and Asia, while the fourth concept has been developed independently. Even though all four concepts represent complementary approaches, each concept is designed with an inner vertex detector, a tracking system based on either a gaseous Time Projection Chamber (TPC) or silicon detectors, a calorimeter, a muon system, and a forward system of tracking and calorimetry. Table 9.2 shows some of the key parameters of each detector concept and figure 9.5 show graphical renderings of all concepts.
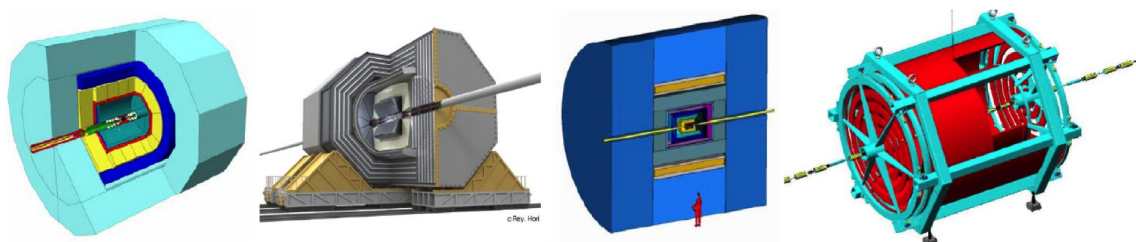


**Figure 9.5:** Graphical illustrations of the LDC, GLD, SiD and Fourth "4th" detector concept (from left to right).

| parameter | unit | GLD | LDC | SiD | "Fourth" |
|---|---|---|---|---|---|
| vertex technology | | Si pixel | Si pixel | Si pixel | Si pixel |
| vertex barrel layer | # | 6 | 5 | 5 | 5 |
| vertex endcaps layer | # | 2 | 0 | 4 | 4 |
| tracking technology | | TPC/Si | TPC/Si | Si | TPC / drift |
| tracking inner radius | [cm] | 45 (TPC) | 30 (TPC) | 20 (Si) | 20 (TPC) |
| tracking outer radius | [cm] | 200 (TPC) | 158 (TPC) | 127 (Si) | 140 (TPC) |
| Si tracker barrel layer | # | 4 | 2 | 5 | - |
| Si tracker endcaps layer | # | 7 | 7 | 4 | - |
| ECAL | | Scint.-W | Si-W | Si-W | Crystal |
| HCAL | | Scint.-Fe | Scint.-Fe | RPC/GEM - W | fiber |
| magnetic field strength | [Tesla] | 3 | 4 | 5 | 3.5 / -1.5 |
| solenoid radius | cm | 400 | 300 | 250 | 300/550 |

**Table 9.2:** Key parameters of the four proposed ILC detector concepts. The two experiments listed in grey shaded columns indicate the proposed merger of those two into a joint detector concept called *ILD*.

## Global Large Detector (GLD) Concept

The GLD concept consists of a silicon pixel vertex detector in its center, surrounded by a silicon strip detector and a large gaseous tracking system. The electromagnetic calorimeter (ECAL) is foreseen to be a sandwich of tungsten and scintillators, while the hadronic calorimeter (HCAL) is made of a sandwich of iron and scintillators. The superconducting coil will have a radius of 4 m with a field strength of 3 Tesla. In the forward region, there will be an electromagnetic calorimeter which will provide nearly full solid angle coverage down to very forward angles.

## Large Detector Concept (LDC)

The LDC detector concept is built around a precision Time Projection Chamber (TPC) tracking system with 3.2 m diameter. A highly granular Si-W electromagnetic calorimeter and a Fe-scintillator sandwich hadronic calorimeter are placed together with the TPC, an intermediate tracker and a vertex detector inside a superconducting coil, which operates at 4 Tesla. The vertex detector consists of five layers of pixel detectors in the barrel region and the intermediate tracker will have several layers in the barrel and endcap regions. The iron return yoke of the coil will house muon detectors. A schematic view of one quadrant of the LDC proposal is shown in figure 9.6.

While the central tracking element will be the TPC, its geometry defines areas where it suffers from inefficiencies, e.g. in the endcap region. Therefore, four supplementary tracking elements are foreseen:

- a Silicon Inner Tracker (SIT), which provides track matching between the vertex detector and the TPC.
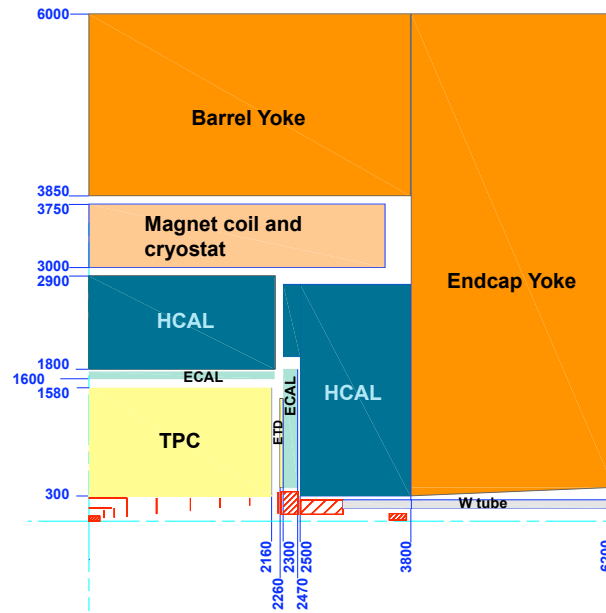
**Figure 9.6:** One quadrant of the LDC detector concept showing its main components.

- a Forward Tracking Detector (FTD), for track reconstruction in the forward angular region beyond the TPC coverage.

- an end-cap Tracking Detector (ETD), which acts as a link between the TPC endplate and clusters in the end-cap calorimeter. The ETD also improves track reconstruction for particles affected by the material in the TPC endplate.

- A similar argument can be made for linking tracks between the TPC and clusters in the electromagnetic calorimeter in the barrel part. For this reason a Silicon External Tracker (SET) is also under study.

At the time of writing this thesis, the GLD and LDC projects are about to merge, since it was discovered that both projects are similar enough to become collaborators rather than being competitors. The first joint meeting of the GLD and LDC collaboration took place in January 2008, and the new, joint detector concept will be called *International Large Detector* (ILD). Its design will incorporate parts of both former concepts and intensive studies will be performed to find the optimal performance between them.

**Silicon Detector (SiD) Concept**

The SiD detector concept is, in contrast to all others, fully based on silicon. It comprises a silicon pixel vertex detector in its center, which is surrounded by 10 layers of silicon strip sensors. A highly pixelized silicon-tungsten electromagnetic calorimeter and a multilayer, segmented hadron calorimeter are chosen to optimize particle flow calorimetry. To keep the cost of the silicon sensors on an affordable level, a 5 Tesla solenoid is placed on a relatively small radius, yielding a high bend radius in order to determine the transverse momentum.

**Fourth ("4th") Concept**

Some parts of the detector of the so called *"4th" Concept* take advantage of the other detector concepts. The pixel detector is the SiD design and the inner strip tracker and TPC are similar to those being developed by the GLD and LDC (or ILD) concepts. The calorimeter is a highly granulated dual-readout fiber sampling calorimeter, able to measure both electromagnetic and hadronic energy. This concept is based on an iron-free magnet configuration, which means that the return flux of the superconducting magnet creating the 3.5 Tesa field is compensated by another solenoidal coil located outside the muon system, as shown in figure 9.7. This allows a back-bend of the muons' tracks for a second momentum measurement similar to the other concepts. This layout would ease the push-pull-solution because the lack of iron in the yoke reduces the weight of the whole experiment significantly.
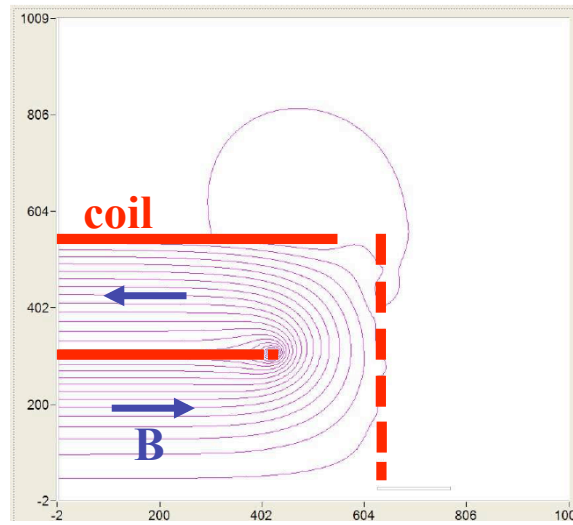


**Figure 9.7:** Two-coil configuration of the Fourth detector concept.

# 10  Silicon Sensors for ILC Experiments

## 10.1  Material Budget Considerations

Precision measurements, as foreseen for the ILC, will require high spatial resolution of the involved detectors, mainly limited by the granularity of the detectors. For binary readout, e.g. if only one strip of a silicon detector is hit by the particle, the resolution $\sigma$ is limited by the strip pitch (see equation 3.51). Another limitation of the resolution of tracking devices is given by multiple scattering.

### 10.1.1  Multiple Scattering

A charged particle traversing any kind of matter is randomly deflected by many small-angle scattering processes. Summing up all individual scattering processes of a particle, e.g. when traversing a thin detector layer, the particles' flight direction is changed. The main contribution to the deflection of charged particles is caused by Coulomb scattering, while for hadronic projectiles also strong interactions contribute. The Coulomb scattering distribution is Gaussian for small deflection angles, but at larger angles it behaves like Rutherford scattering with larger tails than described by a Gaussian distribution [101].

For a thin layer of traversed material the standard deviation of the projected scattering angle of a particle can be approximated by

$$\langle \Theta_{\text{plane}} \rangle = \frac{13.6\,\text{MeV}}{\beta\,c\,p}\, z\, \sqrt{\frac{x}{X_0}} \left[ 1 + 0.038 \ln \left( \frac{x}{X_0} \right) \right] \tag{10.1}$$

using $p$ for the momentum, $\beta = v/c$ for the relative speed and $z$ for the charge number of the incident particle with respect to the elementary charge. The thickness of the scattering medium is given in units of radiation lengths $x/X_0$. This equation describes scattering in a single, homogeneous material taking only a Gaussian distributed scattering process into account [20]. In this approximation, the scattering solid angle $\Theta_{\text{space}}$ can be defined by

$$\langle \Theta_{\text{space}} \rangle^2 = \langle \Theta_{\text{plane}} \rangle_x^2 + \langle \Theta_{\text{plane}} \rangle_y^2 \tag{10.2}$$

where the *x* and *y* axes are orthogonal to the direction of motion.

Equations 10.1 shows that the amount of multiple scattering is inversely proportional to the parti-
cle's momentum (energy). Thus, the tracks of low energy particles are more deflected by scattering
processes. The single adjustable parameter to minimize scattering is the thickness of the scattering
medium.

## 10.1.2 Material Distribution

Figure 10.1 shows the distribution of the material budget of the CMS Tracker, separated by both
subsystems and services. These plots show that there are huge contributions by electronics, cables,
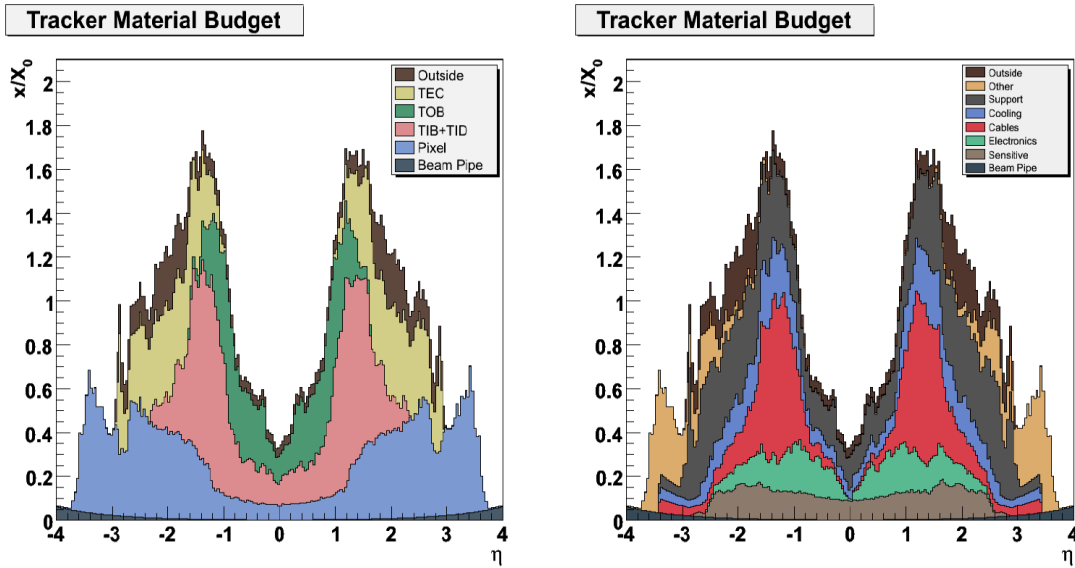


**Figure 10.1:** Material budget of the CMS Tracker, split up into subsystems (left) and services (right) [102].

cooling and support, with some minor contributions of the active material (silicon) itself and the
beam pipe. In the worst region at around $\eta = \pm 1.4$, the material makes up 170 % of $X_0$. This mate-
rial creates some undesirable effects, including multiple scattering, photon conversion, production
of bremsstrahlung photons and delta rays, and hadronic interactions. Especially for the high preci-
sion measurements foreseen at the ILC, this would reduce the detector performance dramatically.
Thus, the present detector concepts have to take material minimization as one of the primary design
goals into account. Simulations for e.g. the SiD concept show a maximum of 20% $X_0$ at a similar
$\eta$ range [100], equal to a reduction by the factor of 8.5. Possible approches to reduce the material
for the various types of services are discussed below.

## 10.2 Support Material Minimization

A large fraction of the non-active material in CMS (e.g. carbon fiber and aluminum) act as support for other heavy elements: cooling pipes, cables, electronics. Thus, a reduction of these components would diminish the support material as well. Despite from this obvious fact, another possibility in optimizing the support structures would be new, light-weight materials.

Currently, various metal foams are becoming popular as support materials in aviation and space industry. Metal foam is a cellular structure consisting of a solid metal – frequently aluminum – containing a large volume fraction of gas-filled pores. The defining characteristic of metal foams is a very high porosity: typically 75-95% of the volume consists of void spaces, which increases its radiation length by the same level. To retain or even increase mechanical stiffness, a very thin layer of conventional metal can be applied on top and bottom of the foam material (see figure 10.2)
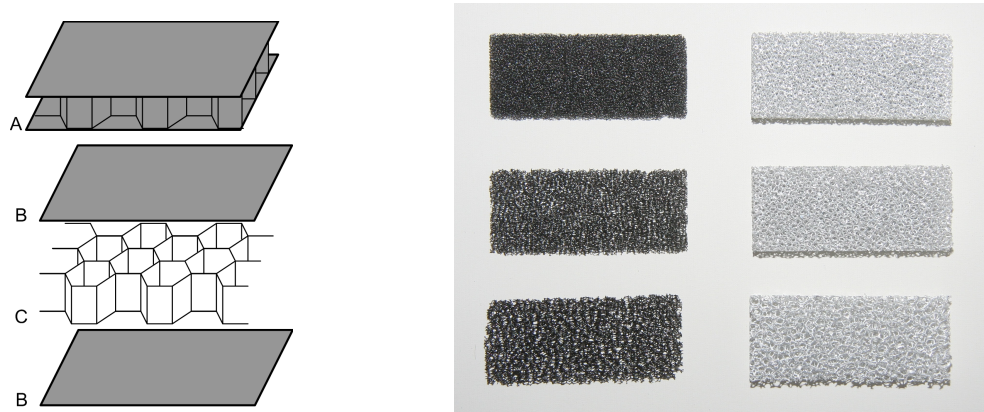


**Figure 10.2: Left:** Composition of a solid metal–foam sandwich. Two solid sheets of aluminum (B) and aluminum foam (C) together form a rigid sandwich structure (A).
**Right:** Carbon fiber (black) and aluminum (silver) foam of different porosities.

Such foam material can not only be used for the overall support structure, but also for the module frame, i.e. as sensor carrier material.

## 10.3 Cooling Considerations

The cooling system of the CMS Tracker has to chill the whole tracker volume to $-10\,°C$ to keep radiation defects of the silicon sensors at a low level. Moreover, it has to dissipate approximately $33\,kW$ of power, produced by more than 73,000 APV chips . Thus, each module needs to be thermally connected to the pipes of the cooling system to dissipate the heat created by the front end chips. The cooling pipes themselves, the cooling inserts to establish the thermal contact, but also manifolds and the coolant liquid contribute to the total material budget in a negative way.

For CMS, a high cooling demand can hardly be avoided, since it is driven by both the radiation environment and the high APV clock frequency caused by the LHC bunch crossing time of 25 ns.

For the ILC, the cooling requirements are very different. Because of the 'clean' environment of $e^+e^-$ collisions the radiation levels will be much lower than for any LHC experiment. This means that the silicon sensors do not need to be cooled below room temperature. Moreover, the proposed time structure of the ILC beam (see previous chapter) allows to take advantage of intermitted operation to reduce the overall power dissipation.

### 10.3.1 Power Cycling

The pulse rate of the proposed International Linear Collider is 5 Hz. A few thousand single bunches of particles ('bunch train') are collided at the ILC within 1 ms. During this time, the collisions occur and the detectors need to be active. This time period is followed by another period of approximately 199 ms, where no collisions take place. If the FE electronics are switched off during the latter period and is powered on shortly before the bunch train collides in the experiment, the integrated power would be decreased by a factor of up to 200. Figure 10.3 shows a possible implementation. One has
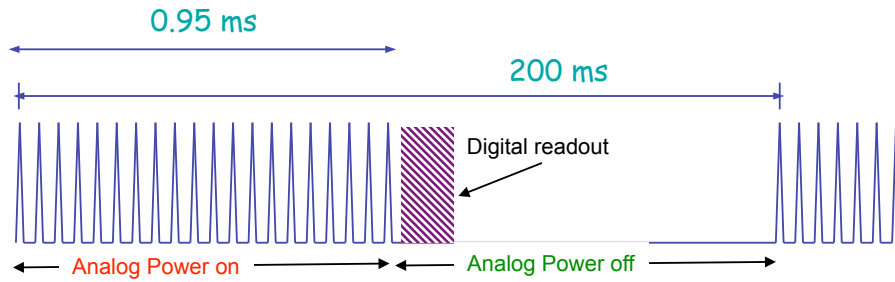


**Figure 10.3:** Beam structure of the ILC with power cycling option. During the time period between two bunch trains, the analog power of the front end electronics can be switched off to reduce the integrated power consumption.

to distinguish between analog and digital part of the front-end electronics. While the digital part is necessary for monitoring and configuration purposes and possibly for signal digitization, the analog part takes care of the signal path, comprising amplifier, shaper and analog pipeline. We assume that the FE electronics of such a detector will also contain signal digitization, avoiding analog signal paths to the off-detector electronics. A readout chip with these properties is already under development [103] and will eventually serve 512 or 1024 channels. Currently, using the 130 nm process technology, each channel has a power consumption of approximately 290 µW (preamplifier and shaper).

The total area of silicon strip detectors in the LDC detector concept will be 121 m$^2$ (see table 10.1 and [104]). Assuming strips with a pitch of 50 µm and an average strip length of 30 cm (via daisy-chained sensors), the total number of channels will be 8 million. Taking these numbers into account and assuming a (conservative) duty cycle of 1/100, the integrated (averaged) analog power will be only 23 W. In that case, an air ventilation cooling seems sufficient, and thus the material for cooling pipes, manifolds and their support can be saved.

| Endcap Layer | inner radius [cm] | outer radius [cm] | area [m$^2$] |
|---|---|---|---|
| FTD1 | 4 | 13,8 | 0.11 |
| FTD2 | 4.75 | 14 | 0.11 |
| FTD3 | 4.75 | 28 | 0.48 |
| FTD4 | 8.75 | 28 | 0.44 |
| FTD5 | 12.25 | 28 | 0.40 |
| FTD6 | 15.75 | 28 | 0.34 |
| FTD7 | 18.75 | 28 | 0.27 |
| ECT1 | 40 | 162 | 15.48 |
| ECT2 | 40 | 162 | 15.48 |

| Barrel Layer | radius [cm] | length [cm] | area [m$^2$] |
|---|---|---|---|
| SIT1 | 15 | 60 | 0.57 |
| SIT2 | 29 | 90 | 1.64 |
| SET1 | 151 | 440 | 41.75 |
| SET2 | 159 | 440 | 43.96 |

**Table 10.1:** Area of each silicon strip tracking layer in the LDC concept report, separated for barrel (left) and endcap regions (right).

However, possible drawbacks of this design have to be mentioned. Switching analog power of several thousands FE chips on and off with a rate of 5 Hz is a challenging task for a power supply system. To avoid oscillations, channels have to be individual switched on and off with different delays, with the disadvantage of losing time in the switching phase and thus increasing the net power consumption.

## 10.4 Novel Powering Schemes

The largest fraction in the material budget of the CMS Tracker is taken up by cables. In current silicon sensor tracking systems, each detector module is powered independently. For CMS, 1944 Multi-Service Cables (MSC) are needed to distribute power to all modules. Aluminum is used as conductor material in order to take advantage of the lower mass density and higher radiation length compared to copper. This minimizes the weight of the cables by 60 % with the drawback of a 30 % reduction of the electric conductivity. Nonetheless, copper Low Impedance Cables (LIC) are used for connecting the Tracker to the PSUs.

Alternative powering schemes have to be discussed to get rid of a large fraction of cables. One possible solution is to power a large numbers of detector modules using a single power cable and a constant current source, called *serial powering* (see figure 10.4). Module power is then derived locally using shunt regulators. ATLAS successfully tested this method already for a future upgrade of their tracking system with promising results [105]. This scheme would allow a reduction of cables by up to a factor of 50. Moreover, external voltage regulation via sense lines becomes obsolete. However, the local shunt regulators have to be inside the tracker volume taking space and dissipate some power itself. Another drawback is the possibility to lose all modules in the line if one shunt regulator fails. Other concerns are about noise pickup in the serial line in a huge system.

Another possibility to address the cabling problem is the use of higher voltages, somewhat similar to the high-voltage power lines in the electric power network. In this scenario, the modules are still powered independently, but by a higher voltage than actually needed by the FE electronics. This
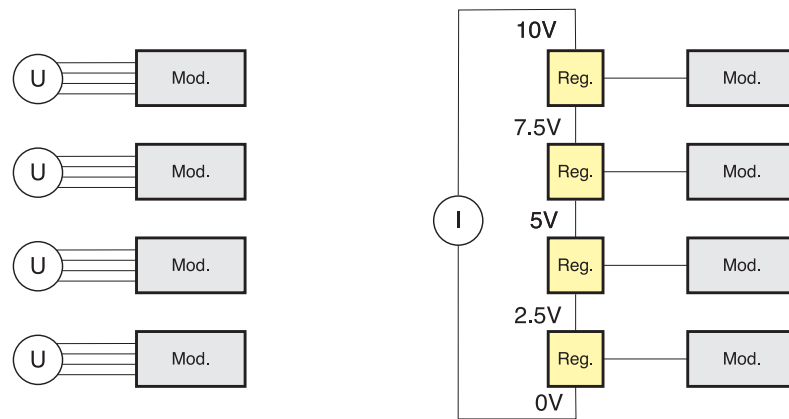
**Figure 10.4:** Conventional, parallel powering system (left) and serial powering scheme (right), where the modules (grey) are connected by shunt regulators (yellow).

implies thinner cables because of lower currents, and hence also the voltage drop inside the cables is of less concern. DC/DC converters have to be used locally to generate the low voltage levels actually needed by the FE electronics, with the drawback that additional heat from the converters has to be dissipated. It has to be evaluated if only one HV line for both the sensor bias and the DC/DC converter input is feasible. In this case the number of cables for one module is reduced to an absolute minimum.

Both solutions lead to an increased amount of electronics inside the tracker, either by shunt regulators or DC/DC converters, which generate additional heat themselves, which adds up to the cooling budget. On the other hand, both techniques reduce the total power loss in the cables which can be as high as the power actually delivered to the FE electronics using a conventional power system (This is the case for CMS).

## 10.5  Module Design Improvements

The basic building block of a semiconductor tracking detector is a silicon module. Up to now, a module design was always comprising the silicon sensor as the active detector element which was glued onto a frame. The electric connectivity of the strips to the readout chip was performed via wire-bonding, first from the sensor to a pitch adapter (PA) and then from the PA to the readout chip. This results in two rows of bond wires which are exhibited. Experience from CMS has shown that some bond wires were damaged on 10 to 15 % of the modules during their installation onto petals. Moreover, the pitch adapters and FE hybrids also contribute to the material budget. Hence, innovative module design could not only ease handling, but also minimize the radiation length.

## 10.5.1 Dual Metal Layer

Novel connection methods between the sensor and the readout chip are under investigation which reduce the material budget. A second metal layer in the silicon sensor can be used as an 'integrated' pitch adapter by providing routing lines directly on the sensor. This layer needs to be added on top of the strip metalization, but before the final passivation is applied. An oxide layer between the two metal layers acts as insulator. A similar approach was already successfully used for past experiments, e.g. the DELPHI microvertex detector [106].

The largest drawback of this idea are increased noise figures of such a detector system, since the extra strip length increases both the strip resistance and the capacitive load of the readout chip (compare section 3.9). In order to minimize the capacitance, a very thick oxide layer between the two metal layers would be required according to the equation of a parallel-plate-capacitor (see eq. 3.29), but is technologically challenging. Also cross-talk can degenerate the signal quality, if the routing lines cross many underlying readout strips. Detailed calculations are ongoing and test structures to measure the influence of various routing designs are currently under investigation.

## 10.5.2 Flip-Chip Bonding

Even with an integrated routing layer on the sensor, the connection to the readout chip is still possible via one row of wires bonds, but a more elegant solution would be a face-down mounting of the readout chip directly onto the sensor's bond pads, as it was already done for the CMS pixel detector (see figure 2.6 in the introduction). Usually such a method – often referred to as *flip-chip* technique – adds tiny solder balls on the chip pads in the last processing step, which then connect directly to the pads on the sensor provided by the routing layer. Obviously, the pitch and layout of the bond pads on both sensor and readout chip must match. The actual connection needs heat in order to melt the balls and establish the electric connection. The temperature necessary for this "reflow" needs to be kept at an absolute minimum since heat in the sensors causes diffusion processes which would deteriorate the detector behavior. A drawback of this method is that the sandwich compound cannot easily be repaired compared to bond wires. This technique requires very flat surfaces, which are not always easy to achieve, or sometimes difficult to maintain during heat-up and cool down.

For flip-chip bonding, two techniques have to be discussed separately.

### Fine Pitch Indium Bump-Bonding

A bump-bonding technology using Indium balls as conductor is currently used for fine pitches (e.g.[107]). Since it is a very cost-intensive process, which needs to have indium applied on the pads of both the sensor and the readout chip, it is only affordable in research. Figure 10.5 shows the sensor and the readout chip of the CMS pixel detector, after Indium has been applied and before both will be put together.
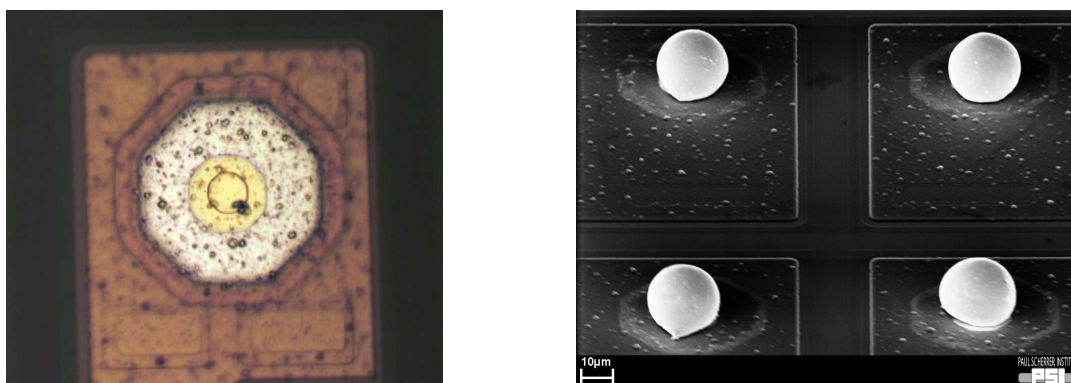
**Figure 10.5:** Indium bump bonding was used for the CMS pixel detector at PSI [107]. Indium balls were applied to pads of both the sensor (left) and the readout chip (right).

**Commercial Bump-Bonding Techniques**

For larger pitches, the so called Controlled Collapse Chip Connection (C4) using solder bumps was introduced by IBM already in 1964. A number of alternatives to the solder bumps have since been developed, including gold balls, molded studs or electrically conductive plastics. These techniques are affordable and thus suitable for industrial mass production. The only drawback is that the minimum pitch is between two to three times higher than for indium bump-bonding. Assuming a readout chip with 512 channels and a size of $1\,cm^2$, the pitch would be approximately $450\,\mu m$ if the pads were equally distributed across the total chip area, which is, however, not feasible in practice. Considering the APV25 as an example, its block diagram (see figure 6.6) already suggests a linear arrangement of the elements. The analog pipelines, each consisting of 192 cells, consumes about half of the actual chip size. Hence, the bond pads can only be located on small areas at the chip corners, which significantly decreases the pitch and bond pad size. Consequently, the application of commercial bump-bonding processes for HEP experiments is doubtful.

One promising technique is called stud-bonding and makes use of gold "studs" which are regular bonding wires thermo-compressed onto the aluminum pads and cut just above the ball. This avoids any so called Under Bump Metal on corresponding aluminum pads of the other component. Contact from the cut wire is made using either conductive adhesive film, or gold-to-gold ultrasonic bonding. In that latter case, though, gold bonding pads are needed on the bonding pads on both sides, but the use of ultrasonic energy extensively reduces the bond temperature and force [108].

## 10.5.3  Detector Thinning

Another method to achieve the necessary low material level inside the tracker is to thin the active detector material itself, this means to reduce the silicon sensor thickness from a typical $300\,\mu m$. Industry has shown that it is possible to achieve silicon films as thin as 30-50 μm. However, the detector signal scales linearly with the detector thickness. Thus, a thickness reduction to $50\,\mu m$

implies that it is also necessary to reduce the electronic noise in the detector system by a factor of 6 in order to maintain SNR. However, this will probably be hard to achieve, since techniques like the 'in-sensor routing' presented above, increase the length of the readout lines and thus the noise of the system.

Different approaches can be followed for detector thinning. Since there are no technologies for the direct production of ultra-thin wafers, standard wafers (e.g. with 300 µm thickness) need to be thinned. There are four primary methods for this: mechanical grinding, chemical mechanical polishing, wet etching and atmospheric downstream plasma dry chemical etching. Thanks to its high thinning rate, mechanical grinding is the most common technique at present. Such thinned wafers must then be attached to another wafer to increase their mechanical stability during the planar process, when ion implantation, oxide deposition and metal sputtering are performed on the top side.

Another possibility is to thin a fully equipped detector after all processing steps were performed on a wafer with normal thickness. This process is usually performed for wafers housing electronic chips, since the silicon bulk material has no operative function throughout its thickness, e.g. APV25 chips were successfully thinned to 50 µm thickness by grinding [109]. In case of a sensor, however, a treatment of the backplane is required after grinding to re-establish the $n^{++}$ and aluminum layers there. Since the $n^{++}$ layer is applied by thermal diffusion, it would require the wafer to be heated up with negative impact to the front side strips.

### 10.5.4 Double Sided Readout

Silicon strip sensors achieve a high spatial resolution along one coordinate, namely perpendicular to the strips. If a 2D hit information is needed, one must either use double sided strip detectors (DSSD), which have orthogonal strip implants on either side, or combine two single sided strip detectors (SSSD) in a way that their strip axes are rotated against each other (not necessarily perpendicular). In certain layers of the barrel and certain discs of the endcaps, CMS uses so called 'double-sided modules' comprising two normal sensor modules rotated by 100 mrad ($\approx 5.7°$).

**Stereo Modules**

Stereo modules are used in CMS. Two single modules are glued or screwed back-to-back together under a certain angle. The size of this angle determines the spatial resolution along the strip axis.

Looking to a coordinate system of two sensors rotated by the stereo angle $\alpha$ (see figure 10.6) and expressing the hit strip in one coordinate system in the other system, the z position of the hit (along the strips of the not rotated sensor) is calculated by

$$z = \frac{x_1}{\tan(\alpha)} - \frac{x_2}{\sin(\alpha)} \qquad (10.3)$$
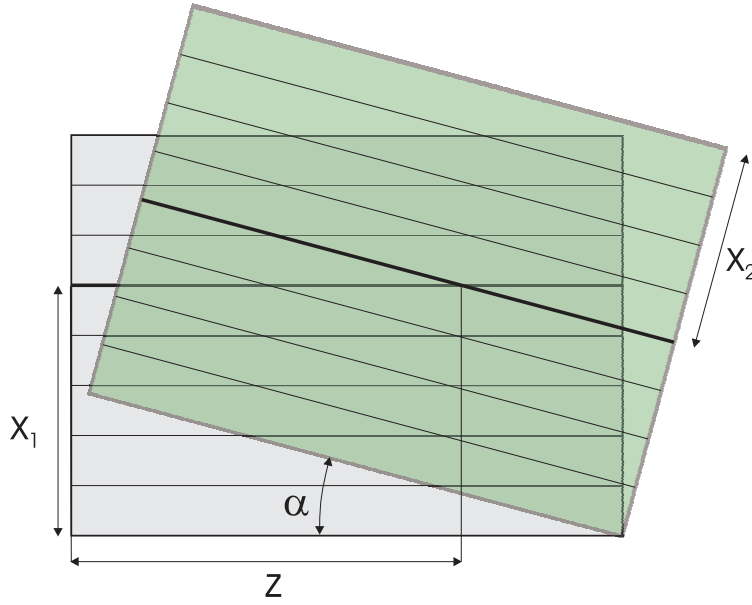
**Figure 10.6:** Principle of stereo modules: two sensors, rotated by an angle $\alpha$, allow the determination of the distance $z$ from the hit position $x_1$ and $x_2$.

where $x_1$ and $x_2$ are the hit positions (strip numbers) measured on each sensor on local coordinates.

Using the error propagation formula

$$\sigma_z = \left(\frac{\partial z}{\partial x_1}\right)^2 \sigma_1 + \left(\frac{\partial z}{\partial x_2}\right)^2 \sigma_2 \tag{10.4}$$

leads to the following equation for the resolution of two stereo sensors in z direction:

$$\sigma_z = \frac{\sigma_{r\phi}}{\tan\alpha} \sqrt{1 + \frac{1}{\cos^2\alpha}} \tag{10.5}$$

where $\sigma_{r\phi}$ is the resolution achieved on each sensor plane. In case of binary readout, it becomes to

$$\sigma_{r\phi} = \frac{\text{pitch}}{\sqrt{12}} \tag{10.6}$$

Figure 10.7 shows the $z$ resolution (assuming binary readout) as a function of the stereo angle $\alpha$ for various strip pitches. For a typical CMS sensor with a pitch of 80 µm and the stereo angle $\alpha = 5.73°$ (100 mrad), the resolution along the strip axis is 326 µm. Even for 50 µm pitch (at the same angle), the resolution is 204 µm. Larger angles would improve $\sigma_z$, but also imply complications in the module design.

For the desired precision of a future ILC experiment, however, the obtained resolution using a small stereo angle would not be sufficient. Thus, the only way to keep the resolution on a low level for both axes would be a stereo angle of 90 degree, which means that the modules have to be mounted perpendicular to each other.

## z resolution vs. stereo angle
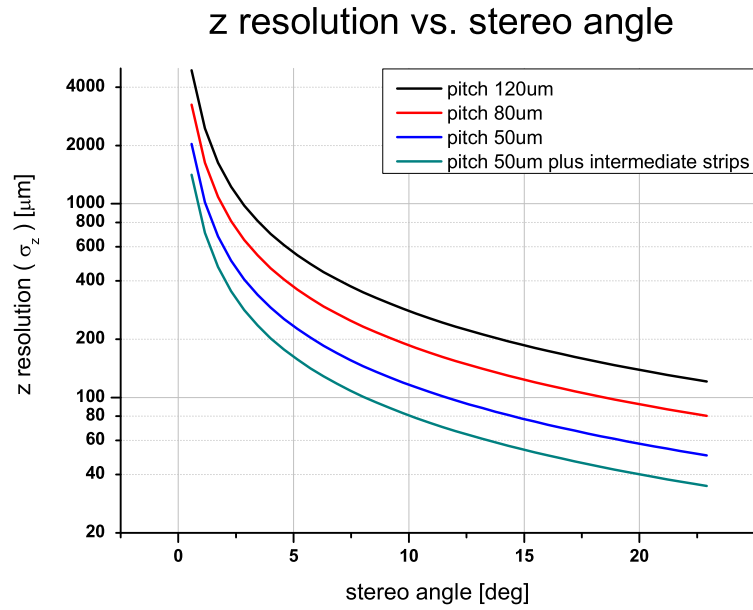


**Figure 10.7:** Resolution along the strips ($z$-direction) vs. angle $\alpha$ of a stereo module for different strip pitches.

In that way, the conventional FE electronics also needs to be mounted perpendicular to each other. Therefore, integrated routing lines in the sensor should at least allow the FE electronics to be on the same side. If two sensors are not affordable in terms of material budget, a single sensor with double sided readout (DSSD) must be taken into account.

### Double Sided Sensors

Double sided silicon sensors are segmented by strips on both sides of the wafer. A spatial point can be reconstructed for a traversing particle as both measured signals originate from the same charge cloud.

A problem in producing these kind of detectors is the insulation of the strips. The naive solution to simply segment the $n^+$ region fails. An electron accumulation layer builds up between the $n^+$ strips causing shorts between all strips. Thus, either *p-stop* or *p-spray* techniques have to be used to circumvent this problem. In the first one, $p^+$ strips are implemented around the $n^+$ strips, causing an insulation. In the latter case, a large-area $p$-type surface doping is applied to compensate the negative acceptor atoms preventing the formation of an accumulation layer.

Obviously, such sensors must be processed on both sides, adding complexity to the production, since all planar process machines are designed for single-sided processing only (as it is always sufficient in industrial semiconductor production). The extremely reduced yield caused many semiconductor detector vendors to abandon this technology. However, double sided sensors are essential components for keeping the material budget in the innermost tracking layers of an future ILC experiment on a low level.

### 10.5.5 Module Arrangement

The radial design of the CMS Tracker end caps (figure 10.8 left) suffers from the problem of many different module types. It happend several times during the module production that petal integration got stuck because of one particular module type missing. The modules for ring 1 are especially susceptible to this problem, since their total number is only 312, split into *normal* (R1N) and *stereo* (R1S) versions. During the module production, 6 % spares were produced on top of the installed quantity, driven by the number of ordered sensors. This results in only 9 spare modules for each type, R1N and R1S, respectively. If one single transfer box – usually containing nine modules – would have been lost during shipping, all available spares would have been eaten up.

To circumvent similar problems in the future, a design as shown in the right drawing of figure 10.8 should be foreseen. It takes advantage of only one module type which can be produced in masses reducing the risks described above with the drawback that the modules have to overlap the fiducial end cap radius.
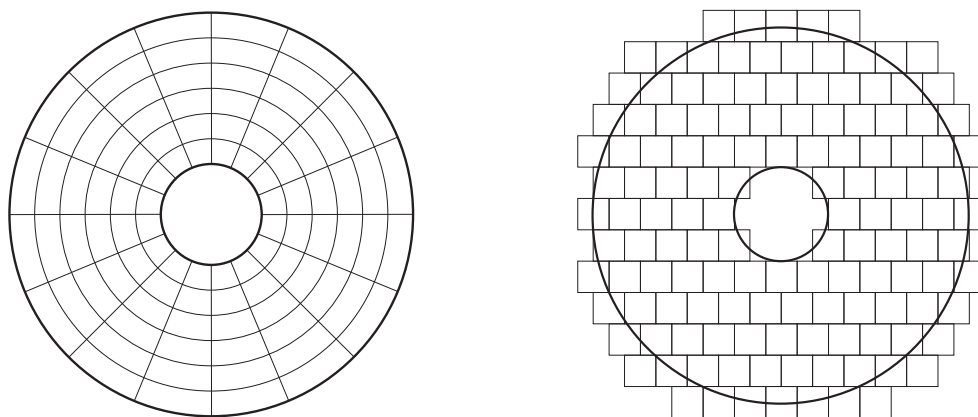


**Figure 10.8:** End cap layout as it was used for CMS and other experiments with radial module arrangement (left) and alternative layout using rectangular modules (right).

## 10.6 Sensor Design for ILC Experiments

Currently, research and development is starting to implement all considerations presented in the previous sections in actual devices and to test their feasibility. A lose collaboration with the name *Silicon for the Linear Collider* (SiLC) was formed by groups and institutes interested in these developments[1]. Their aims are described in the *Memorandum of Agreement* (MoA) as "*to carry out a rigorous R&D program geared towards a viable design of the overall tracking system for an LC detector both in the case it is associated to a TPC central tracker (as in LDC and GLD detector concepts) or it makes a whole Silicon tracker such as proposed in the SiD detector concept. Independent of the detector concept the main requirements for the tracking system are high performances*

---

1. More information about SiLC can be found at `http://silc.in2p3.fr/`.

*in impulsion and spatial resolutions together with a very low material budget and full detector coverage. Important breakthroughs on electronics, sensor technology, mechanics and detector design are requested to achieve these goals*" [110].

### 10.6.1 Work Program

To achieve the goals of the SiLC MoA in terms of sensors, considering material reduction and high precision needs, a work program was defined, which is basically divided into two steps.

Step 1 has already been started and comprises mostly preparatory steps for the long term goals, in particular building silicon detector modules with fine pitch and long strips. Another important point is to improve the test structures and test setups to allow effective testing and determination of process parameters during sensor production. Along this, tests of new readout chips are foreseen, which are utilizing DC coupling and the power cycling technique (see 10.3.1).

The next step, starting in 2009, is separated into three objectives: a) To build silicon detectors with in-sensor routing by an additional metal layer and to test the crosstalk and capacitive load of those sensors. b) Vendors interested in double sided sensors for the inner detector layers will be asked to build prototypes of those sensors, possibly utilizing internal routing layers as well. c) To start a similar program for larger sensors made on 8" or even 12" inch wafers necessary for external layers around the TPC. For cost reduction of those sensors, the use of DC coupling should also be evaluated.

### 10.6.2 SiLC Sensor Baseline

Key parameters for silicon strip sensors were defined in order to get comparable results when different sensor producers will be evaluated. These parameters are called *baseline design* and describe electric parameters only, leaving the process parameters up to the producer.

Since future silicon strip sensors for the ILC will need a very high resolution, a fine readout strip pitch is required. A strip pitch of 50 μm was chosen in balance between high resolution and feasibility. A smaller pitch becomes complicated in terms of wire bonding, probing the strips with needles, but also because of the fact that the charge generated by particles traversing the detector is shared by too many strips reducing the effective S/N ratio. Intermediate strips in between the readout strips, resulting in 25 μm pitch, are also considered.

The sensor bulk material is agreed to be *p*-on-*n* float zone silicon, which means that there are $p^+$ implanted strips in *n*-type bulk material, which should be of high resistivity (5-10 kΩ cm) and rather thin (100-300 μm). However, the lower limit of the thickness is given by the noise behavior of the readout chip.

The detector must have a very low dark current of <1nA per strip, since the noise is mostly defined by the dark current and bias resistors. This implies very high values for the bias resistor in the order

of 20 to 50 MΩ, realized either using poly-silicon, punch-through (PT) or FOXFET technique. While poly-silicon was chosen for LHC (since it tolerates more radiation), PT or FOXFET would be cheaper, but need to be evaluated.

## 10.6.3 HPK Sensor Order

A first implementation of the baseline design was accomplished by Hamamatsu, where 30 sensors were ordered. The wafer uses *n* bulk material with a resistivity between 6 and 7 kΩ cm. Poly-silicon resistors with $20 \pm 10\,\mathrm{M\Omega}$ were chosen as biasing method. Beside the main sensor, four large test structures and several smaller ones were implemented, which are shown in figure 10.9. The sensors were successfully tested and fully comply with the specifications. The IV curve of all
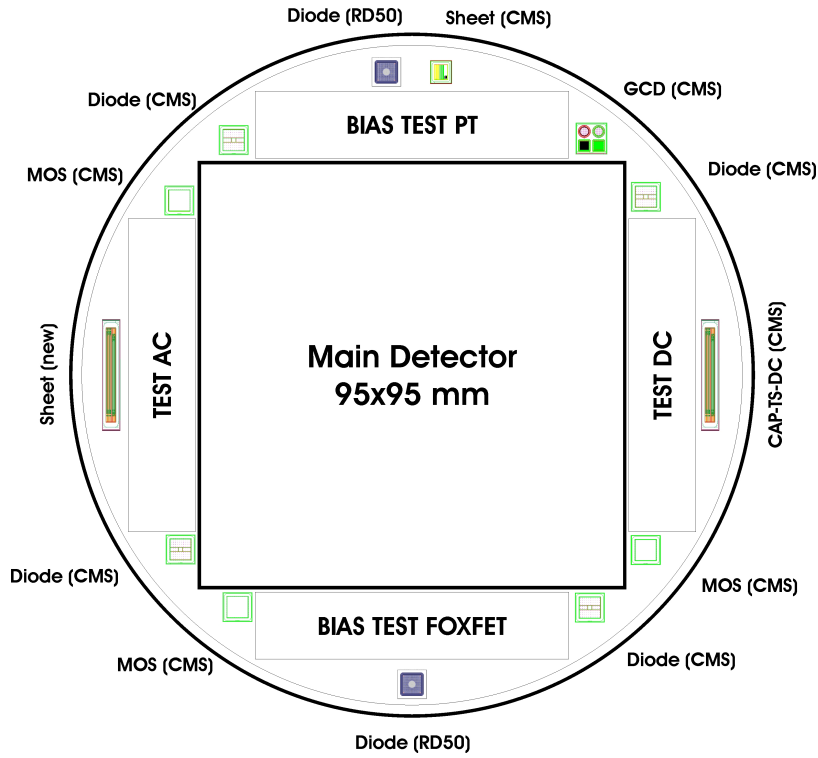


**Figure 10.9:** Layout of the wafer hosting the first detector following the SiLC baseline design. Four large test structures around the detector containing between 128 and 256 strips and several smaller test structures like diodes and MOS structures can be seen.

tested sensors is shown in figure 10.10 together with the distribution of the full depletion voltage obtained by both, HPK and our measurements. The sensors will be used to build modules for various purposes, e.g. a combined test of a prototype TPC together with silicon detectors at DESY [111].

Four test structures, located around the main detector, are intended for specialized purpose. Two of them, called *TESTAC* and *TESTDC* are geometrically identical. While the first one utilizes AC coupling of the strips by a dielectric layer, the latter one has the dielectric shorted and thus the strips are DC coupled. Both contain 256 strips with a pitch of 50 μm, which are arranged in 16
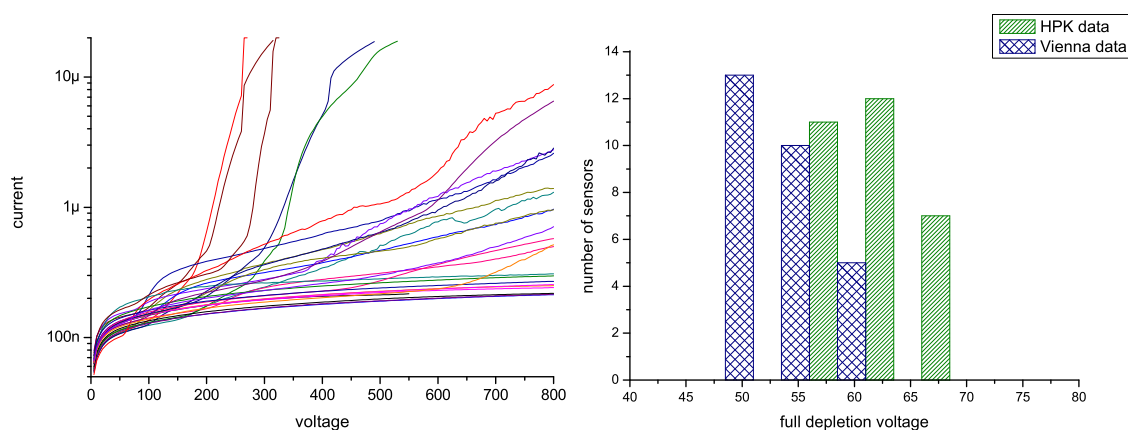
**Figure 10.10:** Results of IV measurements (left) and full depletion voltages (right) of the HPK sensors following the SiLC baseline.

groups. Within one group, each of the 16 strips has the same geometry, but the strip width and the configuration of the intermediate strips change from one group to the next, as shown in table 10.2. Both structures will be used to determine the configuration with the best resolution, by taking the hits in a beam telescope as reference while measuring the signal sharing within each group by the APV25 readout chip.

The other two large test structures consist of 128 strips, which are connected to the bias line either by the punch-through (PT) or FOXFET technique rather utilizing poly-silicon bias resistors. These structures will be used to determine the optimal biasing technique.

## 10.6.4  Improvement of Test Structures

Some effort already started to improve the test structures which were used during the CMS sensor production. Process monitoring using these structures worked extremely well, but the structures themselves had not been optimized in various aspects. One example is the sheet structure, which was used to measure the resistivity of poly-silicon, the implant and aluminum layer. Since the aluminum lines were too short, the measurement results were very low and in the same order as the contact resistance of the needles. Thus, it was almost impossible to disentangle the contact and wire resistance from the actual measurement results. By introducing either a 4-wire measurement of this parameter or by simply increasing the length of the lines, the measurement becomes much more reliable. It is evident that the structures have to be developed in parallel with the test stations and their capabilities in order to take most advantage of the measurements. Almost all test structures can be improved by similar methods like the one presented for the aluminum resistivity. Thus, a first iteration already started and structures with a slightly modified design were processed by ITE Warsaw[2], as shown in figure 10.11. After few more optimization steps we will be ready to include the finalized test structures to every wafer processing run, while collecting the results in a dedicated process parameter database.

---

2. The Institute of Electron Technology (ITE) in Warsaw is a major Polish research center with the primary focus on semiconductor micro- and nanotechnology. http://www.ite.waw.pl/

| group | number of strips | strip width [μm] | intermediate strips |
|:-----:|:----------------:|:----------------:|:-------------------:|
| 1     | 16               | 6                | no                  |
| 2     | 16               | 10               | no                  |
| 3     | 16               | 12.5             | no                  |
| 4     | 16               | 15               | no                  |
| 5     | 16               | 20               | no                  |
| 6     | 16               | 25               | no                  |
| 7     | 16               | 6                | single              |
| 8     | 16               | 7.5              | single              |
| 9     | 16               | 10               | single              |
| 10    | 16               | 12.5             | single              |
| 11    | 16               | 15               | single              |
| 12    | 16               | 17.5             | single              |
| 13    | 16               | 6                | double              |
| 14    | 16               | 7.5              | double              |
| 15    | 16               | 10               | double              |
| 16    | 16               | 12.5             | double              |

**Table 10.2:** Strip width and configuration of intermediate strip for the *TESTAC* and *TESTDC* structures, summing up to a total of 256 strips.

## 10.6.5 In-Sensor Routing

The next step in optimizing modules for the ILC is to move from conventional pitch adapters and FE hybrids to bump-bonding and in-sensor routing. As a first step, a collaboration with a wafer processing company (ON Semiconductor[3]) has started in order to process wafers with a second metal layer. Once they are ready, measurements on them will help to optimize the future layout in order to minimize the strip capacitance and cross talk, thus increasing the S/N ratio of a future module utilizing this routing technique.

---

3. ON Semiconductor located in Roznov (Czech Republic) is a supplier for a broad portfolio of semiconductors, electrical components and electronic devices. They produced part of the ATLAS pixel detectors and prototypes for the DELPHI microvertex detector. http://www.onsemi.com/
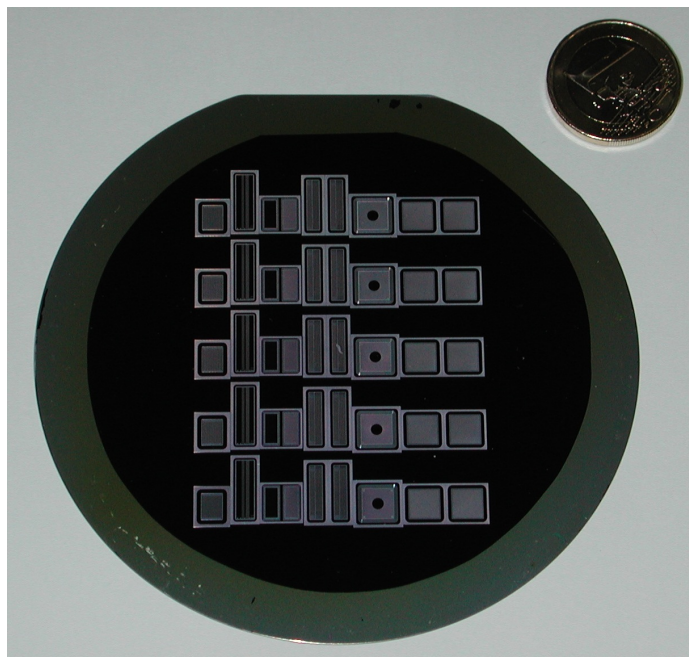
**Figure 10.11:** Wafer housing the first version of improved test structures.

# 11 Summary and Conclusion

> Well, we have frankly enjoyed
> more than anything these secret
> workings of natures.
>
> *(James Joyce in*
> *"Finnegans Wake")*

Curiosity is the stimulus of science. For fundamental research, the standard model of particle physics describes most observable attributes of our universe very well. However, there are still some open questions, which engage physicists to build stronger particle accelerators to look into more and more details of the fundamental constituents of atoms and the forces between them.

One questions is about the origin of mass of fundamental particles, which was explained by the theory of Prof. Peter Higgs already 40 years ago. However, its experimental verification still has to be performed. Similar things are true for questions of cosmology, e.g. why there is a huge excess of matter in respect to antimatter in the universe. Some questions even arose very recently, like for the origin of dark matter and dark energy, which both are proposed to be the largest constituents of the universe, much more than the baryonic matter we are made of. Some may also ask for the reasons of the different strength of the four fundamental forces and a possible unification at extremely high energy scales. Supersymmetric partners to the normal fundamental particles are possible candidates for dark matter and could also explain questions related to the force unification. However, no such particles have been observed yet.

## 11.1 Large Hadron Collider

In the next few years, science will make a huge leap forward in addressing some, or even many, of these problems by the largest and most complex machine ever built, the Large Hadron Collider. After a nine-year construction phase it will finally begin circulating beams of protons in summer 2008. Protons will be accelerated in opposite directions up to a center-of-mass energy of 14 TeV and collided at four interaction points.

The Compact Muon Solenoid (CMS) experiment is built around one of those interaction points (IP). It consists of different particle detectors, which are arranged in concentric layers around the IP, with the silicon pixel and strip tracking detector in the center, surrounded by electromagnetic and hadronic calorimeters and finally muon detection systems.

## 11.2 CMS Tracker

The CMS Strip Tracker is the largest tracking device ever built from silicon detectors. More than 800 people from all over the world were involved in its construction and commissioning. It comprises more than 24,000 silicon sensors, which had to be thoroughly tested in an initial step. The tools necessary for these tests had to be developed together with a database, storing all measurement results and taking care of logistics and inventory.

The Quality Test Centers were responsible for the overall test of the sensors. The system to perform strip-by-strip measurements of different electric parameters was developed particularly for testing of those senors. It worked very well for this purpose, but for future needs, e.g. to test sensors with finer strip pitch for the ILC, it needs to be adopted in terms of speed and flexibility.

The sensors were used to build modules and larger sub-structures, e.g. petals for the end caps. The module production was driven by the availability of the individual components at the module production centers. As there were many institutes involved, the logistics to provide each institute with the required parts at the right time was a complex task and took advantage of the logistics database and additional tools developed especially for this purpose. This situation was complicated by the high number of different module types as well. Since a relative percentage of spares was foreseen for each type, the absolute number of spares became very small for modules of the inner rings, where the total number of modules is low. The module production suffered from a high failure rate of almost 15 % mostly because of accidentally touched bonds. Thus, it was necessary to dis-assemble bad modules to save their sensors for re-use to avoid a cost-intensive additional order.

The commissioning of the CMS Tracker at CERN was the first common test of large, final substructures. In total, 2168 modules from all sub-detectors (about 14 % of the total number) were successfully operated. The aim of the test was not only to test these modules again, but also helped to gather experience in operating the detector system as a whole. Significant progress was made in different domains, e.g. the Tracker Control and Safety Systems (TCS and TSS), the online Data Acquisition (DAQ) and the Data Quality Monitoring (DQM). Almost 5 million cosmic muon events were recorded at different temperatures varying between $+15°C$ and $-15°C$, which were subsequently used for first analysis and alignment studies. Problems like noise pickup in the TOB sub-detector was successfully adressed during this test. At the end of the slice test in June 2007, the Tracker was ready for delivery to the CMS experiment as a "single scientific instrument". At the time of writing these sentences, the CMS Tracker is being connected to the services necessary for its operation, after it was successfully installed in the center of the CMS experiment (see figure 11.1).

Even if the first particles created by proton-proton collisions will be detected by the CMS Tracker in summer 2008, it will probably take years until the discovery of any new particle can be announced. This is partly caused by the fact that it is hard to specify detailed properties, e.g. of the Higgs particle within a high-luminosity event, because of the high background induced by the proton-proton interactions. For every bunch crossing at nominal luminosity, more than 1000 particles will be created in average.
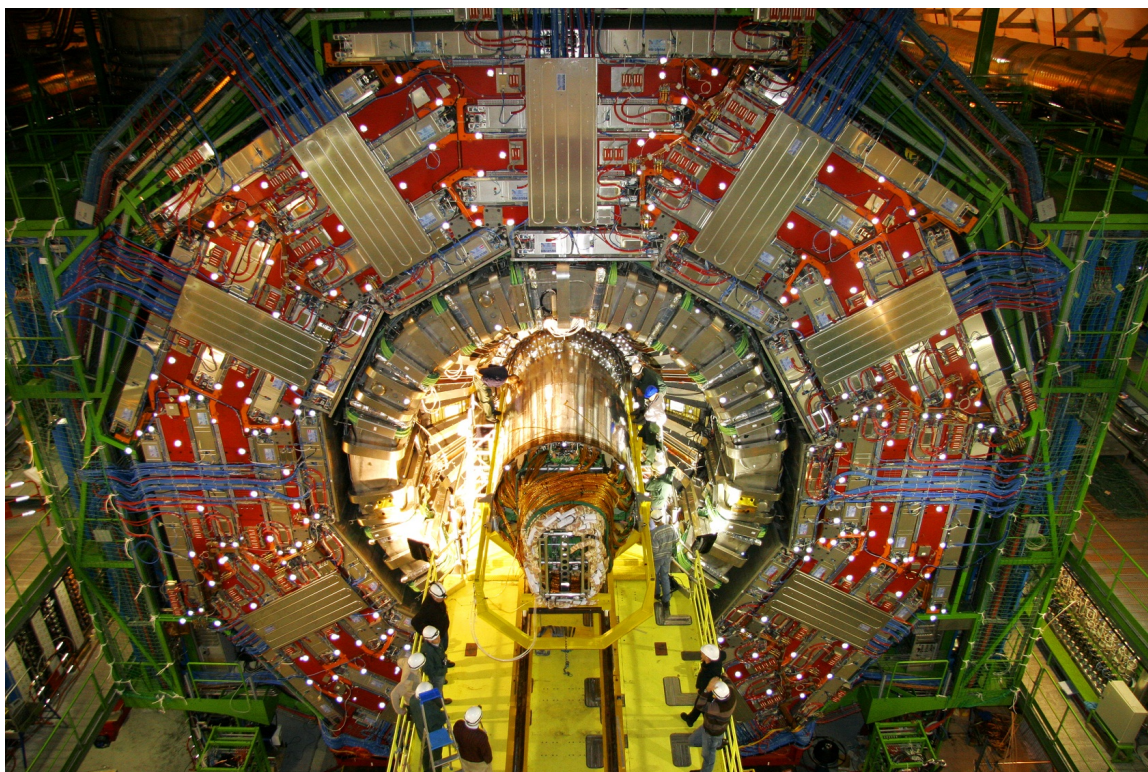
**Figure 11.1:** Installation of the CMS Tracker in the center of the experiment on December 21st, 2007.

## 11.3 International Linear Collider

The International Linear Collider (ILC) is being proposed for precision measurements of particles discovered by the LHC. It will collide electrons and positrons at $2 \times 500\,\text{GeV}$ in its first expansion stage, avoiding synchrotron radiation losses by its linear design. The ILC should repeat the success of the LEP accelerator, which performed precision measurements of the *W* and *Z* bosons, first discovered by its predecessor $Sp\bar{p}S$, a hadron accelerator.

According to the timescale, the ILC should become operational around 2020. Thus, R&D on its detectors have to start now, taking advantage of the experience gathered during the construction of the LHC and its experiments. Many problems encountered during assembly and commissioning of the CMS Tracker are still very well known by the involved people. Moreover, many components of the system were custom made with little documentation available. Before all this knowledge is lost, the key parameters and issues of the present design need to be evaluated to avoid the repetition of known problems for the ILC.

To achieve its design goal as a precision machine, the ILC has stringent requirements to the resolution of its tracking detectors. The most crucial point is multiple scattering caused by material inside the tracker. Thus, different approaches have to be followed to keep the material needed for cables, electronics and support structures on an absolute minimum.

Novel powering techniques are under investigation in order to reduce the cables. One method, called serial powering, drives a constant current through a cable line, allowing the modules to create their needed supply voltages by shunt regulators by themselves. A large fraction of material in the CMS Tracker is caused by cooling pipes. At the ILC, power cycling of the FE electronics would help to keep the average power consumption on a low level. It has to be investigated whether air cooling will be then sufficient. Improvements of the sensor design, e.g. by adding a second metal layer for signal routing, would help to abandon pitch adapters in future modules. If bump-bonding techniques can be adapted and afforded, the readout chips can directly be placed onto the sensor, and the front end hybrids can be saved as well.

The enormous effort which will be necessary to design and evaluate techniques for the future ILC, though, should not prevent us to follow the exciting discoveries the LHC will make – hopefully soon.

# Acknowledgements

# Appendix A

# TrackerDB Tables and Data

## A.1  Numbering scheme for object_id's

| 3 | 0 | 2 | 2 | 0 | 6 | 5 | 1 | 8 | 0 | 3 | 8 | 0 | 6 |
|---|---|---|---|---|---|---|---|---|---|---|---|---|---|
| 1 | 2 | 3 | 4 | 5 | 6 | 7 | 8 | 9 | 10 | 11 | 12 | 13 | 14 |

digit 1:

| 1 | ALICE |
|---|---|
| 2 | ATLAS |
| 3 | CMS |
| 4 | LHCb |
| HC | LHC |

digit 2-3:

| 01 | Pixel |
|---|---|
| 02 | Tracker |
| 31 | EB |
| 32 | EE |
| 33 | ES |
| 04 | HCAL |
| 05 | Muon |
| 06 | RPC |
| 07 | Alignment |
| 08 | Magnet |
| 09 | Infrastructure |
| 10 | TriDAS |
| 11 | Offline |
| 12 | Luminosity |
| 90 | General Purpose |

digit 4:

| 1 | STM |
|---|---|
| 2 | HPK |

digit 5-6:

| 01 | IB1 |
|---|---|
| 02 | IB2 |
| 03 | OB1 |
| 04 | OB2 |
| 05 | W1 |
| 06 | W2 |
| 07 | W3 |
| 08 | W4 |
| 09 | W5A |
| 10 | W5B |
| 11 | W6A |
| 12 | W6B |
| 13 | W7A |
| 14 | W7B |
| 15 | W1tid |
| 18 | W4S |
| 20 | W6BS |

**Figure A.1:** Numbering scheme of the 14 digits of the object_id for the LHC [112]. This example shows the object_id of a HPK silicon sensor of type W2. Each group of digits of the object_id have different meanings. Digits 1 to 6 are described by the tables. Digit 7 is the last character of the production year (200x), digit 8-12 are the production batch of the vendor and the last digits 13-14 are the sensor number within this batch.

## A.2 History Table

The table A.1 shows the results of the following query for a particular object_id (30200020026989):

```
select * from history where object_id=30200020026989
```

In this example, the object is an module which has been built in Santa Barbara and was shipped to different centers later.

## A.3 TrackerDB Main Tables

| OBJECT_ID | POSITION | TRANSFER_ID | CURRENT_ACTION | CURRENT ACTION VERSION | CENTER | FAULTY | SEQUENCE | HISTORY_ID |
|---|---|---|---|---|---|---|---|---|
| 30200020026989 | ready | | Registration | 1 | SANTA-BARBARA | F | 20.02.2004 18:25 | 230102 |
| 30200020026989 | running | | GANTRYVAL | 1 | SANTA-BARBARA | F | 21.02.2004 12:01 | 230148 |
| 30200020026989 | ready | | GANTRYVAL | 1 | SANTA-BARBARA | F | 21.02.2004 22:56 | 230156 |
| 30200020026989 | ready | | GANTRYVAL | 1 | SANTA-BARBARA | F | 24.02.2004 14:30 | 232775 |
| 30200020026989 | ready | | MODBOND | 1 | SANTA-BARBARA | F | 03.03.2004 20:26 | 240831 |
| 30200020026989 | shipping | 30299990001074 | MODBOND | 1 | COURIER | F | 09.03.2004 18:54 | 250607 |
| 30200020026989 | ready | 30299990001074 | shipping | 1 | AACHEN-1 | F | 16.03.2004 14:31 | 257690 |
| 30200020026989 | shipping | 30299991000460 | shipping | 1 | COURIER | F | 03.08.2004 17:31 | 454156 |
| 30200020026989 | ready | 30299991000460 | shipping | 1 | AACHEN-3B | F | 03.08.2004 17:35 | 454206 |
| 30200020026989 | faulty | | FREEACTION | 1 | AACHEN-3B | T | 17.09.2004 17:22 | 493953 |
| 30200020026989 | ready | | FREEACTION | 1 | AACHEN-3B | T | 11.10.2004 17:56 | 511057 |
| 30200020026989 | ready | | REPAIR | 1 | AACHEN-3B | F | 11.10.2004 18:00 | 511314 |
| 30200020026989 | faulty | | FREEACTION | 1 | AACHEN-3B | T | 18.03.2005 14:15 | 716880 |
| 30200020026989 | shipping | 30299990004358 | FREEACTION | 1 | AACHEN-3B | T | 19.04.2005 14:07 | 772830 |
| 30200020026989 | ready | 30299990004358 | shipping | 1 | AACHEN-REPAIR | T | 19.04.2005 14:14 | 772895 |
| 30200020026989 | ready | | MODVALIDATION | 2 | AACHEN-REPAIR | T | 09.06.2005 14:23 | 869454 |
| 30200020026989 | shipping | 30299990004382 | MODVALIDATION | 1 | COURIER | T | 14.06.2005 9:32 | 884413 |
| 30200020026989 | ready | 30299990004382 | shipping | 1 | KARLSRUHE-IEKP | T | 16.06.2005 9:22 | 891178 |
| 30200020026989 | shipping | 30299990009818 | shipping | 1 | COURIER | T | 30.03.2006 14:58 | 1464134 |
| 30200020026989 | ready | 30299990009818 | shipping | 1 | VIENNA | T | 30.03.2006 14:59 | 1464160 |
| 30200020026989 | ready | | MODVALIDATION | 2 | VIENNA | T | 25.10.2007 10:28 | 2082843 |
| 30200020026989 | shipping | 30299990010696 | MODVALIDATION | 1 | COURIER | T | 25.10.2007 10:50 | 2082848 |
| 30200020026989 | ready | 30299990010696 | shipping | 1 | AACHEN-1 | T | 26.10.2007 16:55 | 2083005 |

**Table A.1:** Table *history* showing the results for a query for a particular module.

| column name | description |
| --- | --- |
| OBJECT_ID | object_id of the treated object |
| POSITION | shipping, running, ready, faulty, |
| | (ready_for_action, ready_for_shipping) |
| TRANSFER_ID | contains the transfer_id if the |
| | history entry belongs to a transfer |
| CURRENT_ACTION | Registration, Assembly, De-assembly, |
| | type change, version change, shipping |
| | or any elementary ACTION |
| CURRENT_ACTION_VERSION | elementary ACTION version (1,2,...) |
| CENTER | one of the center listed in the |
| | table center_description |
| FAULTY | false (not faulty) or true (faulty) |
| SEQUENCE | date and timestamp when each entry was inserted |
| HISTORY_ID | integer number acting as |
| | primary key for the table |

**Table A.2:** Field description of the history table.

| column name | description |
| --- | --- |
| OBJECT_ID | object_id of the treated object |
| OBJECT | one of 44 objects, e.g. SEN, HYB, MOD, AOH; |
| | but also ROD, PETAL, TEC and TOB |
| TYPE | type identifier of the object. Depends on |
| | the object, e.g. 14.2 for sensors |
| VERSION | version number, e.g. 1,2 or 99 for sensors |
| CONTAINER_ID | object_id of parent when this object_id |
| | is assembled into a larger structure |
| NUMBER_IN_CONTAINER | position when more than one |
| | object is needed to build a composite object |

**Table A.3:** Field description of the object_assembly table.

| column name | description |
| --- | --- |
| OBJECT | one of 44 objects, e.g. SEN, HYB, MOD, AOH; |
| | but also ROD, PETAL, TIB, TEC and TOB |
| TYPE | type identifier of the object. Depends on |
| | the object, e.g. 14.2 for sensors |
| VERSION | version number, e.g. 1, 2 or 99 for sensors |
| DESCRIPTION | verbose (text) description of the object |
| TYPE_DESCRIPTION | matches to TYPE. e.g. 'W7B' for |
| | TYPE=14.2 for sensors |
| VERSION_DESCRIPTION | verbose (text) description of the version |

**Table A.4:** Field description of the object_description table.

| column name | description |
|---|---|
| TRANSFER_ID | 14 digit number (special object_id) identifying a transfer. The format of transfer_ids is 3029999* (often printed as barcode on the shipping box) |
| RECEIVER | center receiving the transfer |
| CARRIER | name of the carrier, which is a "virtual" center. (typically called "COURIER") |
| SENDER | center issuing the transfer |
| ISSUED_AT | date and time when the transfer was inserted |
| ARRIVED_AT | date and time when the transfer reception has been acknowledged |
| DESCRIPTION | verbose text describing the shipment, e.g. airway bill number |

**Table A.5:** Field description of the transfers table.

| column name | description |
|---|---|
| OBJECT_ID | object_id of the treated object |
| TEST_ID | primary key of the table. Linked to the column *test_id* of the history table |
| TOOL_ID | number describing the measurement setup. linked to table *tool_description* |
| PARENT_ACTION | name of the composite action table (e.g. VALIDATION) |
| INPUT_ID | number describing the version of the action table. linked to table *action_input_description* |
| TDATE | date and time of the measurement |
| ⋮ | |
| ⋮ | [further columns with actual measurement |
| ⋮ | results; e.g. v_depl_v or v_break_v,... ] |
| ⋮ | |
| CVTEST_VAL | conformity flag, e.g. *:0:* (test passed) ,or *:-1:* (failed) |
| STATUS | *valid* or *reference*. Only the latest entry has *reference* state, older measurements are *valid* |
| TCOMMENT | space for comment text |

**Table A.6:** Field description for action tables.

## A.4  Oracle Connection Credentials

The connection credentials to connect to TrackerDB using Oracle client drivers are described by the contents of the tnsnames.ora file. The identifier to connect to the production database is called *CM-STRKDB*, while *PROD9* and *TEST10* are used to connect to the test database. The file is listed below. Its location on the server *dbserver.hephy.at* is `/home/oracle/9iR2/network/admin/`.

```
# TNSNAMES.ORA Network Configuration File:
# /home/oracle/9iR2/network/admin/tnsnames.ora
# Generated by Oracle configuration tools.

CMSTRKDB =
  (DESCRIPTION =
    (ADDRESS_LIST =
      (ADDRESS = (PROTOCOL = TCP)(HOST = ccdbcl01.in2p3.fr)(PORT = 1521))
      (ADDRESS = (PROTOCOL = TCP)(HOST = ccdbcl02.in2p3.fr)(PORT = 1521))
    )
    (LOAD_BALANCE = ON)
    (FAILOVER = ON)
    (CONNECT_DATA =
      (SERVER = DEDICATED)
      (SERVICE_NAME = cccmstrktaf.in2p3.fr)
      (FAILOVER_MODE =
        (TYPE = SELECT)
        (METHOD = BASIC)
        (RETRIES = 5)
        (DELAY = 2)
      )
    )
  )


PROD9 =
  (DESCRIPTION =
    (ADDRESS_LIST =
      (ADDRESS = (PROTOCOL = TCP)(HOST = cccmstrk.in2p3.fr)(PORT = 1521))
    )
    (CONNECT_DATA =
      (SID = cmstrk)
    )
  )


TEST10 =
  (DESCRIPTION =
    (ADDRESS_LIST =
      (ADDRESS = (PROTOCOL = TCP)(HOST = ccdbcl01.in2p3.fr)(PORT = 1521))
      (ADDRESS = (PROTOCOL = TCP)(HOST = ccdbcl02.in2p3.fr)(PORT = 1521))
    )
    (CONNECT_DATA =
      (SERVICE_NAME = ccdev10g.in2p3.fr)
    )
  )
```

# Appendix B

# Petals in the Tracker Endcaps

| TEC+ | Sector 1 Front | Sector 1 Back | Sector 2 Front | Sector 2 Back | Sector 3 Front | Sector 3 Back | Sector 4 Front | Sector 4 Back |
|---|---|---|---|---|---|---|---|---|
| Disc 1 | 30250100000001 | 30250300000037 | 30250100000080 | 30250300000017 | 30250300000011 | 30250300000062 | 30250300000099 | 30250300000011 |
| Disc 2 | 30250100000006 | 30250300000048 | 30250100000070 | 30250300000026 | 30250100000060 | 30250100000084 | 30250100000062 | 30250300000029 |
| Disc 3 | 30250100000045 | 30250300000020 | 30250100000049 | 30250300000095 | 30250100000081 | 30250300000016 | 30250100000083 | 30250300000051 |
| Disc 4 | 30250200000021 | 30250400000039 | 30250200000099 | 30250400000085 | 30250200000060 | 30250400000095 | 30250200000088 | 30250400000024 |
| Disc 5 | 30250200000046 | 30250400000033 | 30250200000093 | 30250400000034 | 30250200000057 | 30250400000009 | 30250200000047 | 30250400000044 |
| Disc 6 | 30250200000023 | 30250400000036 | 30250200000096 | 30250400000086 | 30250200000043 | 30250400000067 | 30250200000126 | 30250400000010 |
| Disc 7 | 30250200000147 | 30250400000003 | 30250200000070 | 30250400000037 | 30250200000095 | 30250400000080 | 30250200000050 | 30250400000100 |
| Disc 8 | 30250200000051 | 30250400000013 | 30250200000017 | 30250400000043 | 30250200000005 | 30250400000096 | 30250200000138 | 30250400000094 |
| Disc 9 | 30250200000028 | 30250400000051 | 30250200000071 | 30250400000099 | 30250200000139 | 30250400000057 | 30250200000097 | 30250400000005 |

| TEC+ | Sector 5 Front | Sector 5 Back | Sector 6 Front | Sector 6 Back | Sector 7 Front | Sector 7 Back | Sector 8 Front | Sector 8 Back |
|---|---|---|---|---|---|---|---|---|
| Disc 1 | 30250100000063 | 30250300000010 | 30250100000035 | 30250300000008 | 30250100000068 | 30250300000003 | 30250100000094 | 30250300000012 |
| Disc 2 | 30250100000096 | 30250300000006 | 30250100000019 | 30250300000032 | 30250100000023 | 30250300000083 | 30250100000073 | 30250300000090 |
| Disc 3 | 30250100000041 | 30250300000005 | 30250100000065 | 30250300000068 | 30250100000004 | 30250300000038 | 30250100000003 | 30250300000054 |
| Disc 4 | 30250200000068 | 30250400000011 | 30250200000032 | 30250400000090 | 30250200000018 | 30250400000022 | 30250200000140 | 30250400000098 |
| Disc 5 | 30250200000069 | 30250400000056 | 30250200000080 | 30250400000027 | 30250200000037 | 30250400000008 | 30250200000010 | 30250400000048 |
| Disc 6 | 30250200000016 | 30250400000097 | 30250200000130 | 30250400000021 | 30250200000077 | 30250400000052 | 30250200000004 | 30250400000091 |
| Disc 7 | 30250200000067 | 30250400000028 | 30250200000053 | 30250400000061 | 30250200000015 | 30250400000015 | 30250200000026 | 30250400000040 |
| Disc 8 | 30250200000031 | 30250400000066 | 30250200000012 | 30250400000049 | 30250200000007 | 30250400000068 | 30250200000063 | 30250400000012 |
| Disc 9 | 30250200000072 | 30250400000087 | 30250200000113 | 30250400000065 | 30250200000100 | 30250400000047 | 30250200000079 | 30250400000092 |

**Table B.1:** List of Petals in Tracker Endcap TEC+. Sector 2 and 3 were read out during the slice test.

| TEC- | Sector 1 Front | Sector 1 Back | Sector 2 Front | Sector 2 Back | Sector 3 Front | Sector 3 Back | Sector 4 Front | Sector 4 Back |
|---|---|---|---|---|---|---|---|---|
| Disc 1 | 30250100000088 | 30250300000091 | 30250100000032 | 30250300000075 | 30250100000078 | 30250300000007 | 30250100000026 | 30250300000080 |
| Disc 2 | 30250100000082 | 30250300000045 | 30250100000016 | 30250300000027 | 30250100000022 | 30250300000099 | 30250100000040 | 30250300000082 |
| Disc 3 | 30250100000020 | 30250300000100 | 30250100000014 | 30250300000077 | 30250100000075 | 30250300000073 | 30250100000071 | 30250300000004 |
| Disc 4 | 30250200000059 | 30250400000004 | 30250200000041 | 30250400000146 | 30250200000049 | 30250400000014 | 30250200000074 | 30250400000031 |
| Disc 5 | 30250200000061 | 30250400000069 | 30250200000064 | 30250400000002 | 30250200000014 | 30250400000055 | 30250200000011 | 30250400000006 |
| Disc 6 | 30250200000054 | 30250400000019 | 30250200000009 | 30250400000059 | 30250200000136 | 30250400000063 | 30250200000056 | 30250400000041 |
| Disc 7 | 30250200000129 | 30250400000081 | 30250200000045 | 30250400000026 | 30250200000001 | 30250400000076 | 30250200000081 | 30250400000025 |
| Disc 8 | 30250200000038 | 30250400000053 | 30250200000094 | 30250400000074 | 30250200000075 | 30250400000084 | 30250200000022 | 30250400000079 |
| Disc 9 | 30250200000066 | 30250400000060 | 30250200000089 | 30250400000089 | 30250200000065 | 30250400000064 | 30250200000085 | 30250400000038 |

| TEC- | Sector 5 Front | Sector 5 Back | Sector 6 Front | Sector 6 Back | Sector 7 Front | Sector 7 Back | Sector 8 Front | Sector 8 Back |
|---|---|---|---|---|---|---|---|---|
| Disc 1 | 30250100000092 | 30250300000044 | 30250100000043 | 30250300000064 | 30250100000009 | 30250300000076 | 30250100000054 | 30250300000035 |
| Disc 2 | 30250100000005 | 30250300000058 | 30250100000028 | 30250300000036 | 30250100000097 | 30250300000034 | 30250100000008 | 30250300000072 |
| Disc 3 | 30250100000024 | 30250300000041 | 30250100000055 | 30250300000092 | 30250100000100 | 30250300000050 | 30250100000085 | 30250300000043 |
| Disc 4 | 30250200000024 | 30250400000007 | 30250200000048 | 30250400000083 | 30250200000039 | 30250400000082 | 30250200000008 | 30250400000078 |
| Disc 5 | 30250200000106 | 30250400000016 | 30250200000013 | 30250400000077 | 30250200000086 | 30250400000088 | 30250200000002 | 30250400000150 |
| Disc 6 | 30250200000027 | 30250400000073 | 30250200000058 | 30250400000093 | 30250200000044 | 30250400000054 | 30250200000116 | 30250400000075 |
| Disc 7 | 30250200000090 | 30250400000050 | 30250200000082 | 30250400000018 | 30250200000035 | 30250400000062 | 30250200000092 | 30250400000072 |
| Disc 8 | 30250200000073 | 30250400000045 | 30250200000137 | 30250400000070 | 30250200000098 | 30250400000030 | 30250200000042 | 30250400000020 |
| Disc 9 | 30250200000040 | 30250400000141 | 30250200000083 | 30250400000042 | 30250200000030 | 30250400000123 | 30250200000078 | 30250400000032 |

**Table B.2:** List of Petals in Tracker Endcap TEC-

# Bibliography

[1] W.-M. Yao et al. *Review of Particle Physics*. Journal of Physics G, 33: 258–270, 2006. 1, 4, 34

[2] G. Arnison et al. *Experimental observation of isolated large transverse energy electrons with associated missing energy at $\sqrt{s}$ = 540 GeV*. Phys. Lett., B122: 103–116, 1983. 1

[3] G. Arnison et al. *Experimental observation of lepton pairs of invariant mass around $95\,GeV/c^2$ at the CERN SPS collider*. Phys. Lett., B126: 398–410, 1983. 1

[4] P. W. Higgs. *Broken symmetries, massless particles and gauge fields*. Phys. Lett., 12: 132–133, 1964. 1

[5] ALEPH Collaboration, DELPHI Collaboration, L3 Collaboration, OPAL Collaboration, and The LEP Working Group for Higgs Boson Searches. *Search for the Standard Model Higgs boson at LEP*. Physics Letters B, 565: 61–75, 2003. 1

[6] CMS Collaboration. *CMS Technical Design Report – The Electromagnetic Calorimeter*. CERN/LHCC 97-33, 1997. 5

[7] CMS Collaboration. *CMS Technical Design Report – The Hadronic Calorimeter*. CERN/LHCC 97-31, 1997. 6

[8] R. Gluckstern. *Uncertainties in track momentum and direction due to multiple scattering and measurement errors*. Nuclear Inst. and Methods in Physics Research, A, 24: 381, 1963. 9

[9] *CMS Physics – Detector Performance and Software*, volume 1 of Technical Design Report, 2006. CERN/LHCC 2006-001. 9, 125

[10] W. Erdmann. *The 0.25 μm front-end for the CMS pixel detector*. Nuclear Inst. and Methods in Physics Research, A, 549(1-3): 153–156, 2005. 10

[11] A. Furgeri. *Quality Assurance and Irradiation Studies on CMS Silicon Strip Sensors*. PhD thesis, Institut für Experimentelle Kernphysik, Universität Karlsruhe, 2005. IEKP-KA/2005-1. 10, 43, 44, 55

[12] K. Kloukinas, W. Bialas, F. Drouhin, C. Ljuslin, A. Marchioro, E. Murer, C. Paillard, and E. Vlasovc. *FEC-CCS: A common Front-End Controller card for the CMS detector electronics*. In Proceedings of the 12th Workshop on Electronics for LHC and Future Experiments, Valencia, September 2006. CERN. 11

[13] K. Gill, G. Dewhirst, R. Grabit, A. Sandvik, J. Troska, and F. Vasey. *80Mbit/s Digital Optical Links for Control, Timing and Trigger of the CMS Tracker*. In Proceedings of the 8th Workshop on Electronics for LHC Experiments, Colmar, September 2002. CERN. 11, 106

[14] M. Friedl. *Analog optohybrids for the readout of the CMS silicon tracker*. Nuclear Inst. and Methods in Physics Research, A, 518(1-2): 515–518, 2004. 11

[15] S. Baird, K. Bell, E. Corrin, J. Coughlan, C. Day, C. Foudas, E. Freeman, W. Gannon, G. Hall, R. Halsall, J. Salisbury, A. Shah, S. Taghavirad, and I. Tomalin. *The Front-End Driver Card for the CMS Silicon Strip Tracker Readout*. In Proceedings of the 8th Workshop on Electronics for LHC Experiments, Colmar, September 2002. CERN. 11, 130

[16] G. Lutz. *Semiconductor Radiation Detectors: Device Physics*. Springer, Berlin, 2007. ISBN: 3540716785. 15, 17, 27, 31

[17] S. M. Sze. *Physics of Semiconductor Devices*. Wiley & Sons, 1981. ISBN: 0471056618. 16, 29, 31, 33

[18] C. Kittel. *Einführung in die Festkörperphysik*. Oldenbourg, 2005. ISBN: 3486577239. 17, 20

[19] B. Sapoval and C. Hermann. *Physics of Semiconductors*. Springer, Berlin, 2003. ISBN: 0387406301. 19

[20] W.-M. Yao et al. *Review of Particle Physics – Passage of particles through matter*. Journal of Physics G, 33, 2006. 22, 23, 24, 161

[21] M. Friedl. *The CMS Silicon Strip Tracker and Its Electronic Readout*. PhD thesis, TU Wien, 2001. 594650 II. 25, 26, 50, 92, 94

[22] D. Landau. *On the Energy Loss of Fast Particles by Ionization*. In Collected Papers of L. D. Landau. Pergamon Press, Oxford, 1965. 25

[23] E. Barberis, N. Cartiglia, C. Levier, J. Rahn, P. Rinaldi, H. Sadrozinski, R. Wichmann, T. Ohsugi, Y. Unno, H. Miyata, et al. *Capacitances in silicon microstrip detectors*. Nuclear Inst. and Methods in Physics Research, A, 342(1): 90–95, 1994. 29, 46

[24] J. Härkönen, E. Tuominen, K. Lassila-Perini, M. Palokangas, M. Yli-Koski, V. Ovchinnikov, P. Heikkilä, L. Palmu, and S. Kallijärvi. *Processing and recombination lifetime characterization of silicon microstrip detectors*. Nuclear Inst. and Methods in Physics Research, A, 485(1-2): 159–165, 2002. 30

[25] B. V. Zeghbroeck, *Principles of Semiconductor Devices*. URL: http://ece-www.colorado.edu/~bart/book/. 30

[26] S. Ramo. *Currents Induced by Electron Motion*. Proceedings of the I.R.E. 27, 27: 584–585, 1939. see also http://www-physics.lbl.gov/~spieler/physics_198_notes_1999/PDF/IX-1-Signal.pdf. 34

[27] G. Lindström. *Radiation damage in silicon detectors*. Nuclear Inst. and Methods in Physics Research, A, 512(1-2): 30–43, 2003. 37, 38, 39

[28] P. M. S. Lazo, D.M. Woodall. *Silicon and silicon dioxide neutron damage functions*. Technical Report SAND87-0098, Sandia National Laboratories, 1987. 37, 38

[29] R. Wunsdorf. *Systematische Untersuchungen zur Strahlenresistenz von Siliziumdetektoren für die Verwendung in Hochenergiephysik-Experimenten*. PhD thesis, Universität Hamburg, 1992. 39

[30] M. Moll. *Radiation Damage in Silicon Particle Detectors*. PhD thesis, Universität Hamburg, 1999. DESY-THESIS-1999-040. 40, 41

[31] S. Yong Choi and F. Lehner. *What do we know about radiation damage in silicon detectors*. Technical Report D∅ note 3803, The D∅ Experiment, Fermilab, 2000. 40

[32] *Supply of Silicon Micro-Strip Sensors for The CMS Silicon Strip Tracker*, Invitation to Tender, 2000. IT-2777/EP/CMS. 43, 44, 45, 46, 47, 50, 51, 53, 65, 67, 70

[33] *Specifications for the Quality Control and Assurance of the CMS Silicon Sensors*, 2000. 45, 54, 70, 72

[34] T. Bergauer. *Process Quality Control of Silicon Strip Detectors for the CMS Tracker*. Master's thesis, TU Wien, 2004. 45, 46, 47, 50, 53, 55, 71

[35] S. Albergo, M. Angarano, P. Azzi, E. Babucci, N. Bacchetta, A. Bader, G. Bagliesi, A. Basti, U. Biggeri, C. Biino, et al. *Optimization of the silicon sensors for the CMS Tracker*. Nuclear Inst. and Methods in Physics Research, A, 466: 300–307, July 2001. 46

[36] L. Borrello, A. Messineo, E. Focardi, and A. Macchiolo. *Sensor design for the CMS Silicon Strip Tracker*. CMS Note 2003/020, 2000. 51

[37] R. Adolphi. *Construction and calibration of the laser alignment system for the CMS tracker*. PhD thesis, RWTH Aachen, 2006. 52, 148

[38] J. Agram, M. Angarano, S. Assouak, T. Bergauer, G. Bilei, L. Borrello, M. Brianzi, C. Civinini, A. Dierlamm, N. Dinu, et al. *The silicon sensors for the Compact Muon Solenoid tracker – design and qualification procedure*. Nuclear Inst. and Methods in Physics Research, A, 517(1-3): 77–93, 2004. 53, 54

[39] F. Hartmann. *The CMS all-silicon tracker – strategies to ensure a high quality and radiation hard silicon detector*. Nuclear Inst. and Methods in Physics Research, A, 478(1-2): 285–287, 2002. 54

[40] C. Piasecki. *Studien an Siliziumstreifendetektoren Und Deren Qualitätssicherung für CMS*. Master's thesis, Institut für Experimentelle Kernphysik, Universität Karlsruhe, 2001. IEKP-KA/2001-12. 55

[41] J. Hacker, T. Bergauer, M. Krammer, and R. Wedenig. *Development of an automatic characterisation system for silicon detectors*. Nuclear Inst. and Methods in Physics Research, A, 485(1-2): 61–66, 2002. 57

[42] T. Bergauer. *Monitoring of the Fabrication Process of Silicon Strip Sensors for Large Scale Productions*. In Proceedings of the International Symposium On Detector Development For Particle, Astroparticle And Synchrotron Radiation Experiments (SNIC 2006), Stanford Linear Accelerator Center, Stanford, California, 2006. SLAC-R-842 eConf: C0604032. 57

[43] M. Friedl. *TRHX Temperature and Humidity Measurement System Project*, 2001. 59

[44] E. Widl. *Results and Further Developments of the Qualification Procedures for the CMS Tracker Silicon Microstrip Sensors*. Master's thesis, TU Wien, 2004. 827364 II. 60, 84

[45] *Agilent 4284A Precision LCR Meter Operation Manual*, Japan, January 2000. 62

[46] T. Bergauer, J.-C. Fontaine, J.-M. Helleboid, and M. Krammer. *Long-term stability tests of Si strip sensors for the CMS tracker*. Nuclear Inst. and Methods in Physics Research, A, 494 (1-3): 205–209, 2002. 71

[47] F. Hartmann, T. Bergauer, J.-C. Fontaine, M. Frey, A. Furgeri, and M. Krammer. *Corrosion on silicon sensors*. Nuclear Inst. and Methods in Physics Research, A, 569(1): 80–83, 2006. 72

[48] E. Codd. *A relational model of data for large shared data banks*. Communications of the ACM, 13(6): 377–387, 1970. 73

[49] R. Brun and F. Rademakers. *ROOT, An Object-Oriented Data Analysis Framework*. 84

[50] S. Hänsel. *Quality of the CMS Tracker End Cap Silicon Strip Modules*. Master's thesis, TU Wien, February 2006. 91, 97, 98, 103

[51] M. French, L. Jones, Q. Morrissey, A. Neviani, R. Turchetta, J. Fulcher, G. Hall, E. Noah, M. Raymond, G. Cervelli, et al. *Design and results from the APV25, a deep sub-micron CMOS front-end chip for the CMS Tracker*. Nuclear Inst. and Methods in Physics Research, A, 466(2): 359–365, 2001. 92

[52] L. Jones, *APV25-S1 Users Guide Version 2.2*. URL: http://www.te.rl.ac.uk/med/projects/High_Energy_Physics/CMS/APV25-S1/pdf/User_Guide_2.2.pdf. 92, 95

[53] M. Raymond, *APV25 Power Consumption*. URL: http://www.hep.ph.ic.ac.uk/~dmray/pdffiles/Detailed%20APV25%20Power%20Consumption.pdf. 94

[54] C. Vander Velde. *Technical specification for the CMS Tracker silicon module pitch adapters*, 2002. IT-3050/EP/CMS. 96

[55] A. Honma et al. *An Automated Silicon Module Assembly System for the CMS Silicon Tracker*. 2002/005, 2002. 97

[56] L. Fiore. *The role of automation in the construction of the CMS silicon strip detector*. Nuclear Inst. and Methods in Physics Research, A, 473(1-2): 39–43, 2001. 97

[57] S. Costa. *Technical Specifications for Bonding of the CMS Silicon Tracker Modules*, 2001. CMS Tracker bonding working group internal note. 98

[58] T. Franke. *Development and Evaluation of a Test System for the Quality Assurance during the Mass Production of Silicon Microstrip Detector Modules for the CMS Experiment*. PhD thesis, RWTH Aachen, 2005. 98, 99

[59] M. Axer, F. Beissel, C. Camps, V. Commichau, G. Fluegge, T. Franke, C. Ilgin, J. Mnich, J. Niehusmann, M. Poettgens, et al. *Testing of FE Hybrids and Si detector modules for the CMS Tracker*. Nuclear Inst. and Methods in Physics Research, A, 485(1-2): 73–77, 2002. 99

[60] D. Oellers. *Kühlung des CMS Spurdetektors*. Master's thesis, I. Physikalische Institut B, RWTH Aachen, 2005. 105

[61] J. Troska et al. *Implementation of the timing, trigger and control system of the CMS experiment*. IEEE Trans. Nucl. Sci., 3(53): 834, 2006. 107, 120

[62] J.-C. Fontaine. *Production of the CMS Tracker End Cap sub-structures*. Nuclear Inst. and Methods in Physics Research, A, 581: 310–313, 2007. 109

[63] M. H. Zöller. *private communication*. 110, 111, 128

[64] R. Brauer. *Integration of the End Cap TEC+ of the CMS Silicon Strip Tracker*. PhD thesis, RWTH Aachen, in preparation, 2008. 112

[65] E. Chabert. *Intégration d'un bouchon du trajectographe silicium de l'expérience CMS et étude de la distribution de la masse invariante des paires de quarks top*. PhD thesis, Université Claude Bernard Lyon 1, 2007. 112

[66] D. Abbaneo et al. *Tracker Operation and Performance at the Magnet Test and Cosmic Challenge*. CMS Note 2007/029, 2007. 116

[67] A. Bocci, R. D'Alessandro, S. Paoletti, and G. Parrini. *The Powering Scheme of the CMS Silicon Strip Tracker*. In Proceedings of the 10th Workshop on Electronics for LHC Experiments, Boston, 2004. CERN. 118

[68] P. Azzi and L. Demaria. *Tracker Detector Performance and Simulation Tuning with Cosmic Ray Data at the Tracker Integration Facility*. CMS Note 2008/xxx (in preparation), 2008. 119, 121, 134, 137, 142, 145, 146

[69] H. van der Bij, O. Boyle, and R. McLaren. *S-LINK, a Data Link Interface for the LHC era*. In Xth IEEE Real Time Conference 97, Beaune, France, September 1997. 120

[70] J. Varela. *CMS L1 Trigger Control System*. CMS Note 2002/033, 2002. 120

[71] E. Widl. *private communication*. 124, 150

[72] M. Kozlovszky et al. *A TCP/IP transport layer for the DAQ of the CMS experiment*. Nuclear Inst. and Methods in Physics Research, A, 1-2(534): 125–129, 2004. 125

[73] R. Bainbridge, G. Baulieu, S. Bel, J. Cole, N. Cripps, C. Delaere, A. C. A. Jesus, F. Drouhin, J. Fulcher, A. Giassi, K. Gill, D. Giordano, L. Gross, K. Hahn, S. Mersi, L. Mirabito, M. Nikolic, V. Radicci, S. Tkaczyk, and M. Wingham. *Data acquisition software for the CMS strip tracker*. Journal of Physics: Conference Series, 2007. 125

[74] R. Bainbridge et al. *Commissioning and Calibrating the CMS Silicon Strip Tracker*. In Proceedings of the 12th Workshop on Electronics for LHC and Future Experiments, pages 419–423, Valencia, September 2006. CERN. 127

[75] R. Turchetta. *Spatial Resolution of Silicon Microstrip Detectors*. Nuclear Inst. and Methods in Physics Research, A, 335: 44–58, 1993. 130

[76] M. Friedl. *private communication*. 131

[77] CMS Tracker Alignment Group. *CMS Tracker Alignment at the Tracker Integration Facility*. CMS Note 2008/xxx (in preparation), 2008. 131, 146, 148, 149, 150

[78] *The CMS Offline WorkBook*. URL: https://twiki.cern.ch/twiki/bin/view/CMS/WorkBook. 132

[79] W. Adam. *Track and Vertex Reconstruction in CMS*. Nuclear Inst. and Methods in Physics Research, A, 582: 781–784, 2007. 132, 133

[80] R. Frühwirth. *Application of Kalman filtering to track and vertex fitting*. Nuclear Inst. and Methods in Physics Research, A, 262(2-3): 444–450, 1987. 133, 149

[81] S. Dutta, *Tracker Data Quality Monitoring*. URL: http://cern.ch/cms-btau-datahandling/Monitoring/. 133

[82] C. Lionidopulus. *Physics and Data Quality Monitoring at CMS*. In Proceedings of the Computing in High Energy and Nuclear Physics Conference, Mumbai, 2006. 133

[83] M. Raymond et al. *Final Results from the APV25 Production Wafer Testing*. In Proceedings of the 11th Workshop on Electronics for LHC and Future Experiments, pages 453–457, Heidelberg, September 2005. 134

[84] *Electronic Logbook (elog) of TIF runs*. URL: http://tacweb.cern.ch:8080/elog/. 134

[85] *TIF Run Summary*. URL: http://cmsmon.cern.ch/cmsdb/servlet/RunSummaryTIF. 134

[86] *DcsLastValue, a webpage providing slow control information.* URL: `http://cmsmon.cern.ch/cmsdb/servlet/DcsLastValue`. 134

[87] *The CMS Storage Manager.* URL: `https://twiki.cern.ch/twiki/bin/view/CMS/FilterUnitOutputHandling`. 135

[88] M. Mennea, I. Osborne, A. Regano, and G. Zito. *CMS Tracker visualization tools.* Nuclear Inst. and Methods in Physics Research, A, 548(3): 391–400, August 2005. 135

[89] N. DeFilippis, D. Giordano, G. Bagliesi, T. Boccali, A. Bocci, F. Palla, S. Sarkar, R. Bainbridge, and L. Mirabito. *Computing system for the Tracker Integration Facility.* CMS IN 2007/014, 2007. 135

[90] C. Noeding, *TIF data analysis – FNAL Reconstruction.* URL: `https://twiki.cern.ch/twiki/bin/view/CMS/TIFDataAnalysis_FNALReconstruction`. 137

[91] G. Kaussen. *Silicon Strip Detector Qualification on Integrated Substructures during the Commissioning of the Tracking System for the CMS Experiment.* PhD thesis, RWTH Aachen, in preparation, 2008. 139, 143

[92] *Event Display based CMS tracker DQM monitoring.* URL: `http://webcms.ba.infn.it/cms-software/cms-grid/index.php/Main/CMSTrackerVisualizationSoftware`. 140

[93] Y. Gotra, *Study on TOB wing noise.* URL: `http://indico.cern.ch/getFile.py/access?contribId=17&sessionId=2&resId=1&materialId=slides&confId=18486`. 144

[94] C. Delaere, *Pulse shape study – Results from the ISHA/VFS tuning.* URL: `http://indico.cern.ch/getFile.py/access?contribId=34&sessionId=4&resId=0&materialId=slides&confId=15910`. 144

[95] W. Adam and C. Noeding. *Track Reconstruction with Cosmic Ray Data at the Tracker Integration Facility.* CMS Note 2008/xxx (in preparation), 2008. 146, 147

[96] M. Boezio, V. Bonvicini, P. Schiavon, A. Vacchi, N. Zampa, D. Bergström, P. Carlson, T. Francke, P. Hansen, E. Mocchiutti, M. Suffert, M. Hof, J. Kremer, W. Menn, M. Simon, M. Ambriola, R. Bellotti, F. Cafagna, F. Ciacio, M. Circella, C. N. De Marzo, P. Papini, S. Piccardi, P. Spillantini, E. Vannuccini, S. Bartalucci, and M. Ricci. *Energy spectra of atmospheric muons measured with the CAPRICE98 balloon experiment.* Phys. Rev. D, 67 (7): 072003, Apr 2003. doi: 10.1103/PhysRevD.67.072003. 148

[97] V. Karimäki, T. Lampén, and F.-P. Schilling. *The HIP Algorithm for Track Based Alignment and its Application to the CMS Pixel Detector.* CMS Note 2006/018, 2006. 149

[98] E. Widl and R. Frühwirth. *A Large-scale Application of the Kalman Alignment Algorithm to the CMS Tracker.* Journal of Physics: Conference Series, 2007. 150

[99] M. Stoye. *Calibration and Alignment of the CMS Silicon Tracking Detector.* PhD thesis, Universität Hamburg, 2007. CMS TS-2007/017. 150

[100] *International Linear Collider – Reference Design report*, August 2007. 151, 154, 155, 162

[101] W. Scott. *The theory of small-angle scattering of fast charged particles.* Reviews of Modern Physics, 35: 231, 1963. 161

[102] R. Ranieri. *Tracker Geometry and Material Budget: Introduction & Overview.* Tracker Material Budget Review Meeting, 2008. 162

[103] T. P. J.F. Genat. *Silicon strip readout using deep-submicron technologies*. In Proceedings of the 12th Workshop on Electronics for LHC and Future Experiments, Valencia, September 2006. CERN. 164

[104] LDC Working Group: D. Kiseilewska et al. *Detector Outline Document for the Large Detector Concept*. 164

[105] M. Weber, G. Villani, M. Tyndel, and R. Apsimon. *Serial Powering of silicon strip detectors at SLHC*. Nuclear Inst. and Methods in Physics Research, A, 579(2): 844–847, 2007. 165

[106] V. Chabaud, P. Collins, H. Dijkstra, J. Gomez Cadenas, R. Keranen, S. Masciocchi, et al. *The DELPHI silicon strip microvertex detector with double sided readout*. Nuclear Inst. and Methods in Physics Research, A, 368: 314–332, 1996. 167

[107] C. Broennimann, F. Glaus, J. Gobrecht, S. Heising, M. Horisberger, R. Horisberger, H. Kästli, J. Lehmann, T. Rohe, and S. Streuli. *Development of an Indium bump bond process for silicon pixel detectors at PSI*. Nuclear Inst. and Methods in Physics Research, A, 565(1): 303–308, 2006. 167, 168

[108] C. Pang, K.-Y. Hung, and M.-L. Sham. *High Frequency Thermosonic Flip Chip Bonding for Gold-to-Gold Interconnection*. In 2004 Electronic Components and Technology Conference, pages 1461–1465, 2004. 168

[109] M. Pernicka. *private communication*. 169

[110] A. Savoy-Navarro for the SiLC Collaboration. *SiLC Memorandum of Agreement*. 173

[111] S. Haensel, T. Bergauer, M. Dragicevic, M. Krammer, T. Barvich, F. Hartmann, B. Ledermann, T. Müller, and H. Simonis. *SiLC Sensors for the Large Prototype TPC at DESY*. EUDET Memo 2007/028, December 2007. 174

[112] A. Ball. *CMS Numbering & labelling scheme*. proposals of June 2001, updated, May 2006. 185

# Curriculum Vita

## Thomas Bergauer

Schumanngasse 67/3/2
1170 Wien
email: thomas.bergauer@oeaw.ac.at

## Personal

|  |  |
|---:|:---|
| Birth: | 29 May 1975, Hollabrunn (Austria) |
| Nationality: | Austria |

## Education

| | |
|---:|:---|
| since Oct 2004: | Working for PhD in experimental particle physics. |
| Oct 2004: | Finished diploma study with degree "Diplomingenieur" (M.Sc.). |
| Mar. 1999: | Completed first section of study (roughly equivalent to B.Sc.) |
| Oct. 1995: | Start of study "technical physics" at the University of Technology, Vienna |
| 1994 to 1995: | Military service (Austrian Federal army) |
| June 1994: | Graduation from college ("Matura"), passed with distinction |
| 1989 to 1994: | Technical college ("HTL") for electronics, Hollabrunn |
| 1986 to 1989: | Grammar School ("Gymnasium"), Hollabrunn |
| 1982 to 1986: | Elementary school, Hollabrunn |

## Employment

| | |
|---|---|
| since Oct. 2001: | Institute of High Energy Physics of the Austrian Academy of Sciences, Vienna (semiconductor detectors group) |
| July to Sept 2000: | Summer Student at CERN |
| July to Aug. 1998: | Max-Planck-Institut für Physik, Munich (semiconductor detectors group) |
| 1991-1998: | during Summer of each year: internships at Siemens Corporation, Vienna (programming) |

## Others

| | |
|---|---|
| IT skills: | excellent knowledge of Linux and Networking; good knowledge of C programming and script languages like PHP, bash, Perl; excellent knowledge of SQL; good knowledge of Labview; fair knowledge of Fortran programming language |
| Mother Tongue: | German |
| Foreign Language: | fluent written and spoken English |